

Copyright
by
Chayawee Wangcharoenrung
2005

The Dissertation Committee for Chayawee Wangcharoenrung
certifies that this is the approved version of the following dissertation:

**Development of Adaptive Transducer Based on Biological Sensory
Mechanism**

Committee:

Raul G. Longoria, Supervisor

Richard H. Crawford

Mark F. Hamilton

Richard R. Neptune

Harold H. Zakon

**Development of Adaptive Transducer Based on Biological Sensory
Mechanism**

by

Chayawee Wangcharoenrung, B.Eng., M.S.

DISSERTATION

Presented to the Faculty of the Graduate School of
The University of Texas at Austin
in Partial Fulfillment
of the Requirements
for the Degree of

DOCTOR OF PHILOSOPHY

THE UNIVERSITY OF TEXAS AT AUSTIN

May 2005

Dedicated to my parents
Chaiyaporn and Wallapa Wangcharoenrung
Thank you for everything

Acknowledgments

After all these years, I've compiled quite a long list of people who have contributed in some way to the completion of this dissertation. I would like to express my sincere gratitude to them.

I am greatly indebted to Dr. Raul G. Longoria for his enthusiasm, guidance, and patience. Throughout my stay at the University of Texas, he provided encouragement, advice, good teaching, and lots of ideas. I would have been lost without him.

I wish to thank Dr. Mark F. Hamilton for allowing me to use the Acoustics and Transducers Laboratory, to conduct all experiments, and to call it “my second home” in Austin. The facility and condition of the laboratory have made my work and experimentations an excellent experience. I also would like to thank my dissertation committee members, Dr. Harold Zakon, Dr. Richard Crawford, and Dr. Richard Neptune for reading and providing comments for this dissertation.

I am forever grateful to my family for supporting me through these years. I would like to thank my mother, Wallapa, who always reminded me to take myself less seriously, my father, Chaiyaporn, who has always been a hard working role model, my sisters, Rapeesupa and Cheerakanya, who have taken good care of my parents while I have not been able to, and Pimwadee for all the encouragement and being the very special person she is.

I am indebted to many student colleagues for providing a stimulating and fun environment in which to learn and grow. I am especially grateful to students in the System Modeling and Experimentation Research Group, Dr. Nikolaos Kiritsis,

Dr. Hanzhong Zhang, Dr. Seyoon Kim, Gilberto Lopez, and Chinmaya Patil for all our useful discussions, Kai Zhang for being such a wonderful office mate, Bonnie Roberts, Michael Everitt, and Ravel Thai for helping me to refresh all my basic understanding of things.

Finally, I'd like to thank Mother Nature for creating such a complex and elegant sensor mechanism, which has always inspired and perplexed me. This makes me wonder if it is possible for humans to ever understand all her secrets.

C. Wangcharoenrung
Austin, Texas 2005

Development of Adaptive Transducer Based on Biological Sensory Mechanism

Publication No. _____

Chayawee Wangcharoenrung, Ph.D.
The University of Texas at Austin, 2005

Supervisor: Raul G. Longoria

An adaptive sensor concept and prototype has been developed based on a sensing element which is analogous to and inspired by the arrangement of outer hair cells and inner hair cells between the basilar membrane and tectorial membrane which form the organ of corti in mammalian cochlea. The bio-inspired design was supported by development of a bond graph model of the electromotility (active response) of outer hair cells. Outer hair cells perform like actuators and simulation results using this model are compared with physiological data found in the literature to verify its characteristic response. Insight gained from the model is used to develop a sensor structure analogous to the organ of corti and designed to measure acceleration. A piezoelectric bimorph was selected as the transducer basis, and a bond graph model of the bimorph in an accelerometer configuration was formulated to aid control design and simulation.

There is no published data regarding the type of information transmitted among the inner hair cells, outer hair cells, and brain. Consequently, a controller intended to adjust the adaptation process similar to what might exist in the cochlear system has been developed for the sensor and based on a model referenced adaptive

control algorithm. Simulations verify that the algorithm can successfully control and enhance performance of the sensor.

Practicability of the design is evaluated by a series of experiments on a prototype. This study focused on using a controller structure that was programmed, implemented, and tested using programmable logic based on FPGA technology. The experiments evaluated how well the adaptive sensor could meet a specified performance requirement. Implementation issues that arise, such as the need for differentiators in the adaptive controller or internal propagation of vibration within the sensor structure, hinder the tuning ability. Nevertheless, the trends indicate that the algorithm can meet the desired performance if certain limitations can be overcome. Finally, recommendations have been made for expansion of the research in such fields as an alternative structure for tuning, sensor networking, and reference sensor configuration.

Table of Contents

| | |
|---|------------|
| Acknowledgments | v |
| Abstract | vii |
| Chapter 1. Introduction | 1 |
| 1.1 Background | 3 |
| 1.2 Objectives | 9 |
| 1.3 Overview | 10 |
| Chapter 2. Hair Cells: Their Physiology, Mechanism, and Networks | 12 |
| 2.1 Hair cells | 12 |
| 2.2 Different kind of hair cell networks | 26 |
| 2.2.1 Network of hair cells as a mechanism for sound processing . . | 26 |
| 2.2.2 Network of hair cell function as an angular accelerometer . . . | 28 |
| 2.2.3 Network of hair cell function as a linear accelerometer | 29 |
| 2.2.4 Network of hair cell function as a mechanism for water wave pressor transducer | 31 |
| 2.2.5 Network of hair cell function as a electroreceptors | 32 |
| 2.3 Summary | 34 |
| Chapter 3. Dynamic System Modeling of Hair Cell | 36 |
| 3.1 Mechanical system model | 37 |
| 3.2 Mechanically gated apical potassium channels | 40 |
| 3.3 Potential gated basolateral potassium channels | 44 |
| 3.4 Dependence of plasma membrane potential on potassium and its channel | 48 |
| 3.5 Equivalent circuit model of hair cell | 50 |
| 3.6 Electromotility of plasma membrane | 52 |
| 3.6.1 One dimensional 2-port capacitor electromotility model | 54 |
| 3.6.2 Two dimensional 3-port capacitor: impedance method | 57 |

| | | |
|-------------------|---|------------|
| 3.6.3 | Two dimensional 3-port capacitor: the energy method | 61 |
| 3.7 | A bond graph model of the hair cell | 63 |
| 3.7.1 | Model Description | 63 |
| 3.7.2 | Simplified Bond Graph Model | 66 |
| 3.7.3 | Equation Formulation | 68 |
| 3.7.4 | Parameterization | 68 |
| 3.8 | Simulation and model verification | 69 |
| 3.9 | Parameters sensitivity analysis | 72 |
| 3.10 | Frequency response characteristics | 73 |
| 3.11 | Discussion | 77 |
| 3.12 | Summary | 78 |
| Chapter 4. | Biomimetic Sensor: A Design Discussion | 83 |
| 4.1 | Sensor classification | 83 |
| 4.2 | Desired performance and characteristic | 85 |
| 4.3 | Basic sensor structures | 87 |
| 4.3.1 | Microscale multiplates capacitive sensor | 87 |
| 4.3.1.1 | Simple multiplates capacitor structure | 88 |
| 4.3.1.2 | Rotating sensing capacitor plates micro force sensor | 92 |
| 4.3.1.3 | Parameterization | 97 |
| 4.3.1.4 | Dynamic response | 100 |
| 4.3.2 | Macroscale piezoceramic bimorph sensor | 103 |
| 4.3.2.1 | Piezoceramic bimorph | 104 |
| 4.3.2.2 | Bimorph constitutive relations | 107 |
| 4.3.2.3 | S-bender bimorph | 110 |
| 4.4 | Sensoriactuator accelerometer structure | 113 |
| 4.5 | Summary | 118 |
| Chapter 5. | Development of Adaptive Algorithms | 120 |
| 5.1 | Why use model reference adaptive control (MRAC)? | 120 |
| 5.2 | MRAC with gain scheduling controller design formulation | 122 |
| 5.2.1 | Adaptive rule using MIT gradient method | 125 |
| 5.2.2 | Adaptive rule using Lyapunov stability theory | 129 |

| | | |
|-------------------|---|------------|
| 5.2.3 | Gain scheduling integration | 133 |
| 5.3 | Adaptive controller for bimorph accelerometer | 134 |
| 5.3.1 | The plant | 134 |
| 5.3.2 | Reference model design | 137 |
| 5.3.3 | Feedback algorithm | 140 |
| 5.3.4 | Gradient method adaptive controller | 143 |
| 5.3.5 | A discussion on adaptive parameter reduction | 150 |
| 5.3.6 | Lyapunov rule adaptive controller | 153 |
| 5.4 | Simulations | 156 |
| 5.5 | Summary | 171 |
| Chapter 6. | Experimental Methodology, Apparatus, and Results | 173 |
| 6.1 | Design of experimental apparatus | 173 |
| 6.2 | Experimental set up | 179 |
| 6.3 | Determination of model parameters | 184 |
| 6.3.1 | Damping via logarithmic decrement | 184 |
| 6.3.2 | Comparison of predicted and measured sensing response . . . | 186 |
| 6.3.3 | Comparison of predicted and measured actuating response . . | 188 |
| 6.4 | Programmable logic gates for controller prototype | 190 |
| 6.4.1 | Amplitude quantization | 191 |
| 6.4.2 | Discrete time control | 192 |
| 6.5 | Experimental results | 195 |
| 6.6 | Discussion | 201 |
| 6.6.1 | Discussion of result | 201 |
| 6.6.2 | Sensor Calibration | 203 |
| 6.7 | Summary | 205 |
| Chapter 7. | Conclusion and Recommendation | 207 |
| 7.1 | Brief summary of the work | 207 |
| 7.2 | Original contribution of this study | 208 |
| 7.3 | Recommendation and future research | 209 |
| Appendix | | 213 |

| | |
|---------------------|------------|
| Bibliography | 218 |
|---------------------|------------|

| | |
|-------------|------------|
| Vita | 233 |
|-------------|------------|

Chapter 1

Introduction

Since the beginning of time, mankind has built sensors to make sense of the environment and actuators to cause events in the environment. Typically, these sensors and actuators are separate devices designed for function and by a mechanism thought most suitable. Sensors and actuators commonly have fixed structure and dynamic range resulting from mechanical constraints. It is conventionally taught that a ‘perfect’ sensor should have linear characteristics with infinite bandwidth so that measured signals can be conveniently related back to the physical variables of interest, has zero mass so that it does not affect the system it is installed on, occupies zero space so that it can be placed everywhere, has an infinite impedance such that it does not draw power from the system, and can operate without consuming any energy. Although newly invented technologies have allowed engineers to build sensors that approach these ideal attributes, it can be realized that perhaps the perfect sensor by this standard will be hard if not impossible to fabricate. A question then arises: Does a sensor has to have these criteria in order to be considered perfect?

Nature employs a different philosophy in sensor construction. It has been observed that natural sensors usually have nonlinear characteristics, flexible structure, narrow bandwidth, coupled with actuator, network arranged, very sensitive, and adaptive. Some of these qualities are clearly opposite to what have been considered as perfect as stated above. The acousticolateral system of vertebrate is particularly interesting due to its ubiquity among vertebrates and its many interesting sensory features that are not yet understood. All organs belonging to this system are built

around hair cells and their network structure. The success of this natural system may be inferred from its presence in various kinds of mammalian sensory organs such as in organ of corti, vestibular organ, and otolith organ. Similar forms of this mechanism are also present in the lateral-line organ and electroreceptors in aquatic animals. These organs are involved in animal activities such as hunting and body coordination. Hair cells in these organs are not only working in the role of sensing cells but also as effecting (actuating) cells. Both sensing and actuating cells in these organs are usually linked and arranged in a network.

It is proposed that borrowing ideas from what can be observed from these hair cell-based sensors might support building a class of sensor that exhibit those features found in natural hair cell sensory organs. A feature of particular interest is adaptation, the ability to change performance characteristics according to changes in the environment in a way that improves performance of the system. Although the adaptation mechanism(s) has not yet been understood fully in animal sensory systems, this mechanism has a dominant effect in most of their behavior. Recent understanding in engineered adaptive systems from control and systems theory is explored in the process of sensor design in order to mimic this behavior of nature.

It is expected that a concept for a modular sensor that can be arranged in many forms can be developed that will have an adaptation mechanism that can adjust its dynamic range and/or bandwidth yet with a simple structure that can be built small or large. This kind of sensor can have a significant impact in sensor development. For example, cost of production can be decreased since fewer model types need to be built. Adaptation can result in a more robust sensor that does not need frequent factory calibration, and an ability to arrange sensors in an array may provide means for designing data-efficient information streams by signal pre-processing in a way similar to that performed by a mammalian cochlea. The results

of this study may also have indirect impact in the field of natural science because it can be used as an example of how sensor and effector cells might communicate to achieve adaptation.

1.1 Background

Sensor technology is concerned with two activities: measurement and information processing [17]. Recently, there have been studies focusing on fundamental changes for enhancement of conventional sensor. Improvement from the measurement perspective has been addressed in the field of intelligent sensors and the information processing perspective has been addressed in the field of signal processing. These efforts also recognize a need to introduce such concepts as excitation control, amplification, filtering, data conversion, compensation, and processing into the system and some form of communication between measurement and information processing activities in order to heighten the measurement function.

Perhaps the most significant improvement in the field of displacement type sensors is the introduction of servo (force-balanced) sensing concept. This mechanism is built around a null detector circuit, amplifier, sensor, and actuator. The null detector infers motion and passes a feedback signal through an amplifier and to an actuator in order to provide a counterbalancing force required to maintain the null position. The feedback signal becomes the sensor output.

A force balanced micromachined pressure sensor by Gogoi and Mastrangelo [49] is a recent demonstration of the servo concept. From Figure 1.1 a), the mechanism is composed of 2 pairs of coupled capacitors with one used as a sensor and one as an actuator. When measured pressure P_0 begins to push the middle plate down, the sensing capacitive pairs detect changes in displacement. A charge pump is driven to act as a null balancing circuit and escalates the potential in the top

plate, thus providing a counter balancing force P_E to keep the middle plate in the null position.

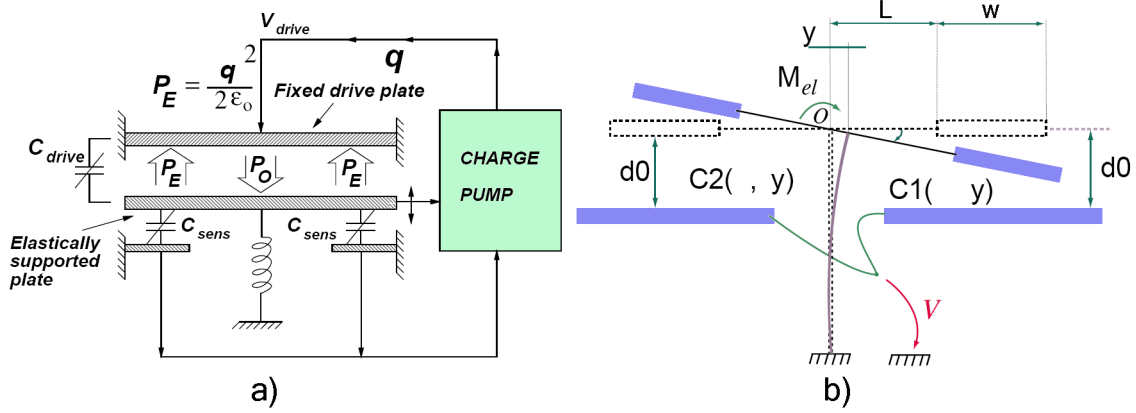


Figure 1.1: shows servo sensors concept a) force-balanced micromachined pressure sensor by Gogoi and Mastrangelo [49] b) inverted clamped electrostatic momentum-actuated accelerometer by Cretu, et al. [38]

The momentum-actuated accelerometer of Cretu, et al. [38] is shown in Figure 1.1 b) and provides another servo-based sensing concept. Under horizontal acceleration, initial moment causes inverted pendulum rotation, which can be picked up by a capacitive sensor. Two actuating capacitive sensor pairs are used to the left and right side of the inverted pendulum. Both of the circuits can be charged up dependently which will shift up the spectral content of vibration, or independently for analysis of a particular frequency. Both devices in Figure 1.1, and servo sensors in general, have a useful frequency range much less than 1000 Hz because of delay in the null-balancing and feedback circuit [127]. They also have a slow recovery time from over-range input (input that exceeds restoring force) due to limited power of the actuating circuit. An example of an off-the-shelf sensor of this type is Analog Device's ADXL-05/50 accelerometers used for airbag deployment, an application for which acceleration energy is mainly at low frequency and the sensor is not repeatedly

reused.

In recent studies, the wide range tunable resonators by D. Scheibner, et al. [28–30] have shown an improved strategy over the servo based sensors for higher frequency measurement. Instead of building a single sensor with broad bandwidth, an array has been built where each sensor is electrostatically charged by a control circuit and tuned to particular frequency. This development is of particular interest to this study because as an array, this sensor works in a similar way to the organ of corti in a mammalian cochlea from a signal processing stand point. Suranthiran and Jayasuriya [106] have proposed another idea for obtaining broad frequency range from a sensor array. Instead of tuning, each sensor has a fixed characteristic. Using frequency domain compensators, signals from the arrayed sensors are combined as if they were a single wide band sensor. This approach is a form of sensor (information) fusion and represent what can be done from the information processing side to improve overall measurement. Regardless of improvement being done on either measuring or processing perspective, both of these devices show that wider frequency range can be achieved by an array of more limited bandwidth sensors. This approach can also improve signal to noise ratio and simplify the signal conditioning circuitry without digitally computed Fourier transformation [28].

Putting sensors in an arrayed configuration can also result in reduction of information. Figure 1.2 shows a simulation result of white noise superimposed on a test signal composed of two frequency components, one at 20 Hz with magnitude of two and another at 100 Hz with magnitude of one. In one case, the signal is sent to a simulated sensor with second order characteristics, and FFT processing is built-in. The second is a simulated sensor array with seven sensors, each working as a third order bandpass with resonant frequencies of 20, 40, 60, 80, 100, 120, and 140 Hz. The result shows that while the conventional sensors with FFT can capture the

spectral property of the signal very well, it requires a lot of processing power with associated time delay. The second sensor shows a similar spectral form found using much less data. In this particular example, with a sampling period of 1 ms over a 2 second length, the FFT result has produced 20000 data points versus seven data points from the array of sensors. A 99.965 percent data reduction!

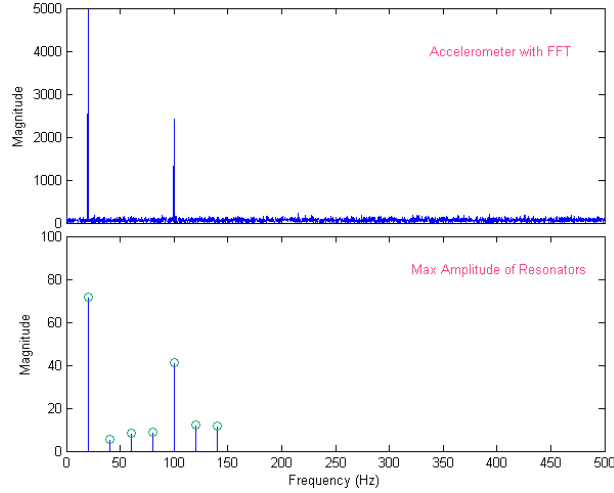


Figure 1.2: shows simulated results between single sensor having built-in FFT algorithm (top) and array of seven sensors having resonant frequency of 20, 40, 60, 80, 100, 120, and 140 Hz. (bottom)

In order to find novel sensor structure, many studies in biomimetics find inspiration from nature. For example, a MEMS acoustic pressure gradient sensor by Andreou, et al. [7] takes its structure from the acoustic sensory organ of the parasitoid fly, *Ormia Ochracea*, which has acute directional hearing although two of its hearing organs are less than one millimeter apart. This concept allows construction of a MEMS device with the same directional capability regardless of the size. An artificial lateral-line flow sensor by Fan, et al. [130] mimics the structure of the hair cells in a fish's lateral-line organ using bulk micromachined device in silicon substrate. A similar concept is also pursued by Noca, et al. from the Jet Propulsion

Laboratory; however, Noca's version of lateral-line organ is built using an array of carbon nanotubes. Both of these studies recognize that this biomimetic lateral-line structure allows measurement of microflows or pressure waves with virtually no impedance.

For years, research in the area of artificial intelligence and evolutionary robotics has recognized that relaxing system constraints can lead to systems better suited for ill-defined situations, in a way system designers have not foreseen. Biologically based elements revolve around their ability to self-regulate and self-proliferate, thus working much better than synthetic elements in unstructured situations. Cariani [21, 22] proposed that allowing a sensor to adapt, evolve, or tune itself was the only way to allow the sensor's performance to exceed its maker. Perhaps the electrometer sensor array adapted by evolution by Keymeulen, et al. [26] is a step in this direction. This sensor array is equipped with automatic determination of electronic circuit configuration using an evolutionary algorithm called evolvable hardware (EHW). This allows the information processing part of sensor arrays to adapt, in order to obtain higher quality of data in situations where high communication bandwidth is not available. An example is for a remote robot vehicle sent in 2001 on a Mars mission. Although this sensor array has been successful in providing a minimized data stream, Chiel and Beer [23] recognize that any adaptive behavior can not be confined to a specific part of the system, but should be a result from reaction between all sub-systems and their environment in order to be truly adaptive. Therefore, adaptation in the signal processing part that does not effect measuring structure, including most modern methods as adaptive filters, can not be referred to as adaptive sensors from this point of view.

A sensor structure that fits best with the adaptive sensor descriptions given above is the adaptive quartz glass sensor by Szabatin, et al. [65]. This sensor has a

control circuit composed of two feedback loops. One is a compensation loop similar to a force-balanced or servo sensor, another is a sensitivity adjustment loop based on a Kalman filter using a Bayesian algorithm from optimal control theory for noise suppression.

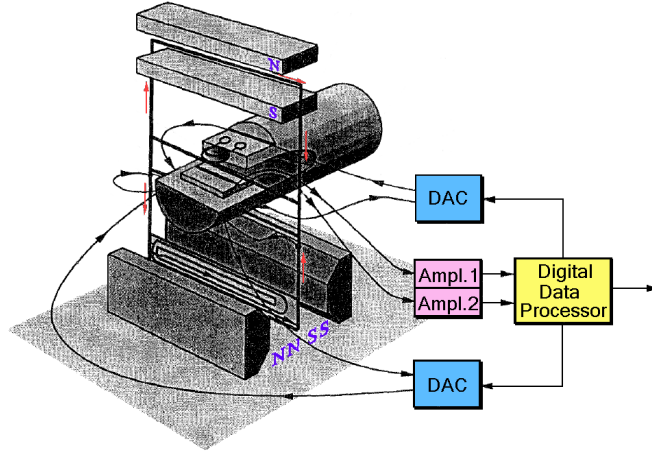


Figure 1.3: shows string-frame accelerometer concept based on quartz glass sensor by Szabatin, et al. [65]

Figure 1.3 shows a physical realization of the adaptive sensor which consists of a thin quartz plate placed between a permanent magnet pair and hanging by a conductive frame. Acceleration causes the frame angular rotation that is detected up by a photodiode and photoelements that promptly send information to a digital data processor. The processor controls a restoring force and sensor sensitivity by controlling direction of the current flow though the frame and a thin metallic spiral on the quartz plate. This study provides an excellent example of the components and rules needed for true adaptive sensor construction, although the study is based primarily on simulations, and this sensor seems to heavily rely on a low resolution photodiode sensor for control feedbacks.

1.2 Objectives

As stated, the primary goal of this dissertation research is to develop a concept for adaptive sensor design by trying to cultivate beneficial characteristics from natural sensor concept. The approach is demonstrated by a modular biomimetic sensor derived from a model of hair cells and their interaction with the basilar and tectorial membranes in the organ of corti of a mammalian cochlea. The goal is *not* to build a synthetic version of cochlea but rather a realization of the high level sensor functionality observed from the mammalian cochlea. Functions of particular interest are frequency selectivity, which is an ability to maintain the frequency selectivity in dynamic environment, wide dynamic range capability resulting from ability to put many of these sensor modules together in an array, and spectral pre-processing. The final goal can not be reached without accomplishing the objectives listed below.

1. A physical model of the hair cell, which is the active transducer of the organ of corti must be developed. The model will provide an understanding of how the hair cell works at a system level.
2. A biomimetic sensor structure has to be designed based on a specific measurement and on the basis of physical model results.
3. A control algorithm that can monitor and maintain sensor performance must be developed.
4. A laboratory prototype must be constructed to demonstrate the effectiveness of the designed structure and the control algorithm implementation. This will provide a basis for testing, calibrating, and evaluating an adaptive sensor.

1.3 Overview

The purpose of this first chapter is to provide background on the current state of development of different active/adaptive sensing structures. The emphasis is on the distinction among intelligent, active, and adaptive sensors and their benefits. The organization of this dissertation is as follows.

Chapter 2 explains some basic physiology and mechanisms of sensory transduction in hair cells. Special properties unique to hair cells are discussed. Because hair cells are basis sensory cells found in many vertebrate sensory organs, discussion on mechanism of these organs are provided together with function and location of hair cells in each of them. Organs of interest include the organ of corti, vestibular organ, otolith organ, lateral line organ, and electroreceptors.

Chapter 3 focus on the development of a mathematical model for outer hair cells using bond graph theory. Special constitutive relations for the plasma membrane and its channels are developed. After the bond graph model of the hair cell is constructed, it is simplified to allow focus on electromotility, a unique active mechanism in the hair cell plasma membrane believed to be responsible for the active cochlear behavior. Simulations in both the time and frequency domain are performed and compared with some published physiological data.

Chapter 4 is devoted to design of the sensor configuration. After some sensor classification is presented, the structure of the bond graph model of the hair cell is discussed. Two different basic analog elements are proposed: the sensing element based on coupling capacitive plates for micro scale sensor, and the sensing element based on piezoelectric bimorph for macro scale sensor. After constitutive relations for both are presented, the bimorph structure is selected for in further development for the reason that the capacitive sensor is more efficient and has less noise only when built at a very small scale.

Chapter 5 describes the development of an adaptive sensor control algorithm. After the model referenced adaptive control (MRAC) method is selected and described, a controller is developed in two ways. One based on MIT's gradient theory, and another based on Lyapunov stability theory. Unlike a conventional control systems plant, some of the control signal can not be canceled out by the feedback signal, which means that controllers developed have to be reduced. A reduced version of both controllers are built and simulated. Simulation shows that with the same loop gains the MIT gradient theory is more stable and has a faster rate of adaptation. For these reasons, the reduced version of an MIT gradient algorithm is selected for implementation on the experimental prototype.

Chapter 6 deals with the experimental part of the research. After a discussion on component selection and fabrication, a finite-element method (FEM) analysis of the sensor is presented and shown to verify the mathematical model. A brief discussion on the experimental setup and equipment used is presented, and then a series of experiments are described as used to find physical parameters for modeling and control applications. A discussion on implementation of the adaptive controller using programmable logic gates is shown, then the controller is physically integrated with sensor prototype. Another set of experiments are performed to demonstrate that the system works as designed. Experimental results are discussed in the end.

Chapter 7 briefly provides a summary of the research that has been completed and recommendations for future research is described. The chapter will also list original contributions from this study.

Chapter 2

Hair Cells: Their Physiology, Mechanism, and Networks

To develop a biomimetic sensor, fundamental understanding of the function of the biological system is very important. The physiology and function of hair cells will be described in this chapter. This description intends to demonstrate how hair cells exhibit a basic sensing mechanism that can form the basis for an adaptive transducer structure. Arrangements of hair cells which are building blocks of various sensing organs in vertebrates will be explained. All information presented here will be used to begin a process of capturing the conceptual mechanism that has been observed in these ‘amazing’ sensory cells.

2.1 Hair cells

Hair cells (see Figure 2.1) are an extremely sensitive mechano-electroreceptor type of cell found mostly in the vertebrate acousticolateral system. They are grouped in specialized sensory regions such as that in the organ of corti (the organ of hearing) the cristae ampullaris of the semicircular canals or the vestibular apparatus, the macula utriculi, macula sacculi, and macula lagenae which together are called the otolith organs, neuromasts and canals of the lateral line organ, and epidermal cavities or electroreceptors [9]. These organs are responsible for such diverse functions as sensing body motor activity, surrounding substrate vibration, prey neurological activity, body coordination, sense of gravity, and detecting pressure fluctuation in the air. Although these organs have different functions, they have similar physi-

cal structure and are believed to be developed from similar ectodermal dorsolateral placodes.

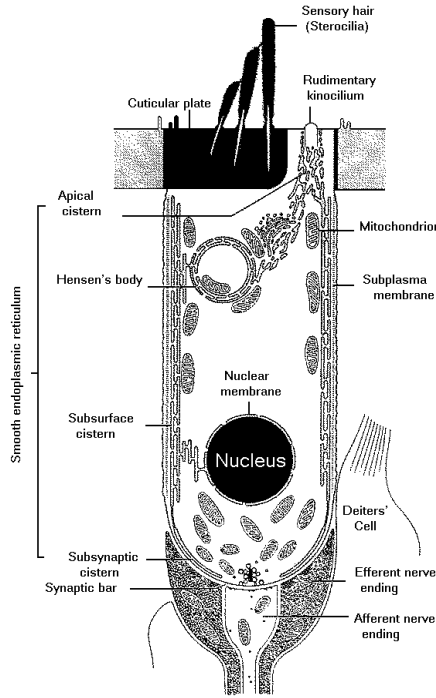


Figure 2.1: Outer hair cell structure (from D. J. Lim et al. 1988, Structure organization of the mammalian auditory hair cells in relation to micromechanics)

Hair cells are usually oriented with the kinocilium either facing the head or the tail of an animal [82]. In vertebrate, hair cells are secondary (epithelial) receptor cells; that is, they are not modified nerve cells but develop locally from ectoderm. By short description, hair cells are cylindrical (for outer hair cells) or flask (for inner hair cells) shaped cell that have a group of cilia or micro villi (or hairs), made from actin filament, protrude from apical end. The stereocilia are arranged regularly often in a hexagonal (diamond) packing pattern. The pattern means each cilia has six neighbors and are equal distance apart. All stereocilia are connected together by three different means. 1) to the next tallest one by fine tip link, 2) to other cilia by

small fibers that extend down the length of each one, called subapical bands [111], and 3) by nebulous lateral contacts [64]. They are also linked to the kinocilium and area well rooted via actin filaments in a dense area of cytoplasm called the cuticular plate [82]. All these linking mechanisms seem to ensure the motion of all stereocilia as a bundle with small relative shearing force.

The primary function of the hair cell is to convert the motion (rotation) of sensory hairs to electrical potential, or impulse, understandable to the nervous system. In Figure 2.1, the outer hair cell of mammalian cochlea are shown. It is noted that sensory hairs or stereocilia only protrude from the cuticular plate. Cilia's length increase progressively toward kinocilium such that the tallest one is located next to kinocilium. The kinocilium is used to indicate the direction of activation of the cell. The deflection of the hair bundle toward the kinocilium results in depolarization of the cell's membrane, or an increase in the attached nerve's firing rate. On the other hand, deflection of the hair bundle away from the kinocilium results in hyperpolarization, or a decrease in the attached nerve's firing rate (as shown in the experiment of Figure 2.2). Kinocilium structure appear to be varied among different kinds of animals. For example, in mammals, it appears as a rudimentary structure or as a hair that has a tip link (believed to made of nonelastic cadherin 23) to stereocilium next to it. However, according to present understanding, disappearance of kinocilium, such as in mammals, does not impair the ability or function of mechanoelectrical transduction of the hair cell.

Hair cells rely primarily on the ionic gradient of the surrounding fluid to modulate the transmembrane potential. The apical part of the cell is bathed in endolymph, a lymph fluid rich in potassium ion (K^+), and the body of the cell is bathed in perilymph, another fluid rich in sodium ion (Na^+). As seen in the Figure 2.1, in cochlear, Deiter's cells support outer hair cells at the basal end, and leave

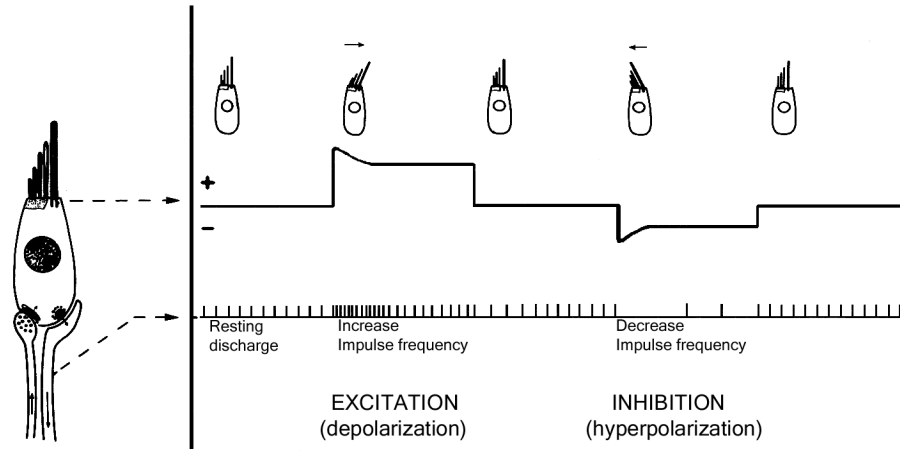


Figure 2.2: Diagram showing stereocilia of hair cell deflection resulting changes in receptor potential (top line) and nerve impulses (bottom line). Excitation or depolarization causes an increase in firing rate of nerve, on the other hand, inhibition or hyperpolarization causes a decrease in firing rate (from experiment of Flock, Transducing mechanisms in the lateral line canal organ receptors, 1967)

the body section of hair cell untouched by other structures. The reticular lamina attached to apical side of hair cell acts as a sealing mechanism between endolymph and perilymph. Efferent nerve endings attach to the basal end of the hair cell and carry signal from eighth nerve of the brain. Afferent nerve endings attach next to the efferent nerve ending used to carry signal away from hair cells to the brain.

What makes the hair cell mechanism so interesting is its sensitivity. According to recent experiments, the hair cell has a dynamic threshold of about 0.3 nanometer for a 0.5 micrometer length of cilia linear deflection, or about 0.003 degree of rotational deflection. This mechanism is so sensitive that it can detect brownian motion of surrounding fluid molecules [45]. Beside this nanometer scale accuracy, the cell can also calibrate or adapt itself to a different threshold, in case the cilia have been under a constant deflection. This “adaptation” mechanism gives

hair cells flexibility to operate without having a precise construction of the physical mechanism. The sensitivity of hair cells is also not subject to the frequency limitation like that in photoreceptor and olfactory receptors because in hair cells, the link between the mechanical displacement stimulus and channel gating is simple and direct, without any intervening biochemical cascade [112].

No matter of its location or function, hair cells have similar mechanism that can be described as following. When the stereocilia deflects (i.e., in activation direction), whether by the direct forcing of fluid or by the indirect motion of the basilar membrane, the tip links between cilia stretch to open mechanically gated transduction channels at the apical end of the cell. This opening allows potassium ions (K^+) to flow from the high concentration of endolymph into the cell. The increase in potassium ions inside the cell is responsible for increasing the cell's transmembrane potential, which depolarizes the cell, and results in an increase of the afferent nerve firing rate.

The higher potential of the cell also results in activation of voltage-activated calcium ion (Ca^{2+}) channels, allowing calcium ions to flow into the cell. Hair cells then use calcium ions as a medium to open the calcium-activated potassium channels that open to the perilymph, allowing deposited potassium ion to flow out. As soon as the loss of potassium ions flowing through calcium gates exceeds the inward flow of potassium through the mechanically gated channels, the hair cell starts to repolarize. This decreases the calcium flow through the voltage gate, and decreases the nerve firing rate. Excess calcium ions are then pumped out by a specific calcium ion ATPase-pump, allowing the cell to completely repolarize and reset to its new position, until the mechanically gated channels kick in to start another cycle of transduction. The mechanism can be visualized as shown in Figure 2.3 [58].

Although all hair cells in vertebrate have a similar structure, a further ex-

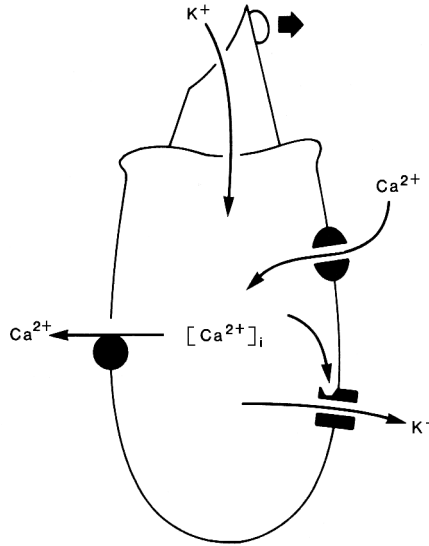


Figure 2.3: Diagram showing significant ion channels of the hair cell. 1) top channel is mechanical (deflection) activated potassium ions channel, 2) top right channel is potential activated calcium channel, 3) bottom right channel is calcium activated potassium channel, and 4) left channel is specific calcium ions pump (From Hudspeth [58]).

amination leads to categorization of hair cells into two types, the inner hair cells (IHCs) or cell of type I, and the outer hair cells (OHCs) or cell of type II. Inner hair cells (see Figure 2.6 below) derive their name from their position at the inner part on basilar membrane of the organ of corti (as shown in Figure 2.4). They generally are flask-shaped and contain an extensive system of tubulovessicular endoplasmic reticulum, golgi apparatus, and mitochondria. This complexity suggests a high level of metabolic activity which may be related to the transduction of mechanical to electrochemical energy. Their endoplasmic reticulum system has only one subsurface cistern layer that is far less developed than what observed in outer hair cells [47]. By average, the human cochlea has about 3500 inner hair cells. Table 2.5

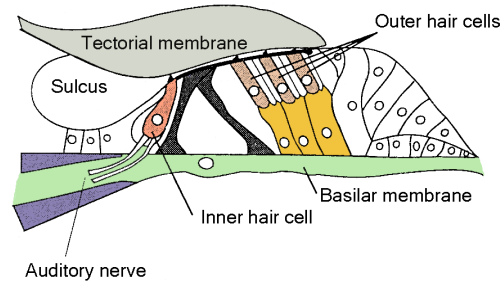


Figure 2.4: Cross section of the organ of corti in mammal, showing position of inner hair cells and outer hair cells (from Yates, et al. [48])

below shows the significant dimensions of inner hair cells in micrometers for various animals. The two values in the table represent the range of dimensions from the base of the cochlea to its apex.

| Name | Cell Body (μm) | Tallest Sterocilia (μm) | Sterocilia Count |
|----------------|-----------------------------|--------------------------------------|------------------|
| Human | 31-34 | 4.5-5.5 | 41-64 (mid) |
| Chinchilla | 35-35 | 1.75-4.75 | 75-85 |
| Cat | N/A | N/A | 60-N/A |
| Rat | N/A | 2.3-4.3 | 32-41 |
| Leaf-nosed Bat | 30-40 | 2.5-7.0 | N/A |

Figure 2.5: Table comparing dimensions of inner hair cells of various vertebrates (modified from Boston university's EAR-LAB web site, <http://earlab.bu.edu/anatomy/cochlea/IHCdimensions.html>)

Outer hair cells (see back on Figure 2.1 at the beginning of chapter) are cylindrical or tube-shaped cells. In mammalian cochlea (as in the cross section shown in Figure 2.4), OHCs have their name from their position in three outer rolls on the middle part of the organ of corti. They also contain a highly organized endoplasmic

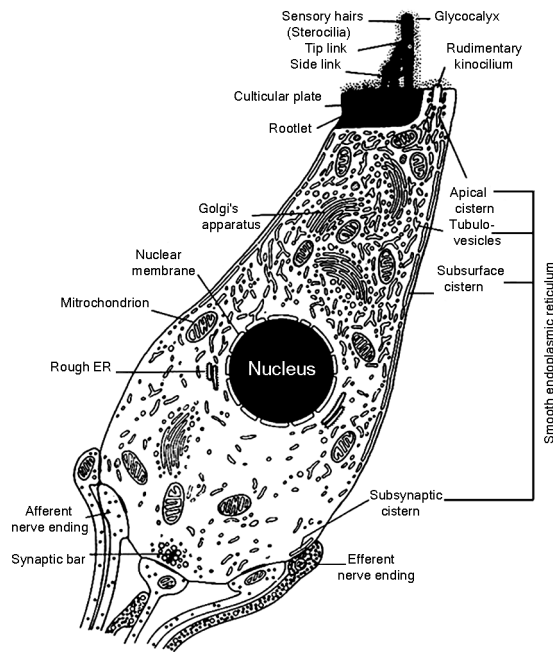


Figure 2.6: Inner Hair Cell structure (From D. J. Lim Et Al, Effect of noise and toxic drugs at the cellular level in the cochlear, Journal Otolarlyngol, 1986)

reticulum system that includes extensive subsurface, apical and subsynaptic cisterns, and the Hessen's body. These structures are similar to what is found in muscle cells. Recently, many researchers also found that OHCs contain contractile proteins in their cell bodies, cell membranes (actin, myosin, tubulin, and prestin [84]), stereocilia (actin, fibrin), and cuticular plates (actin, alpha-actin, fibrin, myosin, tropomyosin) [45]. All of these proteins are believed to be responsible for the ability of outer hair cells to change their length (which will be discussed more later in this chapter). Humans have approximately 12000 outer hair cells in their cochlea. Again, Table 2.7 shows average dimensions of outer hair cells from various sources.

Some phenomena of hair cell transduction mechanics need further examination. The first phenomenon is the mechanism of the tip link. Tip links somehow

| Name | Cell Body (μm) | Tallest Sterocilia (μm) | Sterocilia Count |
|----------------|-----------------------------|--------------------------------------|------------------|
| Mole Rat | 30-75 | 3.5-12 | 120-40 |
| Human | 28-66 | 4.5-8 | 148-46 |
| Chinchilla | 25-45 | 1.0-5.5 | 110-40 |
| Guinea pig | 21-80 | 1.2-5.8 | N/A |
| Cat | 20-50 | 2.0-6.0 | 120-N/A |
| Rat | 15-40 | 2.7-4.4 | 75-62 |
| Leaf-nosed Bat | 8-15 | 1.0-2.5 | N/A |

Figure 2.7: Table comparing dimensions of outer hair cells of various vertebrates (modified from EAR-LAB of Boston university web site, <http://earlab.bu.edu/anatomy/cochlea/IHCdimensions.html>)

open the mechanical channel for potassium ion flow. Since the location of the potassium channels can not be detected under a microscope, it is necessary to study them indirectly. This is accomplished using experiments on hair cells under proteolytic enzyme elastase (which destroys tip links). Alternatively, removal of Ca^{2+} ions from the external medium [45] results in a loss of mechanoelectrical transduction process in the hair cell. It can be clearly seen that when a cilia bundle deflects, it creates relative motion between individual cilium, therefore tension or amount of stretch in the tip link must absolutely play an important role in activation of these mechanically gated channels. Many researchers have been focused mostly on identifying the actual location and mechanism of these channels. However, up until now, the result is still inconclusive. One thing for certain is that these channels are unique stress activated (gated) channels. A very renown speculation of how the channels works is described by the “trap door” hypothesis.

Figure 2.8 illustrates the mechanism of the trap door hypothesis. When

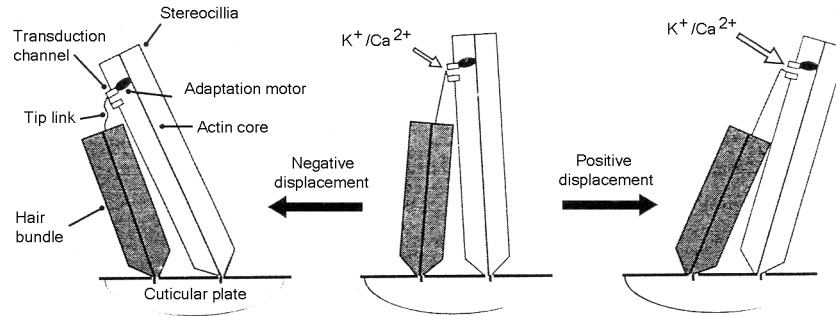


Figure 2.8: The mechanism of tip link to open the mechanically gated apical channels according to trap door theory (From P. G. Gillespie, Molecular machinery of auditory and vestibular transduction, *Current Opinion in Neurobiology*, Vol 5, pp 449–455, 1995)

the cilia is in rest position (as in middle section of the Figure), the channels are slightly opened and this makes the hair cell's transmembrane potential stay in a resting state. The attached nerve firing is at a normal rate. After cilia are excited, the mechanism pulls the tip link as shown in the rightmost figure. This causes the channels to open more and increases the possibility that potassium cation will flow through the channel. The hair cell is then depolarized, which causes the attached nerve to increase its firing rate. The opposite situation is shown in the left section of the Figure 2.8.

Mechanically gated transduction channels are unique because they have never been identified in higher vertebrate. Recent research by Corey, et al. [37] identified a transient receptor ion channel 1, or TRPA1 (ANKTM1), which is the same channel that is activated by mustard, cinnamon oil, or cold temperature as a major candidate for mechanically gated channel in higher vertebrate.

The adaptation motor, shown as black ellipse in Figure 2.8 is thought to be

responsible for adaptive mechanisms which will be discussed later. However, recent research (such as that of Hackney and Furness on immunohistochemical experiments with antibody against the amiloride sensitive sodium channels in 1995, or by Meyer, et al. on measuring of current after loss of tip links in 1998) suggests that the channels might not be located at the end of the tip links [111]. These channels might be distributed on the three-start helical bundle of a five filament structure of tip links. The trap door hypothesis can still be used because it gives a realistic simulation characteristics. For that reason, it is still very popular among recent hair cell model.

The second phenomenon is one of the most important characteristic of the hair cell: electromotility (see Brownell [18]). The electromotility mechanism can be described as an ability of hair cells, specifically outer hair cells, to elongate and contract longitudinally in response to a receptor potential that changes based on mechanical stimulation. This creates an active force in phase with the vibration of the basilar membrane and results in the sharp tuning characteristics of the cochlea. Since its discovery (Brownell, 1983 [18]), the mechanism has been extensively studied. From the structure of the organ of corti in Figure 2.4, it can be seen that the outer hair cell is supported only on its basal part by Deiter's cell and its apical part by reticular lamina. This form of structure allows changing of the outer hair cell's length to modify overall stiffness of the organ of corti. However; the structure around inner hair cells which is the sensor does not allow them to change length.

Questions might be raised as to how much electromotility affects dynamics of the organ of corti, and why the outer hair cells need to work this way ? The answer lies in the stiffness characteristics of the organ of corti. From recent experiments, it has been found that the basilar membrane of the organ of corti has relatively high internal viscosity. However, it is also known that mammalian cochlea have a

very sharp tuning or filtering characteristic. Without additional mechanical forcing, provided by outer hair cells, the cochlea would not be able to overcome the viscous damping effect and would have less selectivity to frequencies. To inject mechanical energy at a specific section of the basilar membrane, outer hair cells have to directly or indirectly receive signals from inner hair cells of the same section.

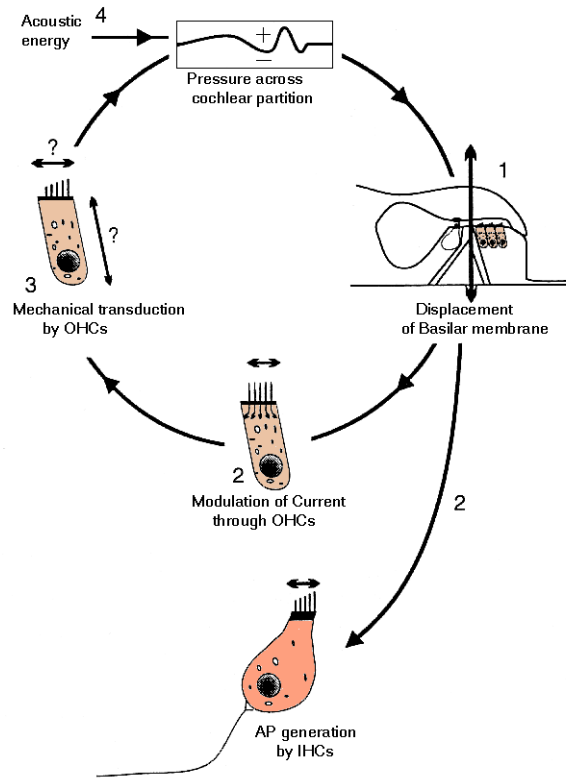


Figure 2.9: Feedback control mechanism thought responsible for electromotility generating force (from Yates, et al. [48]).

Two kinds of hair cells in the organ of corti in mammals are working together in a feedback loop in order to increase frequency resolution of the section of cochlea. In Figure 2.9, the feedback mechanism is shown in order: 1) acoustic stimulation causes the basilar membrane to vibrate, 2) vibration deflects cilia of IHCs and OHCs,

causing K^+ channels to open and both depolarized, 3) outer hair cells change their length, 4) this elongation feeds pressure fluctuation back into the scala, and increases the vibration of the membrane section so it “tunes” to the excitation frequency [48].

The third relevant phenomenon in hair cells is physiological adaptation, or desensitization. It has been known for a long time that many animal sensing systems show lower response (desensitized) as a stimulation is prolonged. It is an ability that helps these natural transducers to distinguish things that change in its environment, dynamic from static, or dangerous from safe. Often there are some special names for the process such as “reflect decay”, desensitization, or adaptation. In hearing mechanism, many of the cochlea’s parts can be considered responsible for this adaptation. Hair cells are one of them. Experiments such as those by Crawford, et al. in 1991 clearly show that hair cell’s response after a step input gradually decreases until it “resets” itself to the new position. The Ca^{2+} concentration of the perilymph is thought to be responsible for this phenomena, and experiments have shown that the rate of adaptation decreases and ceases after reducing and cutting off Ca^{2+} concentration.

Recently, there are many studies on the adaptation mechanism originating in the cilia bundle and tip links’ protein, such as Wu, et al. in 1999 [129], Holt and Corey in 2000 [55], and Vilfan and Duke in 2003 [114]. These researchers discovered that there are two mechanisms underlying the physiological adaptation, and they categorized the mechanisms by the operating timescale as a faster adaptation and a slower adaptation. The fast adaptation operates in the range between 0.3 and five millisecond and is thought to be from binding of Ca^{2+} at the site of the transduction channels or near the transduction channels to stabilize a closed conformation. The slow adaptation operates in the range between tens and hundreds of milliseconds and is thought to be from a Ca^{2+} ion generated active process that regulates effective

strain or stimuli at tip links. Both types of adaptation ultimately decrease the hair cell receptor current in three possible ways: 1) by decreasing the sensitivity of the channels such that a larger deflection is needed to open more channels, 2) by an inactivation so that the number of channels available to be opened is reduced, and 3) by shifting a stimulus response relationship without reduction of sensitivity [55].

The fourth phenomenon is nonlinear time-dependent active cilia bundle movement. For the mammalian outer hair cell, motor proteins such as prestin, is believed to be the source of electromotility and cochlear amplification as discussed by Liberman, et al. [84]. However, for non mammalian systems, the source for amplification is believed to be the active cilia bundle movement which probably results from the interplay between the tip link structure, cytoskeleton of the cilia bundle, and binding of intracellular Ca^{2+} to the channels. According to Choe, et al. [128], currently there are two hypotheses for this mechanism. The first one is stress-induced activation of myosin (probably myosin 1C or so called myosin I β), which is one of the major components in the hair bundle. The second and more popular hypothesis is the interaction of Ca^{2+} with mechanoelectrical transduction channels. There is some evidence suggesting that Ca^{2+} modulates the activities of these channels. There are some observations that increased Ca^{2+} concentration will result in a decline in the transduction current, which implies that Ca^{2+} favors channel closure [128]. A similar mechanism is thought to be responsible for the hair cell physiological adaptation discussed above [45]. An important point here is that the outer hair cells that have plasma membrane electromotility are from mammals, and the outer hair cells that have active cilia bundle movement are non-mammalian. Both types are similarly responsible for active/amplification mechanism and until recently there is no evidence that electromotility and active bundle movement coexist in any hair cells.

2.2 Different kind of hair cell networks

As described previously, the hair cells configuration has been found in many organs of vertebrate and in many forms of sensory transduction. It can be assumed that this sensor structure has some advantages, being sensitive and reliable enough to have widely evolved in various organs. Below, in order to show the potential of these mechanisms, a brief discussion of how nature utilizes hair cells in different sensory transduction organs will be discussed.

2.2.1 Network of hair cells as a mechanism for sound processing

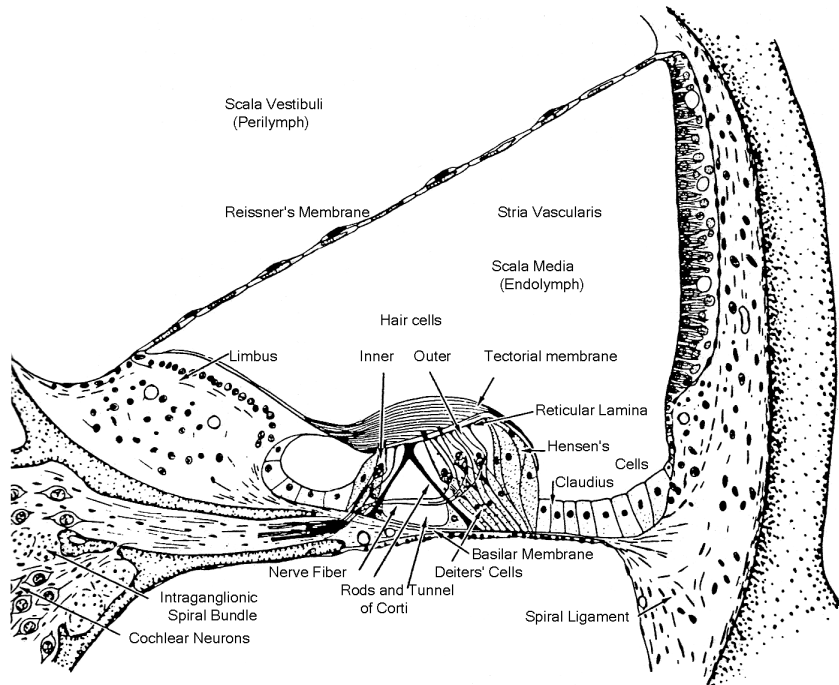


Figure 2.10: Picture shown location of inner hair cells and outer hair cells through cross section of the organ of Corti (from Gelfand [47])

This configuration is probably the most well known and studied of all kinds.

As stated, two types of hair cells, inner and outer hair cells, are arranged in rows between the tectorial membrane and the basilar membrane of the organ of corti located in the mammalian cochlea (see Figure 2.10).

The mechanism of sound processing is best described by referring to Figure 2.9 and 2.10. It is well known that the mammalian cochlea has a spiral shape, and incoming sound is coupled by the middle ear ossicle and transferred to the cochlea through the oval window. A wave is induced in the perilymph media and travels from the scala vestibuli, helicotrema, and scala tympani. The wave travels back to the middle ear cavity through the round window. The basilar membrane, which has a stiffness that changes exponentially along its length, tunes each of its sections to a frequency of the wave by actively exciting a section that has a resonance frequency matching the wave's frequency components. The mechanism is depicted in Figure 2.11.

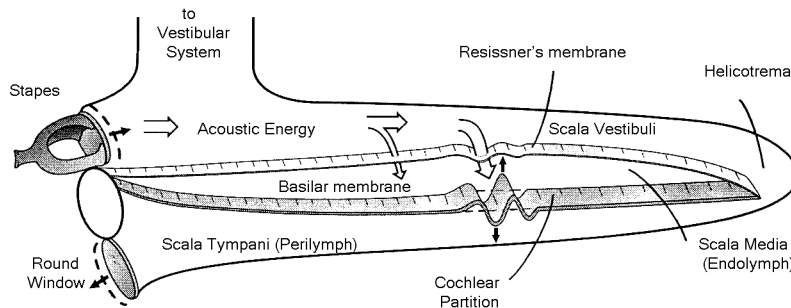


Figure 2.11: A stylized cochlea showing flow of acoustic energy and depicted as if straight by Geisler [45])

Vibration of each section of the basilar membrane causes the tectorial membrane to move relative to the basilar membrane. In each section of the organ of corti, the outer hair cells are arranged in three rows, and inner hair cells are arranged in a single row. Relative movement of the tectorial membrane deflects outer hair cells

and, according to a feedback loop process described in the previous section (see, again, Figure 2.9), the outer hair cells exhibit electromotility which facilitates vibration of the section (and enables the basilar membrane to better tune to a specific frequency). Finally vibration deflects the inner hair cells which ultimately cause an action potential to pass via neurons to the brain.

From an engineering point of view, the basilar membrane functions as a cascaded band-pass filter with hair cells as an input (or somehow a negative resistive element). This mechanism, although complex in operation, has been shown to exhibit a high sensitivity. For example, mammals such as bats utilize interaural time differences between sound arriving at their two ears to navigate with great accuracy. Many references such as Geisler [45] and Gelfand [47] which focus on the mammalian hearing mechanism are recommended for more details.

2.2.2 Network of hair cell function as an angular accelerometer

Cristae ampullaris or crista of the semicircular canals are located in the inner ear of vertebrates. These organs are responsible for sensing angular acceleration and allow animals to maintain coordinated reflexes.

The typical system is composed of three perpendicular canals aligned to each directional plane in space. At the end of each canal is an expanded end called the ampulla. Inside each ampulla is the cristae ampullaris which functions as a receptor sensor. The system comprises the cupula or gelatinous partition, which separates the ampulla into two sections. At the base of the cupula lies a group of hair cells that are supported by sustentacular cells. Cilia of these hair cells are embedded in the cupula (see Figure 2.12 a)).

The working mechanism of this crista is simple. The cupula is a flexible partition that separates the endolymph which has high specific gravity into two

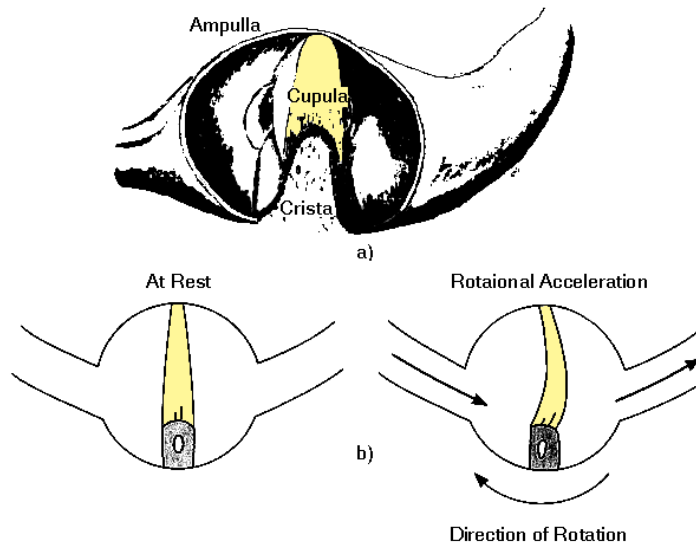


Figure 2.12: a) Cross section of cristae ampullaris (unidentified source), and b) mechanism of cupula deflection under angular acceleration from Ganong [44].

sections. When an animal moves with angular acceleration, higher inertia in the endolymph creates a displacement in the cupula which deflects cilia in the hair cells.

It is also important to note that cristae ampullalis of cyclostomata in fish and amphibia are built around only hair cells of type II (outer hair cells type), while reptiles, birds, and mammals' crista utilize both type I and type II hair cells [9]. By using both types of hair cells, reptiles, birds, and mammals are believed to benefit from the same kind of feedback mechanism between the two types and thus possess more acute senses.

2.2.3 Network of hair cell function as a linear accelerometer

The otolith organ found in most vertebrates is composed of the utricular macula (utricle) which is responsible for sensing horizontal linear acceleration, and the saccular macula (sacculle) which is responsible for sensing vertical linear accel-

ation. Constant application of acceleration in both macula results in reflex righting of the head and postural adjustment. Each macula contains sustentacular cells and hair cells, surmounted by an otolithic membrane in which are embedded crystals of calcium carbonate. The otoliths that range from 3 to 19 micrometers in humans are more dense than the endolymph [44] (see Figure 2.13).

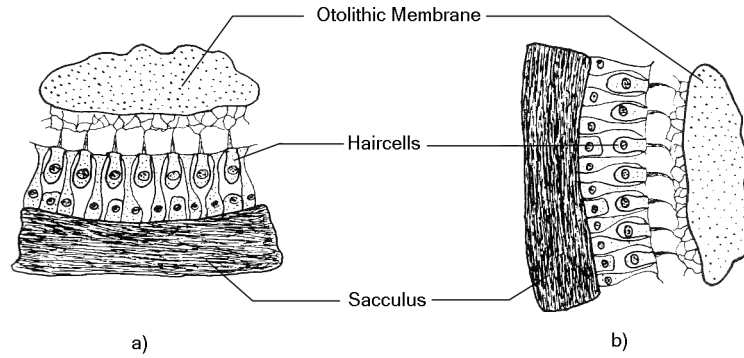


Figure 2.13: Otolith organ, show hair cells positioned between otolithic membrane and sacculus. a) utricle under vertical force and b) saccule under horizontal force. Modified from Akoev and Andrianov [9].

The mechanism of the otolith organ is not difficult to understand. The otolith membranes have higher specific gravity than the surrounding endolymph. Also, the tops of the hair cells processes are embedded or are touching the otolith membrane. When an animal accelerates, inertia causes the membrane and saccular to form a relative shearing velocity that displaces cilia in a direction opposite to the acceleration. A similar mechanism is found in modern day accelerometers.

Fish, birds, and amphibians have another special set of otolith organ that helps them sense position in the water or air. The third otolithic set is found to have iron content from 0.7 to 4.3 percent in birds and has been recently proven to play an important role in bird homing instinct [50]. However, exactly how the mechanism

works is still unknown.

2.2.4 Network of hair cell function as a mechanism for water wave presor transducer

This configuration is an epidermal sensing organ found in most fish, amphibians, urodeles, and cyclostomes' lateral line organs or neuromasts. From an external view, the organ appears as a row of pores running from the head to tail of an animal. The pores might be more dense in the head. Laying underneath is a narrow canal called the lateral line canal which connects pores together. Inside the canal lie many sensing organ each consisting a group of hair cells. The sensing hairs are capped with a jellylike substance called cupular.

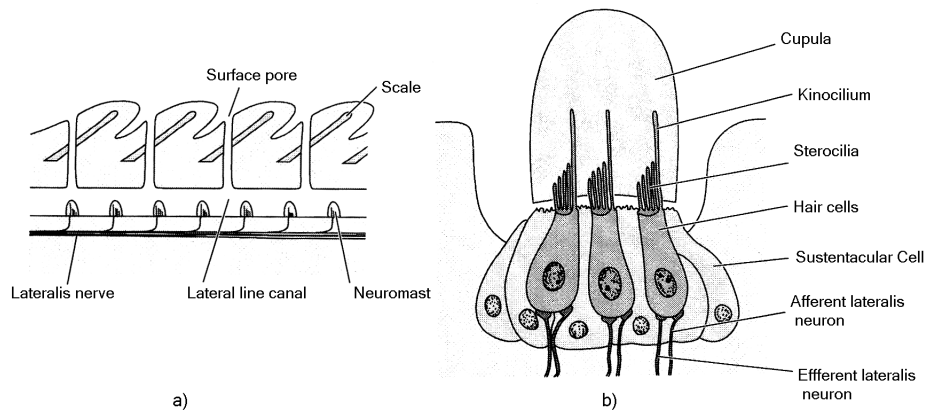


Figure 2.14: a) Lateral-line organ system of a fish, and b) ultrastructure of the sensory epithelium showing arrangement of hair cells. From K. Liem [77]

In an environment such as the sea, seeing may not be the only way to navigate, and fish use the lateral-line system in a similar fashion as bats that use echolocation to navigate and detect prey. However, the lateral-line system is a semipassive detector because it receives pressure waves set up by swimming prey. When fish swim, a bow wave is set up in front of its body, and pressure wave that

is higher than that of the wave flows along its sides. The differences in the two pressures are registered by the lateral line system. As the fish approach an object, such as a rock or the glass wall of an aquarium, the pressure wave around its body is distorted, and these changes are quickly detected by the lateral line system, enabling the fish to swerve or to take other suitable action [91]. There is some evidence that an animal that has the lateral line organ can hear air-borne noise as well. However, the range of frequency is believed to be limited to a relatively low frequency range (lower than 200 Hz [67]).

The working of the lateral line organ is believed to share common principles of operation with a hearing system. However, there is a big difference between these two organs. The lateral line organ lacks ossicles or a middle ear function. This is easy to understand because water waves do not require an impedance matching mechanism to couple fluid into the inner ear with air. This may also explain the inability of fish to sense high frequency noise.

2.2.5 Network of hair cell function as a electroreceptors

The electroreceptor organ is a specialized version of the lateral-line organ system discussed previously. Electroreceptors can be found in most aquatic animals (mostly nocturnal) and is an evolved form of the hair cell. The organ is the most important part of electrolocation systems, such as those found in weakly electric fishes. Although these organs are common, they are found to evolve separately among many types of animals. A standard classification of electroreceptors has not yet been done. However, a widely used classification groups electroreceptor organs according to the method of connection between sensory cell and epidermis for two types: ampullary and tuberous.

In an ampullary electroreceptor (found in nonteleosts, siluriformes, mormyri-

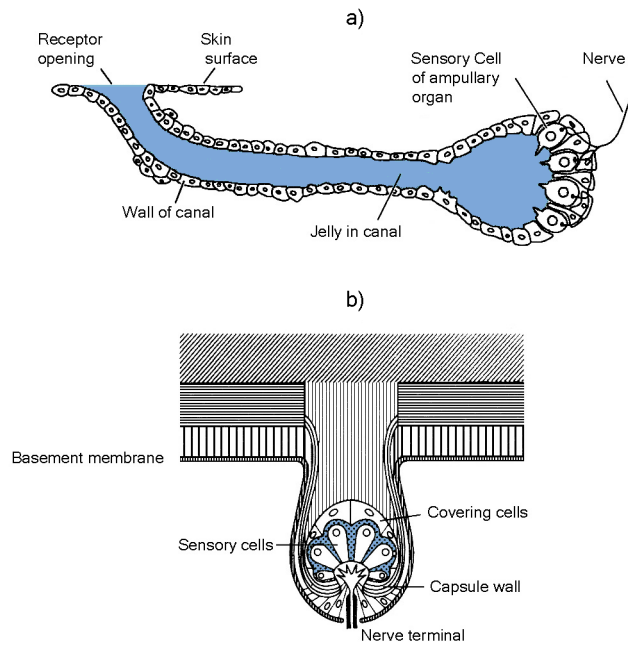


Figure 2.15: Electroreceptor organs a) ampullae of Lorenzini in shark, ampullary type, from Liem [77]. b) gymnotiform receptor organ, tuberous type, from Akoev and Addrianov [9] and Szabo 1974

form, and gymnotiforms), the apical sensory cell membrane is connected by a jelly-field canal to the epidermal surface. In tuberous electroreceptor (found in weakly electric fishes), sensory cells are connected to the surface by way of epidermal cells covering the sense organ [9]. These two types of electroreceptor organs are shown in Figure 2.15.

Electrolocation system is an active detection system working in the same way as the echolocation system in mammals such as bats. The system is composed of two major components. The first is a broadcaster organ called the electric organ discharge (EOD), which is composed of electrogenic cells located mostly in the fish's tail. The second is the electroreceptors which are located on the scales

throughout the body although they are more dense in the head and dorsal edge of fish. The system activates when a fish uses its electrogenic cells to generate a dipole electric field around its body. Typically, the range of dipole is limited to a short distance. However, it is also very dependent on the water conduction. Whenever a fish encounters an object, the electric field generated will be distorted by changes in conduction. If the object is less conductive, the current density will be decreased and the skin of the fish will register that as an electrical dark spot, and vice versa. Electoreceptors on the skin act as potentiometers measuring potential across the skin (transdermal potential), and together they send information to the brain which generates electrical ‘pictures’ of the environment. Physical differences between the two types of electoreceptor give a clue to how each sensor responds. Because the ampullary type has a longer tube, it responds better to low frequency stimuli and to being used primarily for orientation sensing. The tuberous type has a very short or no tube, thus it responds better to a higher frequency and is better used in social communication and electrolocation. Some fishes have only one type, but some have both type of organs.

2.3 Summary

This chapter has described some basic physiology aspects of hair cells and explained some important characteristic. The chapter serves as a short introduction to hair cell physiology, and to their use as as natural adaptive transducers. This chapter is also a reference for some biological jargon and notations that are going to be used throughout this dissertation. More thourough discussions on hair cells can be found in the references. Akoev and Andrianov [9], Geisler [45], and Snyder, et Al. [75] are recommended. The table of Figure 2.16 might be useful for summarization of what has been discussed.

| Organ Name | Measure | Hair Cells Position |
|--------------------|-----------------------|-----------------------------|
| Organ of Corti | Sound Wave | Basilar membrane in cochlea |
| Vestibular organ | Angular acceleration | Cristae Ampullaris |
| Otolith organ | Linear acceleration | Under Otolithic membrane |
| Lateral-line organ | Water wave | Under cupula |
| Electroreceptors | Transdermal potential | Inside receptor canal |

Figure 2.16: Table shown hair cell arrangements in vertebrate

Finally, the average of relevant human acousticolateral physiological data has been listed below as a quick reference and comparison.

- Human cochlea is about 3.5 cm long, spiraling into $2\frac{3}{4}$ turns
- There are approximately 3500 inner hair cells and 12000 outer hair cells
- Inner hair cell is $31\ \mu m$ in length, having 50 cilia of $5\ \mu m$
- Outer hair cell is up to $66\ \mu m$ in length, having 100 cilia of up to $8\ \mu m$
- Basilar membrane is approximately 33.5 mm in length, $125\text{-}500\ \mu m$ width, and $7\text{-}2\ \mu m$ thick from the base to the tip of cochlea.
- Outer hair cell shrink to about 1.25-1.56 nm per a millivolt change in potential, conversely if being blocked the distance, it can generate force of approximately 0.1 nN per millivolt input for electromotility mechanism.

Chapter 3

Dynamic System Modeling of Hair Cell

To gain insight into the hair cell, the various mechanisms can be integrated into an overall system model. This chapter describes the formulation of a mathematical model for hair cells using a bond graph method as an underlying basis [95]. It is proposed and demonstrated here that the bond graph model can provide a systematic way to model the coupled mechanical, electrical and biochemical systems in hair cells. Some model parameter values must be drawn from various experimental studies from the literature to allow verification of the overall static and dynamic characteristics. Some parameters have to be estimated and adjusted for a better model integration. Finally, some special characteristics of the model developed by the bond graph method will be pointed out.

A system model of the hair cell should quantify how it interacts with its environment. A basic hair cell dynamic model must at least consider the mechanics of the cilia bundle along with the cell body, the piezoelectric coupling of the hair cell membrane electromotility, and the ionic current into and out of the hair cell. A bond graph provides a systematic way to model these coupled energetic systems. Thus, in the following sections, the hair cell is modeled by focusing on the smaller subsystems, with each representing a specific domain of energy in the bond graph format. This chapter will not discuss the bond graph method in detail. It is recommended that further details be derived from such books as Karnopp, et al. [33].

3.1 Mechanical system model

As discussed in the last chapter, each outer hair cell is attached to a deiters' cell at the basal part, which in turn sits firmly above the basilar membrane on each section of the organ of corti. On the apical part, the tectorial membrane links the cilia bundle of each outer hair cell with the spiral limbus. Incoming acoustic pressure pushes the basilar membrane in a downward direction and stretches the tectorial membrane while bending the cilia bundle. The mechanism has been intensively discussed by Geisler [45]. Although the tectorial membrane movement creates both longitudinal and bending stress on the hair cell membrane, it is assumed here that the principal mode of vibration of the body is longitudinal, and the bending mode of the cell body is assumed to be minimal and thus ignored for two reasons. First, the bending stiffness of the cilia bundle is much smaller compared to that of the cell body, such that majority of applied shearing force is used to deflect the cilia bundle. Second, the reticular lamina and other structures couple outer hair cells and add stiffness to the movement of the body in the bending mode.

A simple model of the mechanical characteristics of the outer hair cell is constructed to represent its longitudinal vibration. If a reference point is set at the static point of limbus, the relevant longitudinal mechanics of the hair cell can be conveyed as in Figure 3.1. In this model, V_{tect} and β are the magnitude and direction (angle with respect to vertical direction) of the velocity of the tectorial membrane, θ is deflection angle of the cilia bundle from upright position, x_1 is the position of the tip of tectorial membrane, x_2 is the position of the apical part of the hair cell, l is length of cilia bundle, m is effective mass of cell body, k_θ is rotational stiffness of cilia, k is linear stiffness of cell body and membrane, b_θ is rotational damping of cilia bundle, b is linear damping of plasma membrane, F_x is generated electromotile force, and k_{db} represent combined admittance of deiters cell and basilar membrane

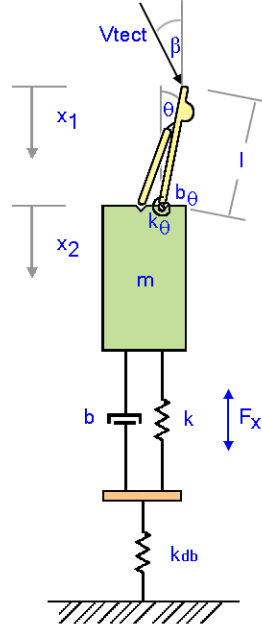


Figure 3.1: This diagram illustrates a baseline hair cell schematic model, considering the parts that are relevant to mechanical vibration.

($k_{db} = \frac{1}{k_{deithers}^{-1} + k_{basilar}^{-1}}$, where $k_{deithers}$ and $k_{basilar}$ represent stiffness of deithers cell and basilar membrane respectively). In order to simplify the model, the following assumptions have been made (see C. Wangcharoenrungs and R. Longoria [116]): 1) all cilia move together as one bundle, 2) the cilia bundle rotate at the base which has rotational stiffness and damping due to endolymph, 3) the cilia bundle has negligible inertia when compared to the cell body, 4) the hair cell's body can be lumped as a single point mass, and 5) the hair cell's plasma membrane has an axial stiffness that is dependent on transmembrane potential.

Based on Figure 3.1, a bond graph is drawn as shown in Figure 3.2. The cilia bundle is modeled similar to a simple linkage. The moment that bends the cilia bundle is separated into two components. One due to axial displacement is

tectorial membrane velocity.

Parameters for this mechanical system model, such as membrane stiffness, can be obtained from both calculation and experiments, as described in the literature (e.g., Iwasa [60]). However, several parameters, such as the effective mass and damping values can not be measured directly and must be estimated by comparing with the overall hair cell mechanical response characteristics, as described by Howard and Hudseph [57]. Model parameterization will be discussed further in section 3.7.4.

This section has dealt exclusively with the mechanical characteristics of the outer hair cell. The inner hair cell, on the other hand, acts mainly as a sensor. The body of the inner hair cell is fixed inside the organ of corti so that its movement is minimal. Thus, a bond graph representation of the inner hair cell mechanical characteristics would be a simpler, representing only the cilia bundle deflection.

3.2 Mechanically gated apical potassium channels

According to the tip-link theory described in the previous chapter, the angle of deflection of the cilia bundle, θ , is related to how much the ionic channel at the apical part opens to allow an inflow of potassium ions. The channels can be considered analogous to resistors and the whole process can be modeled using a modulated resistive element. This is a resistor that relates voltage and current, for example, by $v = R \cdot i$, but the resistance R , is modulated by a system variable such as θ . Thus, $R = R(\theta)$.

It is necessary to have a model that describes how the modulation variable changes. In this case, the channel resistance affects the ion diffusion process. Although Boltzmann statistics are commonly used to describe diffusion dynamics and ionic channel flow in general (such as in Hodgkin and Huxley [53]), Gaussian distribution is better suited in this case for two reasons. First, the primary factor

that influences the flow of ions is hair bundle angle. Second, a Gaussian form provides flexibility in parameterizing the model using statistical results reported in the literature, which will be discussed in detail later.

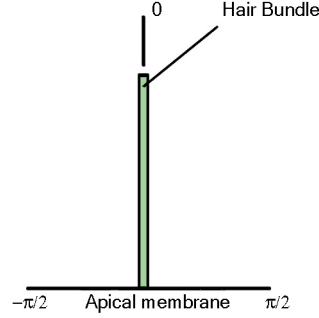


Figure 3.3: Show resting position of hair bundle has been set to zero radian at upright position

As seen in Figure 3.3, based on the assumption that all cilia in the bundle move together as one, the angle of deflection is set to 0 radians at the upright position and it can vary from $-\frac{\pi}{2}$ to $\frac{\pi}{2}$ radians. It is assumed that there are N cilia on this bundle and each can either fully open or fully close their K^+ channel. That is, the more a hair bundle deflects toward the kinocilium in the activation direction, the better chance that each channel will open, thus decreasing the total channel resistance. The probability of a number of channel to fully activate after an input measure, x , is assumed to be governed by a Gaussian distribution as shown in Figure 3.4, which has the probability density function (pdf),

$$f(x) = \frac{1}{\sigma\sqrt{2\pi}} \cdot e^{-\frac{(x-\mu)^2}{2\sigma^2}}. \quad (3.1)$$

Recall, the standard deviation, σ , describes the ‘spread’ of the distribution about the mean, μ ,

$$\sigma = \sqrt{\frac{\sum(x_i - \mu)^2}{N - 1}}. \quad (3.2)$$

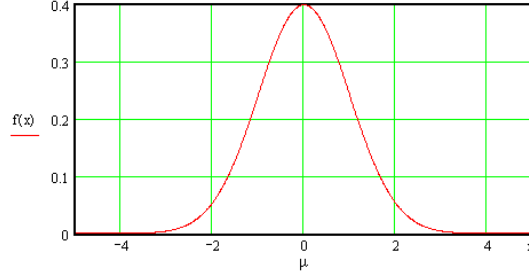


Figure 3.4: The Gaussian normal distribution curve (the famous “Bell Curve”), μ is mean of x , $f(x)$ is frequency of x

The area under the normal distribution curve is the probability, $P(x)$, that all channels are activate relative to: a) all all channel open, $P(x) = 1$, or b) all channels closed which has $P(x) = 0$. The pdf equation integrated from $-\infty$ to x , with, $Z = \frac{x-\mu}{\sigma}$, to find,

$$\begin{aligned}
 P(x) &= \int_{-\infty}^x \frac{1}{\sigma\sqrt{2\pi}} \cdot e^{-\frac{(x-\mu)^2}{2\sigma^2}} dx, \\
 &= \frac{1}{\sqrt{2\pi}} \int_{-\infty}^Z e^{\frac{Z^2}{2}} dZ, \\
 &= \frac{1}{\sqrt{2\pi}} \int_{-\infty}^0 e^{\frac{Z^2}{2}} dZ + \frac{1}{\sqrt{2\pi}} \int_0^Z e^{\frac{Z^2}{2}} dZ, \\
 &= \left(\frac{1}{2} + \frac{1}{2} \operatorname{erf}\left(\frac{Z}{\sqrt{2}}\right)\right), \\
 &= \left(\frac{1}{2} + \frac{1}{2} \operatorname{erf}\left(\frac{x-\mu}{\sqrt{2}\sigma}\right)\right).
 \end{aligned} \tag{3.3}$$

For further detail about statistical variable used above, see Freund and Walpole [41]. Now, result in Equation 3.3 is scaled to use with θ , the angle of deflection, assuming a linear relation between x and θ by setting,

$$x = a\theta + b. \tag{3.4}$$

The probability the a number of K^+ channels are fully opened is scaled with the ratio of channel conductance to maximum channel conductance, g/g_{max} , and equation 3.3 can be rewritten as

$$\frac{g}{g_{max}} = \left(\frac{1}{2} + \frac{1}{2} \operatorname{erf}\left(\frac{a\theta + b - \mu}{\sqrt{2}\sigma}\right)\right), \tag{3.5}$$

or,

$$g = g_{max}(\frac{1}{2} + \frac{1}{2}erf(\frac{a\theta + b - \mu}{\sqrt{2}\sigma})). \quad (3.6)$$

This equation can be compared to the physical system and to the assumptions described previously. First, at the resting position, the angle of deflection, θ , is set at upright (zero radian) position, so $\mu = 0$ and σ can be adjusted according to experimental data. However, in this case, no special relation is found, so the standard deviation is set to unity. Second, by using linear relation between x and θ in equation 3.4, for outer hair cell from two known positions: 1) At approximated activated deflection point or θ of $\frac{\pi}{120}$ radian (inferred from Crawford and Fettiplace [25] data), the channel will have to open at fullest possible, a suitable probability is assumed to be 0.95 or 95 percent probability. Thus, $P = 0.95 = (1 + erf(1.65/\sqrt{2}))/2$. This means $x = 1.65$ at $\theta = \frac{\pi}{120}$ rad: 2) At resting position (θ of approximately zero radian), van Emst, et al.[85] experimental data shows that K^+ channel open at about 27 percent of it maximum, and that is corresponding to $x = -0.613$. These result in two equations with two unknowns,

$$\begin{aligned} 1.65 &= a \cdot \frac{\pi}{120} + b, \\ -0.613 &= a \cdot 0 + b. \end{aligned}$$

Solving above equations get $a = 86.44$, and $b = -0.613$. A similar approach has also been used with apical channel of inner hair cell with open probability of 9 percent at resting position (again from van Emst, et al. [85]) and that yield results of $a = 114.209$, and $b = -1.34$. Ratio of channel conductance to its maximum conductance of outer hair cell and inner hair cell apical potassium channels have been plotted as shown in Figure 3.5.

The result of this approximation as shown in Figure 3.5 has been compared to Boltzmann type of approximation (such as that in van Emst [85]) and found out

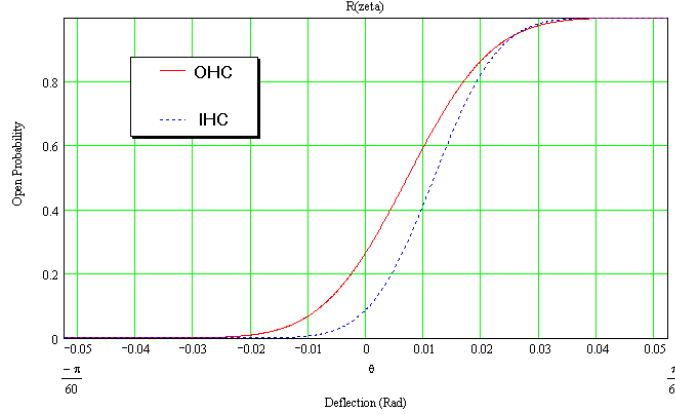


Figure 3.5: Plot of the ratio of estimated channel conductance and maximum channel conductance (g/g_{max}), as a function of the angle of hair bundle deflection, θ , for outer (full line) and inner (dotted line) hair cells.

to give a very similar shape in both the plot and numerical result. Note here that the plot shows an interesting transduction behavior that the hair cells do work best in the deflection range infinitesimally close to their resting point at upright position and a larger deflection will result in a saturation of the transduction channel. At last, a constant is added to the probabilistic equation to model a static conductance of the channel. This yields,

$$g(\theta) = g_{leak} + g_{max} \left(\frac{1}{2} + \frac{1}{2} \operatorname{erf} \left(\frac{a\theta + b - \mu}{\sqrt{2}\sigma} \right) \right). \quad (3.7)$$

where g_{leak} is called a leakage channel conductance. For the final model, recall that conductance is, $g(\theta) = 1/R(\theta)$, where $e = R(\theta) \cdot f$, e is related to ion concentration, and f to ion flow as described in the next section.

3.3 Potential gated basolateral potassium channels

It has become widely known that conductance of each plasma membrane ionic channel depends on such factors as membrane potential, species of sub-

stance, and time. Together, these factors control the level of a cell's potential, firing rate, and refractory period. The derivation of Hodgkin and Huxley in 1952 [53] for cardiac muscle ionic channels' conductance is used here for the reason that this model leads to formulation of the Nernst equation due to German chemist Walther Nernst. The Nernst equation has been extensively used for calculating transmembrane potential and proven to be highly accurate when compared with experimental results.

There are two main factors that drive ions between intracellular fluid and extracellular fluid. A balance between concentration driven flow and transmembrane potential driven flow. First, concentration driven flow can be described by Fick's diffusion law,

$$\overline{j_d} = -D_p \nabla c_p, \quad (3.8)$$

where ∇c_p is the ion concentration gradient, D_p is diffusion constant, and $\overline{j_e}$ is the number of ions moving per time per unit area. Second, the potential driven flow is described by the field law (for ionic mobility),

$$\overline{j_e} = -u_p \frac{Z_p}{|Z_p|} c_p \nabla \phi, \quad (3.9)$$

where Z_p is valence of ions, u_p is ionic mobility which relates to electric conductivity, $-\nabla \phi$ is electric field gradient, and $-u_p \frac{Z_p}{|Z_p|} \nabla \phi$ is mean ion velocity. For ions, the diffusion constant also relates to ionic mobility by,

$$D_p = \frac{u_p R T}{|Z_p| F}, \quad (3.10)$$

where R is universal gas constant (8.314 Joule/K), T is absolute temperature in Kelvin, and F is Faraday's constant of 96487 abs coulomb per gram eq.

A combination of Fick's law and Field law gives the Nernst-Planck equation. That is,

$$\overline{j_p} = -D_p \left(\nabla c_p + \frac{Z_p c_p F}{R T} \nabla \phi \right). \quad (3.11)$$

In an equilibrium condition, total flow equal to zero and integration of Nernst-Planck equation gives Nernst equation,

$$E_m = \frac{RT}{FZ_p} \ln\left(\frac{[C]_e}{[C]_i}\right), \quad (3.12)$$

where, E_m is equilibrium transmembrane potential, $[C]_e$ is extracellular fluid concentration of ion, and $[C]_i$ is intracellular fluid concentration of ion. The Nernst equation is well known and has been widely used to estimate the resting transmembrane potential of a cell. This equation can be rearranged as,

$$\frac{[C]_e}{[C]_i} = e^{\frac{-E_m F Z_p}{RT}}. \quad (3.13)$$

Now, to realize this equation in statistical form just like that used on apical potassium channel, this equation has to be changed and compared with Boltzmann statistics. The following method was used by Weiss and Leong [124], and a linear relation is assumed to exist between concentration of intracellular and extracellular fluid and probability of ions being inside and outside of the cell body. From equation 3.13, a probability equation of the form,

$$\frac{[c]_i}{[c]_e} \Leftrightarrow \frac{P_i}{P_o} = e^{\frac{-E_m F Z_p}{RT}}. \quad (3.14)$$

relates P_i and P_o , which are probabilities of ion being inside and outside, respectively. Therefore,

$$\frac{P_i}{P_{total}} = \frac{P_i}{P_o + P_i} = \frac{1}{\frac{P_o}{P_i} + 1} = \frac{1}{\frac{P_o}{P_i} + 1} = \frac{1}{1 + e^{\frac{-E_m F Z_p}{RT}}}. \quad (3.15)$$

A linear relation is also assumed to exist between probability of ions to be in intracellular fluid and ratio of conductance per maximum conductance of the channel.

That is,

$$\frac{P_i}{P_{total}} \propto \frac{g}{g_{max}}, \quad (3.16)$$

where, g is basal potassium channel conductance. Then,

$$g = \frac{\alpha g_{max}}{1 + e^{-\beta E_m}}, \quad (3.17)$$

where, α and β are constants that can be arrived at from experimental data for a specific kind of cell. This equation can be simplified in resistive form to,

$$r_k(E_m) = \frac{\gamma}{g_{max}}(1 + e^{-\beta E_m}), \quad (3.18)$$

where $r_k(E_m)$ is the nonlinear channel resistance, γ in this case is equal to $\frac{1}{\alpha}$.

Finally, the equation has been plotted against membrane potential using data found in the literature (such as van Emst, et al. [85] and Rattey, et al. [39]). Basal ionic flow can be estimated as, $i_b = E_m/r_k(E_m)$. According to van Emst's model the outer hair cell's basal potassium channel has a conductance of 12.99 nS at -60 mV resting potential which corresponds to a g_{max} of $1.358 \cdot 10^{-7}$ S in our equation. Similarly, inner hair cell basal potassium channel has a conductance of 12.32 nS at -44 mV corresponding to a g_{max} of $7.629 \cdot 10^{-8}$ S, as shown in Figure 3.6. From the figure, it can be clearly seen that this function predicts effect of basal potassium channel in a similar fashion as observed in the studies reported [39, 124]. The plot shows that when transmembrane potential increases, channel resistance decreases to allow potassium to increase flow. On the other hand, whenever transmembrane potential decrease to resting state, the channel increases its resistance. The values of γ and β can be further adjusted to better fit with experimental data and a specific kind of hair cell. In this particular case, a β of 37.4366 (calculated at 310⁰ K temperature) and a γ of 1 (no further scaling) are used to illustrate the basic trends found in typical hair cells.

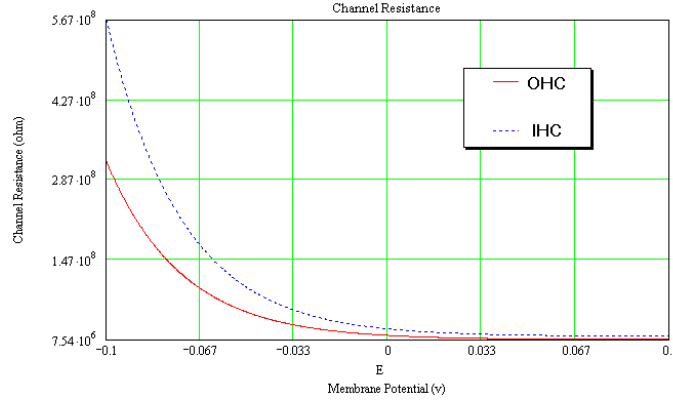


Figure 3.6: Plotting shown relation between transmembrane potential versus basal potassium channel resistance of outer hair cell (full) and inner hair cell (dotted) using data from van Emst, et al. [85].

3.4 Dependence of plasma membrane potential on potassium and its channel

As described in previous chapter, the ionic gating mechanism in hair cells has been found to involve more than one species of ions. However, the process of transmembrane potential generation does not rely on any chemical interaction between these ions and other substance in hair cells. In order to simplify the model, the ion species that play the most important role in this process has to be identified. From inspection and examples of models in the literature, it can be found that the potassium cation (K^+) is responsible for the majority of changes in the membrane potential process. The reason for this is described below.

It has been discussed that changes in transmembrane potential depend on concentration of ions and their specific channel permeability. For hair cells, the situation is special in that the cell is situated between two lymph fluids, endolymph and perilymph. Both of them have a different concentration of ions as shown in the table of Figure 3.7.

| | Endolymph (mM/l) | Hair cell's ICF (mM/l) | Perilymph (mM/l) | Channel Permeability (cm/s) |
|---------------------|---------------------|---------------------------|---------------------|--------------------------------|
| [K ⁺] | 150 | 130 | 4 | 2·10 ⁻⁶ |
| [Ca ²⁺] | N/A | 0.1 | 2.4 | 2·10 ⁻⁷ |
| [Na ⁺] | 1 | 15 | 145 | 2·10 ⁻⁸ |
| [Cl ⁻] | 130 | 130 | 130 | N/A |

Figure 3.7: Table showing concentration of each significant ion species and corresponding permeability coefficient (from Geisler [45], Rattay, et al. [39], Webster [121], and cochlear fluids lab at Washington University).

Another equation for membrane equilibrium potential that accounts for the influence of many ionic species in the internal and external media was first developed by Goldman in 1943 and later modified by Hodgkin and Katz in 1949 [121]. This equation is called the Goldman-Hodgkin-Katz equation which is a modified form of the Nernst equation,

$$E = \frac{RT}{F} \ln \left(\frac{P_K[K]_e + P_{Na}[Na]_e + P_{Ca}[Ca]_e}{P_K[K]_i + P_{Na}[Na]_i + P_{Ca}[Ca]_i} \right). \quad (3.19)$$

where, P is the permeability coefficient of each ion channel.

Using Goldman-Hodgkin-Katz equation shown above, simple calculation can be done. First, for all species, it is assumed that equal permeability of sodium channel to be approximately equal between apical and basal part, but for potassium channel permeability we conservatively approximate that the basal channel is five times more permeable than the potassium channel in the apical channel. For the condition of body temperature of 300 degree Kelvin, we will have $\frac{RT}{F}$ equal to approximately 26.7 mV. The hair cell's membrane resting potential, considering effect of all ionic species, can be approximated to be around -40.4 mV.

Now as seen in the table of Figure 3.7, the potassium channel is typically ten

to hundred times more permeable than that of calcium or sodium. The hypothesis is that the resting potential can be approximated using just the effect of potassium ion. Repeating the previous calculation we find a resting membrane potential of -40.67 mV, a value very close to when all ionic species are considered. It is concluded that the resting potential of a hair cells' plasma membrane can be approximated using the effect of the potassium ionic channel only. This kind of membrane is what electrophysiologists call a "potassium membrane" (as discussed by Webster [121]).

3.5 Equivalent circuit model of hair cell

Electrical behavior of different kinds of cell has been extensively studied by many researchers (e.g., Dallos and Evans [31], Mountain and Hubbard [86], and Rattey, et al. [39]). As discussed previously, ion flow through a cell is driven by both concentration gradient and potential gradient, which generates a balanced point that can be calculated by the Nernst equation. A concentration difference makes plasma membrane, which is a dielectric lipid bilayer, separate charges just like an electrical capacitor. Ion channels distributed throughout a membrane can be considered as a resistor that is modulated by gating behavior specific to each kind of ion. The Nernst potential for each specific channel can be modeled by a voltage source in series to each resistor with polarity placed in a direction opposite to the concentration gradient. In summary, an electrical model can be visualized as in the electrical circuit of Figure 3.8.

As discussed, in this case we consider only potassium ions, and the hair cells are situated between two special kinds of extracellular fluids, endolymph and perilymph. In the apical membrane, the potassium channel is mechanically gated by the hair bundle and the channel can be modeled using a modulated resistance governed by a Gaussian distribution. The basal ionic channel is also modeled by

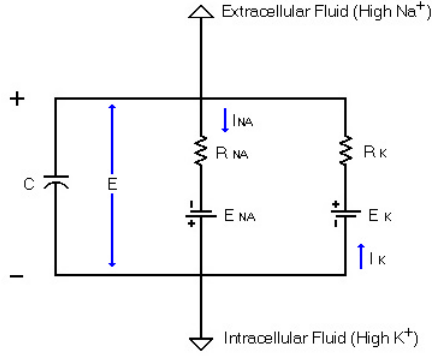


Figure 3.8: Electrical equivalent digram of plasma membrane, C is membrane capacitance, R_{NA} is modulated sodium channel resistance, R_K is modulated potassium channel resistance, E_{NA} is Nernst potential of sodium channel, and E_K is Nernst potential of potassium channel (modified from Webster, et al.[121])

another resistance governed by Boltzmann statistics that has been previously discussed. The general equivalent circuit model is modified for hair cell application as shown in Figure 3.9. The imposed potentials at the endolymph and perilymph determine the three current flows,

$$\begin{aligned} i_a &= g(\theta) \cdot E_a \\ i_b &= \frac{E_m}{r_k(E_m)} \\ \dot{q} &= i_a - i_b \end{aligned} .$$

Despite the simplicity of this equivalent circuit model, a simple simulation using general parameters as seen in Figure 3.10 demonstrates the ability of this equivalent circuit to predict the response of receptor potential (or transmembrane potential) for a change in the angle of deflection input reasonably well. As seen in the plots, the model predicts a resting potential of about -35 mV, which is quite realistic. After 35 millisecond, the hair bundle has been deflected by a displacement impulse to about 0.8 radian (45 degree), this promptly initiates a change in level of the resting potential similar to that discussed in the literature by Webster [121],

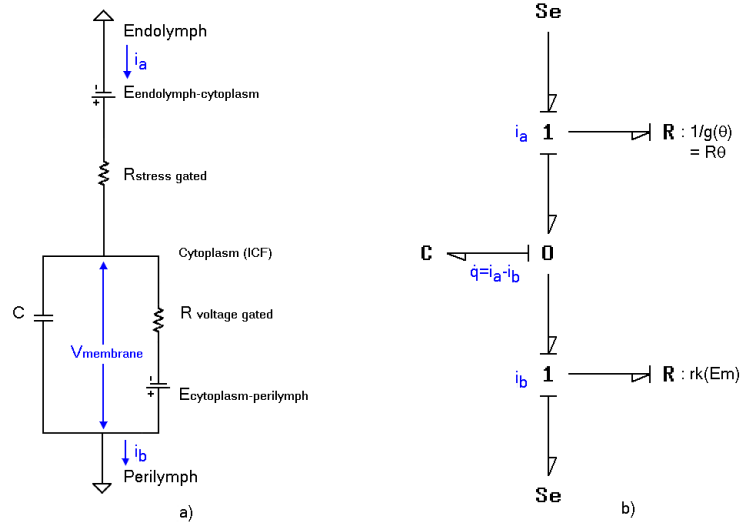


Figure 3.9: a) Equivalent circuit diagram of hair cell ion flow, considering only potassium. The model uses perilymph as a reference. b) A bond graph representation of the model in a)

Hodgkin, et al. [53], and Plonsey, et al. [96]. A transport delay of 3 millisecond has been added to the basal ion channel to simulate a slow effect in basal ion channel that senses calcium ions as a second messenger (as discussed by van Emst, et al. [85]). Note that, the simulation in Figure 3.10 is a test of equivalent ionic channels model only. In physiological systems, hair cells are deflected at much smaller angles than in this simulation.

3.6 Electromotility of plasma membrane

The outer hair cell membrane has been observed to exhibit transductive properties referred to as electromotility. This means that under an electrical potential, the plasma membrane of hair cells responds by changing its length. When the cell's membrane is in depolarized state, the cell's body decreases its length while increasing its diameter to compensate so as to maintain volume. On the other hand,

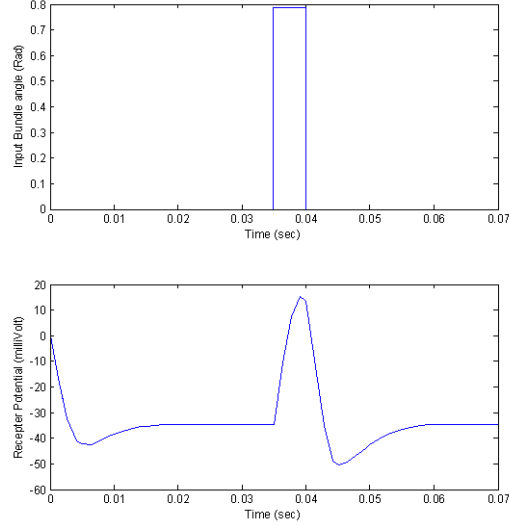


Figure 3.10: Simulation of receptor potential response to impulse deflection in bundle angle. Note that arbitrary initial conditions lead to an initial condition response. Once settled, the bundle deflection input is specified at 35 msec.

when the cell's membrane is in a hyperpolarized state, the cell's body elongates while its diameter decreases. An imposed strain rate on the cell wall conversely generates a transmembrane current. This coupled electro-mechanical behavior is similar that of piezoelectric material [110]. Under in vivo and experimental conditions, the strains developed in the cell wall are small, thus the material of the cell wall can be considered piezoelectric and linear in terms of strain and nonlinear in terms of radial electric field or transmembrane potential [120].

However, the origin of the motility of the hair cell is still under study. No definite description has been given to explain the molecular mechanics of the process until recently. For example, one recent discovery is that the plasma membrane of the outer hair cell is composed of a special motor protein called “prestin” (see Zheng, et al. [66] for details). Another study proposes that the hair cell's membrane

might be folded or bent, assuming that the plasma membrane is tightly connected to the cytoskeleton at the pillar, and that the turgor pressure creates a force that bends each portion of the plasma membrane between the pillar. The mathematical explanation for the bending mechanism is thought to be similar to the folding mechanism of red blood cells (see Raphael, et al. [99] for details).

Nevertheless, two main approaches have been taken for mathematical modeling of electromotility and active force generation. The molecular or area motor approach explicitly includes parameters and relationships for an elementary active motor which allows the derivation of the active strains and force in terms of the motor's characteristics (such as the model of Adachi and Iwasa [6], and Dallos, et al. [93]) and the phenomenological approach based on linear piezoelectric relationships (such as models of Jen and Steel [69], Spector [105], and Spector, et al. [4]).

In this dissertation, a phenomenological approach was adopted for three reasons. First, there exists an extensive knowledge base for modeling of piezoelectricity in the sensor engineering field which can be used as a guide. Second, this approach can be easily integrated into a bond graph modeling method. Third, the bond graph modeling result can be used to guide the engineering of a sensor with hair cell attributes. Three different modeling methods based on phenomenological approach are proposed here for modeling electromotility of hair cell in our study. 1) one dimensional 2-port capacitor, 2) two dimensional 3-port capacitor using linear impedance matrix, and 3) two dimensional 3-port capacitor using nonlinear energy method. Each approach has its own advantages and disadvantage as discussed next.

3.6.1 One dimensional 2-port capacitor electromotility model

A one dimensional model is the simplest type used for modeling a piezoelectricity sensor. As discussed by Busch-Vishniac and Paynter [20], the relationship

is very conveniently integrated into a bond graph model. From this model, the relationship to a capacitive sensor can be easily seen.

The piezoelectric model for a hair cell is based on the assumption that force generated depends on plasma membrane strain (in longitudinal and circumferential direction) and transmembrane potential [4]. This relationship can be expressed as,

$$\begin{bmatrix} F_x \\ F_\theta \end{bmatrix} = \begin{bmatrix} k_{xx} & k_{x\theta} \\ k_{\theta x} & k_{\theta\theta} \end{bmatrix} \cdot \begin{bmatrix} \epsilon_x \\ \epsilon_\theta \end{bmatrix} + \begin{bmatrix} f_x(\Delta V) \\ f_\theta(\Delta V) \end{bmatrix}, \quad (3.20)$$

where, F is resultant force generated, k is stiffness matrix, ΔV is transmembrane potential, x is axial direction, and θ is circumferential direction.

This equation can be simplified by considering only the longitudinal direction. It can be inferred that energy stored in this system, represented by independent intensive variables depends on stored charge, q , and dynamic membrane displacement, x [20]; that is,

$$E = E(q, x). \quad (3.21)$$

One constitutive relation for this two port is,

$$\frac{\partial E}{\partial q} = V = \frac{q}{C}, \quad (3.22)$$

where $C = \frac{\epsilon A}{h}$, ϵ is relative dielectric constant of the membrane, A is membrane area, and h is membrane thickness. The constitutive relation is then,

$$V_c = \frac{q(h_0 + x)}{\epsilon A}. \quad (3.23)$$

This relation comes from $h = h_0 + x$, where the membrane thickness is equal to initial thickness, h_0 , plus a dynamic change in membrane thickness, x .

Since it can be found that,

$$\frac{\partial E}{\partial q} = V_c = \frac{q(h_0 + x)}{\epsilon A}, \quad (3.24)$$

then,

$$E = \int V_c dq = \int \frac{q(h_0 + x)}{\varepsilon A} dq = \frac{q^2(h_0 + x)}{2\varepsilon A} + \phi(x). \quad (3.25)$$

Assume in this case $\phi(x)$ is normal electric strain energy, $\phi(x) = \frac{x^2}{2C_E}$, so energy stored in plasma membrane is,

$$E = \frac{q^2(h_0 + x)}{2\varepsilon A} + \frac{x^2}{2C_E}. \quad (3.26)$$

which makes,

$$F = \frac{\partial E}{\partial x} = \frac{q^2}{2\varepsilon A} + \frac{x}{C_E}, \quad (3.27)$$

and,

$$V_c = \frac{\partial E}{\partial q} = \frac{q(h_0 + x)}{\varepsilon A}. \quad (3.28)$$

The constitutive relations in equation 3.27 and equation 3.28 couple the mechanical and electrical domains in the hair cell in form of 2-port capacitor. Although the simple behavior of hair cell membrane electromotility can be described using this one dimensional 2-port capacitor model, comparison of magnitude of force predicted by equation (3.27) shows significant difference from that observed in studies reported in the literature.

Further analysis also found that the inconsistency between these equations and dynamic behavior of hair cell electromotility stem from the characteristics of the model equations themselves. It has been found by simulations that these equations are not really suitable for predicting the electromotility effect due to three specific reasons. First, the transmembrane potential is in a transverse direction but hair cell contracts and expands in a longitudinal direction, so clearly the one-dimensional model is not appropriate. Second, the polarization energy that has been ignored appears to play a significant role in active force generation in the hair cell plasma membrane. Third, the force generated is predicted to be from Coulombic force

which is always in one direction, regardless of the direction of current flow across membrane. Equation 3.27 simply predicts dynamic effects resulting from an interaction between Coulombic energy and strain energy forces. Further discussions on modeling electromotility mechanism of hair cells using one dimensional equations and the simulation characteristics can be found in Wangcharoenrung and Longoria [116].

For all reasons stated above, it can be seen that a method of modeling electromotility mechanism considering a two dimensional approach has to be developed. This may also compensate for inconsistency in the simulations described. Considerations of more complex, two dimensional 3-port capacitor model will be discussed in the following sections.

3.6.2 Two dimensional 3-port capacitor: impedance method

Impedance matrix methods have been widely used to model general (both inorganic and organic) piezoelectric materials. Although the structure of the hair cell membrane does not have the crystallized structure found in the majority of piezoelectric materials, the motor mechanism of hair cells has shown many of the characteristics analogous to those of piezoelectric materials. Fundamentally, any changes in membrane potential generate electromotile force, and applied force reciprocally generates transmembrane potential.

Recent studies have shown that a linear piezoelectric relationship can be used to model the hair cell membrane electromotility (see Tolomeo and Steel [109] and Spector [105]). This approach describes material piezoelectric characteristics using an impedance matrix (e.g., Davi [32]), which take the form,

$$\begin{bmatrix} \mathbf{T} \\ \mathbf{d} \end{bmatrix} = \begin{bmatrix} C^{(\xi)} & -\mathbf{e} \\ \mathbf{e}^T & \mathbf{K}^{(\epsilon)} \end{bmatrix} \cdot \begin{bmatrix} \epsilon \\ \xi \end{bmatrix}. \quad (3.29)$$

where \mathbf{T} is the Cauchy stress field, ϵ is infinitesimal strain field, \mathbf{d} is electric displacement field, ξ is electric field, $C^{(\xi)}$ is elasticity tensor field evaluated at constant electric field (ξ), $\mathbf{K}^{(\epsilon)}$ is permittivity tensor field evaluated at constant strain (ϵ), and finally \mathbf{e} is piezoelectric stress tensor field.

The piezoelectric model constitutive relation can be expressed in a simplified form that has displacement as independent variable (e.g., see Busch-Vishniac [19]),

$$\begin{bmatrix} \mathbf{T} \\ \xi \end{bmatrix} = \begin{bmatrix} C^{(d)} & -H \\ -H^T & \beta^{(\epsilon)} \end{bmatrix} \cdot \begin{bmatrix} \epsilon \\ \mathbf{d} \end{bmatrix}. \quad (3.30)$$

where now $C^{(d)}$ is the elasticity tensor field evaluated at constant electric displacement, H is $\frac{e}{\mathbf{K}^\epsilon}$, and $\beta^{(\epsilon)}$ is now an inverse of \mathbf{K}^ϵ .

In order to use equation (3.30) for the model, first we estimate elasticity tensor, $C^{(d)}$, using theory of elasticity for thin wall cylindrical shell in two dimensions (as seen in Love [78], and Timoshenko [108]). Basic geometry and notation of the shell used is shown in Figure 3.11.

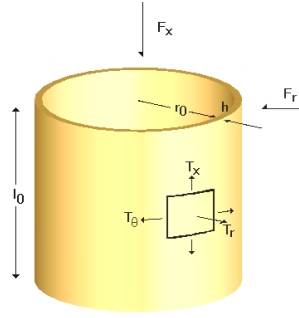


Figure 3.11: Geometry and notation used to represent the plasma membrane deformation in two dimension, force input is positive inward to the body.

The type of material model must be specified for membrane mechanics. While a simple isotropic material may be a good choice, essential parameters are hard to find. Fortunately, Spector, et al. [3] have compiled orthotropic parameters

for hair cell membrane material. Recall that an orthotropic material is defined as a material having a set of principal axes for which there is no shear coupling, but not necessary having the same moduli in the orthogonal direction. From shell theory, strain for thin wall cylindrical plates is related to stress in radial and axial directions for an orthotropic material by,

$$\begin{bmatrix} \epsilon_x \\ \epsilon_r \end{bmatrix} = \begin{bmatrix} \frac{1}{E_1 h} & -\frac{r_0 \nu_2}{E_2 h} \\ -\frac{\nu_1}{E_1 h} & \frac{r_0}{E_2 h} \end{bmatrix} \cdot \begin{bmatrix} T_x \\ T_r \end{bmatrix}. \quad (3.31)$$

where, E in this case is modulus of elasticity of material, ν is the Poisson ratio, h is effective thickness of the shell or plasma membrane thickness, and r_0 is initial radius of the hair cell. The force is define downward positive in the x (1), direction and inward positive in the r (2), direction. Inversion of equation 3.31 result in elasticity tensor $C^{(d)}$ (from equation 3.30) as ,

$$\begin{bmatrix} T_x \\ T_r \end{bmatrix} = \begin{bmatrix} \frac{E_1 h}{(1-\nu_1 \nu_2)} & \frac{\nu_2 E_1 h}{(1-\nu_1 \nu_2)} \\ \frac{\nu_1 E_2 h}{r_0(1-\nu_1 \nu_2)} & \frac{E_2 h}{r_0(1-\nu_1 \nu_2)} \end{bmatrix} \cdot \begin{bmatrix} \epsilon_x \\ \epsilon_r \end{bmatrix}. \quad (3.32)$$

where, $C_{11} = \frac{E_1 h}{(1-\nu_1 \nu_2)}$, $C_{12} = \frac{\nu_2 E_1 h}{(1-\nu_1 \nu_2)}$, $C_{21} = \frac{\nu_1 E_2 h}{r_0(1-\nu_1 \nu_2)}$, and $C_{22} = \frac{E_2 h}{r_0(1-\nu_1 \nu_2)}$.

Now, by considering a stress area of $2\pi r_0$ in axial direction, and $2\pi r_0 l_0$ in radial direction, where l_0 is initial length of the hair cell, the equations can be reformulated for use in the hair cell system model. The constitutive equation can be shown in a convenient form, where a linear relation is assumed between stress and force, strain and displacement, electric field and transmembrane potential, and finally electrical displacement and charge. Transforming equation 3.32 then gives,

$$\begin{bmatrix} F_x \\ F_r \end{bmatrix} = \begin{bmatrix} \frac{2\pi r_0 E_1 h}{l_0(1-\nu_1 \nu_2)} & \frac{2\pi \nu_2 E_1 h}{(1-\nu_1 \nu_2)} \\ \frac{2\pi \nu_1 E_2 h}{(1-\nu_1 \nu_2)} & \frac{2\pi l_0 E_2 h}{r_0(1-\nu_1 \nu_2)} \end{bmatrix} \cdot \begin{bmatrix} \Delta x \\ \Delta r \end{bmatrix}. \quad (3.33)$$

where, h is effective thickness of the shell or plasma membrane thickness, l_0 is initial length of hair cell, and r_0 is initial radius of the hair cell.

The piezoelectric tensor field (H) is usually determined by a specific material's empirical study (e.g., Ikeda [59]), however, experimental data for hair cell

membrane is scarce. It might also be possible to use organic polymer characteristics to approximate the membrane piezoelectric properties, due to structural similarity. A study by Spector, et al., [4] suggests using a simple exponential function to approximate the tensor H , namely,

$$F_x = \begin{cases} a_x^+ [1 - \exp(-b_x^+ \Delta V)] & \text{when } \Delta V \geq 0 \\ a_x^- [1 - \exp(-b_x^- \Delta V)] & \text{when } \Delta V < 0 \end{cases} \quad (3.34)$$

and,

$$F_r = \begin{cases} a_r^+ [1 - \exp(-b_r^+ \Delta V)] & \text{when } \Delta V \geq 0 \\ a_r^- [1 - \exp(-b_r^- \Delta V)] & \text{when } \Delta V < 0 \end{cases} \quad (3.35)$$

These equations have to be modified using a capacitive constitutive relation between voltage and charge, and considering only the major potential gradient in radial (e_r) direction. The constants, a_x^+ , a_x^- , b_x^+ , b_x^- , a_r^+ , a_r^- , b_r^+ , and b_r^- have a requirement for smoothness as,

$$b_x^- = \frac{a_x^+ \cdot b_x^+}{a_x^-}, \quad b_r^- = \frac{a_r^+ \cdot b_r^+}{a_r^-}. \quad (3.36)$$

Finally, $\beta^{(\epsilon)}$ can be considered for this application in only one (radial) dimension to be a simple constitutive relation for a concentric cylinder that has a capacitance given by,

$$C = \frac{2\pi\epsilon_0\epsilon_r L}{\ln(b/a)} \quad (3.37)$$

where, ϵ_0 and ϵ_r are the dielectric constants for free space and relative dielectric constant of plasma membrane, respectively. The constant, b , is the outer radius, a is the inner radius ($b - a$ is membrane thickness, h), and L is the effective length of the outer hair cell.

The linear assumption, however, allows use of the piezoelectric coupling coefficient, e , derived by Tolomeo and Steele [109] in their linear model. The piezoelectric tensor field, H , can then be represented in terms of the piezoelectric coupling

coefficient, e , by,

$$\begin{aligned} H_x &= \frac{e_1 \cdot h}{\varepsilon \cdot l_0} \\ H_r &= \frac{e_2 \cdot h}{\varepsilon \cdot r_0} \end{aligned} \quad (3.38)$$

where ε is the dielectric constant (electric permittivity) of the plasma membrane.

From equations 3.30, 3.33, and 3.38, with a parallel plates capacitor model equation, the membrane piezoelectric (electromotility) mechanism can be represented by a 3-port, 2-dimensional capacitive, $(-\mathbf{C}-)$, element having the constitutive relations,

$$F_x = \frac{2\pi r_0 E_1 h}{l_0(1 - \nu_1 \nu_2)} \cdot \Delta x_2 + \frac{2\pi \nu_2 E_1 h}{(1 - \nu_1 \nu_2)} \cdot \Delta r + \frac{e_1 h}{\varepsilon l_0} \Delta q, \quad (3.39)$$

$$F_r = \frac{2\pi \nu_1 E_2 h}{(1 - \nu_1 \nu_2)} \cdot \Delta x_2 + \frac{2\pi l_0 E_2 h}{r_0(1 - \nu_1 \nu_2)} \cdot \Delta r + \frac{e_2 h}{\varepsilon r_0} \cdot \Delta q, \quad (3.40)$$

and,

$$V_r = \frac{e_1 h}{\varepsilon l_0} \cdot \Delta x_2 + \frac{e_2 h}{\varepsilon r_0} \cdot \Delta r + \frac{h}{2\pi \varepsilon r_0 l_0} \cdot \Delta q. \quad (3.41)$$

This electromotility model is an electromechanical (transducer) coupling between the mechanical subsystem and the plasma membrane electrical circuit subsystem. The overall hair cell model formed is described in the next section.

3.6.3 Two dimensional 3-port capacitor: the energy method

Another alternate three-port two dimensional model that can be considered is based on expansion of the one dimensional model to two dimensions, and includes the polarization energy. We start from the equation describing capacitance for concentric cylinder so that,

$$\frac{\partial E}{\partial q} = V = \frac{q}{2\pi \varepsilon_o \varepsilon_r (l_0 - x)} \cdot \ln\left(\frac{r_0 + h + r}{r_0}\right). \quad (3.42)$$

A very critical assumption for this equation is that the plasma membrane's thickness is constant, and the pressure changing inside hair cell during its motility will only have an effect on cell's length and diameter.

The method applied in the first approach is now considered with strain energy in two dimensions. The Petrov theory of flexoelectricity for active transport, which assumes a linear relationship between membrane polarization enthalpy, Ph , and membrane deformation, e , (as presented in Raphael, et al. [99]) leads to,

$$Ph = f \cdot c \cdot e \quad (3.43)$$

where, f is flexoelectric coefficient, c is membrane curvature. If a linear relation is assumed between membrane curvature and total deflection, as well as between field and transmembrane voltage, the total polarization energy can be expressed as,

$$E_P = \frac{\alpha x}{2\pi\varepsilon_0\varepsilon_r(l_o - x)} \ln\left(\frac{r_0 + h + r}{r_0}\right)q, \quad (3.44)$$

where, α is a constant related to flexoelectric coefficient. We will then have an equation for total energy stored in plasma membrane as,

$$E_{tot} = \frac{\ln\left(\frac{r_0+h+r}{r_0}\right)}{2\pi\varepsilon_0\varepsilon_r(l_o - x)} \cdot \left(\alpha x + \frac{q}{2}\right)q + \frac{1}{2}k_{11}x^2 + \frac{1}{2}k_{22}r^2 + k_{12}xr, \quad (3.45)$$

where k_{nn} is the stiffness of the material that can be inferred from Equation (3.33), yielding a final set of constitutive relations,

$$F_r = \frac{\partial E}{\partial r} = \frac{q \cdot \left(\alpha x + \frac{q}{2}\right)}{2 \cdot (r_0 + h + r)\pi\varepsilon_0\varepsilon_r(l_o - x)} + k_{22}r + k_{12}x, \quad (3.46)$$

$$F_x = \frac{\partial E}{\partial x} = \frac{\ln\left(\frac{r_0+h+r}{r_0}\right)}{2\pi\varepsilon_0\varepsilon_r(l_o - x)^2} \cdot \left(\alpha x + \frac{q}{2}\right)q + \frac{\ln\left(\frac{r_0+h+r}{r_0}\right)}{2\pi\varepsilon_0\varepsilon_r(l_o - x)} \cdot \alpha q + k_{11}x + k_{12}r, \quad (3.47)$$

and,

$$V = \frac{\partial E}{\partial q} = \frac{\ln\left(\frac{r_0+h+r}{r_0}\right)}{2\pi\varepsilon_0\varepsilon_r(l_o - x)} \cdot \left(\alpha x + \frac{q}{2}\right) + \frac{\ln\left(\frac{r_0+h+r}{r_0}\right)}{4\pi\varepsilon_0\varepsilon_r(l_o - x)} \cdot q. \quad (3.48)$$

These three equations represent a two dimensional three port capacitive element. This equation has the advantage of predicting nonlinear behavior of electromotility not present in the linear impedance method. However, the constant α

related to flexoelectric coefficient must be derived from experiments. Up until now, there has been no published experimental data regarding this constant. Therefore, a simulation result using this model will have to rely primarily on trial and error with the value of α and compare with simulation results from other methods.

3.7 A bond graph model of the hair cell

Overall model formulation requires connection of all the subsystem models and selection of model parameters and constitutive relations. With all elements necessary to build a model of hair cell formulated, the complete bond graph model of the outer hair cell is formed by connecting the subsystem models together, as illustrated in the block diagram of Figure 3.12. From the overall bond graph model, causality assignment and equation formulation follow systematic procedures [33].

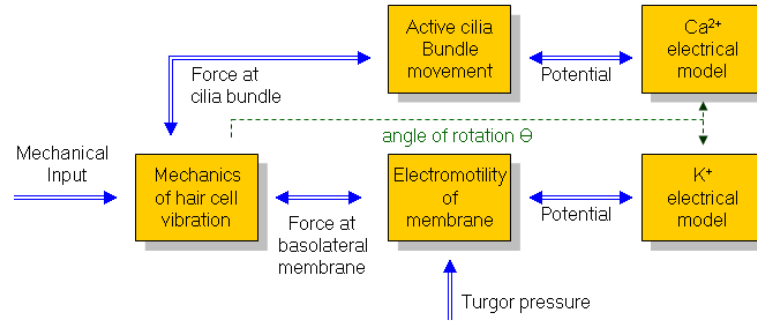


Figure 3.12: Block diagram showing the signal and energy interaction between principle subsystems of the outer hair cell.

3.7.1 Model Description

The hair cell model developed here is composed of: 1) the mechanism of hair cell vibration, being a model for longitudinal vibration of the equivalent mechanical structure of the hair cell using a lumped parameter approach, 2) a piezoelectric or

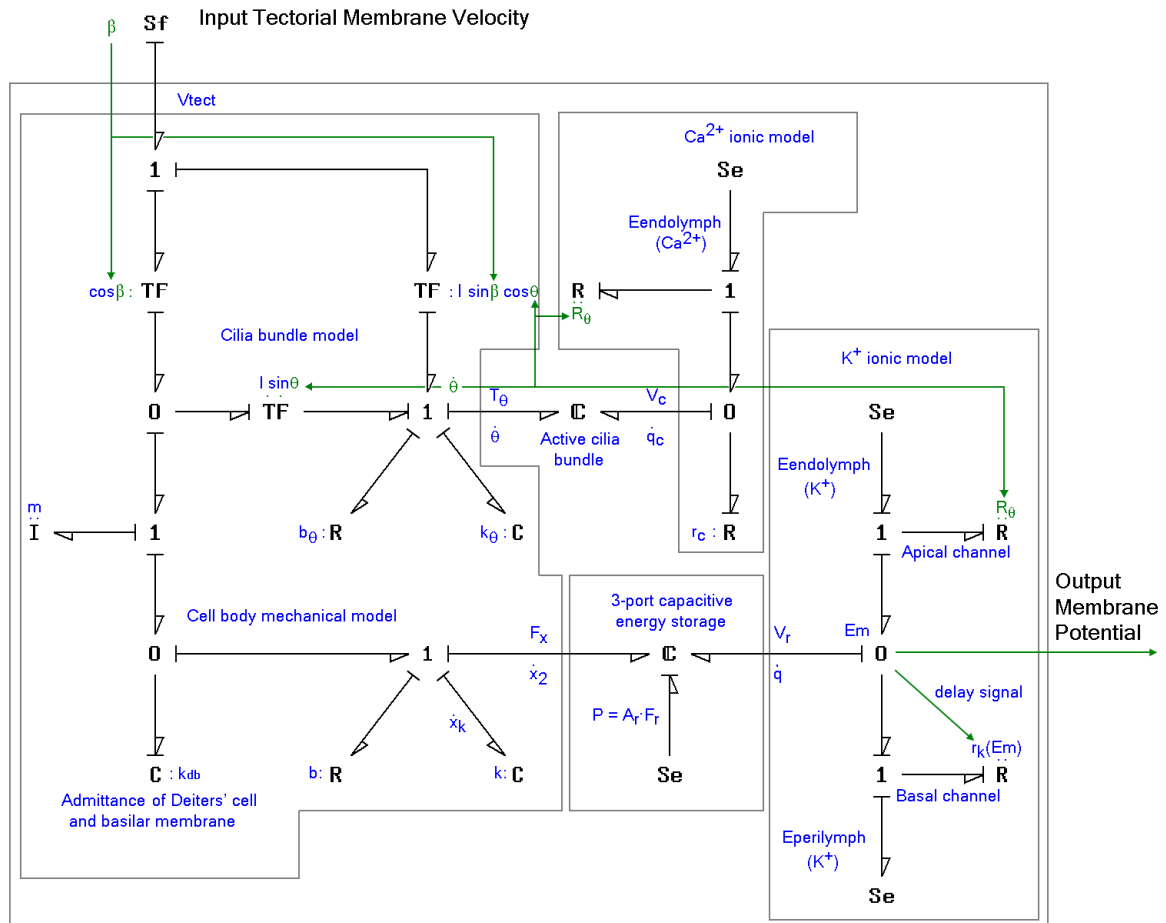


Figure 3.13: Bond graph of outer hair cell.

electromotility model of the plasma membrane, which couples the mechanical and electrical parts of the model, 3) the potassium ion current equivalent circuit model that governs membrane receptor potential, 4) active cilia bundle model which has similar mechanoelectrical coupling structure as electromotility model, and 5) the calcium ion current diffusion model that is governed by a nonlinearity in the cilia bundle. By connecting the bond graphs of each subsystem previously discussed, an overall bond graph model of the hair cell has been developed, as shown in Figure 3.13.

The OHC bond graph model of Figure 3.13 has been separated into five compartments in the same configuration as Figure 3.12. The left-most compartment represents the mechanical characteristics of the hair cell. The right-most compartment and center-top compartments represent the potassium ionic current and calcium ionic current equivalent circuit model respectively. Electromechanical coupling is modeled by multiport capacitive (C) element. Specifically, coupling between potassium current equivalent circuit and mechanics of cell membrane is the 3-port capacitive (C) element having the constitutive relations in equations 3.39, 3.40, and 3.41 (center-bottom compartment). Similarly, a coupling between calcium current equivalent circuit and mechanics of cilia bundle is the 2-port capacitive (C) element (center-middle compartment) which models nonlinearity in the cilia bundle (as discussed in Choe, et al. [128]).

The mechanical compliance of the hair cell structure has been split into two capacitive elements. There is a static compliance quantified by the value $1/k$, where k is the stiffness of the *demembrated* structure of the hair cell (as discussed in Holley and Ashmore [54]). The mechanical compliance is modeled by the mechanical port on the 3-port capacitive (C) element which represents the dynamic compliance of the cell wall that is also related to membrane potential. Looking from opposite direction

of this 3-port, the capacitive element represents the dynamic capacitance of the wall which is also related to mechanical strain. The third port allows consideration of the turgor pressure, P , ($P = A_r F_r$ where A_r is membrane area), surrounding the hair cell structure. In the present study, this pressure was held fixed, and as such did not introduce any dynamics into the problem. The hydrostatic pressure would be needed in the constitutive relations, and the associated volumetric change is related to the mechanical displacement and the charge states on the other bonds of the 3-port.

Finally, a signal bond is used to pass information such as angle of the cilia bundle and is represented by a line with a full arrow. The signal flow symbolizes how the angle of the hair bundle deflection modulates the open level of both potassium and calcium channels at mechanical gated channel inside the cilia.

3.7.2 Simplified Bond Graph Model

In order to compare the bond graph model developed with experiments, the general bond graph model of the outer hair cell will be simplified. Specifically, the condition of interest is a mammalian outer hair cell in a clamped condition. This comparison is made for two reasons. First, active force generation in mammalian cochlea and associated hair cells has been better understood, and recently it has been concluded that the source of force generation motility of the membrane is protein prestin (see Liberman, et al. [84]). Non mammalian OHCs have no prestin thus the mechanism for force generation in non mammalian is believed to be from active bundle movement [94, 114]. However, the mechanism for active bundle is still under study and two famous hypotheses are: 1) stress induced activation of myosin and 2) interaction of Ca^{2+} with mechanoelectrical transduction channels.

Second, a clamped end condition in a hair cell simulates an isolated condition

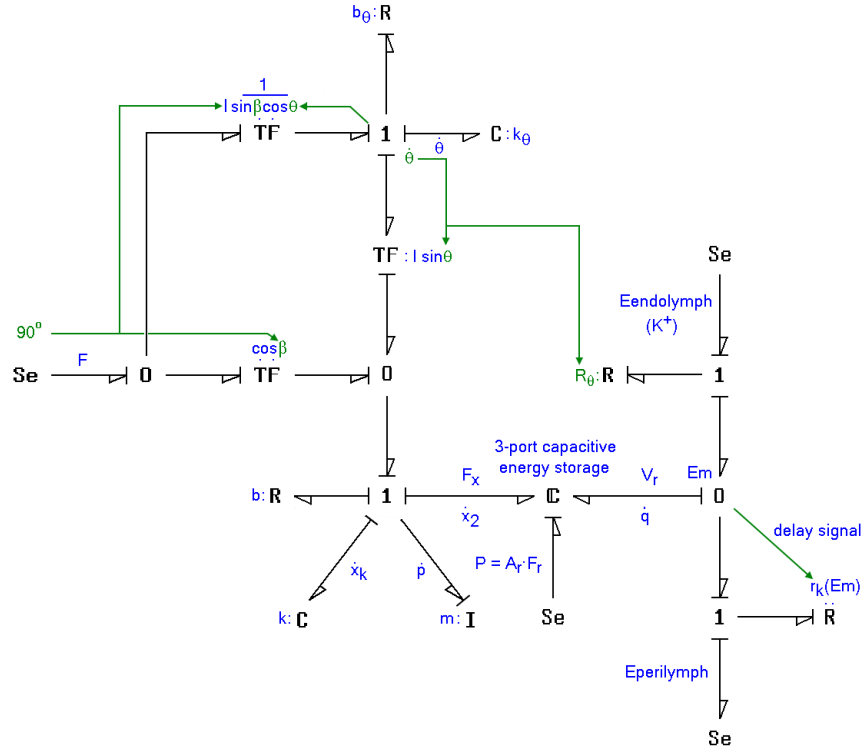


Figure 3.14: Simplified bond graph model of outer hair cell considering : 1) membrane electromotility as the only source active force generation, 2) hair cell is isolated and fixed at end, 3) input is shearing force ($\beta = 90^\circ$).

where changes in the cell's length can be experimentally observed regardless of the impedance of the attached deiters' cell and basilar membrane. An experimental condition where a bimorph is used to drive a glass fiber cantilever with known stiffness (such as in Crawford and Fettiplace [25]), as input to the hair cell can then be approximated by a shearing force applied at the cilia bundle tip. The deflection is made the same as that of the glass fiber cantilever. A simplified bond graph model of the outer hair cell from Figure 3.13 is shown in Figure 3.14. This model can be used to simulate the experiment conditions, allowing verification and tuning of parameters.

3.7.3 Equation Formulation

Causality assignment on the bond graph of Figure 3.13 indicates that there are five independent states, defining the state vector,

$$\mathbf{x} = [\theta \quad x_k \quad x_2 \quad p \quad q],$$

where θ is the cilia angular deflection, x_k is the displacement associated with the mechanical stiffness (apical end), x_2 is the hair cell apical end deflection (equal to x_k), p is the translational momentum of the hair cell equivalent mass, and q is the transmembrane charge. A first-order ordinary differential equation can be written for each of these states to form a 5th order system model, beginning with the form,

$$\begin{aligned} \dot{\theta} &= \frac{1}{b_\theta}(F \cos \theta - k_\theta \theta) \\ \dot{p} &= -\frac{b}{m}p - kx_k - F_x(x_2, q, P) \\ \dot{x}_2 &= \frac{p}{m} \\ \dot{q} &= g(\theta) \cdot (E_{endolymph} - V_r(x_2, q, P)) - \frac{(V_r(x_2, q, P) - E_{perilymph})}{r_k(V_r(x_2, q, P))} \end{aligned}$$

This set of equations requires determination of several variables in terms of the state variables and the inputs to the system. Alternatively, the bond graph model and its associated causality can be used directly to develop a simulation block diagram model in Matlab/Simulink (MathWorks Inc, Natick MA.). The block diagram model can be used to directly solve the system response to initial conditions or to specified input and forcing (e.g., $F(t)$) conditions.

3.7.4 Parameterization

Parameters required for the outer hair cell system model have been taken from various sources. For example, the orthotropic membrane properties are from Spector, et al. [3], piezoelectric coupling constants from Tolomeo and Steele [109], and the mechanical properties of the bundle from Crawford and Fettiplace [25].

Cilia bundle experiment results from Howard and Hudspeth [57] have been used to “tune” the mechanical damping parameter in the model. Physically, the outer hair cell is assumed to have an average size with cell length of $50\ \mu m$, diameter of $10\ \mu m$, bundle length of $5\ \mu m$, and total membrane capacitance is approximately 31.5 pF (Housley and Ashmore [56]). The cell is assumed to have a density of water and an approximate mass of $4 \cdot 10^{-12}$ kg. The effective mass is approximated to be a third of total mass (Rao [97]). Constants for apical potassium channel from Equation 3.7 are $a = 86.44$, $b = -0.613$, g_{max} of 3.72 nS, and g_{leak} of 1.013 nS (van Emst, et al. [85]). There are a number of articles that include tabulated collections of physiological constants, such as Brownell, et al. [120] and Synder, et al. [75], that can be used for comparison.

3.8 Simulation and model verification

A simulation block-diagram model derived from the bond graph model has been formed with Matlab/Simulink. Using this simulation model, two model verification case studies were conducted. First, time-domain simulations were used to verify that the model provides predictions of hair cell response similar to what has been observed for in vitro experiments of outer hair cells.

The response of the system in response to a shearing step input of 0.05 nN for 40 millisec is shown in Figure 3.15. The magnitude of excitation has been set to be a force that deflects the cilia bundle to an approximate horizontal distance of 62.5 nm (about θ of 0.73 degree) and the hair bundle has been assumed to initially rest at 0.01 degree (considering positive degree is a deflection toward kinocilium). The simulation predicts a resting membrane potential of -51.72 mV, which is comparable to a range between -50 mV and -60 mV as widely reported in the literature. The receptor potential response to a cilia bundle deflection is found through simulation

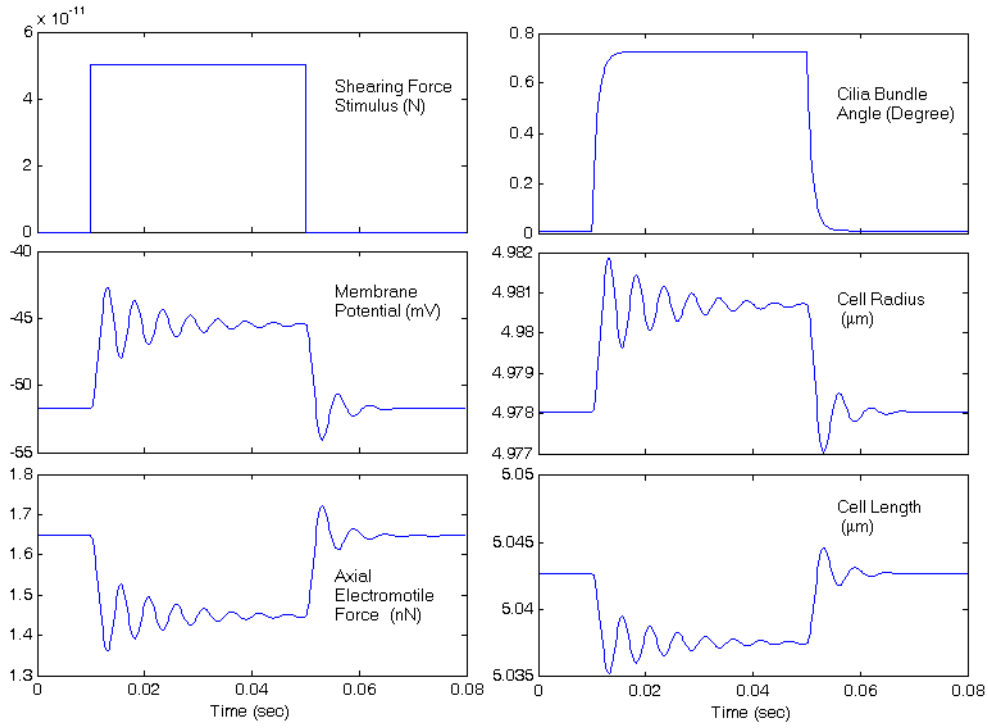


Figure 3.15: Simulation results for an outer hair cell excited by shearing force of 0.05 nN for 40 millisecc.

to have underdamped characteristics with a damped frequency of 185 Hz, similar to what has been reported in Figures 5 and 6 of Crawford and Fettiplace [25] or Hudspeth [58]. The mechanical response of the cilia bundle is similar to what normally detect in experiments (e.g., Howard and Hudspeth [57]). Finally, the simulation confirms that a piezoelectric model for the electromotility mechanism provides results similar to the observed behavior for in vivo response of hair cells; namely, elongation and radial contraction is predicted at a depolarized state and length contraction and radial expansion occur when the hair cell is hyperpolarized.

A second simulation of the system under changes in lymph fluid potential has been used to further verify the prediction of electromotility behavior. Time-domain

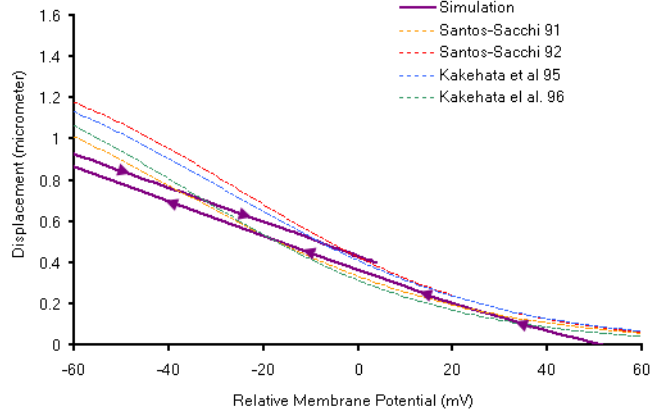


Figure 3.16: Comparison between simulation results (overlaid bold line) and Boltzmann approximations of electromotility behavior from various research groups. Data taken from Table 3 of Snyder, et al. [75] and arrows show progression through time.

transient response is plotted in Figure 3.16 in comparison with Boltzmann type approximation of electromotility with coefficients gathered from various research groups (as shown in Table 3 of Snyder, et al. [75]). Membrane potential is shown in terms relative to the membrane resting potential. Progression though time is indicated by arrows start from beginning of the simulation at +51.7217 mV relative to resting potential to the end of simulation at relative 0 mV. Plotting shows that the lumped parameter model has a response close to those reported in the literature, under conditions where the hair cells operate in a range close to their resting potential. In particular, Figure 3.16 shows that the value of the piezoelectric coupling constant (coefficient of active force) in combination with modulus of elasticity used in the hair cell model provides a linear approximation of the displacement-potential function, with a slope of $0.08226 \mu m/mV$. When plotted against data from the literature, this appears to be a close approximation.

3.9 Parameters sensitivity analysis

A study of the effect of parameters critical to the model simulation results or parameter sensitivity analysis is discussed in this section. Benefits of the analysis are obvious. First, information gathered can be used for selecting the right parameter in order to “tune” the simulation with experimental data. Second, the analysis can be used as a guide for which parameters are more sensitive to the simulation result and need to be given attention.

For the hair cell model developed, the output selected is the receptor potential because it is responsible for both nerve firing and electromotile force generated. A series of simulations from changing parameters of interest equally in percentage will be compared.

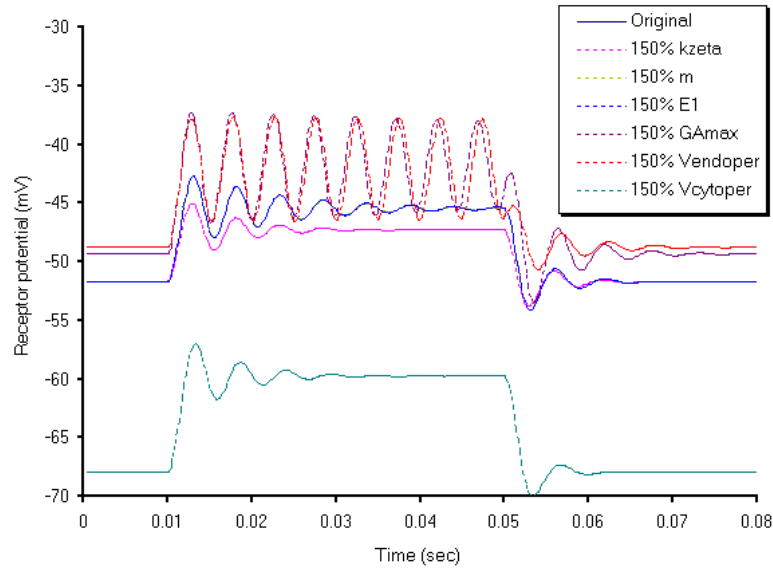


Figure 3.17: Time domain simulation of the outer hair cell model after 150 percent changes of each parameters

Figure 3.17 shows results from this parameter sensitivity study. Parameters

chosen for sensitivity analysis as shown in the legend are stiffness of cilia bundle (kzeta-pink line), mass of cell body (m-light green), modulus of elasticity of cell membrane (E1-blue), conductance of the apical potassium channel (GAmx-maroon), endolymph potential (Vendoper-red), and perilymph potential (Vcytoper-green).

The model shows characteristic changes with changes in each parameter as expected. In particular, increasing stiffness of the cilia bundle effectively changes the system damping ratio resulting in changes in response magnitude and better settling time, which probably results from decreased damping ratio. An increase in both membrane stiffness and mass do not markedly effect electrical response but do change mechanical response (not shown). Changing channel conductance and endolymph potential similarly result in shifting of the response and resting potential in a more positive (depolarization) direction except that increasing channel conductance results in decreased damped frequency of the response. Increasing perilymph potential affects the system in an opposite direction. That is, the increase in perilymph potential shifts the response and resting potential toward the hyperpolarization direction.

3.10 Frequency response characteristics

A behavior of particular interest in hair cell dynamics is the frequency response, which can provide insight into the frequency selectivity enabled by the electromotility mechanism. A transfer function between transduction current and receptor potential for a passive RC (resistor-capacitor) circuit model, for example, has been shown to have a low-pass characteristic which leads to questions concerning the underlying mechanism of electromotility in the high frequency hearing range (ie. between 10 kHz to 40 kHz).

Dallos and Evans [31] and Spector, et al. [5] hypothesize that the outer hair

cell should be able to create and inject force back to each section of the cochlea on a cycle by cycle basis. This leads to consideration of an evaluation of the hair cell as an actuator. The transfer function that is used to quantify this aspect is between shearing force input at the tip of hair bundle and membrane potential, in decibel (dB) unit of volt per newton.

Dallos and Evans [31] also proposed a model based on extracellular or endocochlear potential gradient as a driving potential at high frequency. However, in our nonlinear model, the electromotile force generated at high frequency is lower when using endocochlear potential as driving gradient, thus the results shown in this dissertation are using conventional endolymph-perilymph gradient as driving potential.

As stated, the model developed in this study shows that the outer hair cell is an inherently nonlinear system. For such a system, a frequency response analysis can be conducted using a describing function method. A describing function is an amplitude and frequency dependent quasi-linear system, with the output being an approximation of the true nonlinear output [46]. A practical method for constructing a describing function is presented by Schwartz and Gran [102]. Consider a system with a sinusoidal input having amplitude A and frequency ω . A describing function, $N(A, \omega)$, is found by,

$$N(A, \omega) = \frac{1}{T \cdot A} \cdot \int_0^T f[A \sin(\omega t)] \{ \cos(\omega t) - j \sin(\omega t) \} dt, \quad (3.49)$$

where $T = 2\pi/\omega$ is an input period, and $f(x)$ represents a nonlinear function. In this case, the nonlinear system of interest is the hair cell simulation model.

The describing functions derived from the model of the outer hair cell have been divided into three frequency ranges similar to Spector, et al. [5] for comparison. The describing function for a low frequency range between approximately 15 to 1000 Hz is shown in Figure 3.18, for a mid-frequency range of 1-4 kHz in Figure 3.19,

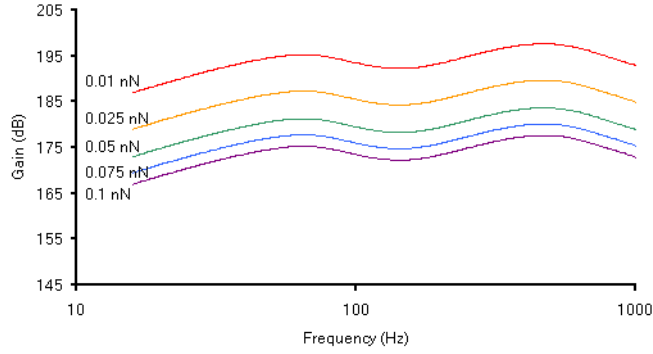


Figure 3.18: Gain of describing function in low frequency (15-1000 Hz)

and for a high-frequency range of 10-40 kHz in Figure 3.20. The forcing input was sinusoidal and varied between 0.1 nN, which is an approximated amplitude that deflects cilia bundle to its saturation, and 0.01 nN which is approximately an order of magnitude less. Approximately 10000 simulations were performed for describing function in low frequency in order to capture all resonant frequencies; however, mid and high frequency describing functions are results of approximately 600 simulations since only trends are needed.

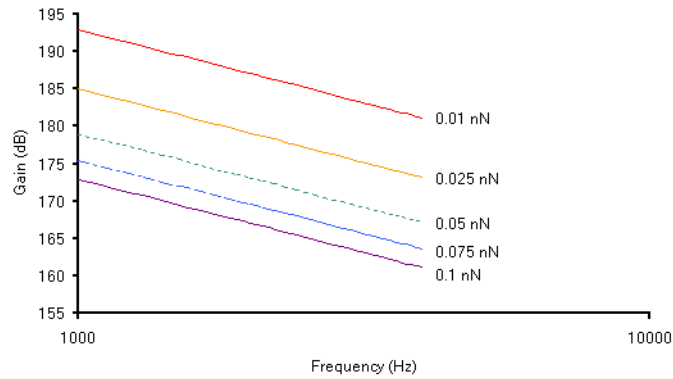


Figure 3.19: Gain of describing function in mid frequency (1-4 kHz)

Describing function gain over the range of frequencies examined shows a

strong dependence on both input amplitude and frequency. At low frequency range, the describing function shows resonant frequencies that should result from membrane stiffness and cell body's inertia. At higher frequency, the describing function shows that the model does have a low pass characteristic with a slope of -20 dB per decade (first order lowpass). Since a second order response has a slope of -40 dB in high frequency and there is only one inertia in the system, this describing function can be approximated by a combination of second order and an inverse of first order low pass with cut off frequency close to resonant frequency of second order.

For this model, using endocochlear potential as a driving potential increases the slope of the DF at high frequency, thus conventional lymph potential is used. Two peak frequencies in low range as shown in Figure 3.18 are at approximately 60 and 470 Hz and markedly increase at lower input amplitude. The behavior over the frequencies observed leads to a hypothesis that the outer hair cell may act as a 'mechanical regulator' of vibration in a given section of the organ of corti, as will be explained in the following section.

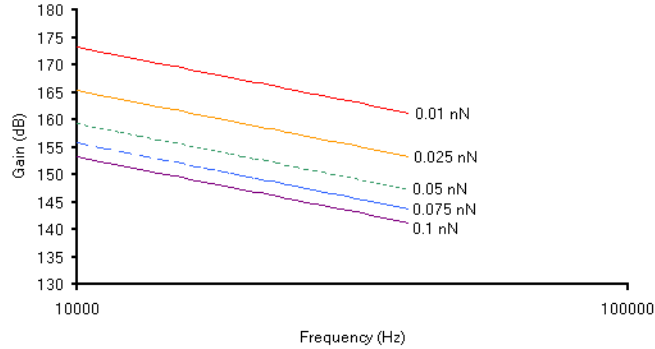


Figure 3.20: Gain of describing function in high frequency (10-40 kHz)

3.11 Discussion

The bond graph model for an outer hair cell provides a system level perspective, complementing most of the model studies found in the literature that primarily focus on the constitutive behavior of hair cell elements. These studies include recent electromotility models by Deo and Grosh [35, 36] and Iwasa [60] or transduction channels model by Weiss and Leong [124]. While constitutive models focus on understanding the specific behavior of hair cells, a systems approach focuses on the interaction between the various subsystems and how they enable hair cells to function successfully as sensors and actuators. Some specific benefits can be gained by integrating the system model with models of the cochlea, or studying the transducer characteristics unique to hair cells.

A unique characteristic of the bond graph model developed in this dissertation is its ability to represent interaction between subsystems. In the bond graph model, these interactions are represented by signal bonds, modulation structures, and multiport energy storage elements. These model elements are not available in other reported attempts to build system level models using analog circuit elements such as by Neely [89], Cohen and Furst [24], Mountain and Hubbard [86], Dallos and Evans [31], Spector, et al. [5], Rattey, et al. [39], and van Emst, et al. [85]. The bond graph formulation not only allows an explicit connection of how mechanical strain in the cilia bundle controls mechanical gated transduction channels, how the receptor potential modulates the voltage gated channels, or how the energy is exchanged between mechanical and electrical domain, but also has an ability to combine constitutive relations from other models in order to create a realistic dynamic simulation of the hair cells.

Time domain characteristics, such as those shown in Figure 3.16, clearly illustrate that a linear impedance matrix model can be used to approximate the

electromotility mechanism quite well in a narrow region close to their resting potential. Considering that hair cells mostly operate in the region where transmembrane potential is close to the resting value, the results can be considered satisfactory. However, the overall bond graph model can be easily modified to capture nonlinear “saturation” characteristics simply by changing the constitutive relations – the model structure (interconnection between subsystems) remains the same.

Frequency domain characteristics of outer hair cells have been derived using a describing function analysis, revealing a sort of regulating mechanism. This behavior indicates that when an incoming forcing amplitude at a specific frequency becomes weaker, the mechanism produces a higher gain that generates higher membrane potential (ratio) which in turn generates a higher magnitude of vibration and achieves self-regulation. On the other hand, when the system is under a higher amplitude of forcing input, an amplification in the mechanism disappears since this is less preferred. This trend seems to continue throughout all ranges of input frequencies.

3.12 Summary

The development of a system level bond graph model of an outer hair cell has been described in this chapter. This model was used to develop a computer-based model for predicting outer hair cell dynamics in both time and frequency domain. It should be made clear that the model study described in this chapter relies on parameters that have been borrowed from various experimental studies reported in the literature on different biological species. The intent was to make sure parameter values were within the correct order of magnitude so that trends in the system response could be observed.

Time-domain performance measures are found to exhibit favorable trends

that are comparable to those reported by other research groups. The describing function analysis shows that the active nature of the outer hair cell, a phenomenon attributed to electromotility, may serve to regulate vibration of the organ of corti. This property is directly related to a cochlear frequency selectivity. More study is required to show how this model can be integrated within a (distributed-parameter) model of the cochlea, and this remains as future work. The insight gained from this type of modeling study not only can contribute to an understanding of the role hair cells play in hearing but also can be assumed to provide a parameterizable and controllable system that can be used for sensory function.

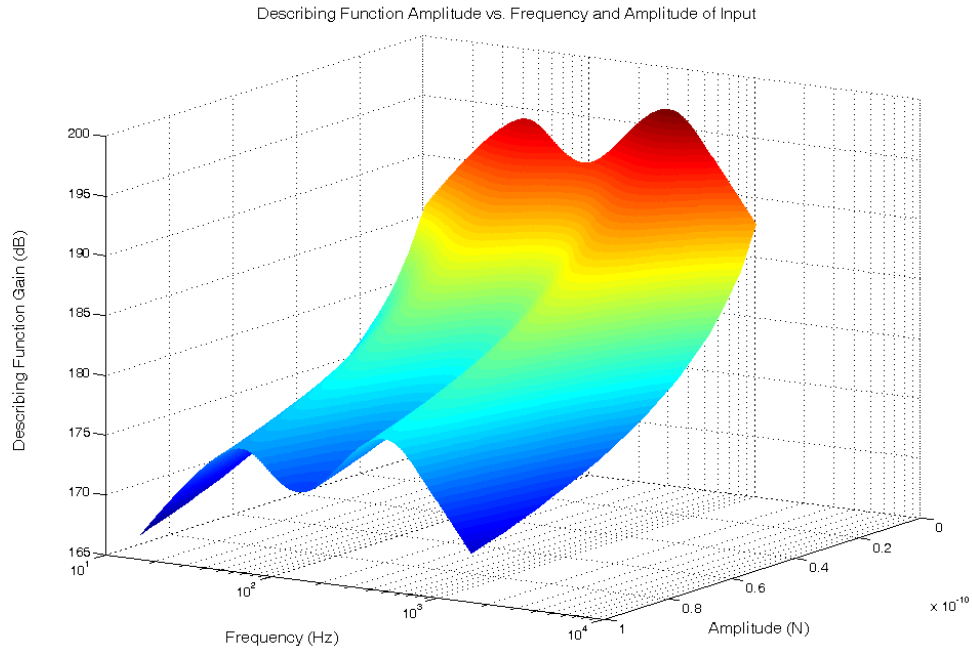


Figure 3.21: Surface plot of the gain of describing function in low frequency

This model is built according to the present general understanding of how hair cells function. It can serve as a base structure for modification in the case that

new behaviors are discovered or can be simplified and parameterized for a study of specific behaviors or species which should be beneficial for the field of neurobiology. However, the goal of the remaining chapters in this dissertation is to describe how the model formulated in this chapter was used to realize an engineered sensor with a model structure inspired by the hair cell.

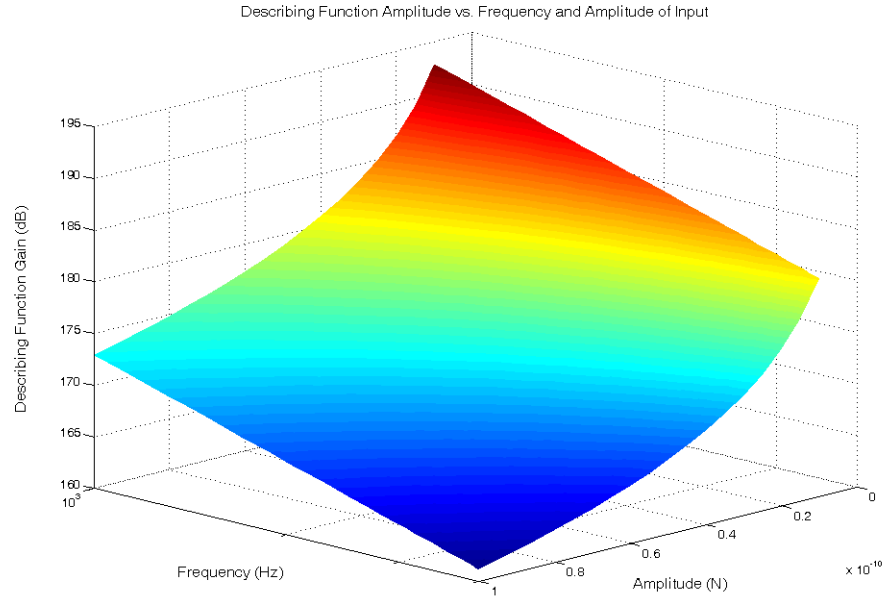


Figure 3.22: Surface plot of the gain of describing function in mid frequency

Gain of describing functions from Figure 3.18, 3.19, and 3.20 are partial results obtained from the describing function gain surface plots shown in Figure 3.21, 3.22, and 3.23. To visualize the total system behavior, an overall describing function surface plot generated from approximately 15000 simulations is finally shown in Figure 3.24.

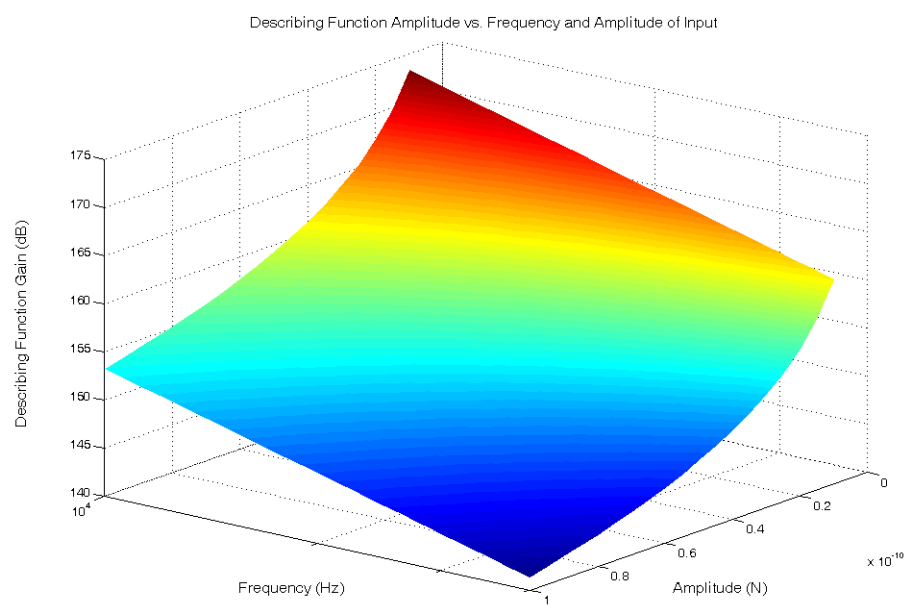


Figure 3.23: Surface plot of the gain of describing function in high frequency

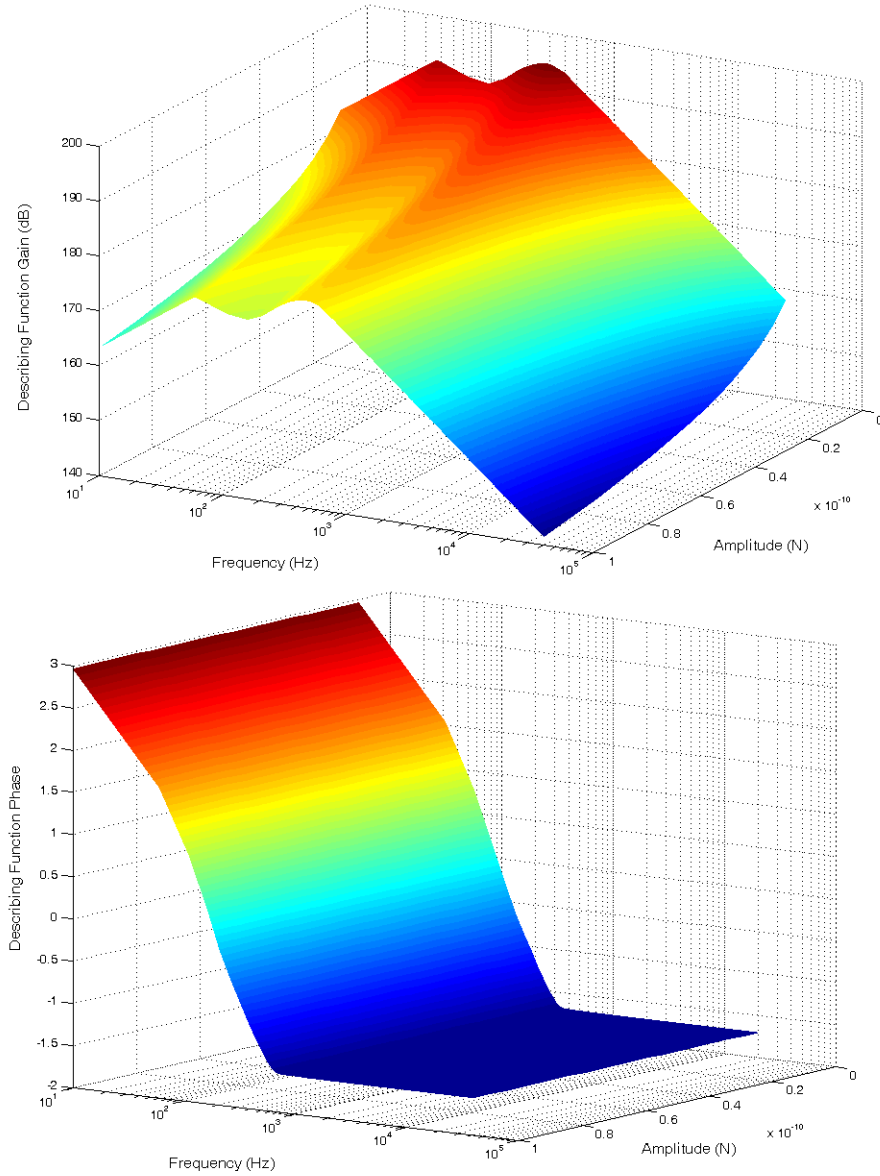


Figure 3.24: Surface plot of the describing function of outer hair cell model showing overall trend (magnitude on the top and phase angle on the bottom)

Chapter 4

Biomimetic Sensor: A Design Discussion

The energetic structure of the hair cell has been examined by the bond graph model in the last chapter. In this chapter, the discussion will focus on using the insight gained to guide design of a sensor. The goal is to transform the hair cell structure and organ of corti, in some part, to another kind of structure while maintaining key composition. The benefit of this transformation is rather obvious. The analogous ‘synthetic’ sensor structure should be easier to manage, measure, construct, and control. This will also allow further study into the mechanism performance and behavior without dealing with organic systems.

4.1 Sensor classification

Before proceeding, the fundamental question “what is it that is going to be measured ?” should be addressed. To do just that, it is important to review measurands of common sensors. White [126] classifies the majority of sensors as,

- Acoustic related such as wave amplitude, phase, and polarization
- Biological related such as biological identity, concentration, and their states
- Chemical related such as chemical identity, concentration, and their states
- Electric related such as charge, current potential, and field
- Magnetic related such as field, flux and permeability
- Mechanical related such as position, velocity, acceleration, force, stress, pressure, strain, stiffness and so on
- Optical related such as wave amplitude, phase, spectrum and velocity

- Radiation related such as energy, intensity, and type
- Thermal related such as temperature, flux, specific heat, and conductivity

From this categorization, it can be clearly seen that the hair cell structure belongs to the mechanical type, and can be related to such physical variable as acceleration, pressure, and force. Designing for one of these specific measurands, although not easy in some cases, allow you to infer others (e.g., force measurand can infer acceleration).

Baxter [12] has categorized sensors that are being used for physical related parameter measurements, based on conversion phenomena, shown here in order of market consumption for 1999, as 1) photoelectric, 2) inductive, 3) magnetic-actuated, 4) capacitive, 5) ultrasonic, and 6) magnetic. While theory shown simple types of displacement-sensitive measurement to be either resistive, inductive, capacitive, and piezoelectric; a comparison between market adoption and simplicity leave two choices: capacitive sensor and piezoelectric sensor.

Examination of a hair cell's bond graph's structure shows that the system dynamics are modeled by a multiport -C- element, which represents the piezoelectricity behavior of the plasma membrane, as well as energy conversion between the mechanical and electrical energy domains. Thus, a capacitive type of sensor would seem to be a consistent choice. However, to design a capacitive sensor that can generate enough force to modulate its own mechanical properties is not an easy task. Capacitive sensors have been widely used in sensors because they have desirable linear characteristics. This type of sensor is rarely used in actuation applications. Further analysis of the system structure reveals that the piezoelectric material can also be modeled by a multiport capacitive (-C-) element [20], and since the piezoelectric sensor has been widely used for both sensing and actuation applications, it presents another appropriate candidate.

4.2 Desired performance and characteristic

Additional factors that govern the design process for any sensor are the desired performance and characteristic. The sensor structure developed here should enable the sensor to show similar performance as that found for in vivo inner and outer hair cells and their interaction with the basilar membrane, organ of corti, and cochlear configuration. The performance features include the following:

First, the final structure of the system should be able to perform as a band-pass filter. This characteristic is what makes the cochlea successful in decomposition of an input signal into components, each corresponding to a band of frequencies. The method of processing the input has been shown to allow instantaneous frequency decomposition of the signal as stated in previous chapters.

Second, the structure should be adaptable. In this case it means that the system should be able to change properties such as the stiffness by active force such that it can modulate its characteristics in response to a signal from controller.

Third, the system should be composed of two basic elements. A sensing element analogous to inner hair cells and an actuating (effecting) element analogous to the outer hair cells, both of which form a sensoriactuator pair. Sensing element is going to be used as a reference in adaptation decision.

Fourth, the structure should be controllable, at least the actuator element should be controllable so that controller can change system behavior as needed.

Fifth, the structure should be observable. By monitoring the system through a sensing element, the state of the system operation should be able to be determined via monitored variables. Since the system is adaptive and characteristics of the system are changing over time, an observable system will help controller in a decision making process.

Sixth, the structure should have some sort of gain control. For example, when the magnitude of the input is larger than the normal sensing range, the system should be adaptable in a way that it can become desensitized to the input, thus expanding the range of the input that the system can measure. On the other hand, if the input becomes smaller, the system should adapt so that it can get a stronger signal output that can be differentiated from noise.

Seventh, the structure should be able to be arranged as a distributed sensing device, just like hair cells, the basilar membrane, and the tectorial membrane form distributed sensing elements along the organ of corti in the cochlea. This sensor, when functioning as a band pass filter, should be able to be arranged so that each arrayed sensor is sensitive to a different band of frequency (as discussed in the first characteristic) thus forming a sensing mechanism that has a method for signal processing analogous to that of cochlear function. This arrangement of the sensing elements has another advantage. By changing the number of elements in the distributed structure, the structure can be changed according to the application. Adding sensing elements can increase the bandwidth of the sensor structure. On the other hand, reducing number of sensing elements decreases structure bandwidth, but makes the system more modular and suitable for a specific application.

Examining the bond graph model structure of the outer hair cell, it is believed that the characteristics presented below may be responsible for the desired features,

- Local positive feedback loop: The hair cell dynamic behavior is highly dependent on a positive feedback, which controls how the hair cell modulates its structural stiffness in phase with input stimuli. This results in reduction of damping for each organ of corti section and allows for a sharper band-pass filter.

- Presence of cilia as a transformer: The transformer element in the model represents how the cilia endow the hair cell with good sensitivity. Not only can the presence of cilia provide a mechanical advantage, but it also allows their mechanism to accept stimuli in a less constrained manner.
- Capability to work both as sensor and actuator: It can be seen from the bond graph that a change in the lymph's fluid potential would also result in a generation of force. The hair cell plasma membrane works like a symmetric 2-port capacitive (-C-) element. This means that not only can deflection of the cilia bundle result in changing the membrane potential, but also modulating the membrane potential will result in generation of force which effectively changes cilia bundle stiffness and causes it to deflect.

4.3 Basic sensor structures

Based on insight gained from bond graph modeling in the last section, two different basic sensor formations will be further described. Sensor designs based on a capacitive sensing for a microscale sensor and piezoelectric sensing for a macroscale sensor are discussed in the following.

4.3.1 Microscale multiplates capacitive sensor

The first basic structure is based purely on a capacitive sensing element. A structure based on the concept of parallel plate capacitors is proposed. This basic sensing element is made of three parallel conductive plates forming a set of coupling capacitors similar to servo sensors discussed in the first chapter. However, in this case, the middle plate is a sensing plate, with a potential depending on its degree of rotation (or its position between two charged conductive plates). The structure appears as 2-port in a way that differences in electrostatic force between

two sides of the middle plate modulate the rotational stiffness of the beam. This also allows generation of force in both directions, since a normal capacitive force can only generate force by pulling two plates together in one direction. Advantages of this design are that it can have a very linear and predictable behavior, it has good environment stability, and does not require precision components. However, such a structure has drawbacks that have been discussed, such as it has to be fabricated so that noise due to stray and fringe effects can be canceled, and it can not create large forces at macro-scale without large voltage. Development of this type of sensor is more suitable for micro scale (MEMS) sensors which will be discussed below.

4.3.1.1 Simple multiplates capacitor structure

The simple multiplate capacitor sensor structure has been widely used in modern capacitive sensor designs. An example might be the Analog Devices AD XL-05/50 series 1-axis force-balanced accelerometer used in deployment of automobile air bag system. This type of structure has proven to have a wide dynamic range while having a linear characteristic due to feedback servo and null-balancing circuit. A configuration with three plates considered to have a similar structure to the hair cell's membrane is chosen as shown in Figure 4.1 a). While this similarity will become more evident after subsequent discussion, to begin, constitutive relations for this capacitive sensor will be shown underneath.

Three plate capacitors as shown are assumed to have the same area, A , and to be in an environment that has a dielectric constant of ε_a on the top section and ε_b on the bottom section with media conductivity of σ_a on the top and σ_b on the bottom. For this case, the top and bottom plates are stationary while the middle plate is a sensing plate. Mode of operation can be either area variation (transverse motion), displacement variation (vertical motion), or a combination of both. An

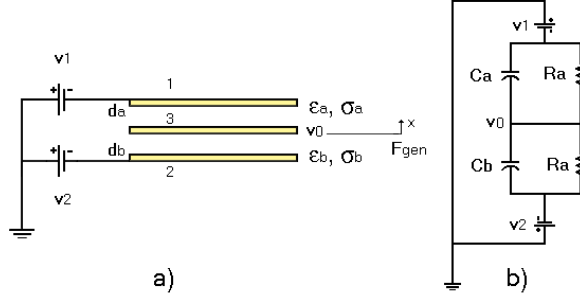


Figure 4.1: Three plates capacitor a) its geometry, b) its equivalent circuit.

equivalent circuit of this three plates device is shown in Figure 4.1 b), and the corresponding capacitance and resistance are,

$$\begin{aligned} C_a &= \frac{\varepsilon_a A}{d_a}, & R_a &= \frac{d_a}{\sigma_a A}, \\ C_b &= \frac{\varepsilon_b A}{d_b}, & R_b &= \frac{d_b}{\sigma_b A}, \end{aligned} \quad (4.1)$$

where R_a and R_b make this a leaky capacitance.

The output of this system can be either current through connecting a wire with known resistance at middle plate, or potential of middle plate using a buffer amplifier. Choice of output measurement depends on mode of operation to a degree. In this case, considering that the system operates by displacement variation, a voltage measurement will give a system transfer function that can be approximated by simple impedance analysis (using Kirchoff law at middle plate) as,

$$\frac{(V_1 - V_0) \cdot (C_a s R_a + 1)}{R_a} = \frac{(V_0 - V_2) \cdot (C_b s R_b + 1)}{R_b}, \quad (4.2)$$

where, V_0 is potential of the middle plate, and $s = j\omega$. With rearrangement, a transfer function for the system is,

$$V_0 = \frac{(C_a s V_1 + \frac{V_1}{R_a} + C_b s V_2 + \frac{V_2}{R_b})}{(C_a s + \frac{1}{R_a} + C_b s + \frac{1}{R_b})}. \quad (4.3)$$

Most of the time, the impedance of the media between the capacitor gap is very high compared with capacitance value is preferred since it creates a linear

transfer function. Thus an approximation to Equation 4.3 on the condition that media between the gap has a very low conductivity is,

$$V_0 = \frac{C_a V_1 + C_b V_2}{C_a + C_b}. \quad (4.4)$$

If the distance of the middle plate changes by x , a transfer function between middle plate voltage and change in distance, x , and when the top and bottom sections have the same dielectric constant,

$$V_0 = \frac{\frac{\varepsilon A}{d_0 - x} V_1 - \frac{\varepsilon A}{d_0 + x} V_2}{\frac{\varepsilon A}{d_0 - x} + \frac{\varepsilon A}{d_0 + x}}. \quad (4.5)$$

However, what makes the three plate capacitor structure special is its ability to generate a controllable force. This generated force is the result of two electrostatic forces. The first one (directing upward according to Figure 4.1) is due to the difference potential between plate number 1 (top plate) and plate number 3 (sensing plate), and the second one (directing downward according to Figure 4.1) is due to potential difference between plate number 2 (bottom most plate) and 3 (sensing plate). That is,

$$\begin{aligned} F_{gen} &= F_{top} - F_{bottom} = \frac{1}{2} \frac{C_a}{(d_a - x)} (V_1 - V_0)^2 - \frac{1}{2} \frac{C_b}{(d_b + x)} (V_0 - V_2)^2 \\ &= \frac{1}{2} \frac{\varepsilon_a A}{(d_a - x)^2} (V_1 - V_0)^2 - \frac{1}{2} \frac{\varepsilon_b A}{(d_b + x)^2} (V_0 - V_2)^2. \end{aligned} \quad (4.6)$$

For the case when the sensing plate stays in the middle, ($x = 0$ and $d_a = d_b = d$), and media between the two sides is the same, $\varepsilon_a = \varepsilon_b = \varepsilon$, and input potential at plate 1 and 2 are equal of magnitude but opposite direction, $V_1 = -V_2 = V_i$,

$$F_{gen} = \frac{2\varepsilon A}{d^2} V_i V_0. \quad (4.7)$$

From Equation 4.5 and 4.6, it can be seen that three plate capacitor can function like a 3-port, similar to membrane electromotility of the outer hair cell. A constitutive relation can be found by realizing the potential energy stored between

the plates in terms of q_a , charges stored between plate 1 and 3, q_b , charges stored between plate 2 and 3, and x , position of the middle plate as independent parameters; that is,

$$U_{q,x} = \frac{(d-x)q_a^2}{2\varepsilon A} + \frac{(d+x)q_b^2}{2\varepsilon A}, \quad (4.8)$$

where it is assumed that the middle plate initially stays in the middle, thus $d_a = d_b = d$. Note that potential energy stored in the capacitor has been defined as $U_q = \frac{q^2}{2C} = \frac{1}{2}CV^2$, where C is capacitance, and V is potential difference, as discussed in the last chapter.

Now, the constitutive relations of the three plate capacitor can be found by finding a derivative of energy stored respect to each independent variable,

$$F_{gen} = \frac{\partial U_{q,x}}{\partial x} = -\frac{q_a^2}{2\varepsilon A} + \frac{q_b^2}{2\varepsilon A}, \quad (4.9)$$

$$V_1 - V_0 = \frac{\partial U_{q,x}}{\partial q_a} = (d-x)\frac{q_a}{\varepsilon A}, \quad (4.10)$$

and,

$$V_0 - V_2 = \frac{\partial U_{q,x}}{\partial q_b} = (d+x)\frac{q_b}{\varepsilon A}. \quad (4.11)$$

These equations can be verified by substituting equation 4.10 and 4.11 into equation 4.9, giving the same result as equation 4.6. Simultaneously solving equation 4.10 and equation 4.11, in the case that there is equal charge on both sides gives the same result as equation 4.5.

Constitutive relations in equations 4.9, 4.10, and 4.11 can be represented by a multiport -C- element in bond graph. The equation also shows interdependence between mechanical and electrical energy domain. Therefore, the simple three plate capacitor can be considered an analogous system to the hair cells plasma membrane electromotility mechanics.

4.3.1.2 Rotating sensing capacitor plates micro force sensor

Based on the simple multiplate capacitor concept that has just been discussed, a sensor analogous to the outer hair cell model has been designed. By examining the special characteristic of a hair cell as well as its performance requirement, as discussed above, a rotating sensing plate capacitive sensor is proposed. Figure 4.2 shows a diagram of the plate geometry. This design is intended to be used as an active microscale force sensor or a micro flow sensor.

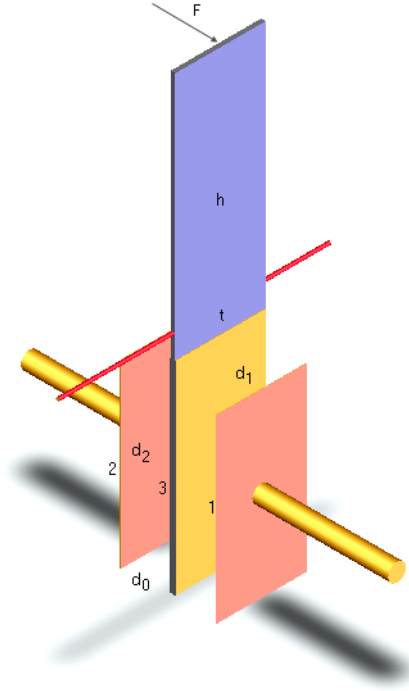


Figure 4.2: shows the proposed rotating sensing plate, 3-plate capacitive sensor

There are reasons behind the way the sensors previously described have been designed. As shown, the middle plate is now a lever rotating around a (red) rod with a bottom (yellow) section having a conductive surface on both side. The middle lever, which will be used to sense force or pressure, is positioned between two fixed

parallel conductive plates, thus forming a three plate capacitive sensor similar to the simpler one that has just been discussed.

The reason why the middle plate is set to rotate is to provide a robust coupling in the same way as the cilia bundle of hair cells. Capacitive plates are set on the opposite side of the fulcrum, because a lever advantage is needed so the electrostatic force can create as much torque as possible. The fulcrum of the beam will be set at its longitudinal centroidal distance to balance the effect of its weight in rotation. The sensor package must also be magnetically shielded from stray and fringe effects.

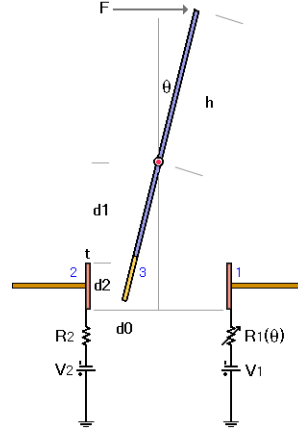


Figure 4.3: Relevant dimensions of a rotating sensing multiplate capacitive sensor.

Figure 4.3 show basic dimensional notation for the sensor under study. The angle of the middle plate from the vertical line is θ , distance from apex of the beam to the fulcrum is h , distance from fulcrum to middle conductive surface is d_1 , length of conductive surfaces (all three plates have an equal length) are d_2 , the distance between the middle conductive surface to left (1) and right (2) conductive surface is equally set at d_0 , potential source at right conductive surface is V_1 , potential source at left conductive surface is V_2 , and resistors corresponding to left and right

conductive plates are R_1 and R_2 , respectively. To keep the structure analogous to apical channel conductance of outer hair cells, the resistor of the right conductive plate is a modulated resistor which depends on the angle of the middle plate. This creates a loop similar to that of the hair cells' apical channel, which depends on the angle of the cilia bundle rotation. A physical realization of R_1 might be a material that has piezoresistive properties because of its change in resistance due to strain.

A constitutive relation can be found, similar to the non-rotating middle plate case, by calculating a potential energy stored in terms of independent variables. For this case, the independent variables are θ , q_a , and q_b . Where q_a and q_b are charge stored on the right side (between plate 1 and 3) and left side (between plate 2 and 3) of the middle plate respectively. Considering θ is positive when the middle plate rotates clockwise,

$$U_{\theta, q_a, q_b} = \frac{[d_0 - (d_1 + d_2/2)\sin(\theta)]}{[2\epsilon t(d_2 - (d_1 - d_1\cos(\theta)))]} q_b^2 + \frac{[d_0 + (d_1 + d_2/2)\sin(\theta)]}{[2\epsilon t(d_2 - (d_1 - d_1\cos(\theta)))]} q_a^2. \quad (4.12)$$

Similar to the simpler case, constitutive relations are a result of differentiation with independent state variables; that is,

$$T = \frac{\partial U_{\theta, q_a, q_b}}{\partial \theta} = \frac{(d_1 + d_2/2) \cdot \cos(\theta)}{2\epsilon t(d_2 - d_1 + d_1\cos(\theta))} (q_a^2 - q_b^2) + \frac{[d_0 - (d_1 + d_2/2)\sin(\theta)]}{[2\epsilon t(d_2 - (d_1 - d_1\cos(\theta)))]} \cdot d_1 \sin(\theta) \cdot q_b^2 + \frac{[d_0 + (d_1 + d_2/2)\sin(\theta)]}{[2\epsilon t(d_2 - (d_1 - d_1\cos(\theta)))]} \cdot d_1 \sin(\theta) \cdot q_a^2, \quad (4.13)$$

$$V_1 - V_0 = \frac{\partial U_{\theta, q_a, q_b}}{\partial q_a} = \frac{[d_0 + (d_1 + d_2/2)\sin(\theta)]}{[\epsilon t(d_2 - (d_1 - d_1\cos(\theta)))]} q_a, \quad (4.14)$$

and,

$$V_1 - V_0 = \frac{\partial U_{\theta, q_a, q_b}}{\partial q_b} = \frac{[d_0 - (d_1 + d_2/2)\sin(\theta)]}{[\epsilon t(d_2 - (d_1 - d_1\cos(\theta)))]} q_b. \quad (4.15)$$

where T is torque generated by electrostatic force. For the case that the sensor is very small, the distance between the three plates will be very short, thus the middle plate rotation angle can be considered very small, and the constitutive relation can

consider $\sin(\theta) \sim \theta$ and $\cos(\theta) \sim 1$, thus,

$$T = \frac{(d_1 + d_2/2)}{2\epsilon t d_2} (q_a^2 - q_b^2), \quad (4.16)$$

$$V_1 - V_0 = \frac{[d_0 + (d_1 + d_2/2)]\theta}{\epsilon t d_2} \cdot q_a, \quad (4.17)$$

and,

$$V_0 - V_2 = \frac{[d_0 - (d_1 + d_2/2)]\theta}{\epsilon t d_2} \cdot q_b. \quad (4.18)$$

It can be seen that these equations with small angle approximation are much simpler, and thus will be used for further design and simulations.

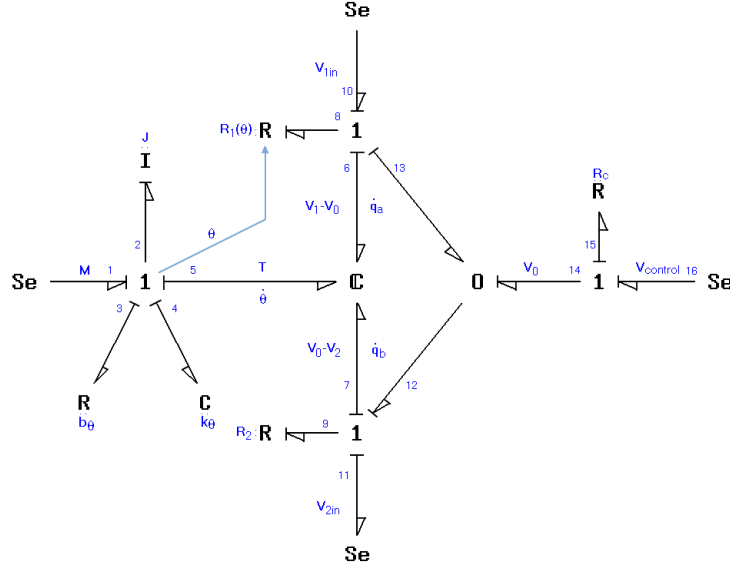


Figure 4.4: Bond graph model representation of the rotating sensing plate multiplate capacitive sensor.

A bond graph model of the rotational three plate capacitor is shown in Figure 4.4. This bond graph structure clearly shows a similarity with that of the hair cell bond graph. The three port capacitive (C) element in the middle represents the rotational three plate capacitor. On the left side of the three port (C) is the model

for mechanical rotation of the lever, an inertia element (I) to represent the lever inertia, a resistive element (R) corresponding to friction at the fulcrum and shaft, and another capacitive element (C) to represent a rotational spring designed to hold the lever at the fulcrum point and bring the whole mechanism back to its resting equilibrium.

The thin full-arrow line indicates a signal bond that shows how the lever angle modulates the piezoresistive element, $R_1(\theta)$. The right most effort, Se , is a potential source denote $V_{control}$ that represents a source designed to control generated electrostatic moment. This control source is connected in series with a resistor, R_c , used to limit the current through the middle plate.

The bond graph of Figure 4.4 has fully assigned causality that indicates the system has five independent energy storage elements, and thus five energetic states. The state vector for the bond graph is,

$$\mathbf{x} = [h_2 \quad \theta_4 \quad \theta_5 \quad q_{a6} \quad q_{b7}],$$

where h is angular momentum of the middle plate, θ_4 is the displacement of the rotational spring, θ_5 is angle of the middle plate, q_{a6} is charge storage between the right plate and the middle plate, and q_{b7} is charge storage between the left plate and the middle plate. The numerical subscript denotes the number of the bond. Causality assignment on this bond graph also indicates dependence between resistive elements R_1 , R_2 , and R_c , meaning an algebraic loop is present and needs to be solved to determine the states at any time. The equations of motion can be

summarized in state space format as,

$$\begin{aligned}
\dot{h}_2 &= M - \frac{b_g}{f} h_2 - k_\theta \theta_4 - \frac{d_1+d_2/2}{2\epsilon t d_2} (q_{a6}^2 - q_{b4}^2) \\
\dot{\theta}_4 &= \frac{h_2}{f} = \dot{\theta}_5 \\
\dot{q}_{a6} &= \frac{(R_2+R_c)}{((R_1(\theta_5)+R_c)(R_2+R_c)-R_c^2)} (V_{1in} - \frac{(d_0+(d_1+d_2/2)\theta_5)}{(\epsilon t d_2)} q_{a6} + (\frac{R_c}{R_2+R_2} - 1) V_{con} \\
&\quad - \frac{R_c}{R_2+R_c} V_{2in}) \\
\dot{q}_{b7} &= \frac{(R_c+R_1(\theta_5))}{((R_1(\theta_5)+R_c)(R_2+R_c)-R_c^2)} (V_{con} + \frac{R_c}{R_1(\theta_5)+R_c} (V_{1in} - \frac{(d_0+(d_1+d_2/2)\theta_5)}{(\epsilon t d_2)} q_{a6} \\
&\quad - V_{con}) - \frac{(d_0-(d_1+d_2/2)\theta_5)}{(\epsilon t d_2)} q_{b7} - V_{2in})
\end{aligned} \tag{4.19}$$

4.3.1.3 Parameterization

It is necessary to decide on each of the dimensions for the rotational three plate capacitive sensor. This process can include any choices and decisions. However, in this case, some parameters play a more critical role for a sensor's performance. For the sensing mode, potential on the left and the right conductive plates determine resolution of the signal, thus it should be large enough so that significant motion of the middle plate can generate a signal distinguishable from noise. Stiffness of the rotating spring at the fulcrum can be chosen according to the range of forces to be measured. After all dimensions of the sensor have been decided, the range in radians that the middle plate can move according to geometry of the mechanism can be determined.

For actuator mode, the force or moment that the sensor can generate should be determined. Assuming that the middle plate stays in the middle is a condition that demands the highest moment because it is a condition for which the moment arm of the lever is longest. Equation 4.16 in term of voltage is then used to determine moment that can be generated which is then compared with required specification. If the force that can be generated is too small there are two things that can be done. Either increasing the plate width to increase the capacitance area, or increasing the number of coupling plates used. The number of coupling plates can be added by

radially placing more fixed conductive plates and changing the middle lever from a simple straight lever to an asterisk-(or star)-like shape.

The process of sizing the sensor has been simplified by developing a design sheet in Mathcad (Mathsoft Engineering and Education Inc., Cambridge, MA). When design parameters are input to the worksheet, the program automatically calculates and displays sensor performance. Any parameters in worksheet can be modified and the sheet immediately recalculates performance.

Using the steps described and the Mathcad design worksheet, parameters have been given to the design, as an example. Further analysis of this structure will be based on these parameters.

- Power supply of 12 V at plate 1 (V_1), and -12 V at plate 2 (V_2).
- Dimensions, d_0 , is 0.2 mm, d_1 is 0.5 mm, d_2 is 4.5 mm, h is 5 mm, t is 3 mm, and the middle plates is 0.4 mm thick.
- The middle plate is made from aluminum having density of 2800 kg/m^3 thus the plate weight 0.0336 gram and having mass moment of inertia $2.8087 \cdot 10^{-10} \text{ kg.m}^2$.
- Media between the plate is air at 20°C has relative permeability of 1.2.
- All resistors, R_1 , R_2 , and R_c , are set to be equal at $1 \text{ K}\Omega$.
- Design force that can generate is $1 \mu\text{N}$ at the tip using safety factor of 2.
- Number of fin (coupling pair) is one (add more to increase sensing range).

The stiffness value of the rotational spring attached at the fulcrum point (k_θ) has to be decided based on some initial experiments or simulation for the reason that it should provide a good dynamic response in terms of settling time, overshoot, and response time. Considering mechanical side of the model, a damping ratio, ζ , can be found from, $\zeta = \frac{b_\theta}{2\sqrt{Jk_\theta}}$. For common sensors, the ζ is set to be at $\sqrt{2}/2$ or 0.707 to give minimal overshoot and response time. For this case in the design simulation, k_θ of $1 \cdot 10^{-4} \text{ N.m/rad}$ and b_θ of $2.3697 \cdot 10^{-7} \text{ N.m.sec/rad}$ are used.

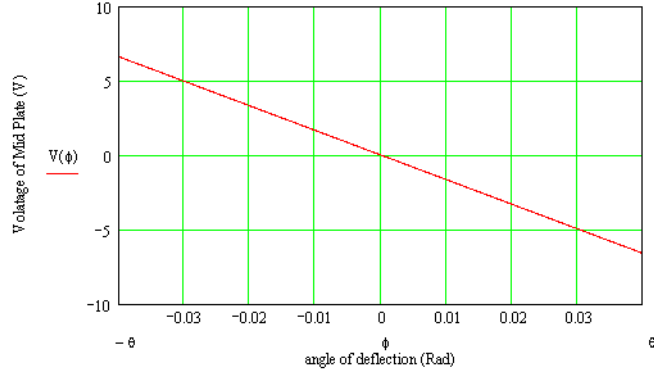


Figure 4.5: Sensing characteristic of the three plates capacitive sensor

The sensing characteristic for this sensor design is shown in Figure 4.5. It can be seen that as the mid plate moves closer to left plate (or rotate in clockwise positive θ direction), the potential will become more negative. On the other hand, if the mid plate rotates in counter clockwise direction, potential of the middle plate becomes more positive. This shows that in a sensing application, the sensor will have a linear characteristic; however, design sheet calculations also show that noise due to parasitic capacitance, even if in a small magnitude, can result in undesired nonlinearity.

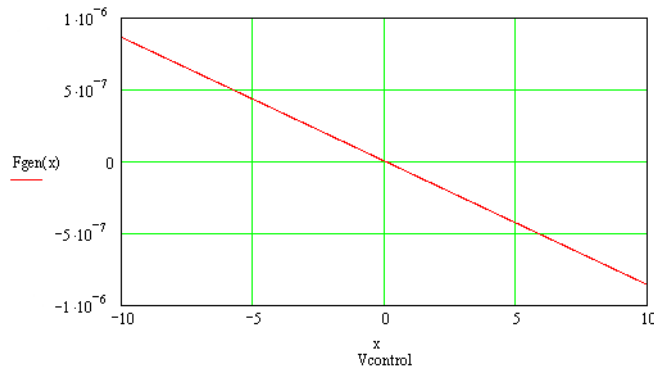


Figure 4.6: Actuating characteristic of the three plates capacitive sensor

Actuating characteristic of the design is shown in Figure 4.6 for a case where the middle plate always stays in the middle. It can be seen that if the potential of the middle plate is controlled to be in the same range of supply potential, the same structure can produce electrostatic force as designed.

4.3.1.4 Dynamic response

Dynamic response of this capacitive sensor is obtained by simulation as a Matlab's Simulink (Mathworks Inc, Natick, MA) block diagram as transformed from the bond graph model. This sensor structure will be simulated and evaluated using in two criteria: time domain and frequency domain response.

For time domain simulation, the left plate and right plate is charged to +12 V and -12 V respectively. That keeps the middle plate in the approximate center position due to balance of electrostatic forces between the two sides and keeps its potential around zero V due to balance in impedance on each side. Imperfection of the beam might cause the middle plate to move toward either side. However, when the middle plate moves, its potential and impedance balance are changed. Electrostatic forces are created so that the plate goes back toward approximate balance position.

Simulation results shown in Figure 4.7 demonstrate that a step force input of $10 \mu N$ applied at the tip of the middle plate (upper left) causes a sudden middle plate deflection to 0.03 degree (upper right). The movement in positive angle decrease potential of the middle plate to -82.5 mV (lower left), and an opposite electrostatic torque is generated at $5.75 \cdot 10^{-20}$ Nm. (lower right) for counter balancing. Measurement of the middle plate potential can be used either as an output since it is linearly related to the middle plate position, or as an input of a feedback control circuit to enhance the sensor performance.

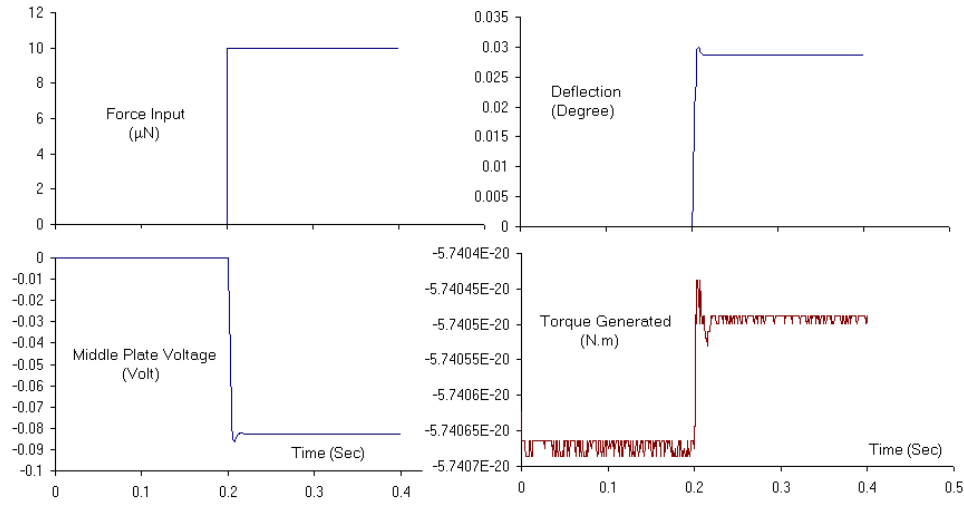


Figure 4.7: Time response of three plates capacitive sensor excited by $10 \mu N$ step input

For frequency domain simulations, a describing function (DF) method has been used as discussed in the last chapter, since the system is nonlinear. The DF of interest is between the middle plate potential and force input (V/N). The range of sinusoidal force input at the tip is varied from $0.1 \mu N$ which will deflect the middle plate to about 0.003 degree to $10 \mu N$ which will deflect the middle plate to about 0.03 degree. The range of frequencies of interest are between 10 Hz to 40 kHz.

In particular, describing function of three plates capacitor as shown in Figure 4.8, plotted in log-log scale, shows two noticeable characteristics. First, the sensor has low-pass characteristic, a negative slope at high frequency is approximately 100 times per decade which indicate that the system has a second order characteristic with overdamped and 10^{12} gain. Second, the describing function shows dependency on input force magnitude similar to that of hair cells'. Specifically, at low magnitude of input force, the system has higher gain than when it has a higher input magnitude.

The simulation above has been performed on this sensor without connec-

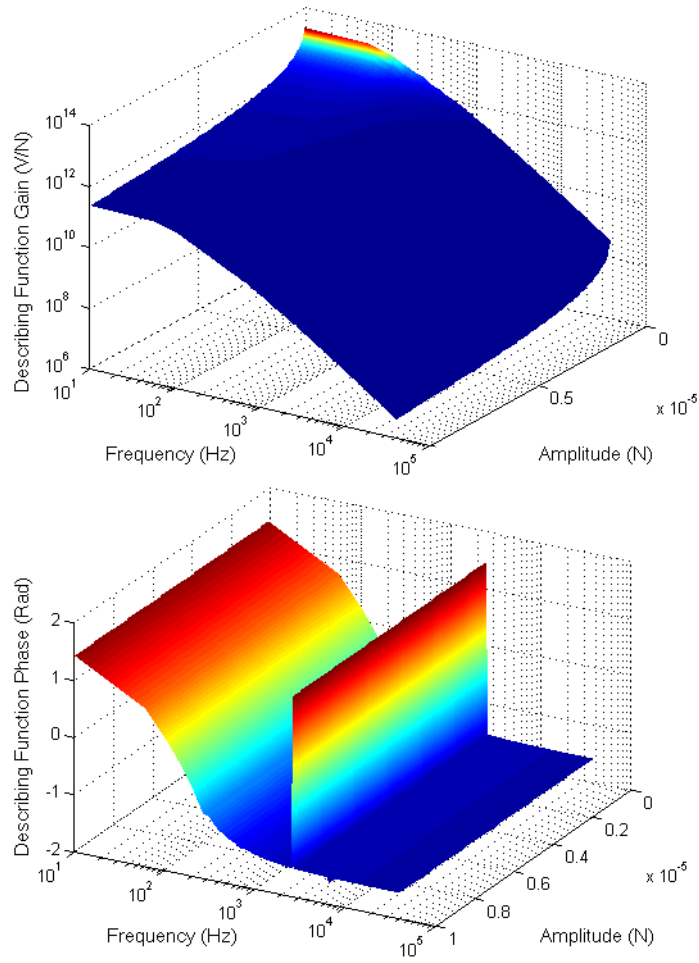


Figure 4.8: Describing function of three plates capacitive sensor considering input force between 0.1 to 10 μN and frequency between 10 to 40000 Hz.

tion to any control algorithm, which can significantly modify system response. For example, a feedback (servo) signal from the angle of the middle plate can be used to control the potential of plate number one and number two to achieve broader bandwidth in frequency response. A nonlinear adaptive control algorithm can also be used to control the sensor as will be discussed more in the next chapter.

Despite its interesting characteristics, a prototype of this sensor is very difficult to construct in the lab environment since capacitive sensors require good magnetic shielding, and the electrostatic force can be considered a major force only when the size of the sensor is small. An attempt to build this sensor at macro-scale resulted in problems due to shielding. For that reason, this kind of sensor will not be further developed.

4.3.2 Macroscale piezoceramic bimorph sensor

The second basic structure is based on a piezoelectric cantilever beam called a bimorph (or polymorph). Bimorph is a cantilever beam structure made of oppositely poled piezoelectric material that is sandwiched together between a very flexible conductive metal beam. If an electrical potential is applied to one of junctions at the base of the bimorph, it will result in bending of the cantilever. Conversely, an applied bending moment at the end of the cantilever will create potential between bimorph terminal junctions. For actuation applications, the bimorph can be small, light, and requires less power to produce an equivalent amount of force than any other structures. In sensing application, the signal produced is hardly affected by noise. Major disadvantages of piezoelectric material are its pyroelectricity, or temperature dependent property, and its nonlinear behavior. However, modern piezoelectric material has been designed so that the pyroelectric effect is minimal. It is proposed here that a bimorph based structure is suitable for a macroscale (and

higher actuation power) sensor that is more suitable to build as a lab prototype.

4.3.2.1 Piezoceramic bimorph

Piezoelectricity is a well known property of dielectric crystalline solid materials which produce electrical charges when it is mechanically stressed and produce mechanical strain when it is subjected to an electrical field. This special characteristic allows piezoelectric materials to be effective for both sensing and actuating applications. However, materials being used for piezoelectric sensors and actuators may not always be entirely crystal. Other materials such as polymers and polycrystalline ceramics can be easily transformed to piezoelectric materials by a process called poling. This process involves using a temporary high-static electric field that rearranges the random domain orientation of material in their original state such that the material structure becomes anisotropic. Well known piezoceramic materials such as barium titanate ($BaTiO_3$) and lead zirconate titanate (PZT) are made by this process.

The bimorph (bender), invented by C. Baldwin Sawyer in 1931, is a special form of piezoelectric transducer that takes advantage of a shear mode [19] in piezoelectric materials. The material structure is composed of two thin panels of piezoceramic elements bonded with a flexible metallic panel in between. The metallic panel is used both as a central electrode and as reinforcement mechanical structure. Application of a potential in the direction paralleled with the polarization of the element drives one layer into expansion while contracting the other in the planes perpendicular to the applied field which results in bending of the panel. This piezoelectric bimorph can also be called a bending motor or bender in an actuating application. Conversely, application of force generates a voltage and the beam is usually called bending generator in sensing applications.

The term “bi” in bimorph comes from the number of layers of piezoelectric material used to build the panel, which is two for this case. If the panel is built from one layer of material, it is called monomorph. If more than two layers are used then the panel is called a polymorph. If piezoelectric materials used to build polymorph layers change their properties continuously, the panel will be called functionally gradient material (FGM) polymorph. Theoretically, the more the number of layers used to build the panel the better the panel’s performance (i.e., larger deflection in actuation mode and higher potential in sensing mode), since mechanical stress is lower due to smaller strain difference between material layers at their interface. Smaller strain also generally results in longer life of the transducer. However, manufacturing difficulty increases greatly as the number of layers increase in polymorph and FGM such that the two layer (bimorph) is still the most widespread format.

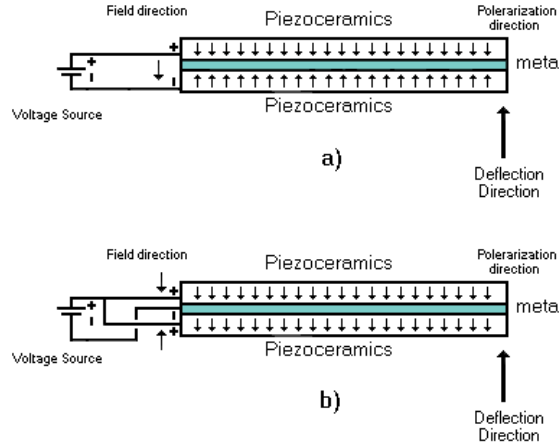


Figure 4.9: Two basic bimorph configurations: a) series type, and b) parallel type.

There are many configurations of bimorph, however, all of them can be categorized into either parallel type or series (antiparallel) type. The difference between the two is direction of polarization elements with respect to applied electrical field

(intensity). For a series type bimorph (see Figure 4.9 a)), polarization of piezoelectric material on the top layer is in opposite direction of the bottom layer. A potential source is connected to the panel in series and generates a field in downward direction as shown. When material is subjected to a field, the top layer that has polarization direction parallel with the field will contract longitudinally; on the other hand, the bottom layer which has an opposite polarization direction to the field will expand longitudinally. This results in bending of the panel upward. A reverse direction of the source will result in downward bending of the panel. The middle metallic panel in a series type bimorph is only used for reinforcement and is electrically irrelevant.

For parallel type bimorph (see Figure 4.9 b)), polarization of piezoelectric material on the top and bottom layers are in the same direction. A potential source has been connected in parallel with the panel so that electrical field is generated and affects the top and bottom layers differently. On top layer, the field has the same direction as polarization in material, thus the layer contracts longitudinally. On the bottom layer, the field has opposite direction to polarization of material and the layer expands. These make the panel bending upward similar to series type bimorph.

A major performance difference between series and parallel type bimorph is that for the same amount of potential input, the parallel type bimorph generates two times more field intensity. Thus, the parallel type can generate almost two times the deflection when compared with a series type bimorph with exactly the same dimension. However, this also means that for the same amount of deflection, a series type bimorph generates a higher potential (i.e., better resolution for sensing).

4.3.2.2 Bimorph constitutive relations

Constitutive relations of the bimorph are required for accurate sensor performance prediction and simulation. As discussed, the bimorph configuration has been chosen because of its analogous characteristic structure with a hair cell's plasma membrane. The bimorph and membrane's constitutive relations have a direct relation between effort and displacement. In another words, both of the structure can be represented by a multiport capacitive (-C-) element in a bond graph.

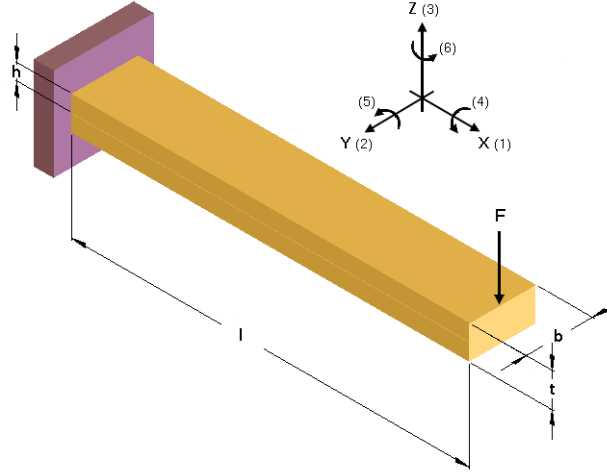


Figure 4.10: Notation on dimension of bimorph and its convention

Figure 4.10 shows basic dimension of the bimorph in cantilever configuration. The beam width is b , the beam length is l , the beam thickness is t , and thickness of only one layer is h . Assuming, for now, that the middle electrode is thin and its dimension is insignificant ($2h = t$). X, Y, Z are orthogonal axes corresponding to axes 1, 2, 3 in Einstein's tensor notation. Axes 4, 5, and 6 are rotational axes taken counterclockwise around axes 1, 2, and 3, respectively. Note that for Einstein's notation, axes 4 is on plane 2-3, 5 is on plane 3-1, 6 is on plane 1-2, and these axes are used to denote surface shear in solid mechanics.

In this section, constitutive relations for a parallel type bimorph will be described since these will be used further in the sensor development. However, constitutive relations for a series type bimorph is very similar to the parallel type. The difference between the two of them are that, the piezoelectric coefficients have negative sign for a parallel type bimorph, while in series type has a positive sign. The electric field strength of a parallel type bimorph is also two times that of a series type bimorph.

As for the model of electromotility in a hair cell, a piezoelectricity effect in a bimorph can be described by an impedance matrix of the form,

$$\begin{bmatrix} \epsilon \\ \mathbf{d} \end{bmatrix} = \begin{bmatrix} \mathbf{s}^{(\xi)} & -\mathbf{D} \\ \mathbf{D}^T & \mathbf{K}^{(\mathbf{T})} \end{bmatrix} \cdot \begin{bmatrix} \mathbf{T} \\ \xi \end{bmatrix}, \quad (4.20)$$

where ϵ is infinitesimal strain field, (\mathbf{T}) is the stress field, \mathbf{d} is electric displacement field, ξ is electric field, $\mathbf{s}^{(\xi)}$ is compliance tensor field evaluated at constant electric field (ξ), $\mathbf{K}^{(\mathbf{T})}$ is permittivity tensor field evaluated at constant stress, and finally \mathbf{D} is piezoelectric strain coupling tensor field.

Einstein's convention is used to assign subscripts for each tensor field. For example, compliance tensor, $\mathbf{s}_{\mathbf{xy}}^{(\xi)}$, means a compliance due to stress in x direction which generating strain in y direction, $\mathbf{D}_{\mathbf{xy}}$ indicates a conversion (coupling) across energy domains of the piezoelectric material which is on the plane perpendicular to x axis, and piezoelectrically induces strain in y direction. Finally, $\mathbf{K}_{\mathbf{xy}}^{(\mathbf{T})}$ indicates dielectricity of electrode (material) on the plane perpendicular to x axis in y direction.

Considering that the piezoelectric beam is long and slender, it can be assumed that the stress in (2) direction is zero. Polarization of materials are in the axis parallel with (3) or thickness direction, and the beam is not being constrained in this direction. Therefore, stress in (3) direction can also assume to be zero [87].

Following Smits [71], equation 4.20 can then be written considering that the upper layer of material has its polarization parallel with applied electric field as,

$$\begin{aligned}\epsilon_1^U &= s_{11}^{(\xi)} T_1^U + D_{31} \xi_3 \\ d_3^U &= D_{31} T_1^U + K_{33}^{(T)} \xi_3\end{aligned}\quad , \quad (4.21)$$

where, superscript U represents the upper element. For the lower layer of material, the applied electric field is antiparallel with polarization and its constitutive relation is,

$$\begin{aligned}\epsilon_1^L &= s_{11}^{(\xi)} T_1^L - D_{31} \xi_3 \\ -d_3^L &= D_{31} T_1^L - K_{33}^{(T)} \xi_3\end{aligned}\quad , \quad (4.22)$$

where, superscript L represents the lower element.

A constitutive equation can be found from the stored potential energy . For this case, the energy stored can be found from the potential energy density equation which take form,

$$u = \frac{1}{2} \epsilon T + \frac{1}{2} d \xi. \quad (4.23)$$

Using equation 4.23 results in energy density equations for the upper and lower layers of the parallel type bimorph as,

$$\begin{aligned}u^U &= \frac{1}{2} s_{11}^{(\xi)} (T_1^U)^2 + D_{31} \xi_3 T_1^U + \frac{1}{2} K_{33}^{(T)} (\xi_3)^2 \\ u^L &= \frac{1}{2} s_{11}^{(\xi)} (T_1^L)^2 - D_{31} \xi_3 T_1^L + \frac{1}{2} K_{33}^{(T)} (\xi_3)^2\end{aligned}\quad . \quad (4.24)$$

A total energy stored can be found from a summation of the integration of equation 4.24 for both top and bottom layer,

$$U = \int_0^h \int_0^b \int_0^l (u^U + u^L) dx dy dz. \quad (4.25)$$

Again, a final constitutive relation can be found from the derivative of the total potential energy result in equation 4.25, with four cases of boundary conditions [71]

as,

$$\begin{bmatrix} \alpha \\ \delta \\ \nu \\ q \end{bmatrix} = \begin{bmatrix} \frac{3s_{11}^{(\xi)}l}{2bh^3} & \frac{3s_{11}^{(\xi)}l^2}{4bh^3} & \frac{s_{11}^{(\xi)}l^3}{4h^3} & \frac{-3D_{31}l}{2h^2} \\ \frac{3s_{11}^{(\xi)}l^2}{4bh^3} & \frac{s_{11}^{(\xi)}l^3}{2bh^3} & \frac{3s_{11}^{(\xi)}l^4}{16h^3} & \frac{-3D_{31}l^2}{4h^2} \\ \frac{s_{11}^{(\xi)}l^3}{4h^3} & \frac{3s_{11}^{(\xi)}l^4}{16h^3} & \frac{3bs_{11}^{(\xi)}l^5}{40h^3} & \frac{-D_{31}bl^3}{4h^2} \\ \frac{-3D_{31}l}{2h^2} & \frac{-3D_{31}l^2}{4h^2} & \frac{-D_{31}bl^3}{4h^2} & \frac{2K_{33}^{(T)}lb}{h}(1 - \frac{D_{31}^2}{4s_{11}^{(\xi)}K_{33}^{(T)}}) \end{bmatrix} \cdot \begin{bmatrix} M \\ F \\ p \\ V \end{bmatrix}, \quad (4.26)$$

where α is angle at the tip of bimorph, δ is vertical tip deflection, ν is volume displacement, q is charge, M is moment at the tip, F is force at the tip, p is uniform load along the beam, and V is potential difference (voltage) between top and bottom layer. It could be seen that the structure of a piezoelectric ceramic bimorph beam can be represented by a 4-port capacitive (C) element.

4.3.2.3 S-bender bimorph

Based on the parallel type bimorph that has just been discussed, a sensor that is analogous to the outer hair cell model can be designed. The special characteristics of hair cells and their performance requirement suggests a sensor structure based on the basic bimorph sensor in Figure 4.11. Sources are connected to the bimorph using 3-junctions, thus it is a parallel type of connection.

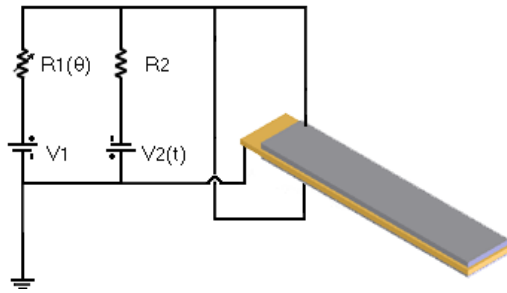


Figure 4.11: Diagram of parallel bimorph sensor analog to hair cell model

A special configuration of parallel bimorph called a “S beam” can be used

(see Figure 4.12). The S beam is a bimorph that has been fixed at the tip by a plate so that the tip stays parallel to the base in cantilever configuration (the tip angle is always zero).

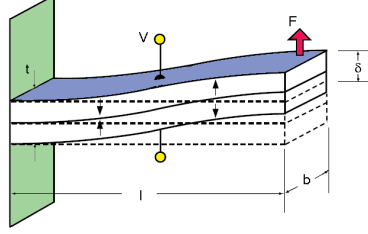


Figure 4.12: Parallel type bimorph in cantilever “S” beam configuration

The four-port impedance of equation 4.26 can be used to find two-port equations for the S beam bimorph by assuming that the bimorph has negligible distributed weight. However, element 2-2 in the compliance matrix of equation 4.26 represents mechanical compliance at the tip of cantilever, which has to be modified to account for the S-beam configuration. An equation for deflection of elastic straight beam fixed at both ends and loaded at the middle is,

$$\delta = \frac{l^3}{192EI} F, \quad (4.27)$$

where δ is maximum vertical deflection, l is length of the beam, E is modulus of elasticity of the beam, and I is area moment of inertia of the beam section. In the case of bimorph, a rectangular cross section is used, so $I = \frac{bt^3}{12}$. Considering that $s_{11}^{(\xi)} = \frac{1}{E}$, $2h = t$, and fixed-fixed beam has 2 time the stiffness of S-beam cantilever. Put all of them together get,

$$\delta = \frac{s_{11}^{(\xi)} l^3}{8bh^3} F. \quad (4.28)$$

Equation 4.28 replaces compliance element 2-2 of equation 4.26. This results in a

two-port compliance of,

$$\begin{bmatrix} \delta \\ q \end{bmatrix} = \begin{bmatrix} \frac{s_{11}^{(\xi)} l^3}{8bh^3} & \frac{-3D_{31}l^2}{4h^2} \\ \frac{-3D_{31}l^2}{4h^2} & \frac{2lb}{h} \left(K_{33}^{(T)} - \frac{D_{31}^2}{4s_{11}^{(\xi)}} \right) \end{bmatrix} \cdot \begin{bmatrix} F \\ V \end{bmatrix}. \quad (4.29)$$

Equation 4.29 is inverted to get a constitutive relation in the form using displacements as independent variables,

$$\begin{bmatrix} F \\ V \end{bmatrix} = \begin{bmatrix} \frac{(4K_{33}^{(T)} s_{11}^{(\xi)} - D_{31}^2)4bh^3}{l^3 s_{11}^{(\xi)} (2K_{33}^{(T)} s_{11}^{(\xi)} - 5D_{31}^2)} & \frac{6D_{31}h^2}{l^2 (2K_{33}^{(T)} s_{11}^{(\xi)} - 5D_{31}^2)} \\ \frac{6D_{31}h^2}{l^2 (2K_{33}^{(T)} s_{11}^{(\xi)} - 5D_{31}^2)} & \frac{s_{11}^{(\xi)} h}{lb (2K_{33}^{(T)} s_{11}^{(\xi)} - 5D_{31}^2)} \end{bmatrix} \cdot \begin{bmatrix} \delta \\ q \end{bmatrix}. \quad (4.30)$$

Equation 4.30 is good only for a purely piezoceramic bimorph. Commercial bimorphs often use stiff metal plates as both conductor and reinforcement shim. The popular choices are brass and stainless steel which greatly increase the stiffness of the beam. Equation 4.27 is used again but considering only shim material to find effective stiffness, and adding to element 1-1 in compliance matrix of equation 4.30 to get the final constitutive relation,

$$\begin{bmatrix} F \\ V \end{bmatrix} = \begin{bmatrix} \frac{(4K_{33}^{(T)} s_{11}^{(\xi)} - D_{31}^2)4bh^3}{l^3 s_{11}^{(\xi)} (2K_{33}^{(T)} s_{11}^{(\xi)} - 5D_{31}^2)} + \frac{8E_{shim}bh^3}{l^3} & \frac{6D_{31}h^2}{l^2 (2K_{33}^{(T)} s_{11}^{(\xi)} - 5D_{31}^2)} \\ \frac{6D_{31}h^2}{l^2 (2K_{33}^{(T)} s_{11}^{(\xi)} - 5D_{31}^2)} & \frac{s_{11}^{(\xi)} h}{lb (2K_{33}^{(T)} s_{11}^{(\xi)} - 5D_{31}^2)} \end{bmatrix} \cdot \begin{bmatrix} \delta \\ q \end{bmatrix}, \quad (4.31)$$

where, subscript “shim” indicates a shim material. Specifically, E_{shim} and h_{shim} are modulus of elasticity and total thickness of shim material, respectively. The constitutive relations 4.31 will be used in further design and simulation of the sensor developed. The term “bimorph” will be used instead of “S beam parallel type bimorph” beyond this point.

Figure 4.13 shows a bond graph model of the bimorph structure shown in Figure 4.11. In the bond graph, a 2-port capacitive (C) element represents the piezoelectric relation in equation 4.31. The zero junction on the right of the 2-port (C) represents an electrical parallel connection of two sources, V_1 and V_2 . In series

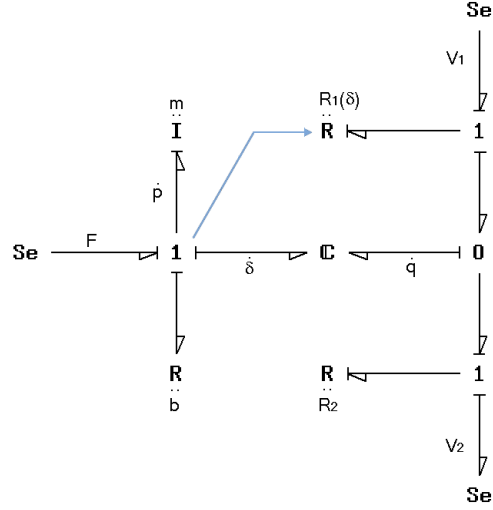


Figure 4.13: Bond graph model of bimorph in Figure 4.11

with V_1 and V_2 are $R_1(\theta)$ and R_2 , respectively. The left side of the 2-port (C) represents mechanical stiffness of the cantilever, where m is effective bimorph beam mass represented by inertia (I) element, and b is effective mechanical damping of the beam, represented by resistive (R) element. Similar to the bond graph structure of the hair cell and micro flow sensor, a signal bond conveying information about the deflection at the cantilever tip (δ) is forming a feed back loop.

4.4 Sensoriactuator accelerometer structure

Now that a basic sensor structure analogous to a hair cell has been proposed, it can be used as a basic building block for a sensing structure. Again, the decision is to focus on accelerometer (mechanical displacement type sensor), and the structure will be analogous to the organ of corti in the cochlea. As described in the previous chapter, the organ of corti is composed of inner hair cells which act like sensors, outer hair cells which act like controlled actuators, a basilar membrane and tectorial

membrane which act like proof mass, and a limbus which is a fixed structure. A section of an accelerometer can be similarly constructed.

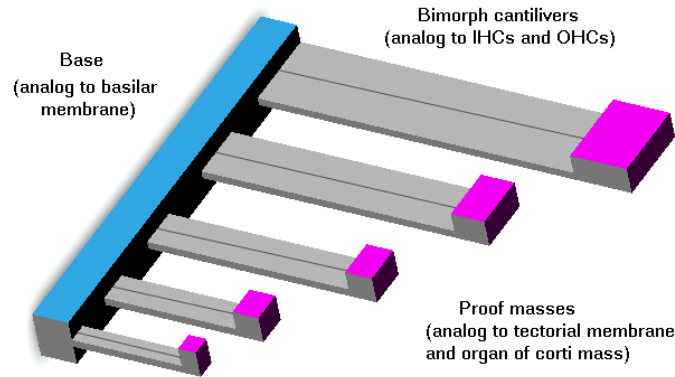


Figure 4.14: Conceptual design of bimorph as distributed accelerometer

Figure 4.14 shows conceptually how an array of accelerometers might be formed. Bimorphs of different sizes can be arranged together with different proof masses at their tip, analogous to changes in mass and stiffness of the organ of corti along the length of the cochlea. Each beam section will be composed of two bimorphs, one acting like a sensor and another acting like an actuator. Two bimorphs can form a sensoriauator couple similar to how inner and outer hair cells are tied together between basilar and tectorial membrane. Each section has mechanical function similar to a conventional accelerometer; however, instead of measuring all bands of frequency each section can be “tuned” to a narrow band of frequencies just like each section in the organ of corti. The length of the bimorphs and the proof masses together play an important role in predetermining the frequency band that each section can detect.

Figure 4.15 shows the detail of each section of the accelerometer concept from Figure 4.14. Each section is composed of a bimorph cantilever that is analogous to the inner hair cell thus working as sensor, and another bimorph cantilever

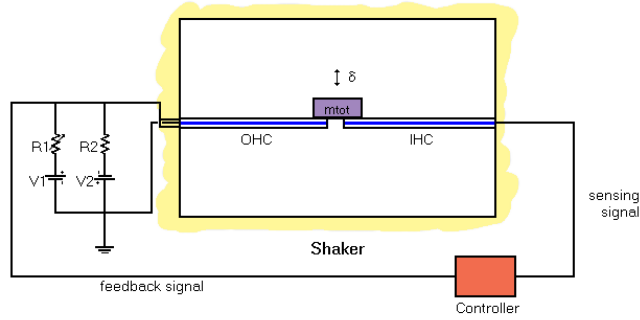


Figure 4.15: Conceptual design of a section of a bimorph accelerometer from Figure 4.14

that is analogous to the outer hair cell and thus working as a controlled actuator. Proof mass (denoted by m_{tot}) has been used to fix both bimorphs together such that they deflect equally by an amount δ . The sensing bimorph will be used to provide an output for the sensor function and as an input in sensor control decisions. The actuator part is responsible for changing system behavior (i.e., by changing its stiffness or creating force) thus making the structure active and adaptive. As discussed at the beginning of this chapter, by adding an adaptive control algorithm, it is expected that the sensor will be improved in two ways. First, an ability will be gained to shift or modify the band pass characteristic. Second, an automatic gain control will be added that can adjust the magnitude range that the sensor can measure. Detailed discussion on the controller synthesis will be provided in the next chapter.

A bond graph model of the conceptual design in Figure 4.15 is shown in Figure 4.16. The flow source (Sf) in the mid bottom of the figure represents the velocity input from a shaker, or the measurand. The inertia (I) element right above the input represents the proof mass of the section. The right side of the proof mass is the model for the sensing bimorph with a 2 port capacitive (C) element representing

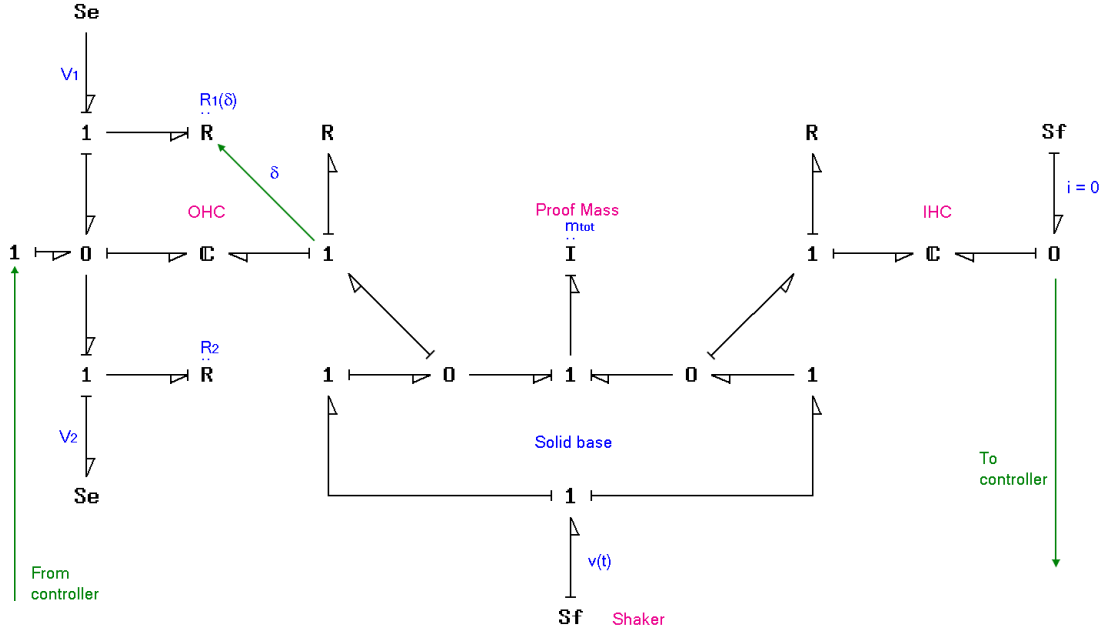


Figure 4.16: Bond graph model of one bimorph accelerometer section from Figure 4.15

a conversion of energy from mechanical to electrical. The measured signal is fed to a controller represented by a full (blue) arrow line on the right. On the left side of the proof mass is a model for the actuating bimorph which is an analog to the model of the outer hair cell previously developed. Controller output is fed to the model in parallel connection with the bimorph on the leftmost zero junction represented by full (blue) arrow line on the left from controller.

Figure 4.17 shows a reduced bond graph from that given in Figure 4.16. Some redundant junctions have been removed to simplify the model. All bonds have been numbered and the system causality shows five independent energy storage elements and thus the system have five energetic states. These states are momentum of the proof mass (p_6), displacement difference between the base and proved mass deflection for both bimorph (δ_9, δ_{14}), and charges stored at both bimorphs (q_{10}, q_{15}).

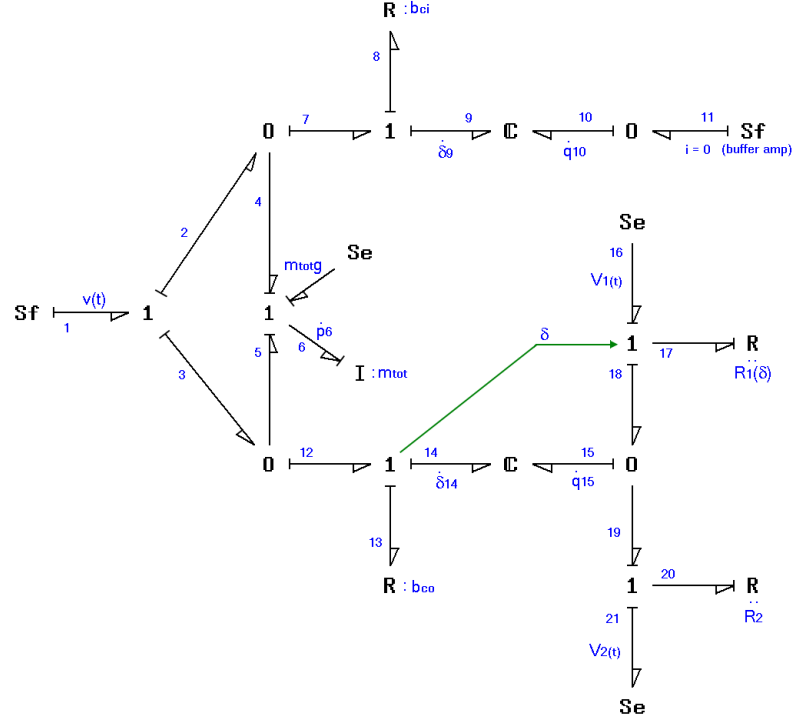


Figure 4.17: Simplification of bond graph model in Figure 4.16

State equations derived from the bond graph are,

$$\begin{aligned}
 \dot{\delta}_9 &= v(t) - \frac{p_6}{m_{tot}} \\
 \dot{\delta}_{14} &= v(t) - \frac{p_6}{m_{tot}} \\
 \dot{p}_6 &= \frac{-(b_{ci}+b_{co})}{m_{tot}} p_6 + C_{11i} \delta_9 + C_{12i} q_{10} + C_{11o} \delta_{14} + C_{12o} q_{15} + (b_{ci} + b_{co}) v(t) , \quad (4.32) \\
 \dot{q}_{15} &= \frac{(V_1(t) - C_{21o} \delta_{14} - C_{22o} q_{13})}{R_{max}(0.5 - \delta_{14}/\delta_{max})} - \frac{(C_{21o} \delta_{14} + C_{22o} q_{15} - V_2(t))}{R_2} \\
 \dot{q}_{10} &= i_{11in}
 \end{aligned}$$

where $R_1(\delta)$ has been assumed to take a linear form ($R_1(\delta) = R_{max}(0.5 - \delta/\delta_{max})$).

A linearized version of equation 4.32 is,

$$\begin{bmatrix} \dot{\delta}_9 \\ \dot{\delta}_{14} \\ \dot{p}_6 \\ \dot{q}_{15} \\ \dot{q}_{10} \end{bmatrix} = \begin{bmatrix} 0 & 0 & \frac{-1}{m_{tgt}} & 0 & 0 \\ 0 & 0 & \frac{-1}{m_{tot}} & 0 & 0 \\ C_{11i} & C_{11o} & \frac{-(b_{ci}+b_{co})}{m_{tot}} & C_{12o} & C_{12i} \\ 0 & \frac{-2C_{21o}}{R_{max}} - \frac{C_{21o}}{R_2} & 0 & \frac{-2C_{22o}}{R_{max}} & 0 \\ 0 & 0 & 0 & 0 & 0 \end{bmatrix} \cdot \begin{bmatrix} \delta_9 \\ \delta_{14} \\ p_6 \\ q_{15} \\ q_{10} \end{bmatrix} + \begin{bmatrix} v(t) \\ v(t) \\ (b_{ci} + b_{co})v(t) \\ \frac{V_2(t)}{R_2} + \frac{2V_1(t)}{R_{max}} \\ i_{11in} \end{bmatrix}, \quad (4.33)$$

where subscript “i” and “o” represent these parts of the bimorphs that act as inner hair cell (sensor) and outer hair cell (actuator), respectively. Parameter from equation 4.31 include, C_{11} is $\frac{(4K_{33}^{(T)} s_{11}^{(\xi)} - D_{31}^2)4bh^3}{l^3 s_{11}^{(\xi)} (2K_{33}^{(T)} s_{11}^{(\xi)} - 5D_{31}^2)} + \frac{8E_{shim}bh_{shim}^3}{l^3}$, C_{12} is $\frac{6D_{31}h^2}{l^2(2K_{33}^{(T)} s_{11}^{(\xi)} - 5D_{31}^2)}$, C_{21} is $\frac{6D_{31}h^2}{l^2(2K_{33}^{(T)} s_{11}^{(\xi)} - 5D_{31}^2)}$, and finally, C_{22} is $\frac{s_{11}^{(\xi)}h}{lb(2K_{33}^{(T)} s_{11}^{(\xi)} - 5D_{31}^2)}$.

4.5 Summary

In this chapter, two basic sensing structures analogous to outer hair cells have been developed. Those relying on multiple capacitive plates are more suitable for a smaller (micro) scale sensor. With physical dimensions in the millimeter range, multiplate capacitors can only produce actuation force in the micronewton range. Smaller scales can yield a higher force without overly excessive voltage level. Sensor designs using piezoceramic bimorphs are more suitable at macroscale. Having physical dimensions in the centimeter range, PZT bimorphs can produce actuation force in tens of centinewton. However, larger dimension yield a higher force. Due to lack of resources for building a microscale prototype, the bimorph basic structure was chosen for further study in this dissertation. A strategy for sensor arrangement has also been developed as an analog of the organ of corti. A mathematical model has

been developed using a bond graph approach. The significant element that has been intentionally left out at this point is a controller that must take a signal from the sensing part and feed a signal to the actuating part. The process of control required governs the entire sensor behavior and thus deserves a thorough discussion. The development of an adaptive control algorithm will be presented in the next chapter.

Chapter 5

Development of Adaptive Algorithms

In this chapter, a controller is designed and implemented for the sensor mechanism developed in the previous chapter in order to enhance its performance. A principle of model reference adaptive control (MRAC) has been chosen because many of its attractive benefits, as will be intensively discussed in this chapter. A simpler method such as classical feedback control technique is also discussed briefly for reference and comparison.

5.1 Why use model reference adaptive control (MRAC)?

It has been discussed in previous chapters that a preferable characteristic for any sensor is the linearity which can be achieved traditionally by using components that have a broad linear behavior. These sensors can be reliably used in an ‘open loop’ fashion. However, modern “smart” sensors have taken a different path. By utilizing a simple controller, such as force feedback in a MEMS accelerometer, modern sensors can utilize nonlinear components operating over a wide range. This dissertation hypothesize that adaptive controller can be used to regulate adaptation in sensor structure designed.

Specification requirements and sensor structure as shown in the last chapter are considered in selecting the principle of controller to be developed. Because of its simplicity, a classical control has always been regarded first in every controller design. However, using classical linear control theory introduces some unavoidable

problems. The method is based on a good linearized version of the system. This implies that the manufacturing process has to be precise and each sensor must be tuned (calibrated) before being used. Also, such conventional sensors can be used only for the design range. Nonlinear and optimal control methods offer tools that can enhance the capability of classical control theory for nonlinear systems and for optimization of some performance characteristics. However, these methods can not regulate the system performance in frequency domain as specified previously.

Adaptive control is a control approach with adjustable parameters and has some sort of mechanism for controller parameter adjustment. The method has been developed for applications in which the system characteristics have not fully known, a complete model of the system can not be made, or *for operation of the system in situations that might have not been expected*. This last characteristic is particularly attractive and motivated to further investigation into developing a controller for a sensor using an adaptive algorithm.

Historically, adaptive control was first devised for an aircraft flight controller that could operate at different altitudes and in all kinds of weather (Gajic and Lelic [43]). There are four major types of adaptive control. First, gain scheduling consists of a set of controllers designed and selected according to a set of situations that have been previously determined. Second, a self tuning regulator (STR) continuously estimates the characteristics of the plant and controller characteristic change according to designer specifications and the estimated plant. This method is also called indirect adaptive control. Third, in model referenced adaptive control (MRAC) the performance of the system is continuously compared to ideal performance of a reference model and the plant is continuously adapted until ideal characteristics are achieved. This method can also be called direct adaptive control because the controller directly specifies how parameters should be updated. Fourth, in stochastic

or dual-expert adaptive control a statistical approach is added to the controller to account for error arising from the process of plant estimation in all other three methods. Adaptive control is an advanced subject of modern automatic control, and there is extensive ongoing research. This chapter does not intend to explain all aspects of the area, but detailed discussions can be found in Astrom and Wittenmark [11], Landau [76], and Wellstead and Zarrop [125]. Notations used in this chapter are similar to the first two listed references.

It was mentioned in the last chapter that one of the major requirements of the adaptive sensor under development is a bandpass filter characteristic which would make it equivalent to each cochlear section (organ of corti). A controller must be able to maintain this filter characteristic in all situations. The MRAC algorithm is selected mainly because a bandpass characteristic can be directly converted to a reference frequency or S domain model using knowledge from filter design theory. Another requirement is an automatic gain control in each section which can also be implemented by integrating gain scheduling control within an MRAC algorithm. Controller design will be discussed beginning in the next section.

5.2 MRAC with gain scheduling controller design formulation

Structure of a model referenced adaptive control is composed of two major components. First, a feed-forward signal for a measurable disturbance and for compensating for its influence. In particular, a control input is fed forward through a reference model and the reference model output is used for error compensation. Second, two feedback closed loops: one called the inner loop is similar to a negative feedback loop in classical control, and another called outer loop is the parameter adjustment loop constructed using an adaptive control law. Controller objective is to control the plant so that its behavior tracks that of the reference model. This

is fundamentally similar to tracker problem in classical control theory. A block diagram example for a basic MRAC is shown in Figure 5.1.

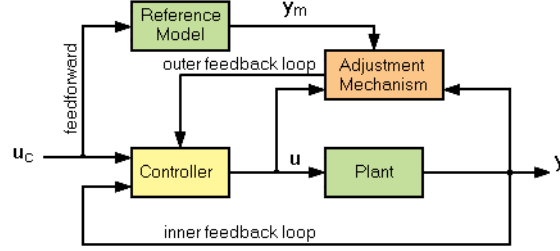


Figure 5.1: Basic structure of MRAC system, where u_c is control input, u is plant input, y_m is reference output, and y is plant output (Adapted from Astrom and Wittenmark [11]).

The two types of MRAC rules include the MIT gradient rule and Lyapunov's stability rule. Each approach has advantages and disadvantages. In this chapter, both of these rule techniques will be developed and compared. However, after some comparison a more suitable method will be selected and used in experimental study.

Formulation of the adaptive control approach can begin with a linear system or plant defined in states space format as,

$$\begin{cases} \frac{dx}{dt} = \underline{A}'x + \underline{B}'u \\ y = \underline{C}'x + \underline{D}'u \end{cases} \quad (5.1)$$

where x is the state vector, and \underline{A}' , \underline{B}' , \underline{C}' , and \underline{D}' are matrices representing the plant.

An input-output transfer function of the linear system in equation 5.1 can be found using Laplace transform as,

$$G(S) = \frac{Y(S)}{U(S)} = \underline{C}'(SI - \underline{A}')^{-1}\underline{B}' + \underline{D}',$$

where S is a differential operator on frequency, “ S ”, domain. Y and U are Laplace transform of plant output y and plant input u . $G(S)$ represent the transfer function of the plant.

A transformation from frequency domain transfer function $G(S)$ back to a state space model in time domain is used to convert system in the form of original states which can not be measured to another equivalent system that has synthetic states that are derivative related to system output which results in,

$$\boxed{\frac{dy}{dt} = py = \underline{A}y + \underline{B}u}. \quad (5.2)$$

where $\underline{B} = \underline{C}'\underline{B}' + \underline{D}'$ and p is defined as a differential operator in time domain.

A reference model of the same order is defined as,

$$\begin{aligned} \frac{dx_m}{dt} &= \underline{A}'_m x_m + \underline{B}'_m u_c \\ y_m &= \underline{C}'_m x_m + \underline{D}'_m u_c \end{aligned}$$

where subscript “m” in every parameter signifies that every parameter belongs to the reference model.

With a similar transformation, a reference model counterpart of the plant is,

$$G_m(S) = \underline{C}'_m (SI - \underline{A}'_m)^{-1} \underline{B}'_m + \underline{D}'_m,$$

in S domain transfer function and,

$$\boxed{\frac{dy_m}{dt} = \underline{A}_m y_m + \underline{B}_m u_c}, \quad (5.3)$$

in time domain states space model with original internal states eliminated.

An adaptive control law is set so that it can effect all states in state space. That is,

$$u = \underline{\Theta}_1 u_c - \underline{\Theta}_2 y. \quad (5.4)$$

$\underline{\Theta}$ s are called controller parameters (vectors) and are functions of time used to adapt the system according to an adaptation law. In case that full control of the system is possible, $\underline{\Theta}_1$ has dimension equal to number of input of the control input multiplied by number of states. Similarly, $\underline{\Theta}_2$ has a dimension equal to number of inputs of the plant multiplied by the number of states. In some references, $\underline{\Theta}_1$ and $\underline{\Theta}_2$ are called \underline{M} and \underline{L} , respectively.

The adaptive control law in equation 5.4 is put into the plant model of equation 5.2 which yields,

$$\frac{dy}{dt} = (\underline{A} - \underline{B}\underline{\Theta}_2)y + \underline{B}\underline{\Theta}_1 u_c. \quad (5.5)$$

From above equation, at a point of convergence which is after the system has adapted, controller parameters are,

$$\underline{B}\underline{\Theta}_1 = \underline{B}_m \Rightarrow \underline{\Theta}_1 = \frac{\underline{B}_m}{\underline{B}} \\ \underline{A} - \underline{B}\underline{\Theta}_2 = \underline{A}_m \Rightarrow \underline{\Theta}_2 = \frac{(\underline{A} - \underline{A}_m)}{\underline{B}} .$$

This equation is suitable only for scalar, and a matrix form can be shown as,

$$\underline{\Theta}_1 = (\underline{B}_m^T \underline{B})^{-1} \underline{B}_m^T \underline{B}_m \\ \underline{\Theta}_2 = (\underline{B}_m^T \underline{B})^{-1} \underline{B}_m^T (\underline{A} - \underline{A}_m) .$$

A plant output error, e , is defined as a difference between the plant output, y , and ideal referenced model output y_m as,

$$\boxed{e = y - y_m}. \quad (5.6)$$

5.2.1 Adaptive rule using MIT gradient method

MIT gradient rule is basically a concept for finding the slope or gradient effect that each adaptive parameter has on the plant output error. From equation 5.5,

$$(pI - \underline{A} + \underline{B}\underline{\Theta}_2)y = (\underline{B}\underline{\Theta}_1)u_c,$$

where I is identity matrix, thus

$$\frac{y}{u_c} = \frac{\underline{B}\Theta_1}{(pI - \underline{A} + \underline{B}\Theta_2)}. \quad (5.7)$$

Similarly, from equation 5.3,

$$\frac{y_m}{u_c} = \frac{\underline{B}_m}{(pI - \underline{A}_m + \underline{B}_m)}. \quad (5.8)$$

Then substituting equation 5.7 and 5.8 into equation 5.6 yields,

$$e = \frac{\underline{B}\Theta_1}{(pI - \underline{A} + \underline{B}\Theta_2)} \cdot u_c - \frac{\underline{B}_m}{(pI - \underline{A}_m + \underline{B}_m)} \cdot u_c.$$

MIT gradient rule can be simply stated as,

$$\frac{d\theta_n}{dt} = -\gamma e \frac{\partial e}{\partial \theta_n}. \quad (5.9)$$

This equation can be described, again, as the dynamics (or change) of each adaptive parameter, θ , is the negative of its gradient on output error, where γ is defined as adaptation gain. The error gradients when the rule is applied to error equation 5.6 are,

$$\frac{\partial e}{\partial \theta_1} = \frac{Bu_c}{(p - A + B\theta_2)}, \quad (5.10)$$

for adaptive parameter Θ_1 in scalar format, and,

$$\frac{\partial e}{\partial \theta_2} = -\frac{B^2\theta_1 u_c}{(p - A + B\theta_2)^2}, \quad (5.11)$$

for adaptive parameter Θ_2 in scalar format.

Using knowledge of convergence between reference model parameters and controlled plant parameters, equations 5.10 and 5.11 have been rewritten in terms of constants ($-A + B\theta_2 \approx A_m$) and output (from equation 5.7). Thus, equation 5.10 has been changed to,

$$\frac{\partial e}{\partial \theta_1} = \frac{Bu_c}{(p + A_m)}.$$

Similarly, using information from equation 5.7, equation 5.11 has been changed to,

$$\frac{\partial e}{\partial \theta_2} = -\frac{By}{(p + A_m)}.$$

From equation 5.9, controller according to adaptation law is,

$$\frac{d\theta_1}{dt} = -\gamma_1 e \frac{Bu_c}{(p + A_m)}, \quad (5.12)$$

for θ_1 and,

$$\frac{d\theta_2}{dt} = \gamma_2 e \frac{By}{(p + A_m)}, \quad (5.13)$$

for θ_2 .

While magnitude of adaptation gains for each parameter are entirely up to choice, they are usually set to allow unity steady state gain for each adaptation loop. Therefore from equation 5.13 and 5.12 adaptation gain can be found as,

$$\begin{aligned} \gamma_1 B &= A_m \Rightarrow \gamma_1 = \frac{A_m}{B} \\ \gamma_2 B &= A_m \Rightarrow \gamma_2 = \frac{A_m}{B} \end{aligned}$$

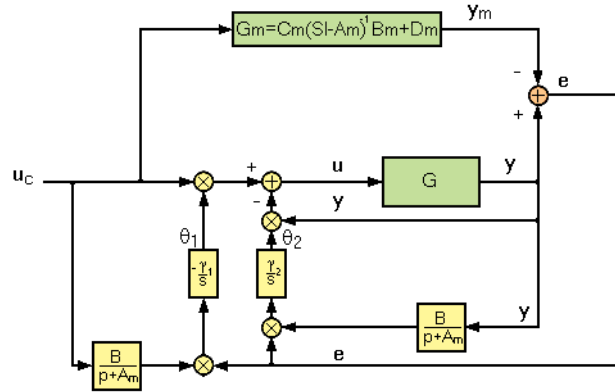


Figure 5.2: Structure of MRAC system using MIT gradient method

A block diagram representing the adaptive controller for the gradient method is shown in Figure 5.2. It can be seen that the normal structure of a gradient MRAC

is composed of filters and integrators. This same structure will keep repeating in every adaptation loop. Presence of integrators in every loop imply that number of states in the system will be doubled using the method of MRAC.

MIT gradient rule has been considered as the first and most computationally simple form of MRAC. This algorithm works well for a majority of systems. However, the theory can not guarantee stability of the control system and occasionally there can arise an instability due to poles (root of the characteristic equation) of the controlled system being placed on the right hand (positive) side of the complex root plane. A slight stability improvement can be added to the MIT gradient rule by modifying the rule so that the system's poles are always stable. That is,

$$\frac{d\theta}{dt} = \frac{\gamma\varphi e}{\alpha + \varphi^T\varphi}. \quad (5.14)$$

where φ is a vector defined as $\varphi = -\frac{\partial e}{\partial \theta}$ and α is a positive definite matrix introduced to ensure stability of the adaptive system by avoiding having pole on the right half plane when φ is very small. The modified MIT gradient rule in equation 5.14 is called "Normalized MIT gradient rule".

Now, apply the normalized rule to the general system discussed, and the same error gradients $\frac{\partial e}{\partial \theta_1}$ and $\frac{\partial e}{\partial \theta_2}$ arise as before. However, equation 5.9 changes to,

$$\frac{d\theta_2}{dt} = \frac{\gamma_2 e (\frac{By}{p+A_m})}{\alpha_2 + (\frac{By}{p+A_m})^2},$$

for θ_2 if the system is first order, and this can be further simplified as,

$$\dot{\theta}_2 = \frac{\gamma_2 e By(p + A_m)}{(p + A_m)^2 \alpha_2 + (By)^2}.$$

Similarly for adaptive parameter θ_1 ,

$$\dot{\theta}_1 = \frac{-\gamma_1 e (\frac{Bu_c}{p+A_m})}{\alpha_1 + (\frac{Bu_c}{p+A_m})^2}.$$

It can be seen that the control system using normalized gradient rule above is a lot more complicated compared to the original gradient rule. Results above show that each adaptation loop may consist of entirely different bandpass filters, while some of the filters in original gradient rule are the same.

5.2.2 Adaptive rule using Lyapunov stability theory

The adaptive rule using Lyapunov theory is an alternate method to design an adaptive system by looking at the stability standpoint. Using Lyapunov stability theory, which is used widely for determining stability in linear, nonlinear, time variant, or time invariant systems. The theory can be briefly stated that “Let $V(x, t)$ be a Lyapunov function of states and time of the system, and the system is uniformly asymptotically stable when and only when $V(x, t)$ is bounded and positive definite while its derivative, $dV(x, t)/dt$, is negative definite.”

Practically, the Lyapunov function usually resembles a quadratic function of energy storage in the system in terms of states. Definiteness of the matrix is also necessary to clarify. The definiteness of a matrix can be determined by a theory that states: “Let \underline{A} be a symmetric real matrix, \underline{A} is positive definite when all eigenvalues of \underline{A} are positive (real number) and \underline{A} is negative definite when and only when all eigenvalues of \underline{A} are negative (real number).”

To continue with the general system discussion, from equation 5.6 the rate of change in output error is,

$$\frac{de}{dt} = \frac{dy}{dt} - \frac{dy_m}{dt},$$

using equation 5.3 which describes the reference model together with equation 5.5 which describes the characteristic of the plant under control. The rate of change in output error has an explicit form as,

$$\frac{de}{dt} = (\underline{A} - \underline{B}\underline{\Theta}_2)y + \underline{B}\underline{\Theta}_1u_c - \underline{A}_my_m - \underline{B}_mu_c.$$

This equation is added and subtracted by $\underline{A}_m y$ and rearranged using $\underline{A}_m y - \underline{A}_m y_m = \underline{A}_m e$. This gives,

$$\dot{e} = \underline{A}_m e + (\underline{A} - \underline{A}_m - \underline{B}\underline{\Theta}_2)y + (\underline{B}\underline{\Theta}_1 - \underline{B}_m)u_c. \quad (5.15)$$

From equation 5.15, a Lyapunov function which is positive definite and having e , $\underline{\Theta}_1$, and $\underline{\Theta}_2$ as independent variables is constructed and used in stability analysis. It also can be seen in equation 5.15 that the first term depends on error, e , the second term depends on $\underline{\Theta}_2$, and the last term depends on $\underline{\Theta}_1$. Let P be a positive definite symmetric matrix and \underline{Q} a positive definite and diagonal matrix. Then, according to Lyapunov theory, the relation between \underline{P} and \underline{Q} is,

$$\underline{A}_m^T \underline{P} + \underline{P} \underline{A}_m = -\underline{Q}. \quad (5.16)$$

Equation 5.16 represents $n - 1$ linear equations in $n - 1$ unknowns, given diagonal matrix \underline{Q} in order to find elements of matrix \underline{P} used in Lyapunov equation. From equation 5.15, Lyapunov function can be constructed in the form,

$$V(e, \underline{\Theta}_1, \underline{\Theta}_2) = \frac{1}{2} \gamma e^T \underline{P} e + \frac{1}{2} tr\{(\underline{A} - \underline{A}_m - \underline{B}\underline{\Theta}_2)^T (\underline{A} - \underline{A}_m - \underline{B}\underline{\Theta}_2)\} + \frac{1}{2} tr\{(\underline{B}\underline{\Theta}_1 - \underline{B}_m)^T (\underline{B}\underline{\Theta}_1 - \underline{B}_m)\}, \quad (5.17)$$

where $tr\{\}$ represents the trace of matrix which is defined as the summation of elements on the main diagonal of the square matrix. Equation 5.17 can be written in scalar form as,

$$V(e, \theta_1, \theta_2) = \frac{1}{2} \gamma e^2 + \frac{1}{2B} (A - A_m - B\theta_2)^2 + \frac{1}{2B} (B\theta_1 - B_m)^2,$$

which, as described before, is in term of quadratic form having γ as a loop gain multiplier. Factor $1/B$ is also introduced as a gain of θ_1 and θ_2 functions for reason of numerical convenience, which will become clearer when we proceed to the next step.

Referring back to Lyapunov stability rule, in order for an adaptive controller to be stable the Lyapunov function must be positive definite, and by selecting a Lyapunov function in quadratic form, the positive definiteness of $V(e, \theta_1, \theta_2)$ has been guaranteed automatically. Thus to make sure that the system is stable it is only necessary to make sure that the derivative of the Lyapunov (dV/dt) stays negative definite. From Lyapunov function 5.17 and equation 5.15,

$$\begin{aligned}
\frac{dV}{dt} &= \frac{\gamma}{2} \left(e^T P \frac{de}{dt} + \frac{de^T}{dt} P e \right) + \text{tr} \{ [A - A_m - B\theta_2]^T \frac{d}{dt} [A - A_m - B\theta_2] \} \\
&\quad + \text{tr} \{ [B\theta_1 - B_m]^T \frac{d}{dt} [B\theta_1 - B_m] \}, \\
&= \frac{\gamma}{2} \left(e^T P A_m e + e^T P [A - A_m - B\theta_2] y + e^T P [B\theta_1 - B_m] u_c \right) \\
&\quad + \frac{\gamma}{2} \left(A_m^T e^T P e + [A - A_m - B\theta_2] y^T P e + [B\theta_1 - B_m] u_c^T P e \right) \\
&\quad + \text{tr} \{ [A - A_m - B\theta_2]^T \frac{d}{dt} [A - A_m - B\theta_2] \} \\
&\quad + \text{tr} \{ [B\theta_1 - B_m]^T \frac{d}{dt} [B\theta_1 - B_m] \}.
\end{aligned}$$

However, from equation 5.16 it is known that $A_m^T P + P A_m = -Q$, thus,

$$\begin{aligned}
\frac{dV}{dt} &= -\frac{\gamma}{2} e^T Q e + \gamma [A - A_m - B\theta_2]^T P e y^T + \gamma [B\theta_1 - B_m]^T P e u_c^T \\
&\quad + \text{tr} \{ [A - A_m - B\theta_2]^T \frac{d}{dt} [A - A_m - B\theta_2] \} \\
&\quad + \text{tr} \{ [B\theta_1 - B_m]^T \frac{d}{dt} [B\theta_1 - B_m] \}.
\end{aligned}$$

Combining all terms together,

$$\begin{aligned}
\frac{dV}{dt} &= -\frac{\gamma}{2} e^T Q e + \text{tr} \{ [A - A_m - B\theta_2]^T (\gamma P e y^T + \frac{d}{dt} [A - A_m - B\theta_2]) \} \\
&\quad + \text{tr} \{ [B\theta_1 - B_m]^T (\gamma P e u_c^T + \frac{d}{dt} [B\theta_1 - B_m]) \}.
\end{aligned} \tag{5.18}$$

In order to verify that dV/dt in equation 5.18 is negative definite, because the first term is already negative, it makes sense to drive the second and last term to negative or zero. Inspection suggests that driving last two terms to zero is the

easiest by setting,

$$\frac{d\theta_1}{dt} = -\gamma B^{-1} P e u_c^T, \quad (5.19)$$

for the third term, and

$$\frac{d\theta_2}{dt} = \gamma B^{-1} P e y^T, \quad (5.20)$$

for the second term. Equation 5.19 and 5.20 govern dynamics of adaptive parameters, thus it can be directly used as an adaptive law which maintains stability of the system.

Reconsidering above equations in scalar format,

$$\frac{dV}{dt} = \gamma e \frac{de}{dt} - (A - A_m - B\theta_2) \frac{d\theta_2}{dt} + (B\theta_1 - B_m) \frac{d\theta_1}{dt}$$

But from equation 5.15, de/dt is known, thus,

$$\begin{aligned} \frac{dV}{dt} &= \gamma e (A_m e + (A - A_m - B\theta_2) y + (B\theta_1 - B_m) u_c) \\ &\quad - (A - A_m - B\theta_2) \frac{d\theta_2}{dt} + (B\theta_1 - B_m) \frac{d\theta_1}{dt} \\ &= \gamma e^2 A_m + (A - A_m - B\theta_2) (y \gamma e - \frac{d\theta_2}{dt}) + (B\theta_1 - B_m) (\gamma e u_c + \frac{d\theta_1}{dt}). \end{aligned}$$

Again, from Lyapunov theory, γ is chosen to be negative and driving second and third terms to zero we get the adaptive law as,

$$\begin{aligned} \frac{d\theta_1}{dt} &= -\gamma_1 e u_c. \\ \frac{d\theta_2}{dt} &= \gamma_2 e y. \end{aligned}$$

Finally, a block diagram representing adaptive controller using Lyapunov's stability method is shown in Figure 5.3.

It can be seen that the block diagram representing Lyapunov's adaptive controller system is less complicated than that of gradient method. Most of the elements used in these two methods remain the same except the absence of filters

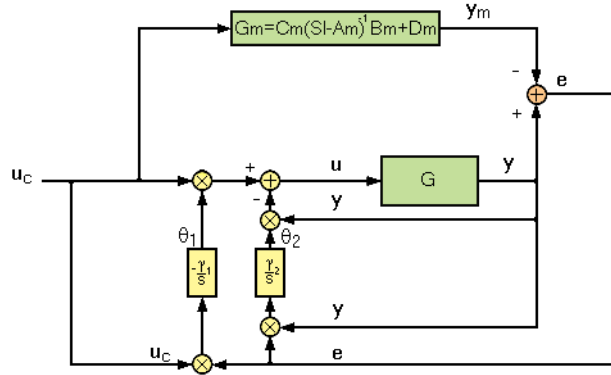


Figure 5.3: Structure of MRAC system using Lyapunov's stability method

in each adaptation loop in the Lyapunov stability method. A conclusion is drawn that the two major methods in MRAC which are going to be used have their own advantages and disadvantages. Computationally, the MIT gradient method is more attractive because it generally requires less steps, however the method results in a more complicated analog control circuit and in some occasions instability might occur. On the other hand, the Lyapunov method is more computationally difficult but its analog circuit requires less components and the system, in theory, should always remain stable.

5.2.3 Gain scheduling integration

In order to add another level of dynamics into the system, an idea of gain scheduling will be added to the referenced model. The reason for including gain scheduling is to create a set of referenced models which can be selected and used according to the level of an incoming signal. A gain scheduling algorithm added into the model referenced controller provides an automatic gain control to the system. This scheduling can be either a programmed algorithm or an analog circuit

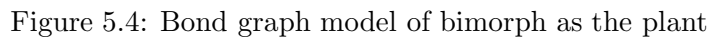
equivalent. Details about how the algorithm is constructed will be provided in the next section.

5.3 Adaptive controller for bimorph accelerometer

In the last chapter, the general bond graph structure of the bimorph accelerometer was developed. In order to attach a signal input and output, the system requires some modification. The bond graph in Figure 5.4, shows a simple model of the plant. A modification in the plant (or accelerometer) at this point is to make a Thevenin's equivalent circuit of the actuator (OHC) side. This consists of a capacitance on bond 15 on the 2-port C, a potential source of V_{in} , and series resistor of R_s which is used to keep integral causality on the 2-port C. The controller observes states of the system from potential out of the sensing (IHC) part of bimorph as V_{out} . Other parts of the bond graph are identical to that of the Figure 4.17 from the last chapter.

5.3.1 The plant

A state space model of the plant can be found directly from the bond graph using constitutive relations from the previous chapter. Again, states are $[\delta_9 \ \delta_{14} \ p_6 \ q_{10} \ q_{15}]$, which can be described physically as the tip displacement of two bimorphs, momentum of proof mass, and charge stored in each bimorph, respectively. Input to the plant are $[v \ V_{in}]$, which is velocity input (shaking velocity of the accelerometer) and potential in from the controller under development. Refer-


$$\underline{A'} = \begin{bmatrix} 0 & 0 & \frac{-1}{m_{tot}} & 0 & 0 \\ 0 & 0 & \frac{-1}{m_{tot}} & 0 & 0 \\ C_{11i} & C_{11o} & \frac{-(b_{ci}+b_{co})}{m_{tot}} & C_{12i} & C_{12o} \\ 0 & 0 & 0 & 0 & 0 \\ 0 & \frac{-C_{12o}}{R_s} & 0 & 0 & \frac{-C_{22o}}{R_s} \end{bmatrix},$$

$$\underline{B'} = \begin{bmatrix} 1 & 0 \\ 1 & 0 \\ (b_{ci} + b_{co}) & 0 \\ 0 & 0 \\ 0 & \frac{1}{R_s} \end{bmatrix},$$

$$\underline{D}' = \begin{bmatrix} 0 & 0 \end{bmatrix}.$$

A state space to transfer function transformation, $C(SI - A)^{-1}B + D$, is used to find a transfer function between two of the input (v and Vin) and output ($Vout$) in frequency domain. The results are,

$$\frac{Vout(S)}{v(S)} = \frac{eeS^2 + ffS}{aaS^3 + bbS^2 + ccS + dd} \quad (5.21)$$

and,

$$\frac{Vout(S)}{Vin(S)} = \frac{-gg}{aaS^3 + bbS^2 + ccS + dd} \quad (5.22)$$

where a set of constants have been defined to shorten equations as, $aa = R_s m_{tot}$, $bb = C_{22o} m_{tot} + R_s b_{ci} + R_s b_{co}$, $cc = b_{ci} C_{22o} + b_{co} C_{22o} + C_{11i} R_s + C_{11o} R_s$, $dd = C_{11o} C_{22o} + C_{11i} C_{22o} - C_{12o}^2$, $ee = C_{21i} m_{tot} R_s$, $ff = C_{21i} C_{22o} m_{tot}$, and $gg = C_{12o} C_{21i}$.

It can be seen that while the plant has five energy storage elements and five energetic states, the denominator in the transfer function is third order. It should be noted here that a pole-zero cancelation occurs in both transfer function 5.21 and transfer function 5.22. The real characteristic equation from determinant of $(SI - A)$ matrix is,

$$CE = \frac{S^2}{aa}(aaS^3 + bbS^2 + ccS + dd) = 0.$$

Because there is only a single output from the plant of five states, to monitor other states a state estimator has to be constructed. However, since the information of each state is not really needed and input is unknown, the plant can be transformed back to state space in term of fictitious states that directly relate to the output and its derivatives. Following the steps shown in equation 5.2, the combination of transfer functions in equation 5.21 and 5.22,

$$Vout(S) = \frac{(eeS + ff)A - ggVin}{(aaS^3 + bbS^2 + ccS + dd)},$$

where A represents acceleration input, which comes from integration of transfer function 5.21. To change this transfer function back to state space, let $y_1 = Vout$,

$y_1 = \dot{V}out = y_2$, $y_2 = \ddot{V}out = y_3$, thus $\dot{y}_3 = -\frac{bb}{aa}y_3 - \frac{cc}{aa}y_2 - \frac{dd}{aa}y_1 + \frac{ee}{aa}\dot{a} + \frac{ff}{aa}a - \frac{gg}{aa}Vin$, where a is acceleration in time domain, and \dot{a} is the rate of change of acceleration.

The state space model of the plant is then modified to,

$$\begin{bmatrix} \dot{y}_1 \\ \dot{y}_2 \\ \dot{y}_3 \end{bmatrix} = \begin{bmatrix} 0 & 1 & 0 \\ 0 & 0 & 1 \\ -\frac{dd}{aa} & -\frac{cc}{aa} & -\frac{bb}{aa} \end{bmatrix} \cdot \begin{bmatrix} y_1 \\ y_2 \\ y_3 \end{bmatrix} + \begin{bmatrix} 0 & 0 & 0 \\ 0 & 0 & 0 \\ \frac{ee}{aa} & \frac{ff}{aa} & -\frac{gg}{aa} \end{bmatrix} \cdot \begin{bmatrix} \dot{a} \\ a \\ Vin \end{bmatrix}. \quad (5.23)$$

Again, referring back to equation 5.2,

$$\underline{A} = \begin{bmatrix} 0 & 1 & 0 \\ 0 & 0 & 1 \\ -\frac{dd}{aa} & -\frac{cc}{aa} & -\frac{bb}{aa} \end{bmatrix},$$

and,

$$\underline{B} = \begin{bmatrix} 0 & 0 & 0 \\ 0 & 0 & 0 \\ \frac{ee}{aa} & \frac{ff}{aa} & -\frac{gg}{aa} \end{bmatrix}.$$

5.3.2 Reference model design

It has been stated several times that a desired characteristic for the accelerometer developed is band-pass. In this section an ideal characteristic of the accelerometer will be constructed by using knowledge of filter design. The first requirement is that the referenced model and the system should have the same order so that a MRAC controller will perform effectively.

Consider a band pass filter that has an order of equal to that of the plant. For example, if the system is 2nd order, to design a band pass filter, combine a low pass filter of first order with a high pass filter of first order to derive a second order band pass filter. The plant shown in the last section is equivalent to a third order system. A logical combination in that case is to combine a second order system with a first order high pass filter to derive a three order resonant band pass filter.

However, the reference model should also dynamics, and it has been stated that the system should have an automatic gain control of some sort. This can be

implemented into the reference model by an algorithm that selects one reference model out of a series of reference models according to a predefined operating condition. For example, when a system has a high output amplitude close to its limit, the controller will select a higher damped reference model so that it can continue the measurement of higher amplitude signal without saturation. This is similar to a combination of gain scheduling adaptive controller and MRAC adaptive controller together. This two tier adaptive controller is adopted here to solve this specific problem.

The algorithm for selecting and generating a reference model is described in the steps below. Each steps can be included either into a computer program or embedded as an analog circuit controller.

1. The maximum potential output, y_{max} (Volts), of the bimorph is measured approximately at its largest deflection for which the linear constitutive relation used to model the bimorph can still be considered valid, given that the sensor is nonadaptive.
2. Signal output from the sensing side (IHC bimorph) of the accelerometer is constantly monitored as y_1 , then the ratio between the system output and maximum allowed output, $\frac{y_1}{y_{max}}$, is calculated.
3. Monitored ratio is now checked in two situations. First, if the ratio of $\frac{y}{y_{max}}$ is less than one, it means that the bimorph limit has not been reached, and damping ratio of the system should remain constant. Second, if the ratio is approaching unity that means the limit of the bimorph will soon be reached, the damping ratio of the reference model should be increased gradually (e.g., if ratio < 1 , then $\zeta = \zeta_0$, else if ratio ≥ 1 , then $\zeta = \zeta + \Delta\zeta$, where ζ is damping ratio of the referenced model, and $\Delta\zeta$ is small value design by programmer).

4. The peak resonant magnitude, M_p (in dB), of the reference model can be calculated using the formula, $M_p = \frac{1}{2\zeta\sqrt{1-\zeta^2}}$.
5. The pass band frequency of the reference model should be known in advance and programmed into the controller. It can be constant in the case that a static band pass characteristic is desired, or it can be changed in the case frequency scanning is desired. The center of the frequency band should be a resonant frequency of second order system, f_r .
6. The second order part of the reference model will take the form,

$$G_{m1} = \frac{(4\pi^2 f_r^2)/(1-2\zeta^2)}{S^2 + \frac{4\pi f_r \zeta}{\sqrt{1-2\zeta^2}}S + \frac{4\pi^2 f_r^2}{(1-2\zeta^2)}}, \quad (5.24)$$

where the equation originates from standard second order transfer function, $\frac{\omega^2}{S^2 + 2\zeta\omega_n S + \omega_n^2}$, but $\omega_r = \omega_n \sqrt{1-2\zeta^2}$, and $f_r = \frac{\omega_r}{2\pi}$.

7. The first order part of the reference model is a high pass filter which has a cut off frequency approximately at the resonant frequency of the second order part. Hence,

$$G_{m2} = \frac{(S/2\pi f_r)}{(S/2\pi f_r + 1)}, \quad (5.25)$$

where this equation originates from first order high-pass transfer function, $(\tau S)/(\tau S + 1)$, and $2\pi f_r = 1/\tau$.

8. The reference model's transfer function is a product of first and second order transfer function in equation 5.24 and equation 5.25 thus,

$$\begin{aligned} \frac{V_{out}(S)}{u_c(S)} &= \frac{S}{(2\pi f_r + S)} \cdot \frac{(4\pi^2 f_r^2)/(1-2\zeta^2)}{S^2 + \frac{4\pi f_r \zeta}{\sqrt{1-2\zeta^2}}S + \frac{4\pi^2 f_r^2}{(1-2\zeta^2)}} \\ G_m &= \frac{(4\pi^2 f_r^2 S)/(1-2\zeta^2)}{S^3 + (\frac{4\pi f_r \zeta}{\sqrt{1-2\zeta^2}} + 2\pi f_r)S^2 + (\frac{4\pi^2 f_r^2}{1-2\zeta^2} + \frac{8f_r^2 \pi^2 \zeta}{\sqrt{1-2\zeta^2}})S + \frac{8\pi^3 f_r^3}{(1-2\zeta^2)}}. \end{aligned}$$

Another set of constants has been defined in parallel with the plant transfer function as, $aa_m = 1$, $bb_m = \frac{4\pi f_r \zeta}{\sqrt{1-2\zeta^2}} + 2\pi f_r$, $cc_m = \frac{4\pi^2 f_r^2}{1-2\zeta^2} + \frac{8f_r^2 \pi^2 \zeta}{\sqrt{1-2\zeta^2}}$, $dd_m = \frac{8\pi^3 f_r^3}{(1-2\zeta^2)}$, $ee_m = (4\pi^2 f_r^2)/(1-2\zeta^2)$, and $ff_m = 0$. Thus,

$$G_m = \frac{ee_m S + ff_m}{aa_m S^3 + bb_m S^2 + cc_m S + dd_m}. \quad (5.26)$$

9. Equation 5.26 is converted from a frequency domain to a time domain model as,

$$\begin{bmatrix} \dot{y}_{m1} \\ \dot{y}_{m2} \\ \dot{y}_{m3} \end{bmatrix} = \begin{bmatrix} 0 & 1 & 0 \\ 0 & 0 & 1 \\ -\frac{dd_m}{aa_m} & -\frac{cc_m}{aa_m} & -\frac{bb_m}{aa_m} \end{bmatrix} \cdot \begin{bmatrix} y_{m1} \\ y_{m2} \\ y_{m3} \end{bmatrix} + \begin{bmatrix} 0 & 0 \\ 0 & 0 \\ \frac{ee_m}{aa_m} & \frac{ff_m}{aa_m} \end{bmatrix} \cdot \begin{bmatrix} \dot{a}_c \\ a_c \end{bmatrix}. \quad (5.27)$$

Again, referring back to equation 5.3,

$$\underline{A}_m = \begin{bmatrix} 0 & 1 & 0 \\ 0 & 0 & 1 \\ -\frac{dd_m}{aa_m} & -\frac{cc_m}{aa_m} & -\frac{bb_m}{aa_m} \end{bmatrix},$$

and,

$$\underline{B}_m = \begin{bmatrix} 0 & 0 \\ 0 & 0 \\ \frac{ee_m}{aa_m} & \frac{ff_m}{aa_m} \end{bmatrix}.$$

5.3.3 Feedback algorithm

This section provides an analysis of how the method of feedback control can be implemented in the plant developed above. There are two reasons for exploring the feedback algorithm. First, it can be used as confirmation on a controllability of the system (plant), and second, as a verification on the plant parameter identification process which will be discussed in the chapter on experimental implementation.

In order to understand how the system can utilize feedback, a feedback parameter must be identified. In the accelerometer, a feedback system can be vi-

sualized as changing input acceleration to inertial force acting on the proof mass, m_{tot} .

For actuating mode, a transfer function between force generated on the tip of actuating (OHC) side of bimorph and input potential, Vin can be found. Referring to Figure 5.4, the plant has an output equation of $F_{14} = C_{11o}\delta_{14} + C_{12o}q_{15}$, and the equation can be written in term of output state space ($Y = CX + DU$) as,

$$F_{14} = [0 \ C_{11o} \ 0 \ 0 \ C_{12o}] \cdot \begin{bmatrix} \delta_9 \\ \delta_{14} \\ p_6 \\ q_{10} \\ q_{15} \end{bmatrix} + [0 \ 0] \cdot \begin{bmatrix} v \\ Vin \end{bmatrix}.$$

Compute a transfer function using Laplace transform matrix, $[C(SI - A)^{-1}B + D]$ and,

$$\frac{F_{14}}{Vin} = H = \frac{m_{tot}C_{12o}S^2 + (b_{co} + b_{ci})S + C_{11i}}{aaS^3 + bbS^2 + ccS + dd}. \quad (5.28)$$

A force feedback system with simple gain (P) controller for this case is shown in Figure 5.5. Transfer function “G” is obtained by multiplying equation 5.21 by $\frac{1}{m_{tot}S}$, resulting in transforming the velocity input term to initial force term. That is,

$$G = \frac{Vout}{F_c} = \frac{C_{21i}R_sS + C_{21i}C_{22o}}{aaS^3 + bbS^2 + ccS + dd}. \quad (5.29)$$

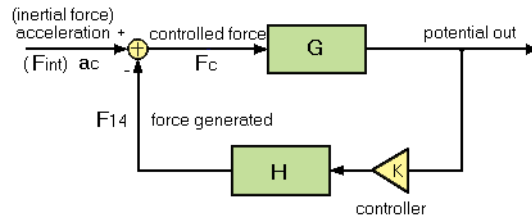


Figure 5.5: Block diagram of force feedback control system for bimorph accelerometer

Transfer function “H” in Figure 5.5 is from equation 5.28, and “K” denotes a proportional (P) controller gain, where the controller for this case has been put in the feedback path, which differs from the standard form where the controller is usually in the forward path. The reason for adopting this form is that the acceleration input will always directly affect the accelerometer, and there is no way that the controller can be otherwise inserted. This special controller position is called “indirect control” at this point, which refers to how the controller can not directly control the plant in its common position although a feedback law can still hold. Thus, according to this feedback configuration,

$$\begin{aligned}\frac{V_{out}}{F_{int}} &= \frac{G}{1 + KGH} \\ &= \frac{(C_{21i}R_sS + C_{21i}C_{22o})(aaS^3 + bbS^2 + ccS + dd)}{(aaS^3 + bbS^2 + ccS + dd)^2 + K(C_{21i}R_sS + C_{21i}C_{22o})(m_{tot}C_{12o}S^2 + (b_{co} + b_{ci})S + C_{11i})}.\end{aligned}\quad (5.30)$$

The proportional controller constant, “K”, in equation 5.30 can be changed to other types of controller/filters as needed according to feedback law. There are two cases that should be considered: a case where K is a constant which creates an AC (higher frequency) sensitive sensor, and a case where K is a transfer function (filter) which improves the bandwidth of the closed loop system.

For the first case, K is a constant which makes the transfer function the same as that shown in equation 5.30. It can be seen that the feedback transfer function, H, has a low pass resonant filter form. What this does for the feedback system is that the actuation part will only generate feedback force for lower frequency range which makes the sensor very sensitive to more AC signal because the DC signal will be fed back and canceled out with input. The AC frequency range that the sensor detects can be adjusted by physically changing dimensions of the actuation

(OHC part) bimorph. This feedback algorithm has been widely used in modern accelerometer.

For the second case, a transfer function for K can be found such that the transfer function of equation 5.30 yields just a simple gain or becomes a zero order transfer function. This will essentially improve the bandwidth of the sensor in the frequency domain and will result in,

$$K = \frac{(C_{21i}R_sS + C_{21i}C_{22o})(aaS^3 + bbS^2 + ccS + dd) - g(aaS^3 + bbS^2 + ccS + dd)^2}{g(C_{21i}R_sS + C_{21i}C_{22o})(hhS^2 + iiS + jj)}$$

where g in above equation is a zero order transfer function gain.

5.3.4 Gradient method adaptive controller

In this section, the adaptive controller based on the MIT gradient method will be applied to the plant (equation 5.23). The steps in development of the controller will strictly follow those discussed previously.

The dimension of matrices under discussion are as follows. For the plant, according to equation 5.23, the plant's state vector \underline{y} is a [3x1] matrix, having a characteristic \underline{A} of [3x3], \underline{B} of [3x3], and input \underline{U} of [3x1] (that is \dot{a} , a , and V_{in} which represent rate of controlled acceleration, controlled acceleration, and input potential.) For the reference model, according to equation 5.27, the model's state vector \underline{y}_m is [3x1] matrix, having a characteristic \underline{A}_m of [3x3], \underline{B}_m of [3x3], and input \underline{U}_c of [2x1] (that is \dot{a}_c and a_c which represent rate of input acceleration and input acceleration.)

The adaptive control law can be constructed using equation 5.4, which gives

$$\begin{bmatrix} \dot{a} \\ a \\ V_{in} \end{bmatrix} = \begin{bmatrix} \theta_{111} & \theta_{112} \\ \theta_{121} & \theta_{122} \\ \theta_{131} & \theta_{132} \end{bmatrix} \cdot \begin{bmatrix} \dot{a}_c \\ a_c \end{bmatrix} - \begin{bmatrix} \theta_{211} & \theta_{212} & \theta_{213} \\ \theta_{221} & \theta_{222} & \theta_{223} \\ \theta_{231} & \theta_{232} & \theta_{233} \end{bmatrix} \cdot \begin{bmatrix} y_1 \\ y_2 \\ y_3 \end{bmatrix}. \quad (5.31)$$

where the equation 5.31 represents 3 linear equations that have 15 unknown adaptive parameters (θ_{xxx}).

Substituting the control law in equation 5.31 into equation 5.23,

$$\begin{bmatrix} \dot{y}_1 \\ \dot{y}_2 \\ \dot{y}_3 \end{bmatrix} = \begin{bmatrix} 0 & 1 & 0 \\ 0 & 0 & 1 \\ \frac{-dd}{aa} & \frac{-cc}{aa} & \frac{-bb}{aa} \end{bmatrix} \cdot \begin{bmatrix} y_1 \\ y_2 \\ y_3 \end{bmatrix} + \begin{bmatrix} 0 & 0 & 0 \\ 0 & 0 & 0 \\ \frac{ee}{aa} & \frac{ff}{aa} & \frac{-gg}{aa} \end{bmatrix} \cdot \dots$$

$$\left(\begin{bmatrix} \theta_{111} & \theta_{112} \\ \theta_{121} & \theta_{122} \\ \theta_{131} & \theta_{132} \end{bmatrix} \begin{bmatrix} \dot{a}_c \\ a_c \end{bmatrix} - \begin{bmatrix} \theta_{211} & \theta_{212} & \theta_{213} \\ \theta_{221} & \theta_{222} & \theta_{223} \\ \theta_{231} & \theta_{232} & \theta_{233} \end{bmatrix} \begin{bmatrix} y_1 \\ y_2 \\ y_3 \end{bmatrix} \right),$$

which gives,

$$\begin{bmatrix} \dot{y}_1 \\ \dot{y}_2 \\ \dot{y}_3 \end{bmatrix} = \begin{bmatrix} 0 & 1 & 0 \\ 0 & 0 & 1 \\ A - B\theta_{231} & A - B\theta_{232} & A - B\theta_{233} \end{bmatrix} \begin{bmatrix} y_1 \\ y_2 \\ y_3 \end{bmatrix} + \begin{bmatrix} 0 & 0 \\ 0 & 0 \\ B\theta_{131} & B\theta_{132} \end{bmatrix} \cdot \begin{bmatrix} \dot{a}_c \\ a_c \end{bmatrix}, \quad (5.32)$$

where,

$$\begin{aligned} A - B\theta_{231} &= \frac{-dd}{aa} - \frac{ee}{aa}\theta_{211} - \frac{ff}{aa}\theta_{221} + \frac{gg}{aa}\theta_{231} \\ A - B\theta_{232} &= \frac{-cc}{aa} - \frac{ee}{aa}\theta_{212} - \frac{ff}{aa}\theta_{222} + \frac{gg}{aa}\theta_{232} \\ A - B\theta_{233} &= \frac{-bb}{aa} - \frac{ee}{aa}\theta_{213} - \frac{ff}{aa}\theta_{223} + \frac{gg}{aa}\theta_{233} \\ B\theta_{131} &= \frac{ee}{aa}\theta_{111} + \frac{ff}{aa}\theta_{121} - \frac{gg}{aa}\theta_{131} \\ B\theta_{132} &= \frac{ee}{aa}\theta_{112} + \frac{ff}{aa}\theta_{122} - \frac{gg}{aa}\theta_{132}. \end{aligned}$$

Equation 5.32 is then compared with equation 5.27 in order to find the convergence point of each adaptive parameters, θ_{xxx} . That is,

$$\begin{aligned} \frac{-dd_m}{aa_m} &= -\left(\frac{dd}{aa} + \frac{ee}{aa}\theta_{211} + \frac{ff}{aa}\theta_{221} - \frac{gg}{aa}\theta_{231}\right) \\ \frac{-cc_m}{aa_m} &= -\left(\frac{cc}{aa} + \frac{ee}{aa}\theta_{212} + \frac{ff}{aa}\theta_{222} - \frac{gg}{aa}\theta_{232}\right) \\ \frac{-bb_m}{aa_m} &= -\left(\frac{bb}{aa} + \frac{ee}{aa}\theta_{213} + \frac{ff}{aa}\theta_{223} - \frac{gg}{aa}\theta_{233}\right) . \\ \frac{ee_m}{aa_m} &= \frac{ee}{aa}\theta_{111} + \frac{ff}{aa}\theta_{121} - \frac{gg}{aa}\theta_{131} \\ \frac{ff_m}{aa_m} &= \frac{ee}{aa}\theta_{112} + \frac{ff}{aa}\theta_{122} - \frac{gg}{aa}\theta_{132} \end{aligned} \quad (5.33)$$

Equations 5.33 also imply that in order to completely control the system, 5 adaptive parameters are needed. It can be seen that each equation is composed of three adaptive parameters where only one of them is needed in order to make equations converge. This redundant condition is favorable in a sense that some of the control loops can be cut off where it is not physically possible or difficult to construct.

To find the plant output error similar to equation 5.6, the transfer function between controlled plant output and input in terms of adaptive parameters has to be found similar to equation 5.7, that is,

$$\begin{aligned} \frac{V_{out}}{a_c} &= \frac{y_1}{a_c} \\ &= \frac{(\frac{ec}{aa}\theta_{111} + \frac{ff}{aa}\theta_{121} - \frac{gg}{aa}\theta_{131})p + (\frac{ec}{aa}\theta_{112} + \frac{ff}{aa}\theta_{122} - \frac{gg}{aa}\theta_{132})}{(p^3 + (\frac{bb}{aa} + \frac{ec}{aa}\theta_{213} + \frac{ff}{aa}\theta_{223} - \frac{gg}{aa}\theta_{233})p^2 + (\frac{cc}{aa} + \frac{ec}{aa}\theta_{212} + \frac{ff}{aa}\theta_{222} - \frac{gg}{aa}\theta_{232})p + (\frac{dd}{aa} + \frac{ec}{aa}\theta_{211} + \dots \\ &\quad \dots \frac{ff}{aa}\theta_{221} - \frac{gg}{aa}\theta_{231}))}. \end{aligned} \quad (5.34)$$

While the transfer function between controlled output and input of the referenced model is,

$$\begin{aligned} \frac{V_{outm}}{a_c} &= \frac{y_{1m}}{a_c} \\ &= \frac{(e e_m p + f f_m)}{(a a_m p^3 + b b_m p^2 + c c_m p + d d_m)}. \end{aligned} \quad (5.35)$$

The plant output error is $e = y - y_m$, thus equation 5.34 is subtracted from equation 5.35 giving,

$$\begin{aligned} e &= \frac{[(\frac{ec}{aa}\theta_{111} + \frac{ff}{aa}\theta_{121} - \frac{gg}{aa}\theta_{131})p + (\frac{ec}{aa}\theta_{112} + \frac{ff}{aa}\theta_{122} - \frac{gg}{aa}\theta_{132})]a_c}{(p^3 + (\frac{bb}{aa} + \frac{ec}{aa}\theta_{213} + \frac{ff}{aa}\theta_{223} - \frac{gg}{aa}\theta_{233})p^2 + (\frac{cc}{aa} + \frac{ec}{aa}\theta_{212} + \frac{ff}{aa}\theta_{222} - \frac{gg}{aa}\theta_{232})p + (\frac{dd}{aa} + \frac{ec}{aa}\theta_{211} + \dots \\ &\quad \dots \frac{ff}{aa}\theta_{221} - \frac{gg}{aa}\theta_{231}))} - \frac{(e e_m p + f f_m)a_c}{(a a_m p^3 + b b_m p^2 + c c_m p + d d_m)}. \end{aligned} \quad (5.36)$$

Now, from the gradient rule ($\frac{d\theta_n}{dt} = -\gamma e \frac{\partial e}{\partial \theta_n}$) in equation 5.8, the error gradient for each adaptive parameters ($\frac{\partial e}{\partial \theta_n}$) can be found as,

$$\begin{aligned}
\frac{\partial e}{\partial \theta_{111}} &= \frac{\frac{ee}{aa} p \cdot a_c}{p^3 + \frac{bbm}{aam} p^2 + \frac{ccm}{aam} p + \frac{ddm}{aam}} \\
\frac{\partial e}{\partial \theta_{121}} &= \frac{\frac{ff}{aa} p \cdot a_c}{p^3 + \frac{bbm}{aam} p^2 + \frac{ccm}{aam} p + \frac{ddm}{aam}} * \\
\frac{\partial e}{\partial \theta_{131}} &= - \frac{\frac{gg}{aa} p \cdot a_c}{p^3 + \frac{bbm}{aam} p^2 + \frac{ccm}{aam} p + \frac{ddm}{aam}} \\
\frac{\partial e}{\partial \theta_{112}} &= \frac{\frac{ee}{aa} \cdot a_c}{p^3 + \frac{bbm}{aam} p^2 + \frac{ccm}{aam} p + \frac{ddm}{aam}} \\
\frac{\partial e}{\partial \theta_{122}} &= \frac{\frac{ff}{aa} \cdot a_c}{p^3 + \frac{bbm}{aam} p^2 + \frac{ccm}{aam} p + \frac{ddm}{aam}} * \\
\frac{\partial e}{\partial \theta_{132}} &= - \frac{\frac{gg}{aa} \cdot a_c}{p^3 + \frac{bbm}{aam} p^2 + \frac{ccm}{aam} p + \frac{ddm}{aam}} \\
\frac{\partial e}{\partial \theta_{213}} &= - \frac{\frac{ee}{aa} \cdot p^2 y}{p^3 + \frac{bbm}{aam} p^2 + \frac{ccm}{aam} p + \frac{ddm}{aam}} \\
\frac{\partial e}{\partial \theta_{223}} &= - \frac{\frac{ff}{aa} \cdot p^2 y}{p^3 + \frac{bbm}{aam} p^2 + \frac{ccm}{aam} p + \frac{ddm}{aam}} \cdot \\
\frac{\partial e}{\partial \theta_{233}} &= \frac{\frac{gg}{aa} \cdot p^2 y}{p^3 + \frac{bbm}{aam} p^2 + \frac{ccm}{aam} p + \frac{ddm}{aam}} \\
\frac{\partial e}{\partial \theta_{212}} &= - \frac{\frac{ee}{aa} \cdot py}{p^3 + \frac{bbm}{aam} p^2 + \frac{ccm}{aam} p + \frac{ddm}{aam}} \\
\frac{\partial e}{\partial \theta_{222}} &= - \frac{\frac{ff}{aa} \cdot py}{p^3 + \frac{bbm}{aam} p^2 + \frac{ccm}{aam} p + \frac{ddm}{aam}} \\
\frac{\partial e}{\partial \theta_{232}} &= \frac{\frac{gg}{aa} \cdot py}{p^3 + \frac{bbm}{aam} p^2 + \frac{ccm}{aam} p + \frac{ddm}{aam}} \\
\frac{\partial e}{\partial \theta_{211}} &= - \frac{\frac{ee}{aa} \cdot y}{p^3 + \frac{bbm}{aam} p^2 + \frac{ccm}{aam} p + \frac{ddm}{aam}} \\
\frac{\partial e}{\partial \theta_{221}} &= - \frac{\frac{ff}{aa} \cdot y}{p^3 + \frac{bbm}{aam} p^2 + \frac{ccm}{aam} p + \frac{ddm}{aam}} \\
\frac{\partial e}{\partial \theta_{231}} &= \frac{\frac{gg}{aa} \cdot y}{p^3 + \frac{bbm}{aam} p^2 + \frac{ccm}{aam} p + \frac{ddm}{aam}}
\end{aligned} \tag{5.37}$$

The error gradients in equation 5.37 are then put into the gradient law to create a differential equation for each adaptive parameter. This results in,

$$\begin{aligned}
\frac{d\theta_{111}}{dt} &= -\gamma_{111}e\left(\frac{\frac{ee}{aa}p \cdot a_c}{p^3 + \frac{bbm}{aam}p^2 + \frac{ccm}{aam}p + \frac{ddm}{aam}}\right) \\
\frac{d\theta_{121}}{dt} &= -\gamma_{121}e\left(\frac{\frac{ff}{aa}p \cdot a_c}{p^3 + \frac{bbm}{aam}p^2 + \frac{ccm}{aam}p + \frac{ddm}{aam}}\right) \\
\frac{d\theta_{131}}{dt} &= \gamma_{131}e\left(\frac{\frac{gg}{aa}p \cdot a_c}{p^3 + \frac{bbm}{aam}p^2 + \frac{ccm}{aam}p + \frac{ddm}{aam}}\right)^* \\
\frac{d\theta_{112}}{dt} &= -\gamma_{112}e\left(\frac{\frac{ee}{aa} \cdot a_c}{p^3 + \frac{bbm}{aam}p^2 + \frac{ccm}{aam}p + \frac{ddm}{aam}}\right) \\
\frac{d\theta_{122}}{dt} &= -\gamma_{122}e\left(\frac{\frac{ff}{aa} \cdot a_c}{p^3 + \frac{bbm}{aam}p^2 + \frac{ccm}{aam}p + \frac{ddm}{aam}}\right) \\
\frac{d\theta_{132}}{dt} &= \gamma_{132}e\left(\frac{\frac{gg}{aa} \cdot a_c}{p^3 + \frac{bbm}{aam}p^2 + \frac{ccm}{aam}p + \frac{ddm}{aam}}\right)^* \\
\frac{d\theta_{213}}{dt} &= \gamma_{213}e\left(\frac{\frac{ee}{aa} \cdot p^2 y}{p^3 + \frac{bbm}{aam}p^2 + \frac{ccm}{aam}p + \frac{ddm}{aam}}\right) \\
\frac{d\theta_{223}}{dt} &= \gamma_{223}e\left(\frac{\frac{ff}{aa} \cdot p^2 y}{p^3 + \frac{bbm}{aam}p^2 + \frac{ccm}{aam}p + \frac{ddm}{aam}}\right) , \\
\frac{d\theta_{233}}{dt} &= -\gamma_{233}e\left(\frac{\frac{gg}{aa} \cdot p^2 y}{p^3 + \frac{bbm}{aam}p^2 + \frac{ccm}{aam}p + \frac{ddm}{aam}}\right)^* \\
\frac{d\theta_{212}}{dt} &= \gamma_{212}e\left(\frac{\frac{ee}{aa} \cdot py}{p^3 + \frac{bbm}{aam}p^2 + \frac{ccm}{aam}p + \frac{ddm}{aam}}\right) \\
\frac{d\theta_{222}}{dt} &= \gamma_{222}e\left(\frac{\frac{ff}{aa} \cdot py}{p^3 + \frac{bbm}{aam}p^2 + \frac{ccm}{aam}p + \frac{ddm}{aam}}\right) \\
\frac{d\theta_{232}}{dt} &= -\gamma_{232}e\left(\frac{\frac{gg}{aa} \cdot py}{p^3 + \frac{bbm}{aam}p^2 + \frac{ccm}{aam}p + \frac{ddm}{aam}}\right)^* \\
\frac{d\theta_{211}}{dt} &= \gamma_{211}e\left(\frac{\frac{ee}{aa} \cdot y}{p^3 + \frac{bbm}{aam}p^2 + \frac{ccm}{aam}p + \frac{ddm}{aam}}\right) \\
\frac{d\theta_{221}}{dt} &= \gamma_{221}e\left(\frac{\frac{ff}{aa} \cdot y}{p^3 + \frac{bbm}{aam}p^2 + \frac{ccm}{aam}p + \frac{ddm}{aam}}\right) \\
\frac{d\theta_{231}}{dt} &= -\gamma_{231}e\left(\frac{\frac{gg}{aa} \cdot y}{p^3 + \frac{bbm}{aam}p^2 + \frac{ccm}{aam}p + \frac{ddm}{aam}}\right)^*
\end{aligned} \tag{5.38}$$

where equations with superscript * are equations that will be considered for indirect and limited control, since all the signals are not physically possible to obtain. These noted equations are exactly five in number, as discussed previously that at least five adaptive parameters are needed to achieve a complete control of the system.

Using the gradient results in equation 5.38 with the adaptive control law in equation 5.31, the MRAC system block diagram for the case that all parameters are physically possible to obtain and control is composed as in Figure 5.6.

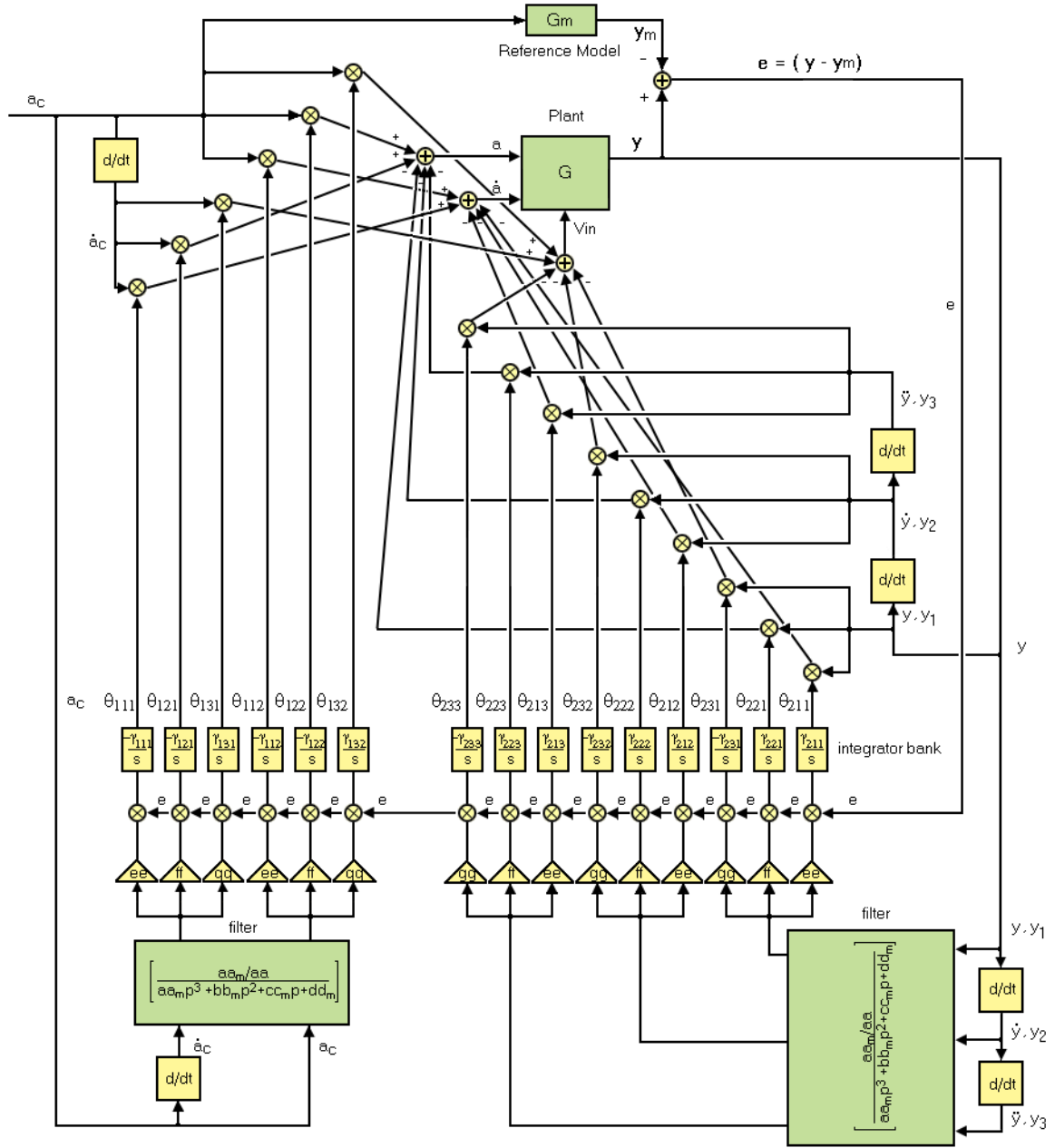


Figure 5.6: Block diagram of MRAC system using MIT gradient method for the case that all parameters are physically possible to control (Full parameter control).

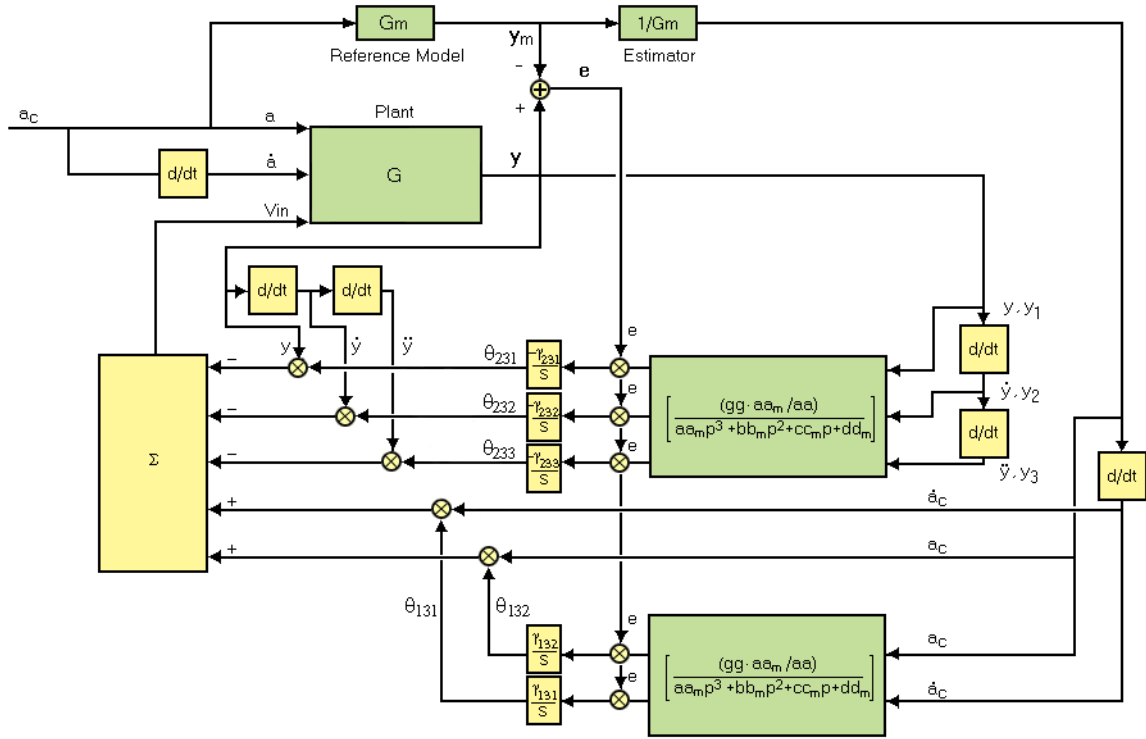


Figure 5.7: Block diagram of MRAC system using MIT gradient method for the case that the control of acceleration is not possible.

Now consider another case where the controller does not have full control over the input. In the accelerometer under development, input acceleration will always affect sensor structure directly. Thus, there is no way to put any kind of controller between the input and the plant unless the controller includes a mechanical system. However approximation of the acceleration can be made using estimator which sends an estimated version of acceleration to the adaptive controller. Because the controller is part of feedback loop, it can be called an indirect controller. The block diagram illustrating this particular condition is shown in Figure 5.7.

As discussed previously, a stability improvement can be introduced into gra-

dient rule by using normalized gradient rule as in equation 5.14, which is stated as $\frac{d\theta}{dt} = \frac{\gamma \varphi e}{\alpha + \varphi^T \varphi}$. Considering the case that full control of all parameters are not possible, as shown in Figure 5.7, adaptive parameters of interest are θ_{131} , θ_{132} , θ_{231} , θ_{232} , and θ_{233} . Substituting results from equation 5.37 (which have superscript *) into equation 5.14 gives,

$$\begin{aligned}
\frac{d\theta_{131}}{dt} &= \frac{\gamma_{131} \cdot e(aa_m p^3 + bb_m p^2 + cc_m p + dd_m) \cdot [(\frac{aa_m \cdot gg}{aa})p \cdot a_c]}{\alpha_{131}(aa_m p^3 + bb_m p^2 + cc_m p + dd_m)^2 + (\frac{aa_m \cdot gg}{aa})^2 p^2 \cdot a_c^2} \\
\frac{d\theta_{132}}{dt} &= \frac{\gamma_{132} \cdot e(aa_m p^3 + bb_m p^2 + cc_m p + dd_m) \cdot [(\frac{aa_m \cdot gg}{aa}) \cdot a_c]}{\alpha_{132}(aa_m p^3 + bb_m p^2 + cc_m p + dd_m)^2 + (\frac{aa_m \cdot gg}{aa})^2 \cdot a_c^2} \\
\frac{d\theta_{233}}{dt} &= -\frac{\gamma_{233} \cdot e(aa_m p^3 + bb_m p^2 + cc_m p + dd_m) \cdot [(\frac{aa_m \cdot gg}{aa})p^2 \cdot y]}{\alpha_{233}(aa_m p^3 + bb_m p^2 + cc_m p + dd_m)^2 + (\frac{aa_m \cdot gg}{aa})^2 (p^2 \cdot y)^2} \\
\frac{d\theta_{232}}{dt} &= -\frac{\gamma_{232} \cdot e(aa_m p^3 + bb_m p^2 + cc_m p + dd_m) \cdot [(\frac{aa_m \cdot gg}{aa})p \cdot y]}{\alpha_{232}(aa_m p^3 + bb_m p^2 + cc_m p + dd_m)^2 + (\frac{aa_m \cdot gg}{aa})^2 (p \cdot y)^2} \\
\frac{d\theta_{231}}{dt} &= -\frac{\gamma_{231} \cdot e(aa_m p^3 + bb_m p^2 + cc_m p + dd_m) \cdot [(\frac{aa_m \cdot gg}{aa}) \cdot y]}{\alpha_{231}(aa_m p^3 + bb_m p^2 + cc_m p + dd_m)^2 + (\frac{aa_m \cdot gg}{aa})^2 \cdot y^2}
\end{aligned} \tag{5.39}$$

It can be seen that equation 5.39 provides adaptive loops that are far more complicated than those from the original gradient rule in equation 5.38. Specifically, it can be seen that the adaptive loops in the original gradient rule use the same static filter structure, but the adaptive loops in the normalized rule form use a different filter structure that are also changed according to plant's input and output. Although the stability in the normalized case is more or less guaranteed, the control system physical circuit will be difficult to implement because no loops repeat.

5.3.5 A discussion on adaptive parameter reduction

Previously, an adaptive control block diagram derived from the MIT gradient law took the form in Figure 5.6, and inaccessible adaptive parameters, θ_s , and their associated feedback loop were simply cut off. This resulted in the much simpler adaptive control system in Figure 5.7. However, this does not necessarily mean that the controlled system can always be reduced by cutting off loops that are impossible to build. A closer look into adaptive algorithm constructed should clarify when or if the system can be reduced in this manner.

First, consider a simple first order system (which will make all equations previously discussed scalar). For gradient approach, the plant output error, e , from equation 5.6 is a difference between plant output (from equation 5.7) and reference model output (from equation 5.8) which results in $e = \frac{B\theta_1}{p-A+B\theta_2}u_c - \frac{B_m}{p-A_m+B_m}u_c$. It can be seen that in order to drive the error to zero, both θ_1 and θ_2 are required to change or adapt. That is, θ_1 should converge to $\frac{B_m}{B}$ and θ_2 should converge to $\frac{B_m-A_m+A}{B}$. Therefore none of the feedback loops can be cut off. For the Lyapunov approach, the equation for consideration is the rate of plant output error equation. From equation 5.15, the rate of error is $\dot{e} = A_me + (A-A_m-B\theta_2) \cdot y + (B\theta_1-B_m) \cdot u_c$. in order to make the rate of error approach zero (or make it a first order differential equation), the second and third term on the right side must be zero, which is the same convergence condition as in gradient approach ($\theta_1 \Rightarrow \frac{B_m}{B}$ and $\theta_2 \Rightarrow \frac{B_m-A_m+A}{B}$). This, again, also means that neither loop can be cut off.

Next, consider the real plant under development which has a characteristic transfer function of third order. For gradient method, the error equation 5.36, has two terms on the right side. To make this error equation go to zero, both terms must match exactly. It can be easily seen that there is some freedom to choose adaptive parameters. For example, one of θ_{111} , θ_{121} , and θ_{131} can be chosen, one of θ_{112} , θ_{122} , and θ_{132} can be chosen, and so on in each term. There are 15 adaptive parameters for the control system, and one can be picked for each three parameters, so only five parameters are actually needed.

In conclusion, this discussion can be summarize in a simple formula for checking if the system can be reduced as,

$$Red = (n \cdot i + n^2) - (n + i), \quad (5.40)$$

where, n is the order of the system, i is number of input, and Red is the number of redundant parameters that can be eliminated. It can be seen that for the first

order SISO system Red is 0, but for the plant under study that is third order with two inputs, Red is 10. This means that ten parameters can cut off.

Another issue that might arise is whether the plant will converge to the reference model after a control loop has simply been cut off without other modification. To address this issue, the gradient method is reworked under reduced condition. Thus a reduced version of 5.36 is,

$$e = \frac{[(-\frac{gg}{aa}\theta_{131})p + (-\frac{gg}{aa}\theta_{132})]a_c}{(p^3 + (\frac{bb}{aa} - \frac{gg}{aa}\theta_{233})p^2 + (\frac{cc}{aa} - \frac{gg}{aa}\theta_{232})p + (\frac{dd}{aa} - \frac{gg}{aa}\theta_{231}))} - \frac{(ee_m p + ff_m)a_c}{(aa_m p^3 + bb_m p^2 + cc_m p + dd_m)}.$$

Similar to the convergence condition of equation 5.33, the new condition is obtain as,

$$\begin{aligned} \frac{-dd_m}{aa_m} &= -\frac{dd}{aa} + \frac{gg}{aa}\theta_{231} \\ \frac{-cc_m}{aa_m} &= -\frac{cc}{aa} + \frac{gg}{aa}\theta_{232} \\ \frac{-bb_m}{aa_m} &= -\frac{bb}{aa} + \frac{gg}{aa}\theta_{233} \\ \frac{ee_m}{aa_m} &= -\frac{gg}{aa}\theta_{131} \\ \frac{ff_m}{aa_m} &= -\frac{gg}{aa}\theta_{132} \end{aligned}.$$

Applying the gradient rule for the new plant output error,

$$\begin{aligned} \frac{d\theta_{131}}{dt} &= \gamma_{131} e \left(\frac{\frac{gg}{aa} p \cdot a_c}{p^3 + \frac{bb_m}{aa_m} p^2 + \frac{cc_m}{aa_m} p + \frac{dd_m}{aa_m}} \right) \\ \frac{d\theta_{132}}{dt} &= \gamma_{132} e \left(\frac{\frac{gg}{aa} a_c}{p^3 + \frac{bb_m}{aa_m} p^2 + \frac{cc_m}{aa_m} p + \frac{dd_m}{aa_m}} \right) \\ \frac{d\theta_{233}}{dt} &= -\gamma_{233} e \left(\frac{\frac{gg}{aa} p^2 y}{p^3 + \frac{bb_m}{aa_m} p^2 + \frac{cc_m}{aa_m} p + \frac{dd_m}{aa_m}} \right), \\ \frac{d\theta_{232}}{dt} &= -\gamma_{232} e \left(\frac{\frac{gg}{aa} p y}{p^3 + \frac{bb_m}{aa_m} p^2 + \frac{cc_m}{aa_m} p + \frac{dd_m}{aa_m}} \right) \\ \frac{d\theta_{231}}{dt} &= -\gamma_{231} e \left(\frac{\frac{gg}{aa} y}{p^3 + \frac{bb_m}{aa_m} p^2 + \frac{cc_m}{aa_m} p + \frac{dd_m}{aa_m}} \right) \end{aligned}$$

which is exactly the same result as in equation 5.38. Therefore, it can be concluded here that the adaptive control algorithm will still converge even if the unnecessary loops have been removed, and there is no need to recalculate the convergence condition.

5.3.6 Lyapunov rule adaptive controller

Following steps discussed previously, the rate of change in plant output error ($\dot{e} = \dot{y} - \dot{y}_m$) in explicit form can be found, similar to equation 5.15 as,

$$\begin{bmatrix} \dot{e}_1 \\ \dot{e}_2 \\ \dot{e}_3 \end{bmatrix} = \begin{bmatrix} 0 & 1 & 0 \\ 0 & 0 & 1 \\ \frac{-dd_m}{aa_m} & \frac{-cc_m}{aa_m} & \frac{-bb_m}{aa_m} \end{bmatrix} \cdot \begin{bmatrix} e_1 \\ e_2 \\ e_3 \end{bmatrix} + \begin{bmatrix} 0 \\ 0 \\ \frac{dd_m}{aa_m} - \frac{dd}{aa} - \frac{ee}{aa}\theta_{211} - \frac{ff}{aa}\theta_{221} + \frac{gg}{aa}\theta_{231} \\ 0 \\ 0 \\ \frac{cc_m}{aa_m} - \frac{cc}{aa} - \frac{ee}{aa}\theta_{212} - \frac{ff}{aa}\theta_{222} + \frac{gg}{aa}\theta_{232} \quad \frac{bb_m}{aa_m} - \frac{bb}{aa} - \frac{ee}{aa}\theta_{213} - \frac{ff}{aa}\theta_{223} + \frac{gg}{aa}\theta_{233} \end{bmatrix} \begin{bmatrix} y_1 \\ y_2 \\ y_3 \end{bmatrix} \\ + \begin{bmatrix} 0 \\ 0 \\ \frac{ee}{aa}\theta_{111} + \frac{ff}{aa}\theta_{121} - \frac{gg}{aa}\theta_{131} - \frac{ee_m}{aa_m} \quad \frac{ee}{aa}\theta_{112} + \frac{ff}{aa}\theta_{122} - \frac{gg}{aa}\theta_{132} - \frac{ff_m}{aa_m} \end{bmatrix} \begin{bmatrix} \dot{a}_c \\ \dot{a}_c \end{bmatrix},$$

where the first term in above equation comes from $[A_m \cdot e]$ which is dependent on the plant output error, e , the second term comes from $[A - A_m - B\theta_2]$ which is dependent on adaptive parameter, θ_2 , and the last term comes from $[B\theta_1 - B_m]$, which is dependent on adaptive parameter, θ_1 .

The next step is to find a relationship between matrices \underline{P} and \underline{Q} as discussed by Lyapunov theory in equation 5.16 which gives,

$$\begin{bmatrix} 0 & 1 & 0 \\ 0 & 0 & 1 \\ \frac{-dd_m}{aa_m} & \frac{-cc_m}{aa_m} & \frac{-bb_m}{aa_m} \end{bmatrix}^T \begin{bmatrix} P_{11} & P_{12} & P_{13} \\ P_{12} & P_{22} & P_{23} \\ P_{13} & P_{23} & P_{33} \end{bmatrix} + \begin{bmatrix} P_{11} & P_{12} & P_{13} \\ P_{12} & P_{22} & P_{23} \\ P_{13} & P_{23} & P_{33} \end{bmatrix} \begin{bmatrix} 0 & 1 & 0 \\ 0 & 0 & 1 \\ \frac{-dd_m}{aa_m} & \frac{-cc_m}{aa_m} & \frac{-bb_m}{aa_m} \end{bmatrix} \\ = - \begin{bmatrix} Q_1 & 0 & 0 \\ 0 & Q_2 & 0 \\ 0 & 0 & Q_3 \end{bmatrix}.$$

This leads to six linear equations with six unknowns in P_{xx} in relation to Q_x as,

$$\begin{bmatrix} 0 & 0 & -2\frac{dd_m}{aa_m} & 0 & 0 & 0 \\ 1 & 0 & -\frac{cc_m}{aa_m} & 0 & -\frac{dd_m}{aa_m} & 0 \\ 0 & 1 & -\frac{bb_m}{aa_m} & 0 & 0 & -\frac{dd_m}{aa_m} \\ 0 & 2 & 0 & 0 & -2\frac{cc_m}{aa_m} & 0 \\ 0 & 0 & 1 & 1 & -\frac{bb_m}{aa_m} & -\frac{cc_m}{aa_m} \\ 0 & 0 & 0 & 0 & 2 & -2\frac{bb_m}{aa_m} \end{bmatrix} \begin{bmatrix} P_{11} \\ P_{12} \\ P_{13} \\ P_{22} \\ P_{23} \\ P_{33} \end{bmatrix} = \begin{bmatrix} -Q_1 \\ 0 \\ 0 \\ -Q_2 \\ 0 \\ -Q_3 \end{bmatrix}.$$

Applying Cramer's rule with the above matrix to find P_{xx} in terms of Q_x , where the determinant of the left side is $8\frac{dd_m}{aa_m}(bb_mcc_m - dd_maa_m)$, the result is,

$$\begin{aligned}
P_{11} &= \frac{bb_mcc_m^2Q_1 - dd_mcc_maa_mQ_1 + bb_m^2dd_mQ_1 + bb_mdd_m^2Q_2 + dd_m^3Q_3}{2dd_m(bb_mcc_m - dd_maa_m)} \\
P_{12} &= \frac{dd_m^2aa_mQ_2 + cc_mdd_m^2Q_3 + bb_m^2cc_mQ_1}{2dd_m(bb_mcc_m - dd_maa_m)} \\
P_{13} &= \frac{aa_mQ_1}{2dd_m} \\
P_{22} &= \frac{dd_maa_m^2Q_1 + cc_mdd_maa_mQ_2 + bb_m^3Q_1 + bb_m^2dd_mQ_2 + dd_m^2bb_mQ_3 + cc_m^2dd_mQ_3}{2dd_m(bb_mcc_m - dd_maa_m)} \\
P_{23} &= \frac{aa_m(bb_m^2Q_1 + bb_mdd_mQ_2 + dd_m^2Q_3)}{2dd_m(bb_mcc_m - dd_maa_m)} \\
P_{33} &= \frac{aa_m(aa_mbb_mQ_1 + aa_mdd_mQ_2 + cc_mdd_mQ_3)}{2dd_m(bb_mcc_m - dd_maa_m)}
\end{aligned} \quad (5.41)$$

where, elements in matrix Q , which are Q_1 , Q_2 , and Q_3 , are often assumed to be positive integer for simplicity. Referring to equation 5.17, the Lyapunov function can be obtained in quadratic positive definite form similar to amount of energy stored in the system (considering limited case where only θ_{131} , θ_{132} , θ_{231} , θ_{232} , and θ_{233} are accessible) as,

$$\begin{aligned}
V(e, \theta) &= \frac{1}{2}\gamma(P_{11}e_1^2 + P_{12}e_1e_2 + P_{13}e_1e_3 + P_{12}e_1e_2 + P_{22}e_2^2 + P_{23}e_2e_3 \\
&\quad + P_{13}e_1e_3 + P_{23}e_2e_3 + P_{33}e_3^2) + \frac{1}{2}\left(\frac{dd_m}{aa_m} - \frac{dd}{aa} + \frac{gg}{aa}\theta_{231}\right)^2 \\
&\quad + \frac{1}{2}\left(\frac{cc_m}{aa_m} - \frac{cc}{aa} + \frac{gg}{aa}\theta_{232}\right)^2 + \frac{1}{2}\left(\frac{bb_m}{aa_m} - \frac{bb}{aa} + \frac{gg}{aa}\theta_{233}\right)^2 \\
&\quad + \frac{1}{2}\left(-\frac{gg}{aa}\theta_{131} - \frac{ee_m}{aa_m}\right)^2 + \frac{1}{2}\left(-\frac{gg}{aa}\theta_{132} - \frac{ff_m}{aa_m}\right)^2
\end{aligned} \quad (5.42)$$

Similar to equation 5.18, the time derivative of Lyapunov function (\dot{V}) of equation 5.42 is $\frac{dV}{dt} = -\frac{\gamma}{2}e^TQe + tr\{[A - A_m - B\theta_2]^T(\gamma P e y^T + \frac{d}{dt}[A - A_m - B\theta_2])\} + tr\{[B\theta_1 - B_m]^T(\gamma P e u_c^T + \frac{d}{dt}[B\theta_1 - B_m])\}$, where the elements are,

$$-\frac{\gamma}{2}e^TQe = -\frac{\gamma}{2}Q_1e_1^2 - \frac{\gamma}{2}Q_2e_2^2 - \frac{\gamma}{2}Q_3e_3^2, \quad (5.43)$$

$$\begin{aligned}
\gamma P e y^T &= \begin{bmatrix} \gamma(P_{11}e_1 + P_{12}e_2 + P_{13}e_3)y_1 & \gamma(P_{11}e_1 + P_{12}e_2 + P_{13}e_3)y_2 \\ \gamma(P_{12}e_1 + P_{22}e_2 + P_{23}e_3)y_1 & \gamma(P_{12}e_1 + P_{22}e_2 + P_{23}e_3)y_2 \\ \gamma(P_{13}e_1 + P_{23}e_2 + P_{33}e_3)y_1 & \gamma(P_{13}e_1 + P_{23}e_2 + P_{33}e_3)y_2 \\ \gamma(P_{11}e_1 + P_{12}e_2 + P_{13}e_3)y_3 \\ \gamma(P_{12}e_1 + P_{22}e_2 + P_{23}e_3)y_3 \\ \gamma(P_{13}e_1 + P_{23}e_2 + P_{33}e_3)y_3 \end{bmatrix}, \quad (5.44)
\end{aligned}$$

$$\gamma Peu_c^T = \begin{bmatrix} \gamma(P_{11}e_1 + P_{12}e_2 + P_{13}e_3)\dot{a}_c & \gamma(P_{11}e_1 + P_{12}e_2 + P_{13}e_3)a_c \\ \gamma(P_{12}e_1 + P_{22}e_2 + P_{23}e_3)\dot{a}_c & \gamma(P_{12}e_1 + P_{22}e_2 + P_{23}e_3)a_c \\ \gamma(P_{13}e_1 + P_{23}e_2 + P_{33}e_3)\dot{a}_c & \gamma(P_{13}e_1 + P_{23}e_2 + P_{33}e_3)a_c \end{bmatrix}, \quad (5.45)$$

$$\frac{d}{dt}[A - A_m - B\theta_2] = \begin{bmatrix} 0 & 0 & 0 \\ 0 & 0 & 0 \\ \frac{gg}{aa} \frac{d\theta_{231}}{dt} & \frac{gg}{aa} \frac{d\theta_{232}}{dt} & \frac{gg}{aa} \frac{d\theta_{233}}{dt} \end{bmatrix}, \quad (5.46)$$

and,

$$\frac{d}{dt}[B\theta_1 - B_m] = \begin{bmatrix} 0 & 0 \\ 0 & 0 \\ -\frac{gg}{aa} \frac{d\theta_{131}}{dt} & -\frac{gg}{aa} \frac{d\theta_{132}}{dt} \end{bmatrix}. \quad (5.47)$$

To drive equation 5.18 to negative definite form, consider that equation 5.43 is already negative, and the terms $\gamma Pe y^T + \frac{d}{dt}[A - A_m - B\theta_2]$ and $\gamma Pe u_c^T + \frac{d}{dt}[B\theta_1 - B_m]$ both have to be driven to zero. Equate equations 5.44 with 5.46 and equation 5.45 with 5.47 which results in,

$$\begin{aligned} \frac{d\theta_{231}}{dt} &= -\gamma \frac{aa}{gg} (P_{13}e_1 + P_{23}e_2 + P_{33}e_3)y_1 \\ \frac{d\theta_{232}}{dt} &= -\gamma \frac{aa}{gg} (P_{13}e_1 + P_{23}e_2 + P_{33}e_3)y_2 \\ \frac{d\theta_{233}}{dt} &= -\gamma \frac{aa}{gg} (P_{13}e_1 + P_{23}e_2 + P_{33}e_3)y_3 \\ \frac{d\theta_{131}}{dt} &= \gamma \frac{aa}{gg} (P_{13}e_1 + P_{23}e_2 + P_{33}e_3)\dot{a}_c \\ \frac{d\theta_{132}}{dt} &= \gamma \frac{aa}{gg} (P_{13}e_1 + P_{23}e_2 + P_{33}e_3)a_c \end{aligned}$$

Using relations given previously as $e_1 = e$, $e_2 = pe_1 = pe$, $e_3 = pe_2 = p^2e$, $y_1 = y$, $y_2 = py_1 = py$, and $y_3 = py_2 = p^2y$, the adaptive law can be found as,

$$\begin{aligned} \frac{d\theta_{231}}{dt} &= -\gamma_{231} \{(P_{13} + P_{23}p + P_{33}p^2)e\} \{y\} \\ \frac{d\theta_{232}}{dt} &= -\gamma_{232} \{(P_{13} + P_{23}p + P_{33}p^2)e\} \{py\} \\ \frac{d\theta_{233}}{dt} &= -\gamma_{233} \{(P_{13} + P_{23}p + P_{33}p^2)e\} \{p^2y\}, \\ \frac{d\theta_{131}}{dt} &= \gamma_{131} \{(P_{13} + P_{23}p + P_{33}p^2)e\} \{pa_c\} \\ \frac{d\theta_{132}}{dt} &= \gamma_{132} \{(P_{13} + P_{23}p + P_{33}p^2)e\} \{a_c\} \end{aligned} \quad (5.48)$$

where γ_{xxx} are adaptive loop gains which can be adjusted independently and come from $\gamma \cdot aa/gg$ in each adaptive law. It can also be seen that the parameter adaptation laws in equation 5.48 are a lot less complicated than in equation 5.39 and 5.38. Specifically, adaptation parameters in 5.48 result from the integral of the gain of the

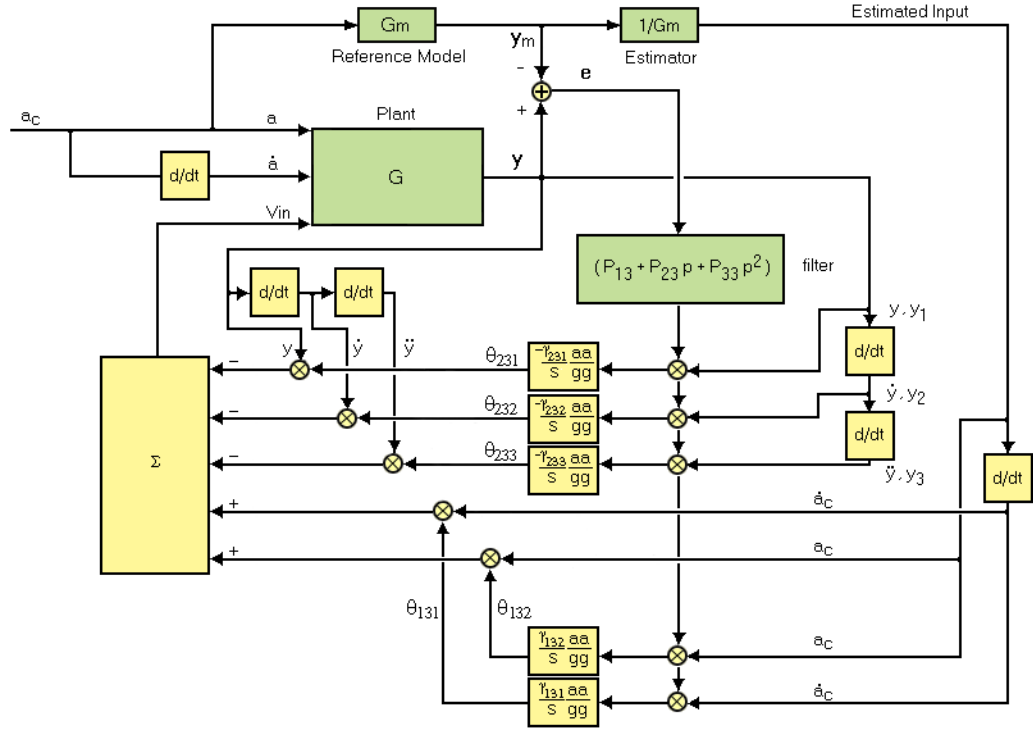


Figure 5.8: Block diagram of MRAC system using Lyapunov stability method for the case that control of acceleration is not possible.

product between filtered plant output error and either plant output or estimated input. While the filtered signal of plant output error are identical in every loop, they significantly reduce the controller structure. The block diagram of the MRAC using Lyapunov stability law is shown in Figure 5.8.

5.4 Simulations

Similar to previous chapters, simulation block diagram models are constructed in the same form as in the bond graphs and models shown earlier. The characteristic of the reference model for each case are in a data file which can be

called by a simulation file as needed.

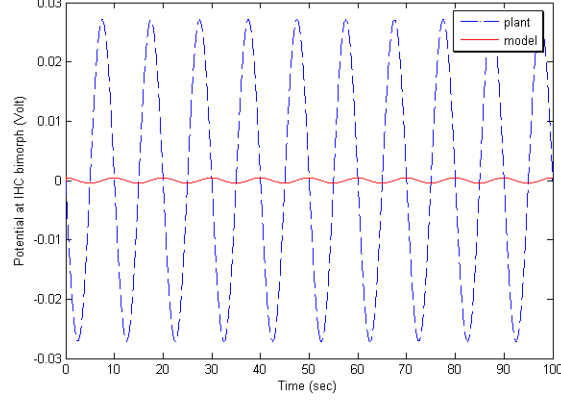


Figure 5.9: Time domain response comparison between the uncontrolled sensor and reference model for 0.1 G and 0.1 Hz sinusoidal acceleration input

The response of the uncontrolled sensor in comparison with the desired reference model in both time and frequency domain is shown in figure 5.9 and 5.10. In time domain response, the system is excited by a sinusoidal acceleration with peak of 0.1 g at a frequency 0.1 Hz. The physical parameters of the sensor used in these simulations are the values estimated for prototype modeling, which will be discussed in more detail in the next chapter. The reference model parameters are then chosen to have the same resonant frequency (220 Hz) and roughly the same resonant peak (8.15 dB).

Because the gain in the frequency response characteristic of the plant and reference model at this frequency are an almost forty decibel difference, it is understandable that the time domain response magnitude comparison between the sensor and desired reference model are almost two order of magnitude differ. This uncontrolled simulation will be used as benchmark reference for easy comparison between different controller rules.

There are two reasons to use low frequency excitations for simulations in

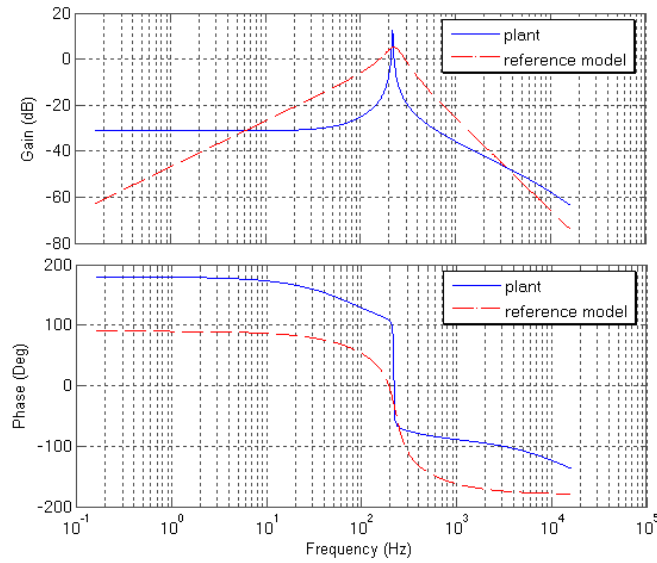


Figure 5.10: Frequency response comparison between the uncontrolled sensor and reference model

this section. First, the magnitude difference between the plant (sensor) and the desired plant (reference model) are far apart at low frequency and that makes it easier to clearly see adaptation in progress. Second, lower frequency usually has less signal variation which makes the ODE solvers run faster/smoothen in the simulation. This is important in this particular case because the control system can have higher number of state variables (i.e. full/unreduced MIT gradient controller has approximately 50 state variables) and in the case that there are differentiator in the controller.

As a demonstration of the method of adaptive control, a simulation on full parameter MIT gradient rule has been performed using all adaptive laws from equation 5.38, and controller diagram as shown in figure 5.6. Each adaptive loop's gains, γ_{xx} , are usually independently chosen after the first successful simulation to “tune” the response. They are set at higher value for faster adaptation and at lower value

for slower adaptation in each loop. However for this demonstration case, all the gains are set to be equally at ten.

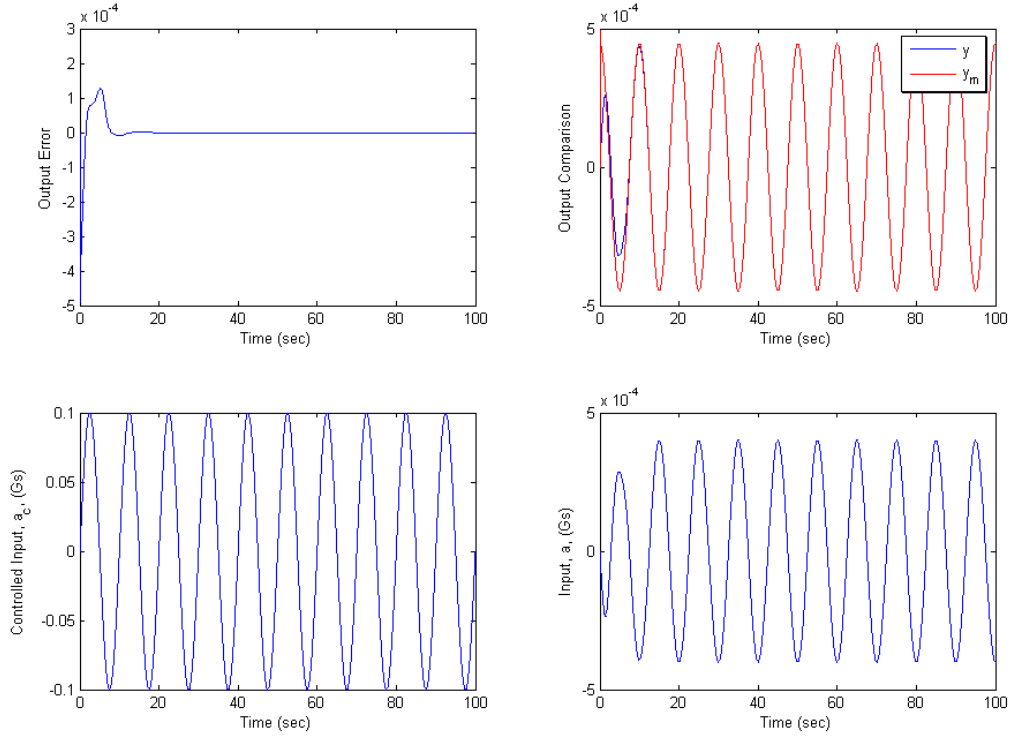


Figure 5.11: Simulation results for the sensor system with full parameter MIT gradient rule controller

The simulation result of full parameter MIT gradient is shown in figure 5.11. The top left section of the figure shows the plant output error, which is the difference between the plant and desired model potential output. The the top right section shows the actual potential output of the sensor (y) in comparison with reference model output (y_m). Thus, when the error on top left section approaches zero, the plant (sensor) is successfully adapted and the output potential of the sensor on the top right section matches that of reference model perfectly. The bottom left shows that an acceleration input and the bottom right part shows that an effective

acceleration goes into the sensor. The figure also shows in this case that successful adaptation occurs approximately after 30 seconds.

Following steps similar to controller synthesis section, indirect/limited control case for MIT gradient rules is now considered. Again, the adaptive laws used are those with superscript * in equation 5.38 and the controller diagram used is from figure 5.7.

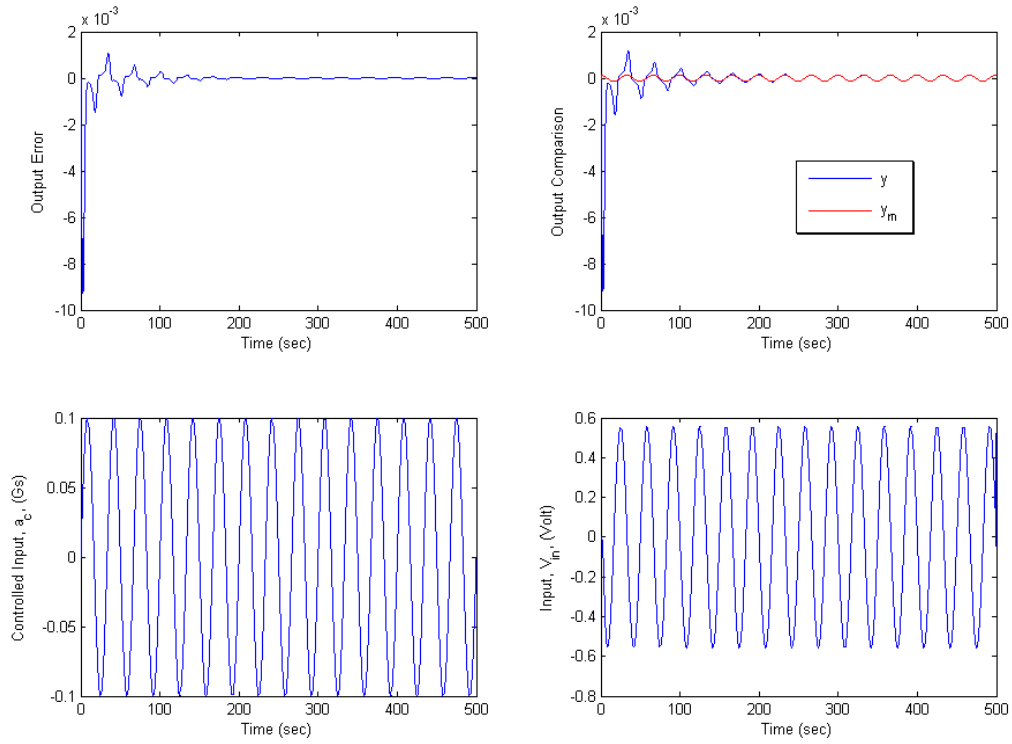


Figure 5.12: Simulation results for the sensor system with limited controllable parameters MIT gradient rule controller

Figure 5.12 shows simulation results for a case similar to the previous one. The difference is that the bottom right of figure 5.12 shows a potential input to the actuator section of the plant. At acceleration input of 0.1 G, 0.03 Hz, and gain of ten, the sensor is fully adapted after approximately 250 seconds. This slow

adaptation time is due to low loop gains which can be adjusted, however, increasing gains in loops usually results in an amplification of noise.

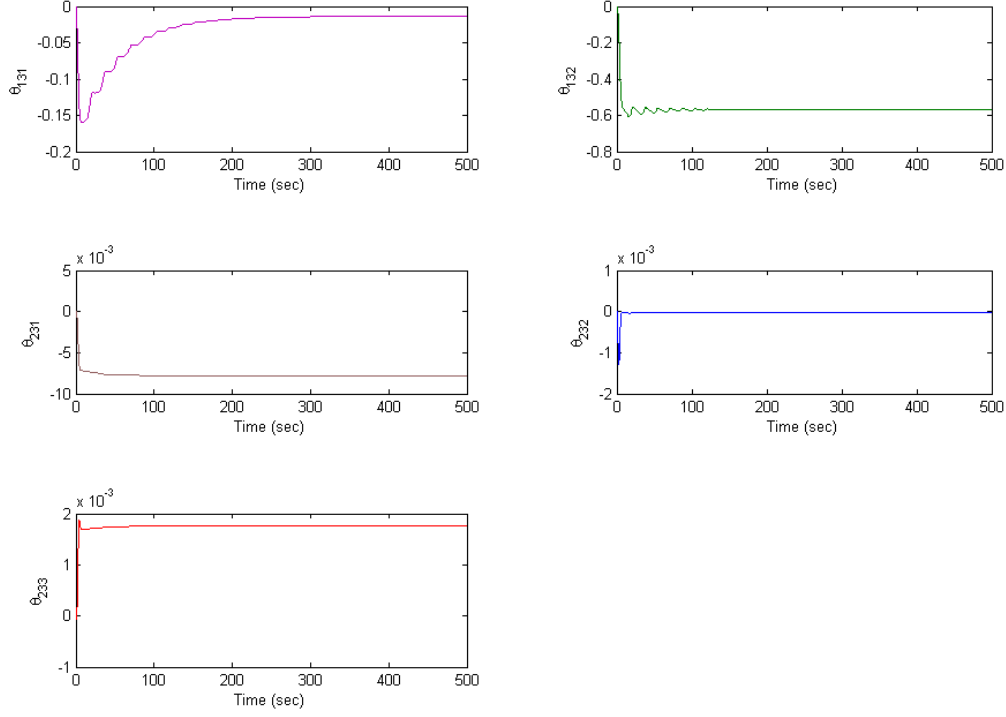


Figure 5.13: Adaptive controller parameters of the sensor system with limited controllable parameter MIT gradient rule controller

Comparison of the upper right plot of figures 5.12 and figure 5.11 reveals a unique characteristic for the limited controllable parameter case. In the full controllable parameter case, the controller is positioned between the input and the plant (sensor), while in limited controllable parameter case, the controller is positioned essentially in the feedback loop. While full controllable parameter case tries to bring the response of the system from complete resting state, the limited controllable parameter case tries to bring back the response of the system already affected by input. This is one of reasons that adaptation time of figure 5.12 is slower than that of figure

5.11.

Figure 5.13 shows each adaptive controller parameter, θ_{xxx} , dynamics. It can be seen that with the same loop gain, θ_{131} takes the longest to reach its final value compared to all other parameters. Thus, it is responsible for the slow adaptation response of the controller. Increasing loop gain γ_{131} in θ_{131} loop will make entire system adapt faster. For information, the final value for each parameters are $\theta_{131} = -13.8$ millivolt, $\theta_{132} = -566.7$ millivolt, $\theta_{231} = -7.8$ millivolt, $\theta_{232} = -0.016644$ millivolt, and $\theta_{233} = -1.8$ millivolt. These values make physical sense because they stay in the limit of analog controller's op-amp saturation potential (12-15 volt).

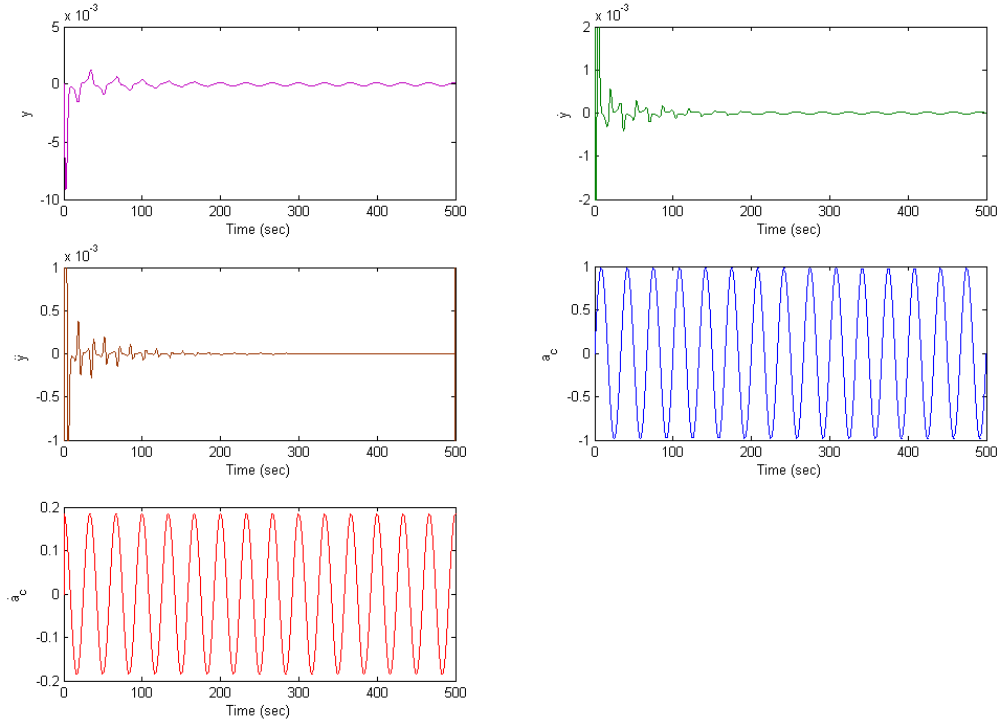


Figure 5.14: State variable dynamics of the sensor system with limited controllable parameter MIT gradient rule controller

Figure 5.14 shows dynamic response of the states y , \dot{y} , and \ddot{y} and input

a_c and \dot{a}_c which can be used with Figure 5.15, which shows component of input voltage V_{in} (which composed of $y \cdot \theta_{231}$, $\dot{y} \cdot \theta_{232}$, $\ddot{y} \cdot \theta_{233}$, $a_c \cdot \theta_{132}$, and $\dot{a}_c \cdot \theta_{131}$), to identify parameters in controller that required higher precision, i.e. higher number of bit in digital quantization should be used when the controller is transferred to programmable logic. In this case, Figure 5.14 and 5.15 show that parameters \dot{y} and \ddot{y} initially jump to higher value and should be allow to used more resource in logic than other parameters.

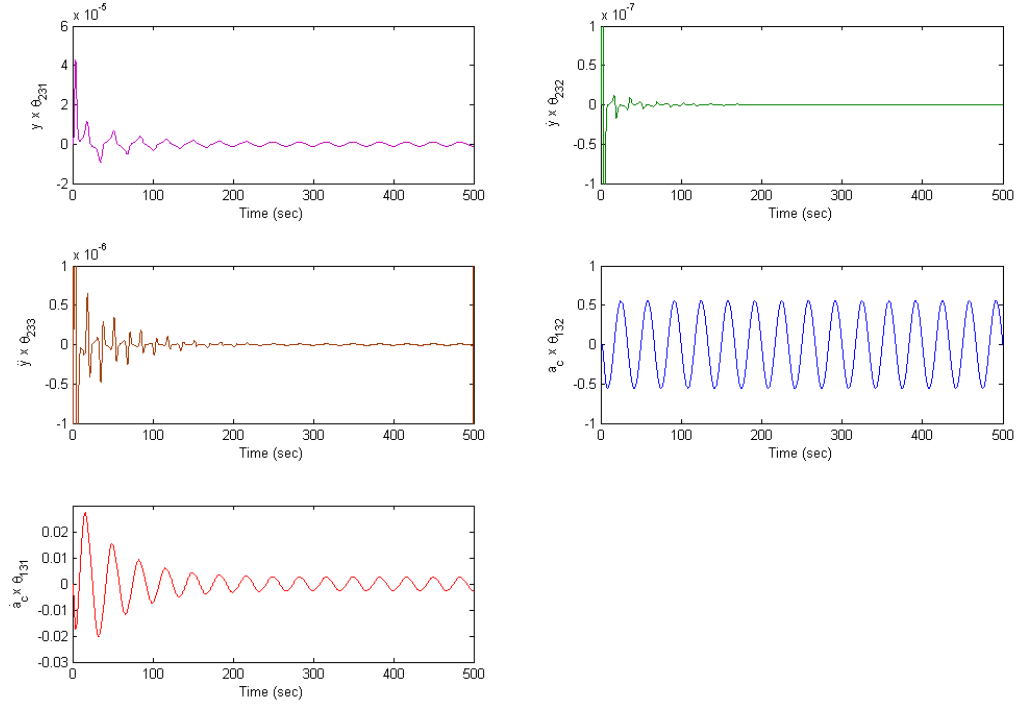


Figure 5.15: Component of input voltage of the sensor system with limited controllable parameter MIT gradient rule controller

Next, the simulation of limited control case for Lyapunov adaptive rule is performed using parameter adaptation laws from equation 5.48 and control block diagram of Figure 5.8. At acceleration input of 0.1 G, 0.03 Hz, all Q_x are set to be

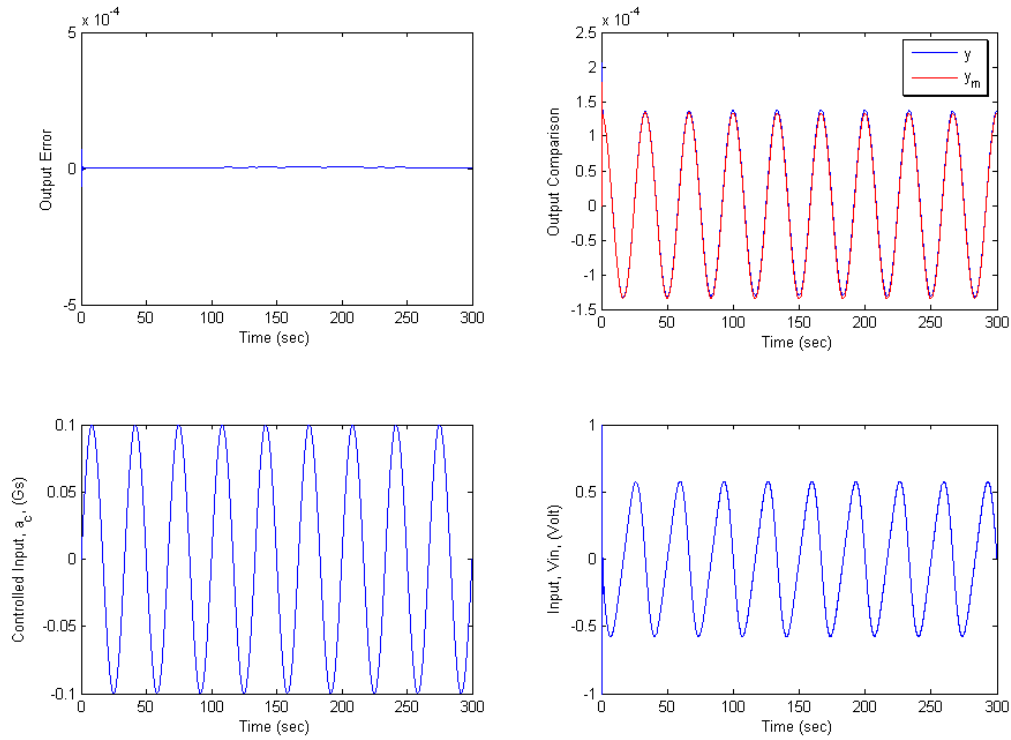


Figure 5.16: Simulation results for the sensor system with limited controllable parameter Lyapunov rule controller

equal at 1, and all γ_{xxx} are set to be equal at $0.5 \frac{g}{a}$. For this case, the controlled sensor has an output response as shown in Figure 5.16, with adaptive controller parameter dynamics as shown in Figure 5.17. Note that the loop gains here are set in terms of $\frac{g}{a}$ such that they have the same level of gain magnitude as in the MIT gradient rule case.

Although the gain has been reduced from 10 to 0.5, limited controllable parameters using Lyapunov rule in Figure 5.16 show a remarkably faster adaptation rate compared with that of the MIT gradient rule (such as in Figure 5.12's top left section). Also, after a certain period of time, the output error does not stay at absolute zero but seems to swing back and forth around reference signal (see top

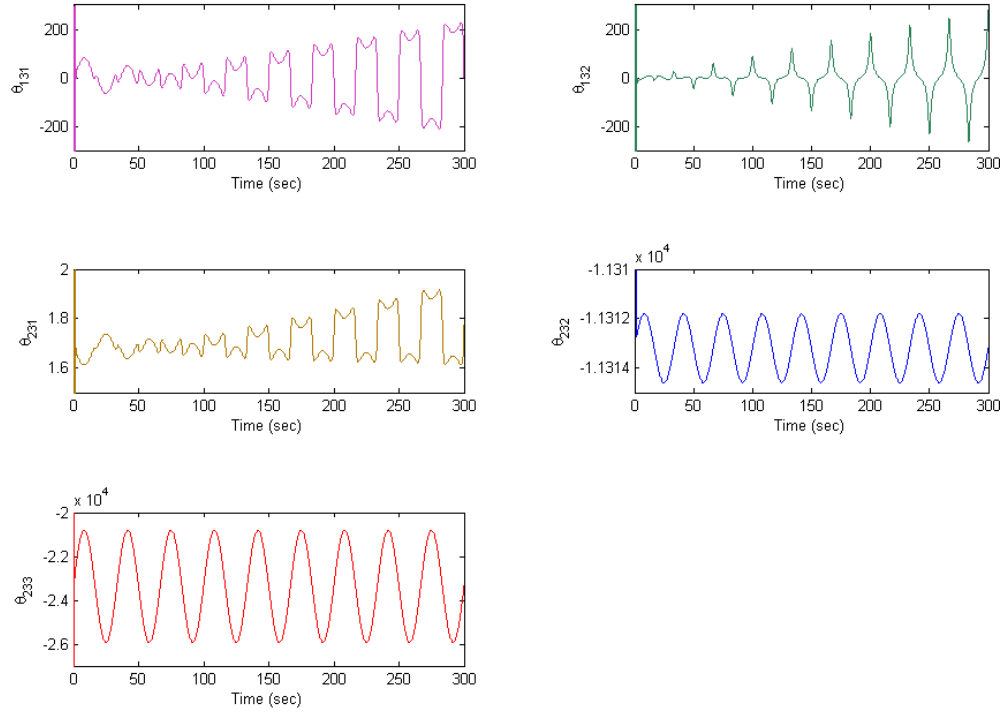


Figure 5.17: Adaptive controller parameters of the sensor system with limited controllable parameter Lyapunov rule controller

right section).

More detail can be inferred from each controller parameters in Figure 5.17, which shows two undesirable characteristics. First, although the system has been adapted to a state that gives a close response in comparison with the reference model, each controller parameter set does not stop adapting. Second, the magnitude of signal required for each case is so large (for example θ_{131} and θ_{132} are in the range of 200 Volts) that an analog control system can not be constructed using simple (low cost) op-amp circuits which may saturate at 12-22 volts.

Figure 5.18 shows a process of adaptation from Figure 5.16 in more detail. It can be seen from top left and right section of the figure that the sensor controlled

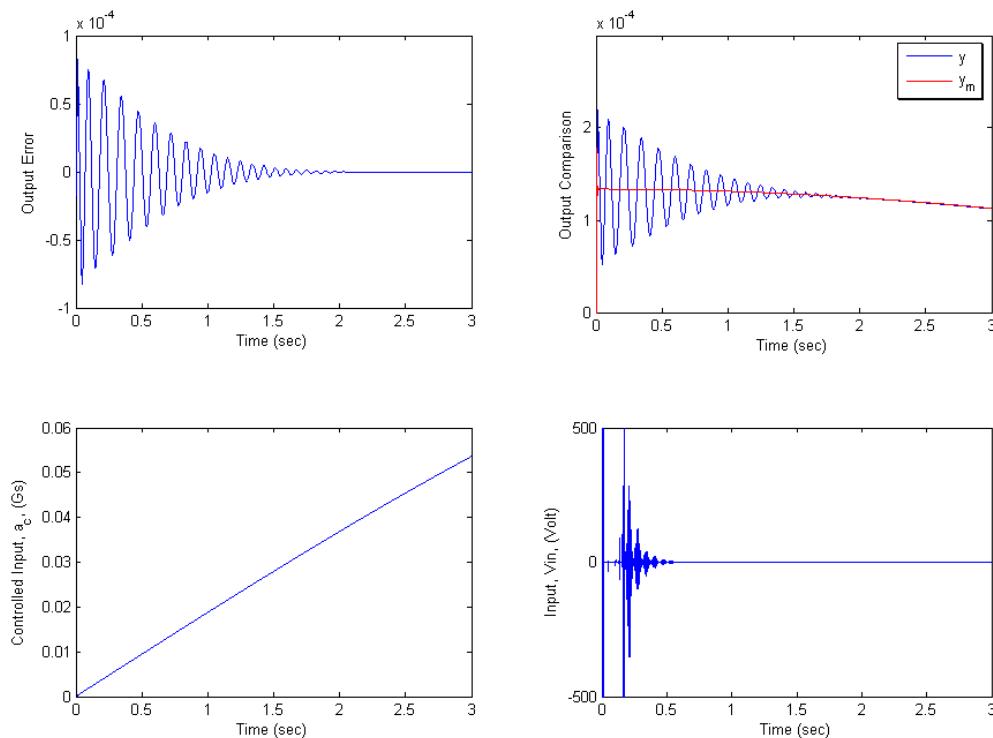


Figure 5.18: An expand version of simulation the results from Figure 5.16

by Lyapunov rule adapts successfully in 2 seconds, and this is a hundred times faster than the MIT gradient rule controller.

The last controller simulation shown here is the construction and simulation of limited controllable parameters with gain scheduling with switching logic. Here, the switching logic and gain scheduling construction will be discussed before showing the simulated results.

As a concept demonstration, a schedule of just two reference models will be used. The goal of switching logic is to detect a condition in which the sensor output has exceeded a range that sensor can operate in linear fashion and switch to another reference model that has a lower gain in that certain frequency. The effect of

switching back and forth to a model that has a suitable gain at particular frequency is similar to a concept of feedback force generation in modern smart sensors. The advantage is that the sensor will always operate in its predictable linear range.

It is also highly desirable that the transition between the two models will be as smooth as possible since there are some second order differentiators in the controller. This requires a reference model signal to be at least second order differentiable at all time.

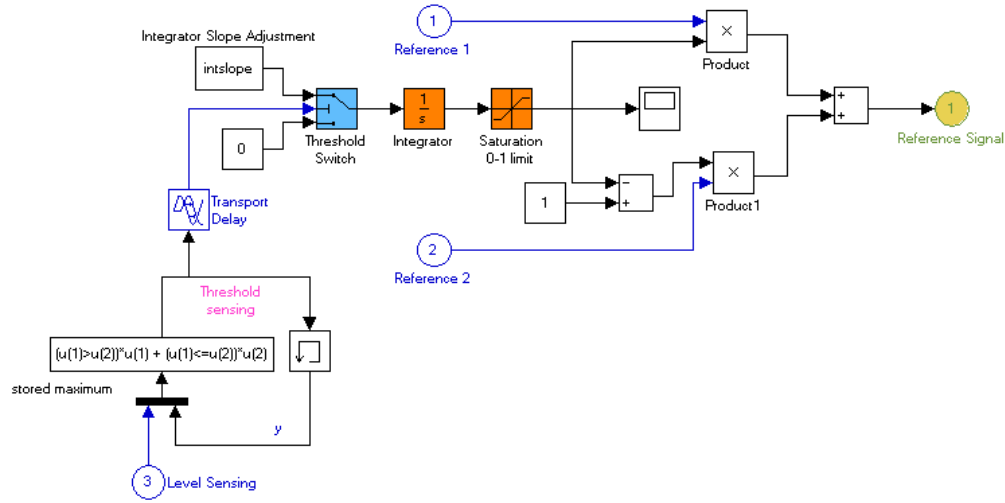


Figure 5.19: Simulink diagram of switching logic and reference model switch designed to be used with adaptive controller

Figure 5.19 shows the simulation (Matlab/Simulink) diagram of the switching logic used for simulation demonstration. Three circles with light background represent inputs to the logic/switch and a circle with dark background represent output of the logic/switch, the number inside each circle indicates junction number. In this case, there are three inputs and one output.

The first and second inputs, indicated by caption a “Reference 1” and “Ref-

erence 2” are reference signals from the two reference models. The third input, indicated by caption “level sensing” is connected to the output of the plant. The block “stored maximum” with its memory feedback block represents a process for finding and storing the maximum amplitude of the signal which helps to decide switching time. This “stored maximum” block is governed by the logic equation,

$$y = (u(1) > u(2)) * u(1) + (u(2) \geq u(1)) * u(2),$$

where y is the output of the block, $u(1)$ is actual signal from sensor output, and $u(2)$ is previous signal maximum. Thus the equation means, if the current signal is higher than previous maximum, the new maximum is the current signal. But if the previous maximum is higher or equal to the current signal, the previous maximum is still to be kept.

Output from “stored maximum” block is then fed to a “transport delay”, where a small delay is applied before switching to prevent a switching at the peak of signal before feeding to the switch block captioned “Threshold Switch”. When switching occurs, the block “Threshold Switch” will switch from bottom constant which is zero to a constant indicated as “Integrator Slope Adjustment”. This will initiate an integration and feed result to an integrator and to a saturation limit. This will result in a ramp signal from zero to one which will be used to phase in one reference signal and at the same time phase out another signal from the summation of two reference signals.

The switching logic is plugged into the adaptive controller based on the MIT gradient rule discussed previously. Figure 5.20 shows results when the acceleration input changes its magnitude widely from 0.001 g to 0.02 g within 100 seconds with constant frequency of 0.1 Hz. Here, a switching threshold, y_{max} , is set to be at approximately 0.17 mV.

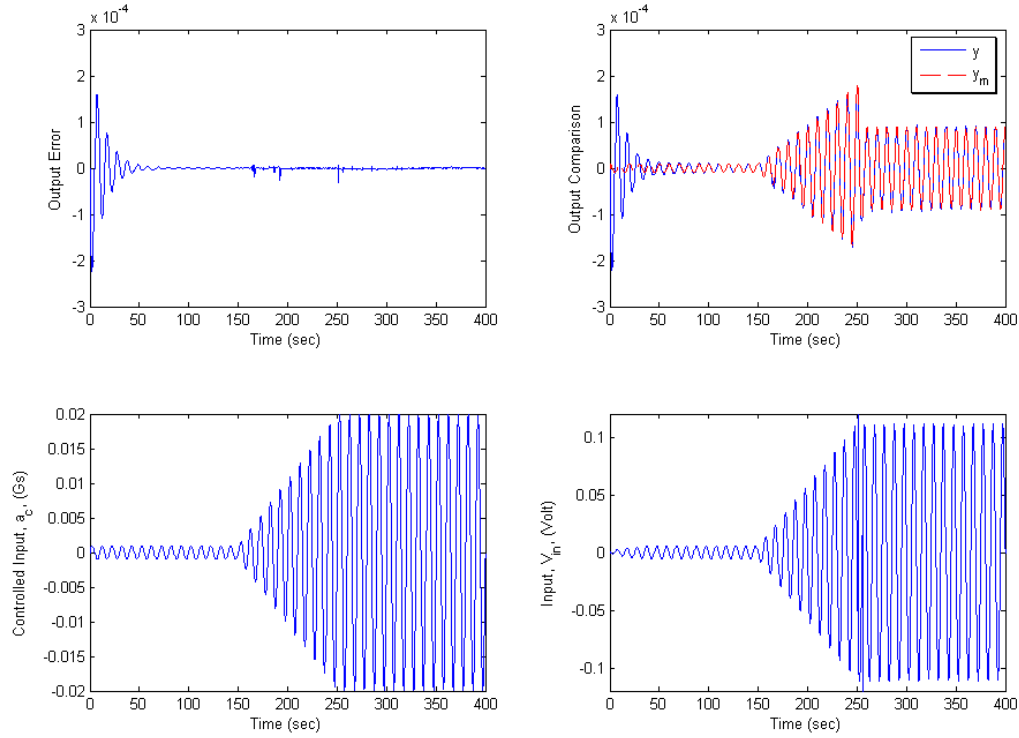


Figure 5.20: Simulation results for the sensor system with limited controllable parameters MIT gradient rule controller with switching logic

Two reference models are used in this simulation. One has a damping ratio of 0.2 and a resonant frequency of 220 Hz, and another has a damping ratio of 0.3 and resonant frequency of 110 Hz. With a high gain of 10000, the sensor is tuned to a reference model that has a lower gain in approximately 100 seconds. At 150 seconds, input acceleration starts to increase linearly to simulate a condition where acceleration magnitude increases beyond the sensor linear range. When the signal from the sensor reaches the predetermined point, a switching occurs and the sensor starts to track another reference model resulting in a magnitude drop (at approximately 250th second).

Figure 5.21 shows controller adaptive parameters for this simulation. It can

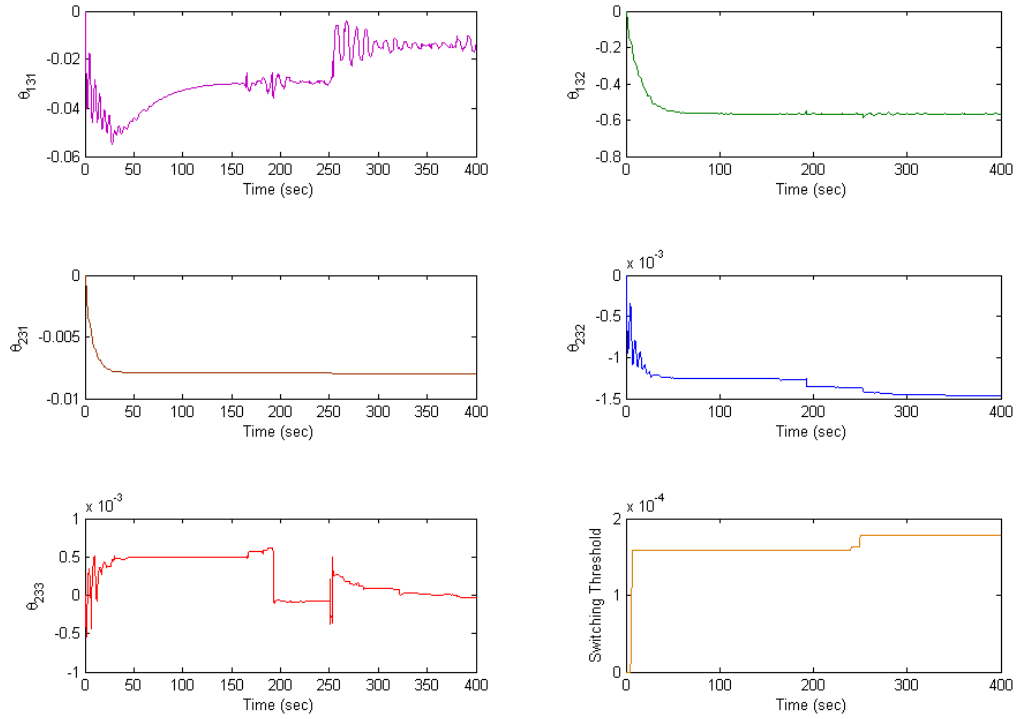


Figure 5.21: Adaptive controller parameters the sensor system with limited control-
lable parameters MIT gradient rule controller with switching logic

be seen that the parameters are re-tuned whenever any changes are needed in the controller. The first re-tune occurred after 150 seconds when the input started to ramp up, and the second re-tune occurred after 250 second when the sensor needed to track the second reference model. The bottom right section of the figure shows the maximum magnitude stored in the switching logic that has just been discussed. It can also be seen that the switching occurred at about 250 seconds where the vertical line crossed the 0.17 mV threshold. After tuning, all controller parameters stay the same, which indicates that the system is stable. All parameters used in these adaptive algorithm simulations are presented in the appendix.

5.5 Summary

This chapter has focused primarily on synthesis of controllers for an adaptive sensor structure. Two candidates for adaptive controllers based on model reference adaptive control theory have been designed. Both are then reduced to indirect and limited controllable parameter cases where only one third of the parameters are physically accessible. Nevertheless, both successfully control the sensor structure as desired. Another adaptive layer is later added based on gain scheduling theory called reference model scheduling. A switching logic is developed in order to make a transition between reference model signals as smoothly as possible. Finally, the last simulation shows a sensor with the adaptive performance as required.

Although the Lyapunov rule adaptive controller has the advantage of guaranteeing system stability, the controller based on the MIT gradient rule is chosen in this case for prototype construction. This decision was made based on the fact that the Lyapunov controller's simulation predicts control signals that have magnitude exceeding the normal range of simple analog control circuits and op-amp saturation levels (12-20 volts). For this particular case, the sensor output error never goes to zero, and controller parameters never seem to stop adapting (in simulation period). Increasing gain to higher order of magnitude seems to stabilize most of the controller parameters in the Lyapunov controller. However, this also brings about an even higher control signal with added noise (higher gain in feedback loop will not only amplify the control signal but also amplify noise).

Aside from better simulation results for the MIT gradient rule adaptive controller, this controller has its own disadvantages. First, instability can be eliminated using a normalized rule, but this will result in a much more complicated controller. For prototype building on programmable logic, for example, which has limited space (as discussed more in the next chapter), a small and uncomplicated controller is re-

quired. This problem can be addressed by performing a simulation of the gain used in controller beforehand to make sure that the system will not go unstable. Unfortunately, adaptive control theory is relatively new, and there is no such theory to address the region of stability based on loop gain the same way as done by a root-locus method for linear feedback control. A second disadvantage is that a suitable gain for the MIT gradient rule adaptive controller might also depend on magnitude of signal input. This basically means that the loop gain has to be selected based on both frequency and magnitude of input signal. This will result in a tedious loop gain tuning. Despite these stringent requirements, tuning, and limitations, an adaptive sensor with the MIT gradient rule adaptive controller is shown to perform as designed through simulation. Its implementation will be discussed in the next chapter.

Chapter 6

Experimental Methodology, Apparatus, and Results

The sensor structure developed in chapter 4, and the controller structure developed in chapter 5 are used together in this chapter to construct a prototype for experimental concept and model verification. This chapter starts with a discussion of the fabrication of the prototype and experimental set up. The process of physical parameter determination is then presented. The adaptive controller prototype is built using a programmable logic controller running on a real-time operating system (RTOS), so a brief discussion on this topic is given. Finally, the results of testing and comparison to simulations from the last chapter will be presented and discussed.

6.1 Design of experimental apparatus

The goal of this section is to discuss how to realize the structure of the sensor designed and shown in Figure 4.15 in chapter 4. Two major support components are the piezoelectric ceramic bimorphs and the base support structure. The bimorphs will be described first, then the design for the base structure customized to fit the bimorphs is presented.

Four identical bimorphs designated by D215 H4 303 YS by the manufacturer, Piezo System Inc, Cambridge, MA, were acquired. These bimorphs are configured to be double quick mount (D), which means there are printed-circuit board (PCB) mounts at both ends suitable for fixing one end to the base and another to the proof mass. There are two layers of piezoelectric material (2), as these are bimorphs. The

beams have a thickness of approximately 0.015 inch (15) which is the thinnest size that can be custom built (the thinner the layer, the less potential required to drive the bimorph in actuator mode). The piezoelectric material used is PSI-5H4E or PZT-5H (H4), which is one of the most sensitive materials for energy conversion between mechanical strain and electrical potential (and vice versa). The beams are 12.7 mm wide and 31.8 mm long (size 303), the smallest size available for double quick mount option. The bimorphs are Y-poled for 3 wires parallel operation (Y), which uses less energy to drive than a series type bimorph. The beams are configured as S-benders (S), where the tip of the beam can remain in parallel to the base. These bimorphs have a rated resonant frequency of 215 Hz.

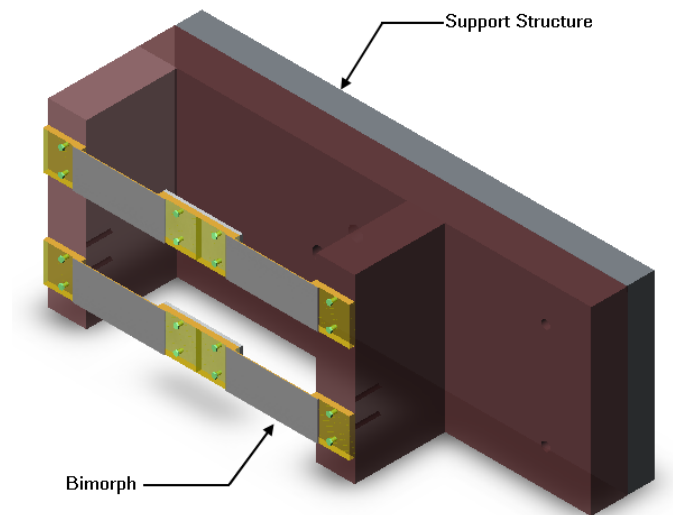


Figure 6.1: Figure shows Solidworks 3D rendering of sensors and support base

Some requirements have to be met when designing the support base for bimorphs. 1) two pairs of bimorphs have to be able to attach to the base (one pair is used for sensor operation, another pair is for adapting reference) and the distance between them should be such that they can be serviced, 2) the base has to

provide an attachment area for a reference accelerometer, 3) the base should be light enough so as to not exceed the weight rating of the shaker equipment (the lighter the better). 4) the base should be easy to fabricate, 5) the base should secure tightly to the shaker, 6) the base has to have its first natural mode in a frequency range higher than that of bimorph structure. The bimorphs are drawn using Solidworks 2005 (SolidWorks Corporation, Concord, MA.) and integrated with design drawing for the support base. The design's 3D rendering is shown in Figure 6.1 and three view drawings are shown in Figure 6.2.

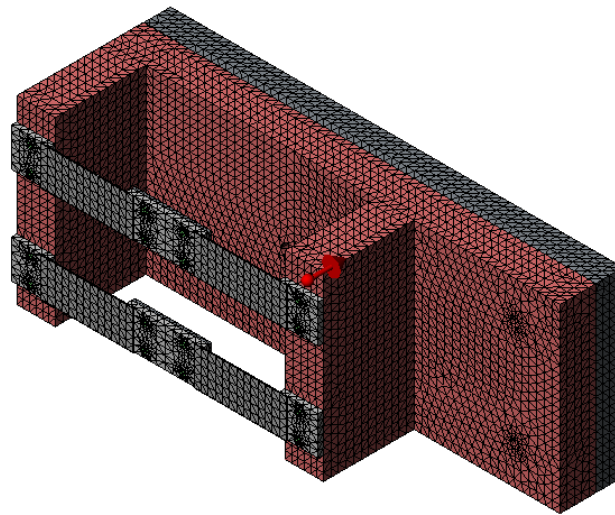


Figure 6.3: Shows COSMOS/Works mesh discretization of bimorphs and base for FEM analysis, arrow (red) shows direction of acceleration/gravity

Clear polished acrylic was chosen for fabricating the support base because it is easy to machine, is light weight, and is one of the strongest available plastics. Acrylic pieces used for building the support base are fixed together by special acrylic adhesive. Each of the pieces are polished to create a perfectly flat surface for mounting bimorphs. Each bimorph pair is attached to the base by four screws.

A base plate, made from 9 mm thick aluminum, is clamped with the bottom part of the support base and used for reinforcement. A CAD/FEM analysis package was used to design the base and bimorph. Modal analysis is critical and helps confirm selection of components and to assess their performance. This is helpful since the bimorph is a composite formed by brass and piezoelectric ceramic, and the base combines acrylic and aluminum components.

COSMOS/Works 2005 (SolidWorks Corporation, Concord, MA.) is used for FEM modal analysis of the bimorphs and base. Figure 6.3 shows a mesh discretization of the structure. Mesh elements are tetrahedra that have a size of 2.5 mm, tolerance is 0.125 mm, total number of nodes are 211820, total number of elements are 145053, and number of degree of freedom are 635100.

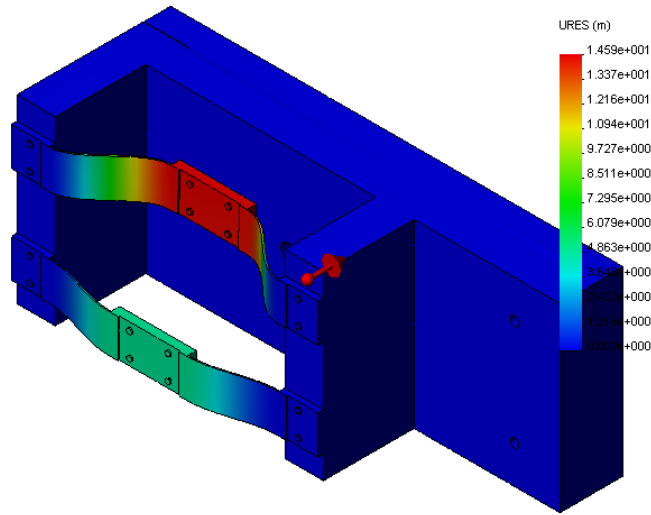


Figure 6.4: Shows 1st mode deflection of the bimorphs and base generated by COSMOS/Works with input acceleration simulated at 1 g.

Figure 6.4 shows the behavior for the 1st mode from a modal analysis. Material properties used in this analysis are: acrylic, which has modulus of elasticity

of 2.4 GPa, Poisson ratio of 0.35, shear modulus of 0.89 GPa, and density of 1200 Kg/m^3 , Aluminum 1060 alloy, which has modulus of elasticity of 69 GPa, Poisson ratio of 0.33, shear modulus of 27 GPa, and density of 2700 Kg/m^3 , Brass which has modulus of elasticity of 100 GPa, Poisson ratio of 0.33, shear modulus of 37 GPa, and density of 8500 Kg/m^3 , PZT-5H which has orthotropic property and will be discussed in later section.

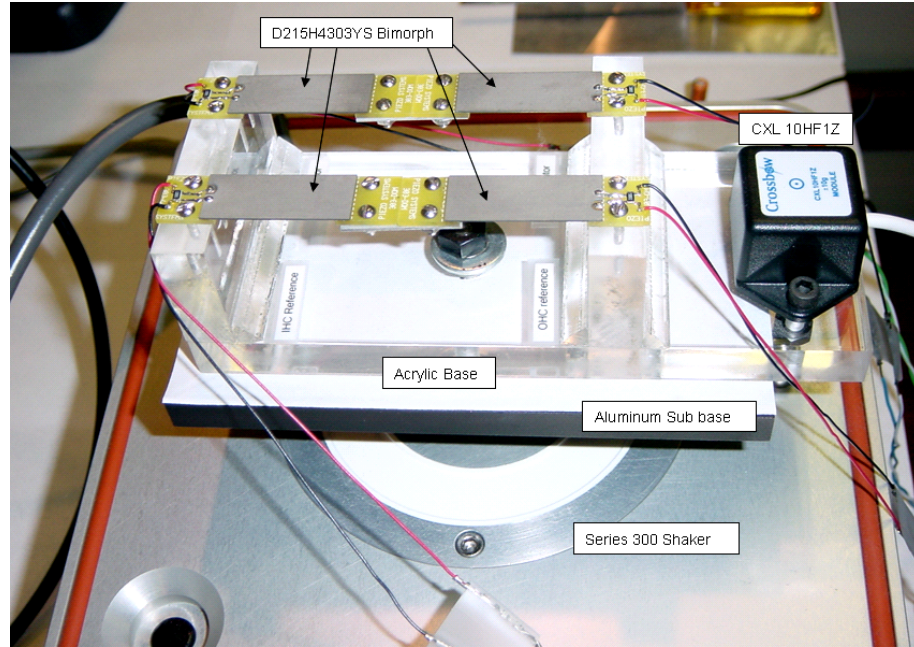


Figure 6.5: Photo showing assembled acrylic support base, aluminum sub base, bimorph, and reference accelerometer CXL 10HF1Z

FEM model analysis shows the first and second mode at 225 Hz, which is associated with deflection of the two bimorph pairs in the direction of acceleration, third and fourth mode at 600 Hz which is associated with twisting of each bimorph, and finally the last, fifth mode, at 625 Hz which is associated with bending of the base. This analysis provided some assurance that the base vibration mode would not interfere with bimorph pairs. The base was then built according to the drawing

and the sensor systems is shown in Figure 6.5.

6.2 Experimental set up

Major equipment and their connections for experiments are shown in Figure 6.6. Equipment is controlled and monitored by a Dimension 4550 personal computer (Dell Inc, Round Rock, TX.) running windows XP professional operating system (Microsoft Corp, Redmond, WA.). User interface and data acquisition software used is NI LabVIEW 7.1.1 with real-time 7.1.1 and FPGA 1.1 module (National Instruments, Austin, TX.). AccelVIEW (Crossbow technology, San Jose, CA.) is used separately for interfacing with and testing the reference accelerometer, CXL 10HF1Z.

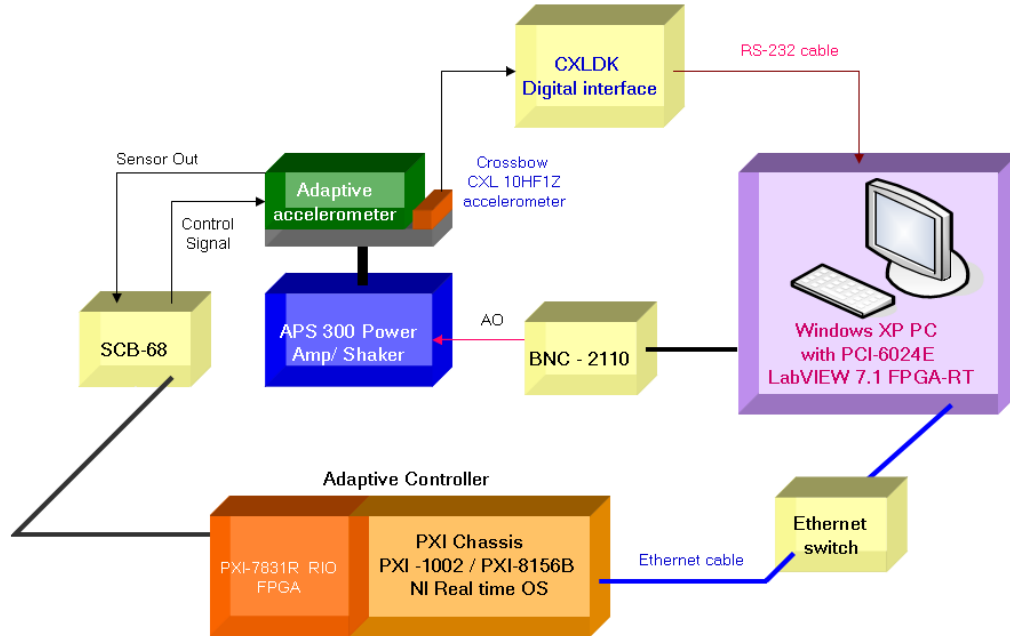


Figure 6.6: Figure shown all equipments connection for this chapter experiments

Acceleration input is monitored and compared with a reference wideband

commercial accelerometer CXL 10HF1Z (Crossbow technology, San Jose, CA.), which is a single axis MEMS accelerometer based on the active Analog Device XL-05 chip. This accelerometer has an acceleration span of 10 g, sensitivity of 100 mV/g, and bandwidth of 0.3-10000 Hz. This accelerometer is connected with a digital interface board, CXLDK (Crossbow technology, San Jose, Ca.), which is composed of a regulator, 12-bit A/D converter, microcontroller, and RS-232 (serial) port interface which provides a connectivity to the personal computer through serial bus. Data output is displayed through AccelVIEW.

Function generation and frequency response measurement is performed using the analog I/O function of a PCI-6024E 12-bit low-cost E series multi function data acquisition (DAQ) card (National Instruments, Austin, TX.) which has 16 analog input channels, 2 analog output channels, 8 digital I/O channels, a sampling rate of 200 kS/s, range of 10 V, 2 24-bit counters, and digital trigger. All the I/O signals are passed through a BNC-2110 connector block which provides all connectivity in shielded single-labeled BNC format.

Input acceleration/vibration waveforms are generated by the DAQ card and are sent to the model 300 permanent magnet electrodynamic portable shaker-amplifier (APS Dynamics Inc, Carlsbad, CA.), which has a force rating of 22 N, frequency range of 5 kHz, soft suspension stroke of 5 mm, stiff suspension stroke of 2.5 mm, and load rating of approximately 1 kg. This shaker has a built-in amplifier which has a maximum output current of 2 A and maximum potential of 1.5 V. The adaptive accelerometer and the reference accelerometer are bolt clamped on the base discussed in the last section. The base is fastened to the portable shaker by a 6 mm diameter stainless steel strut.

Sensing signals from the sensor and actuating signal to the sensor is impedance isolated from the control circuit by an active buffer amplifier section with active low-

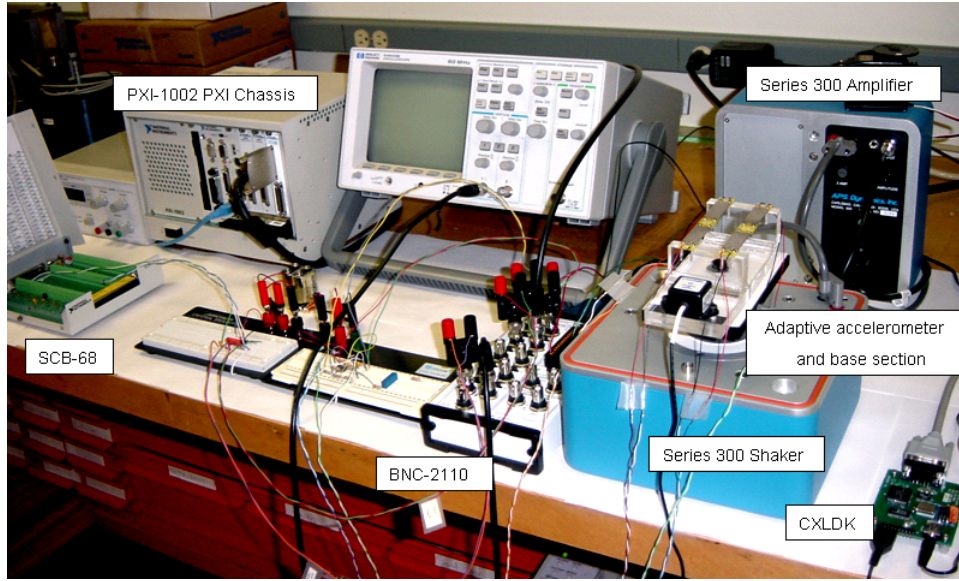


Figure 6.7: Photograph of the overall experiment setup

pass filters. These buffers are built from 1458 dual operational amplifiers with $10\text{ k}\Omega$ resistors and $0.022\text{ }\mu\text{F}$ capacitors. Low-pass filters are designed such that the cut off frequency is at approximately 700 Hz. The circuits were tested and have a low frequency gain of less than two dB (See Figure 6.8).

Controller and switching logic is built using a PXI-7831R PXI-bus reconfigurable I/O board (National Instruments, Austin, TX.) for hardware-in-the-loop (HIL) which has 8 analog input/output channels, 96 digital lines, 16-bit resolution, 10 V range, sampling/updating rate of 1 MS/s, and 11520 logic cells. This reconfigurable I/O board is based on FPGA technology and is programmed/compiled using LabVIEW FPGA module. Xilinx FPGA compiler server installed on the host computer is used to translate LabVIEW VIs to hardware description language (HDL) and to logic gate connections. The interface between the PXI-7831R and the adaptive accelerometer is provided through SCB-68 shield I/O connector block (National Instruments, Austin, TX.) which provides wire terminals within a metal enclosure

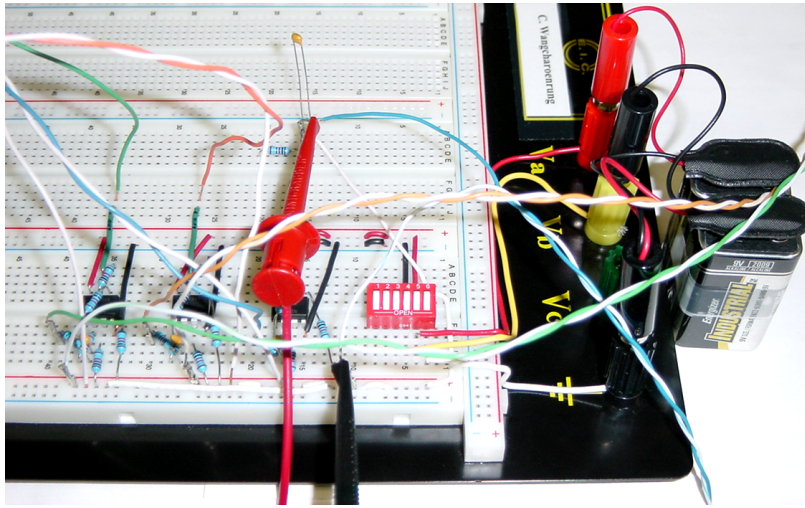


Figure 6.8: Shows buffer amplifier and active low-pass filters section of sensing (left), reference (middle), and actuating (right) bimorphs

for protection of signals from noise corruption.

FPGA, an abbreviation for Field-Programmable Gate Array, is an integrated circuit similar to programmable logic device (PLD) in that it is a type of logic chip that can be programmed and reprogrammed by a user. The FPGA chip usually supports thousands of logic gate cells, each of which can independently take on any one of a limited set of personalities. Each cell is interconnected by wires and programmable switches. Once programmed the logic gates and switches are hardwired and form a fabric of basic building blocks for circuits. A more complex design is achieved by combining these basic circuits together. An entire process is equivalent to building a customized integrated circuit. The FPGA is very suitable for control application because once programmed, it represents an equivalent of analog control circuits that introduce virtually no signal delay.

The PXI-7831R is locally controlled by a PXI-8156B embedded computer (National Instruments, Austin, TX.) which has AMD K-6 450 MHz CPU, 20 GB

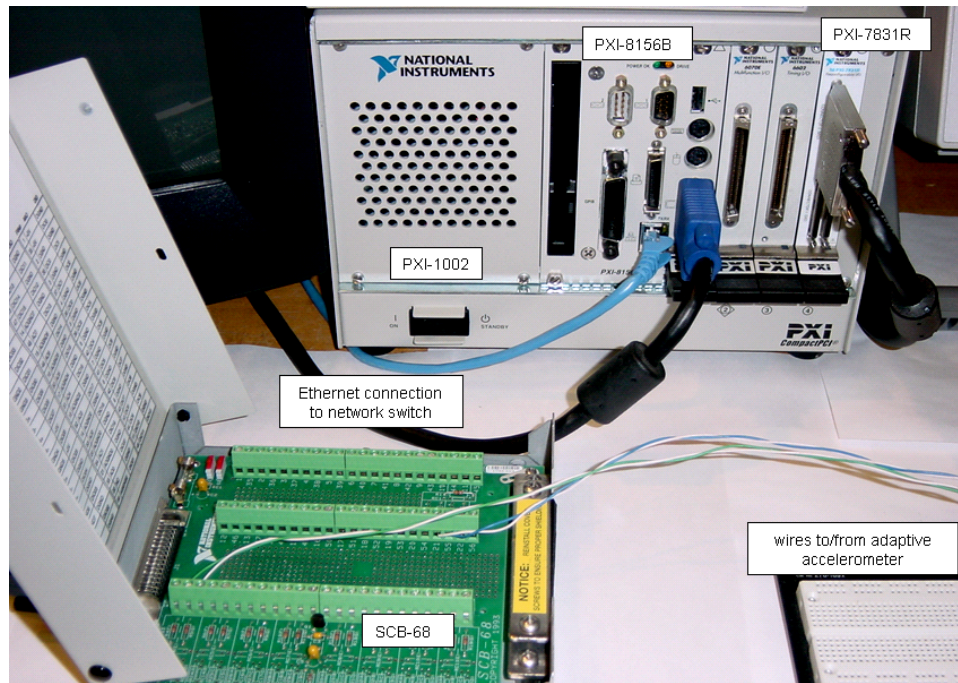


Figure 6.9: Photograph of PXI-1002, PXI-8156B, PXI-7831R, and SCB-68 connection

hard drive, 128 Mb of RAM, and runs a National Instruments version of real-time operating system (NI RTOS 7.1.1). Both PXI-7831R and PXI-8156B are plugged on PXI-1002 PXI chassis (National Instruments, Austin, TX.) and communicate with each other via PXI-bus. PXI, abbreviation for PCI eXtensions for Instrumentation developed and announced by National Instruments in 1997, is based on Peripheral Component Interconnect (PCI) bus, ubiquitous in personal computers with added separated star triggering bus and 10 MHz clock for precise timing. The PXI bus in combination with local embedded computer, real-time OS, and FPGA makes possible the prototyping of a control system with loop timing of up to 25 nanoseconds and precise triggering function not possible by non real-time operating systems such as MAC OSX, Unix, or Microsoft Windows. The PXI-8156B has a built-in network

interface card (NIC) and communicates with the host computer through a Local Area Network (LAN) via Ethernet cable and has its own IP-address assigned by a 10/100 Mbps Ethernet switch.

6.3 Determination of model parameters

Success of a control system depends partly on how accurate the sensor (or plant) is modeled. While most of the physical parameters used for modeling can be calculated, the only way to verify them is through experimentation. This section presents a series of short experiments conducted to find and confirm critical physical parameters.

6.3.1 Damping via logarithmic decrement

The first experiment is designed to find damping ratio coefficient of the bimorphs. Because the bimorph beam represents a simple mass-spring-damper second order system, a simple test with initial displacement and free response should yield information on the effective beam's damped natural frequency ω_d , damping ratio coefficient ξ , and natural frequency ω_n . The logarithmic decrement method [97] defines a relationship between the natural logarithm of the ratio of the peak amplitudes of any two oscillations and the damping ratio coefficient of the system as,

$$\ln \left[\frac{A_0}{A_n} \right] = \frac{2\pi n \xi}{\sqrt{1 - \xi^2}}$$

where A_0 is amplitude of any peak, A_n is amplitude of n^{th} peak. The relation between $\ln \left[\frac{A_0}{A_n} \right]$ and n implies a slope of a straight line, β_n . A relation between this slope and damping ratio coefficient is,

$$\xi = \frac{\beta_n}{\sqrt{4\pi^2 + \beta_n^2}}.$$

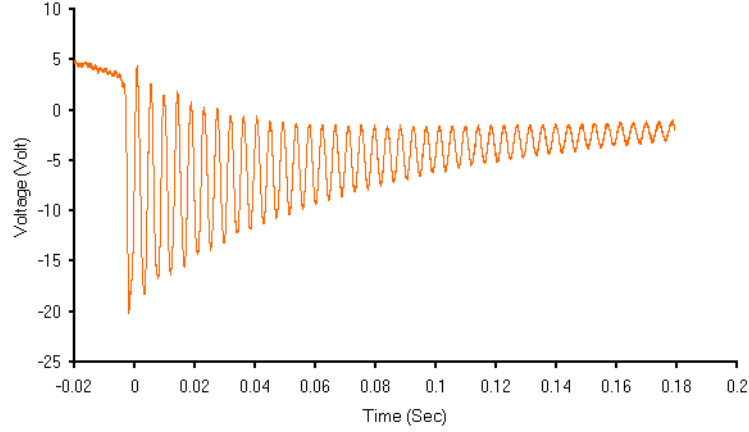


Figure 6.10: Initial displacement response of the bimorph pair

The bimorph pair is set at some initial displacement and released while a TDS 3014B oscilloscope (Tektronix Inc, Beaverton, OR) is used to monitor the sensing output with slope triggering turned on. The result is shown in Figure 6.10.

Setting the first negative peak as A_0 at -1.92 ms, natural logarithm of the first 25 peaks amplitude ratio is shown in Figure 6.11, which shows a good approximation of β_n to be 0.0513, average ω_d of 1432.5 rad/s (approximately 228 Hz), and resulting in ξ of 0.008 from calculation.

Using approximation of equivalent mass and stiffness of bimorphs with standard second order solution for mass-spring-damper, $b = 2\xi\sqrt{m \cdot k}$, yields a damping constant of 0.071805 N-s/m. The equivalent mass used is 3.15 gram which is calculated from half of the real mass (1.375 gram) and mass of the proof mass (1.775 gram) according to Rao [97].

The equivalent stiffness k used is from calculation of 2-port characteristic C_{11} ($k = 2 \cdot C_{11}$), which is a relation between force and displacement from equation

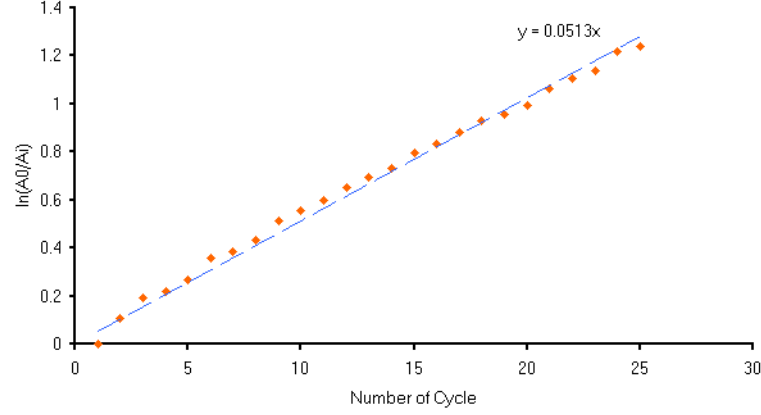


Figure 6.11: shows linear relationship between $\ln \left[\frac{A_0}{A_n} \right]$ and n used to estimate β_n

4.31 in chapter 4 ($C_{11} = \frac{(4K_{33}^{(T)} s_{11}^{(\xi)} - D_{31}^2)4bh^3}{l^3 s_{11}^{(\xi)} (2K_{33}^{(T)} s_{11}^{(\xi)} - 5D_{31}^2)} + \frac{8E_{shim}bh_{shim}^3}{l^3}$, $C_{12} = \frac{6D_{31}h^2}{l^2(2K_{33}^{(T)} s_{11}^{(\xi)} - 5D_{31}^2)}$, $C_{21} = \frac{6D_{31}h^2}{l^2(2K_{33}^{(T)} s_{11}^{(\xi)} - 5D_{31}^2)}$, and $C_{22} = \frac{s_{11}^{(\xi)}h}{lb(2K_{33}^{(T)} s_{11}^{(\xi)} - 5D_{31}^2)}$). Bimorph D215 H4 303YS has a width (b) of 12.7 mm, a length (l) of 31.8 mm, a ceramic layer thickness (h) of 0.1397 mm, and a brass layer thickness (h_{shim}) of 0.127 mm. Material PZT-5H has piezoelectric constant (D_{31}) of $-274 \cdot 10^{-12}$ C/N, elastic constant ($s_{11}^{(\xi)}$) of $16.5 \cdot 10^{-12}$ m²/N, longitudinal coupling factor ($K_{33}^{(T)}$) of $3400 \cdot 8.854 \cdot 10^{-12}$ F/m, and density (ρ) of 7500 kg/m³. All these physical constants result in 2-port capacitive element constants C_{11} of 3070.38 N/m, C_{12} and C_{21} of -51340 V/m, and C_{22} of $9.235 \cdot 10^6$ F.

6.3.2 Comparison of predicted and measured sensing response

The second experiment is designed to compare sensing characteristics between the bond graph model and the real system. The experiment is divided into two stages. The first stage setup uses an acceleration input at constant magnitude of approximately 0.2 g, with frequencies ranging from 10 Hz to 400 Hz. The drive sig-

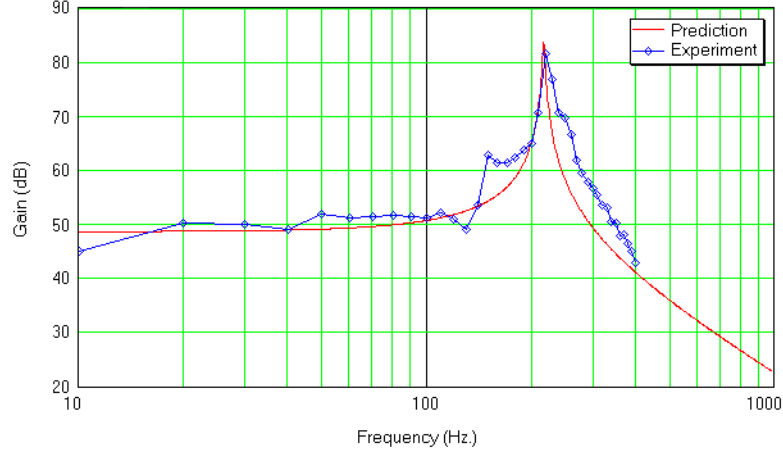


Figure 6.12: Sensing frequency response comparison in dB of mv/g of uncontrolled sensor between experiment (measured) and a predicted from equation 6.1

nal simulated by a sinusoidal signal from DAQ card and sent to the shaker-amplifier. The amplitude of the acceleration is measured by the reference accelerometer in g and signal output from the bimorph is measured in mV. The open loop frequency response of this sensing characteristic of the sensor (without any adaptive control algorithm) is determined.

Bond graph model of this set up is the same as in Figure 5.4 where there is no signal input at bond 17. The transfer function between output sensing potential and input acceleration is a modification of equation 5.21; that is,

$$\frac{V_{out}(S)}{a(S)} = \frac{C_{21i}m_{tot}(R_sS + C_{22o})}{[m_{tot}S^2 + (b_{ci} + b_{co})S + C_{11i} + C_{11o}](R_sS + C_{22o}) - C_{12o}^2}. \quad (6.1)$$

where $b_{ci} + b_{co}$ are combined damping constant found from the logarithmic decrement experiment, 2-port -C- constitutive relations is set to be identical between sensing (i) and actuating (o), and a series resistor R_s of 99Ω is used. Result of this experiment in comparison with its prediction is shown in Figure 6.12.

The second stage of this experiment is opposite to the first stage. The sim-

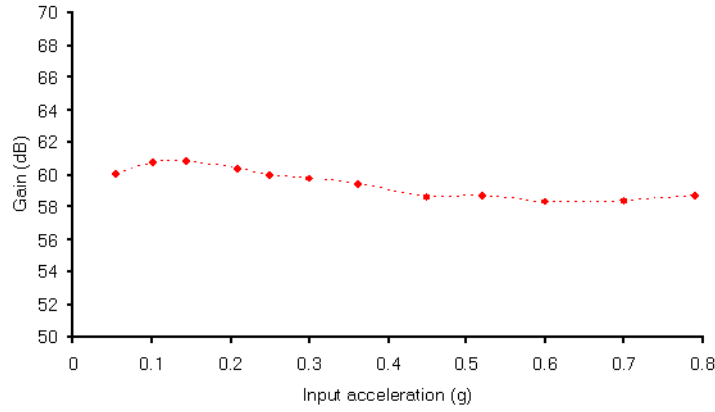


Figure 6.13: Sensing response in dB of mv/g to different magnitude of acceleration at constant frequency of 50 Hz

ulated input acceleration has constant frequency of 50 Hz with magnitude ranging from 0.05 g to 0.8 g. Similar to the first stage, the frequency response is measured in terms of dB of mV/g. The result is shown in Figure 6.13.

The result of this sensing response is very useful because it shows that the accelerometer can be modeled very well using linear elements. In particular, Figure 6.12 shows that the model developed can predict frequency response of the system very well in the range of 20 to 400 Hz. Figure 6.13 shows that the system response magnitude does not depend greatly on amplitude of input which is an indication that the system can be approximated as linear.

6.3.3 Comparison of predicted and measured actuating response

A third experiment is designed to compare actuating characteristics predicted by the model and those measured in the real system. Similar to the last section, this experiment is also divided into two stages. For the first stage, input to the system is a sinusoidal voltage potential with a constant magnitude of 3 V at 50

percent duty cycle for a frequency range from 10 to 400 Hz. In the experiment, this is generated by the DAQ card and passed through a buffer amplifier (built from 741 op-amp and 10 $K\Omega$ resistors). The signal output from sensing part of the bimorph is also measured by the DAQ card.

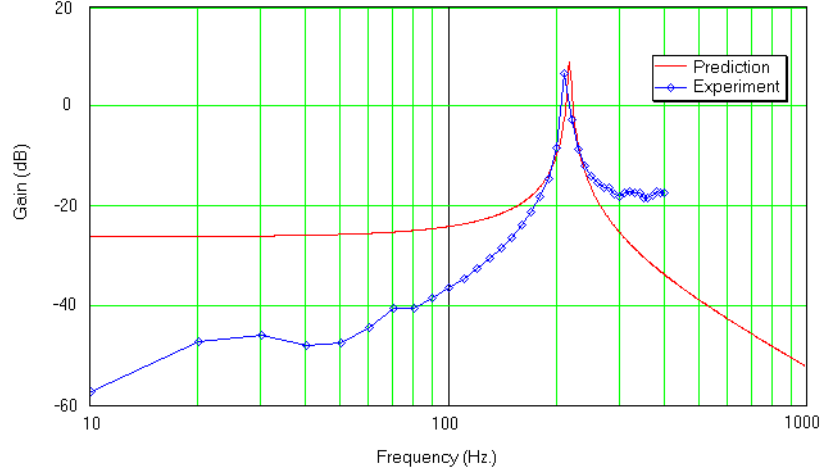


Figure 6.14: Actuating frequency response comparison in dB of mv/mv between experiment and prediction by model

The bond graph model of this set up is the same as in Figure 5.4, where there is no velocity input at bond 1. The transfer function between output sensing potential and input actuating potential is from equation 4.22; that is,

$$\frac{V_{out}(S)}{V_{in}(S)} = \frac{-C_{12o}C_{12i}}{[m_{tot}S^2 + (b_{ci} + b_{co})S + C_{11i} + C_{11o}](R_sS + C_{22o}) - C_{12o}^2}.$$

The result of this experiment in comparison with its prediction is shown in Figure 6.14.

The second stage of this experiment is opposite to the first stage. A simulated input potential is at constant frequency of 50 Hz with magnitude ranging from 1 V to 8.5 V (limit amplitude of battery supply to op-amp). Similar to the first stage,

the frequency response is measured in terms of dB of mV/mV. The result is shown in Figure 6.15.

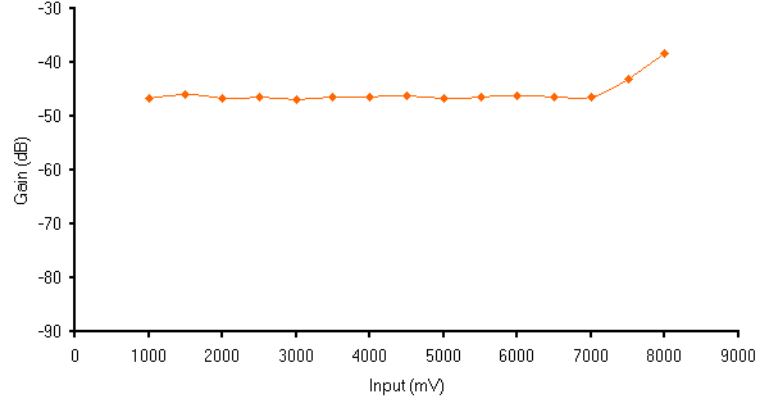


Figure 6.15: Actuating response in dB of mV/mV for different magnitudes of the potential input at constant frequency of 50 Hz

Similar to the last section, the result of this actuating response is useful because it shows that the accelerometer can be modeled using linear elements. In particular, Figure 6.14 shows that the model developed can predict frequency response of the system in the range close to resonant frequency. A deviation from the prediction is thought to be due to either a frequency-dependent damping, vibration feedback from the base of accelerometer, or noise. Figure 6.15 shows that the system response magnitude does not significantly depend on amplitude of input, given that amplitude of input is less than 7 V, which is an indication that the system can be approximated as linear.

6.4 Programmable logic gates for controller prototype

As stated, the logic gate in the FPGA card PXI-7831R is programmed by HDL which is compiled from the LabVIEW FPGA module VIs. In order to program

the FPGA VIs, some concepts of amplitude quantizing and discrete time control should be clarified. Both of them are discussed below.

6.4.1 Amplitude quantization

Because the FPGA reconfigurable I/O board acquires its measurement data to be in 16-bit signed integer format, corresponding to the range of plus and minus 10 volts, and all the control actions and operations can only be accomplished using on fixed-point number representation, a set of data conversions have to be done in order to allow communication between the host (PC or RTOS) computer and the FPGA board. For measured voltage data, the conversions follow the formula,

$$Voltage = \frac{16bit\ Binary\ code}{32768} \cdot 10.0,$$

where this equation can be reversed for digital-to-analog conversion.

The controller parameters are scaled from floating point representation to fixed point representation by 16-bit representation with variable scaling factor to allow the best resolution of the number (refer to National Instruments' document on Pseudo-Floating-Point based PID controller by C. Humberstone). The transformation follows formulas,

$$Scaled\ Factor = 15 - nint[\log_2[nint(Real\#)] + 1],$$

and,

$$Binary\# = nint(Real\# \cdot 2^{Scaled\ Factor}),$$

where the “*nint*” function represents an extraction of the integer part from a real number. This conversion means that for every real number, the data will be converted to a set of two numbers, binary number and its scaled factor. The formula to convert two of the fixed-point numbers back to one floating point number is,

$$Real\# = Binary\# \cdot 2^{-(Scaled\ Factor)}.$$

For example, a real number of 5.4321 will be represented by a binary number of 22250 and its scaled factor of -12. A conversion back will result in 5.431289 which is $2.89 \cdot 10^{-5}$ offset from the real number. This type of offset from conversion is common and unavoidable in this implementation.

6.4.2 Discrete time control

In order to program the continuous time controller developed in chapter 5 into programmable logic in the PXI-7831R (FPGA board), every transfer function developed has to be transformed into a discrete time difference equation. The control block diagram from Figure 5.7 is also modified due to the fact that an estimation of current input is achieved by reference bimorph pairs.

Figure 6.16 shows the block diagram from a reduced version of the MIT gradient method of adaptive control from Figure 5.7. The difference between Figure 5.7 and Figure 6.16 is that an estimation of the current signal is done by an estimator that is an inverse transfer function of reference bimorphs ($TF - 1$) which is assumed to be the same as non-adaptive plant. Therefore, the transfer function, $TF - 1$, is the inverse of the plant model; that is, $\frac{a_c(S)}{y_x(S)} = \frac{aaS^3+bbS^2+ccS+dd}{eeS+ff}$. Using a backward difference method which allows a mapping from S (Laplace) domain to Z (discrete) domain as, $S = \frac{1-Z^{-1}}{T}$, where T is sampling period and Z^{-1} is a delay (shift back in time). This results in,

$$\begin{aligned}
 TF - 1 \Rightarrow a_{c(k)} = & \left[\frac{ee}{ee + ff \cdot T} \right] a_{c(k-1)} + \left[\frac{\frac{aa}{T^2} + \frac{bb}{T} + cc + dd \cdot T}{ee + ff \cdot T} \right] y_{x(k)} \\
 & - \left[\frac{\frac{3aa}{T^2} + \frac{2bb}{T} + cc}{ee + ff \cdot T} \right] y_{x(k-1)} + \left[\frac{\frac{3aa}{T^2} + \frac{bb}{T}}{ee + ff \cdot T} \right] y_{x(k-2)} - \left[\frac{aa}{eeT^2 + ff \cdot T^3} \right] y_{x(k-3)},
 \end{aligned} \tag{6.2}$$

where k is the time index such that k and $k + 1$ have difference in time by a period, T . Similarly, $TF - 2$ is a transfer function of reference model, $\frac{y_m(S)}{a_c(S)} =$

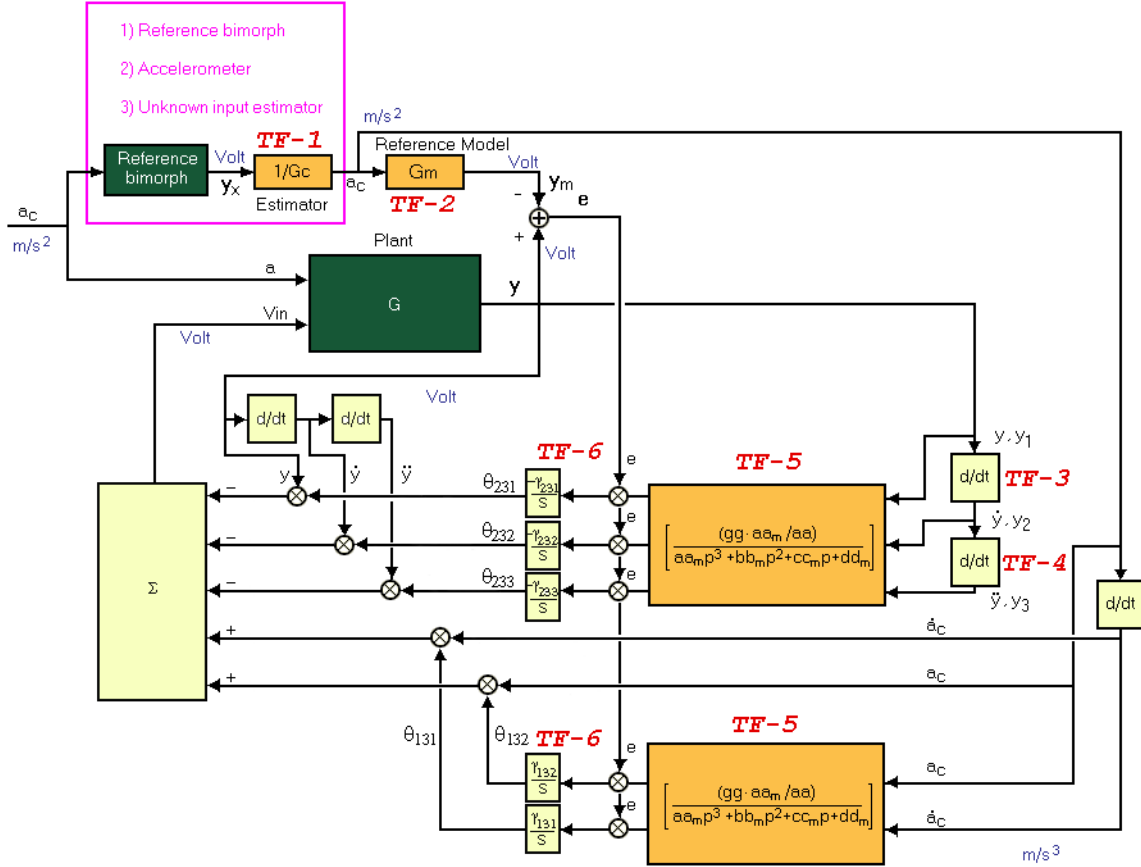
$$\frac{ee_m S + ff_m}{aa_m S^3 + bb_m S^2 + cc_m S + dd_m}, \text{ and can be transformed to difference equation as,}$$


Figure 6.16: shows modified version of the control diagram from Figure 5.7 for estimation of current input. $TF - 1$ to $TF - 6$ are positions of difference equations. There are three shades of block color. Darkest color (green) blocks represent physical systems, lightest color (yellow) blocks represent simple signal manipulation in controller, and medium color (orange) blocks represent signal filters in controller.

$$TF-2 \Rightarrow y_{m(k)} = \left[\frac{\frac{3aa_m}{T^3} + \frac{2bb_m}{T^2} + \frac{cc_m}{T}}{\frac{aa_m}{T^3} + \frac{bb_m}{T^2} + \frac{cc_m}{T} + dd_m} \right] y_{m(k-1)} - \left[\frac{\frac{3aa_m}{T^3} + \frac{bb_m}{T^2}}{\frac{aa_m}{T^3} + \frac{bb_m}{T^2} + \frac{cc_m}{T} + dd_m} \right] y_{m(k-2)} \\ + \left[\frac{\frac{aa_m}{T^3}}{\frac{aa_m}{T^3} + \frac{bb_m}{T^2} + \frac{cc_m}{T} + dd_m} \right] y_{m(k-3)} - \left[\frac{\frac{ee_m}{T}}{\frac{aa_m}{T^3} + \frac{bb_m}{T^2} + \frac{cc_m}{T} + dd_m} \right] a_{c(k-1)}$$

$$+[\frac{\frac{ee_m}{T} + ff_m}{\frac{aa_m}{T^3} + \frac{bb_m}{T^2} + \frac{cc_m}{T} + dd_m}]a_{c(k)}. \quad (6.3)$$

$TF - 5$ is the transfer function between states and its filtered version, $\frac{y_{filtered}(S)}{y(S)} = \frac{gg \cdot aa_m / aa}{aa_m S^3 + bb_m S^2 + cc_m S + dd_m}$ and is transformed to,

$$\begin{aligned} TF - 5 \Rightarrow y_{filtered(k)} = & [\frac{\frac{3aa_m}{T^3} + \frac{2bb_m}{T^2} + \frac{cc_m}{T}}{\frac{aa_m}{T^3} + \frac{bb_m}{T^2} + \frac{cc_m}{T} + dd_m}]y_{filtered(k-1)} \\ & - [\frac{\frac{3aa_m}{T^3} + \frac{bb_m}{T^2}}{\frac{aa_m}{T^3} + \frac{bb_m}{T^2} + \frac{cc_m}{T} + dd_m}]y_{filtered(k-2)} \\ & + [\frac{\frac{aa_m}{T^3}}{\frac{aa_m}{T^3} + \frac{bb_m}{T^2} + \frac{cc_m}{T} + dd_m}]y_{filtered(k-3)} \\ & + [\frac{gg \cdot aa_m / aa}{\frac{aa_m}{T^3} + \frac{bb_m}{T^2} + \frac{cc_m}{T} + dd_m}]y_{(k)}. \end{aligned} \quad (6.4)$$

$TF - 3$ is the first order differential of states, which has its difference equation as,

$$TF - 3 \Rightarrow \dot{y}_{(k)} = \frac{1}{T}y_{(k)} - \frac{1}{T}y_{(k-1)}. \quad (6.5)$$

$TF - 4$ is the second order differential of states, which has its difference equation as,

$$TF - 4 \Rightarrow \ddot{y}_{(k)} = \frac{1}{T^2}y_{(k)} - \frac{2}{T^2}y_{(k-1)} + \frac{1}{T^2}y_{(k-2)}. \quad (6.6)$$

$TF - 6$ is the integral of product of error (e) to form control parameters (θ_{xxx}) which has its difference equation as,

$$TF - 6 \Rightarrow \theta_{xxx(k)} = \theta_{xxx(k-1)} + \gamma_{xxx}Te_{(k)}. \quad (6.7)$$

Each of the transfer function constants is dynamically programmed to FPGA logic gates using the conversion formula described previously. Note that the performance of the adaptive algorithm will be compared with a simpler a PID controller, which has the general governing equation,

$$\frac{U(s)}{E(s)} = K_p[1 + \frac{1}{\tau_i S} + \tau_d S],$$

where $U(S)$ the is controller output, $E(S)$ is the error or difference between desired value and current value, K_p is control gain, τ_i is integral time constant, and τ_d is derivative time constant. Again, the equation is transformed using backward difference method which results in a discrete time velocity PID controller equation,

$$u_{(k)} = u_{(k-1)} + K_p(1 + \frac{\tau_d}{T})e_{(k)} - [K_p(1 + \frac{2\tau_d}{T} - \frac{T}{\tau_i})]e_{(k-1)} + K_p\frac{\tau_d}{T}e_{(k-2)}. \quad (6.8)$$

6.5 Experimental results

The LabVIEW VI for control experiments has been divided into two parts that communicate but operate independently. The first part is the controller VI which runs on the FPGA PXI-7831R card at a loop period of 0.15 ms (6700 Hz). The second part is the user interface and data processing VI which runs on the PXI-8156B as a real-time target at a nondeterministic loop period of between 1-4

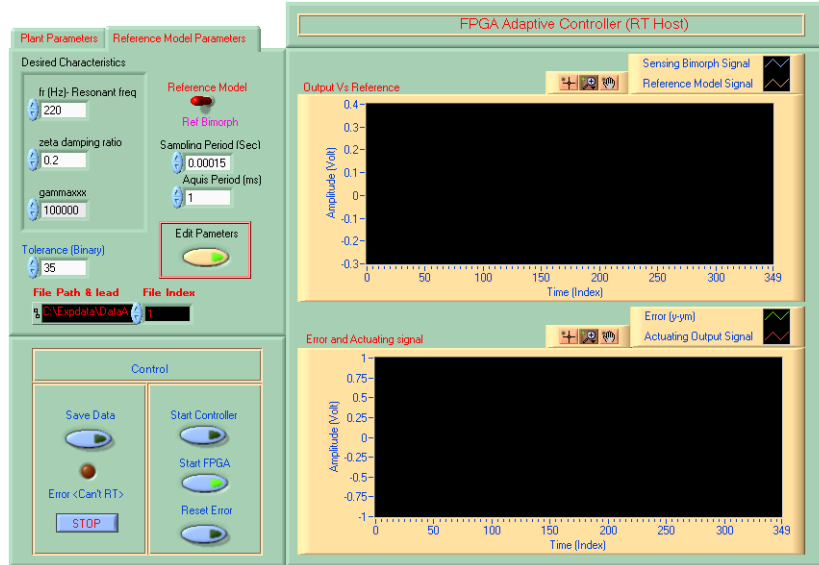


Figure 6.17: User interface VI for adjusting controller configuration and data manipulation.

ms (1000 - 250 Hz).

Communication between two VIs are variables such as controller configurations and monitored outputs. The LabVIEW user interface is shown in Figure 6.17. All parameters shown in the user interface have been previously discussed except the tolerance (binary), which is a binary input range that the controller will ignore (do not response) in order to prevent noise feedback at no input condition. Four responses are transmitted from the controller VI to be plotted and recorded by the user interface VI. These responses are the sensing bimorph signal, reference model signal, error, and actuating signal.

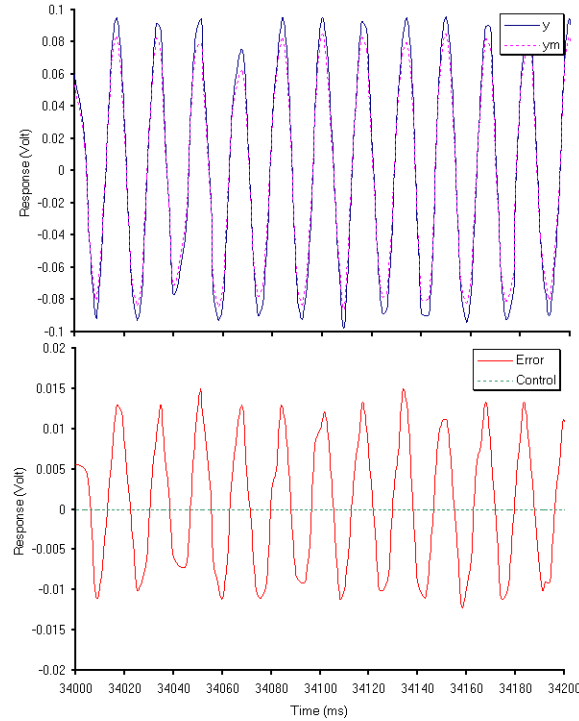


Figure 6.18: Response of the sensor to 60 Hz, 0.185 g input without controller activated. Top: sensing bimorph vs reference bimorph signals, bottom: error signal vs control input.

A simple PID tracker is used as a basis for comparison. The reference model signal is taken directly from the reference bimorph and used as a tracking signal for the sensing bimorph signal to follow. The difference between the two signals is fed to a PID controller which is used to generate an input for the actuation side of the bimorph. Figure 6.18 shows uncontrolled responses of the sensor to a 60 Hz sinusoidal acceleration input of 0.185 g. It can be seen that the reference bimorph generates a signal with slightly less magnitude than the sensing bimorph with approximately no phase shift. The RMS of error signal for this uncontrolled case, as shown the bottom part of Figure, is 0.007 V.

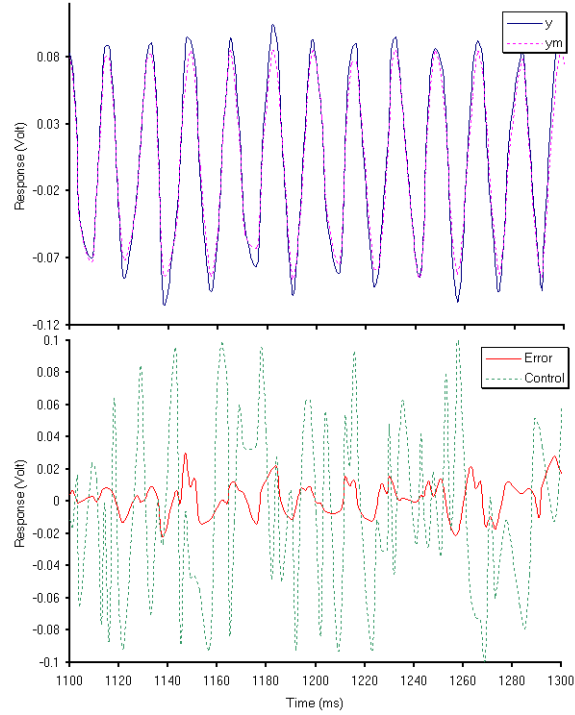


Figure 6.19: Response of the sensor with PID controller tracker to 60 Hz, 0.185 g input. Top: sensing bimorph vs reference bimorph signals, bottom: error signal vs control input.

Because the vibration is sinusoidal at relatively high frequency, anticipation

of the track signal is very important. This make the derivative time constant, τ_d , from PID controller equation 6.8 play an important role in the controller tuning. Figure 6.19 shows the result of tracker with K_p of 1, τ_d of 4, τ_i of 70, and tolerance (binary) of 3. The RMS of error signal for this case is 0.002 V which is a 71.4 percent decrease of error.

Controller based on adaptive algorithm is similarly constructed and tested although it is found that its implementation on the prototype constructed is far from being straightforward. It has been an assumption in chapter 5 that the original acceleration a_c can be estimated using equation $TF - 1$ as shown in the top left frame in Figure 6.16.

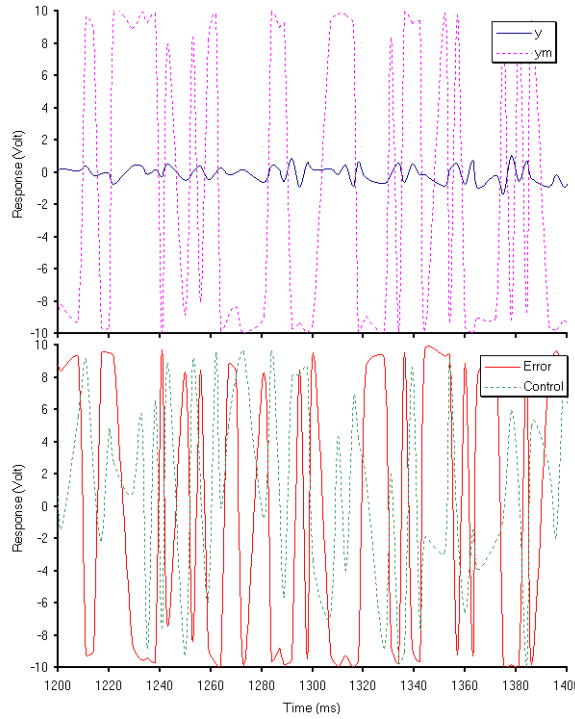


Figure 6.20: Response of adaptive controller to 0.5 g, 60 Hz sinusoidal input using an estimated input from reference bimorph and transfer function $TF - 1$.

The result in Figure 6.20 shows drawback of the transfer function $TF - 1$. In particular equation 6.2 shows that the $TF - 1$ has three zeros in its transfer function thus the feed forward signal not only does need to be smooth at its third order derivative, but it is also required a representation beyond capability of the 16-bit integer used in FPGA. In particular, the reference signal shown in Figure 6.20 is due to integer overflow beyond the value 32768 (10 Volt) and does not represent the true input frequency to the system.

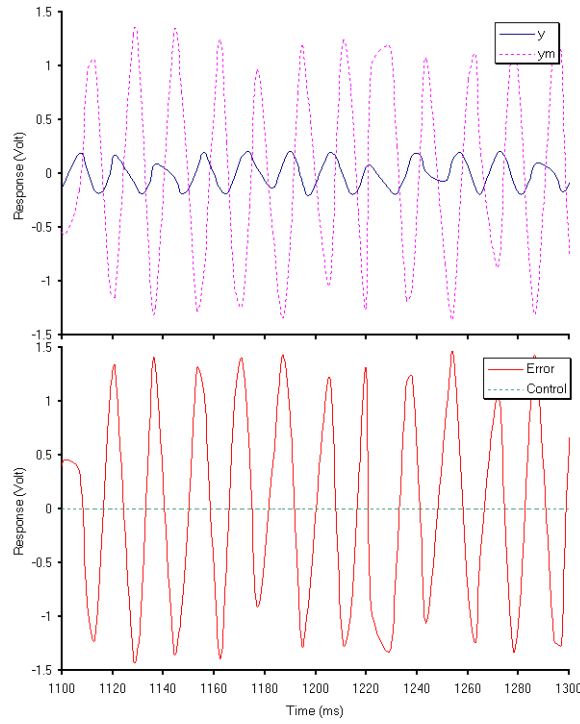


Figure 6.21: Uncontrolled respond of the sensor to 0.5 g, 60 Hz sinusoidal input using signal from reference accelerometer to construct reference model signal.

The reference accelerometer itself can be used as an alternative to the reference bimorph and the estimator in order to obtain a_c . Figure 6.21 shows the uncontrolled system response given the same input condition as in Figure 6.20 but

using the signal from accelerometer to generate the reference model signal. This is resulting in an accurate magnitude and frequency reconstruction. The RMS value of the error signal for this case is 1.237 Volt. The reference model generated for this case is a third order bandpass having a resonant frequency of 220 Hz, damping ratio of 0.2, and out of phase from the uncontrolled sensor.

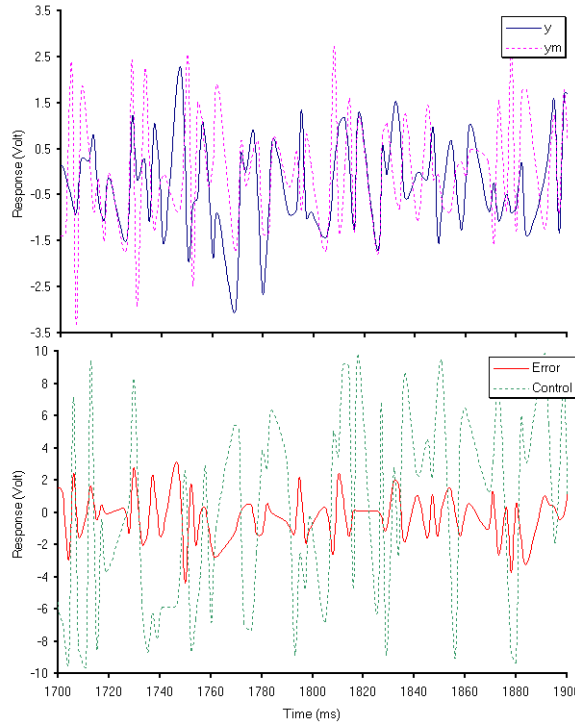


Figure 6.22: Adaptive controlled response of the sensor to 0.5 g, 60 Hz sinusoidal input using the signal from a reference accelerometer to construct reference model signal.

Figure 6.22 shows response of the system with the adaptive controller. Although a comparison between plant and reference model signals does not match perfectly, the RMS of the error for this case is dropped to 0.27 Volt which is a 78.17 percent reduction from before the controller was applied. This is an indication that

the adaptive algorithm does perform as designed. It is also obvious in this case that after the controller is started, there is a frequency distortion in the reference model which is thought to be from a vibration coupling at the base. Another experiment (does not shown here) was performed at a lower input acceleration of 0.075 g at the same frequency and the actuation voltage was limited to 0.8 Volt. Although the vibration coupling was less obvious for this case, feedback loops gain of ten will result in a reduction of error RMS of at least 60.93 percent. The error in responses observed might result from many factors as will be discussed in the next section.

6.6 Discussion

6.6.1 Discussion of result

Implementation of the adaptive sensor algorithm in this chapter has fallen short of expectation built up from successful simulation in chapter 5. The first and probably the major reason is due to the presence of derivatives in various parts of the control loop. These derivatives can usually be lumped with filter blocks in a controller, but were implemented separately here. This is done so that the similar controller can be reused in every feedback loops, which helps when there is a limited number of logic gates. The presence of derivatives poses a serious problem inside the controller whenever there is a ‘jump’ in the signal. The resulting problem is that the controller is prevented from tuning to the right adaptive parameters because of sporadic fluctuations.

A second problem arises because this FPGA chip performs mathematical operations in 16-bit integer format. This can be inadequate for calculations when the system has high gain in feedback loops. This usually results in integer overflow which flips the sign of the resulting number. Since all mathematical operations are internal, detection of numerical overflow is very difficult. The only way to detect this

problem is to send the data to the user interface VI. This type of online monitoring increases the required processing and results in reduction of acquisition period.

A third problem may arise because the experiment has been performed at relatively the low frequency rather than closer to the natural frequency of the sensor as designed. This was done primarily to aid visualization of the process via a user interface VI. Unfortunately, the user interface VI has a very low sampling period restriction due to its internal clock. However, as seen in Figure 6.14, the mathematical model developed and the experimental result on the actuating performance is deviate at frequencies lower than natural frequency. This might be due to an unpredicted nonlinear (frequency dependent) damping, which would result in an incorrect magnitude of input calculated for the adaptive algorithm.

A fourth problem arises from a vibration coupling between the controlled sensor (plant) and reference sensor. It can be seen in Figure 6.22 that after the force is applied at actuation side, the reference signal has a higher frequency which interferes with its original frequency. This is thought to be due to vibration transmission from the actuating bimorph through the solid support base and would result in different vibration sensed between sensing bimorph and reference bimorph (or reference accelerometer).

In the adaptive controller experiments, an input frequency of 60 Hz is used primarily because it is the lowest frequency at which the potential generated by the bimorph has good signal to noise ratio (SNR). Loop gains used in these experiments are 20, the a value different from 10000 used in the simulation to prevent the integer overflow. However, as discussed in chapter 5, although the system seems to be stable, exact time required for adaptation can not be predicted. For experiments shown in this chapter, the controller was allow to adapt for approximately five to six minutes. Adjusting loop gains will affect the adaptation time as discussed in

chapter 5.

Experimental results with a PID controller, although resulting in lower error signal RMS values, can not really be considered successful. Because the acceleration input to the system has been passed through the reference bimorph before being transmitted to the controller, the PID controller only sees history (a delayed version) of the input. This means that the simple PID controller used will never be able to drive the system to a perfect match.

Estimation of the input signal requires some discussion. As seen in the control diagram of Figure 6.16, estimation of input a_c using reference bimorph and transfer function $TF-1$ provides incorrect estimation of the signal due to its smoothness requirement. Although the signal from the other accelerometer can be used to help reconstruct the input signal, it defeats the purpose of this sensor development. A recommended method that can be used for input estimation is an “unknown input observer (UIO)” method [72], which has a potential to not only estimate the input but also states of the system. This approach would result in a complete elimination of all derivatives in the adaptive control algorithm. However this method is still under study, and will take some time before this theory becomes widely accepted.

6.6.2 Sensor Calibration

The sensor calibration issue might be raised in the process of taking this concept to the real production. As discussed previously, the algorithm used for the controller is the model reference adaptive control (MRAC) where a reference signal is generated by the adaptive controller that monitors both input and output at the same time. The controller use this information and a bandwidth requirement programmed into the controller to calculate parameters needed for sensor adaptation. In a sense, the controller is incorporated with a set of “master sensor” parameters

that are continuously adjusted and monitored the system operation. Adaptation is then a process of recalibrating the sensor to meet the controller requirements.

However, the real benefit of MRAC algorithm is that the controller doesn't need to be online at all times. It can be taken off-line whenever the adapting (tuning or recalibrating) is not needed. The controller and master sensor can be kept in a safe place. The unique feature of the MRAC type controller is that it is basically composed of a number of integrator loops that continuously integrate an error signal to search for the most suitable adaptive parameters, and then hold the parameters when the sensor is tracking the signal from the reference model. Taking the controller and master sensor offline is possible by switching off the error signals to all integrators, which will immediately stop the process of adapting.

It is easy to infer that this sensor concept will be as accurate as the master sensor that is used inside the controller (in contrast with conventional sensors which must be manually calibrated). This method allows the sensor to be both accurate and robust. Another application of this sensor concept is that the controller can be kept online at all time continuously monitoring the system. The only problem with this option is that the master sensor in the controller might degrade together with the system, and thus resulting in lower long term accuracy. Still, the advantage of continuous control is that the system dynamics can be adjusted as needed at all time in the controller. However, no matter in what configuration it operates, the true benefit of this adaptive sensor is a capacity to extract frequency component information instantaneously where less amount of data is transmitted from the sensor as discussed in chapter 1.

6.7 Summary

In this chapter the experimental aspect of the research has been discussed. The chapter begins with a discussion on fabrication of the support components for the sensor and then equipments and instrumentations used for the experiments are introduced. Experimentation began with a series of system identification studies in order to confirm the physical parameters used in mathematical modeling and control system design. After equations for binary number representation and discrete time control equations on programmable gated arrays is presented, the experimental results are presented. Although PID tracking controller results show that this simpler controller method can be used to reduce error between reference and sensing bimorphs to some degree, it does not make sense to use because it requires an active reference signal to operate.

Adaptive control experiments have found that implementation of the adaptive sensor does not measure up to the simulations in the last chapter. The reasons found are partly due to adaptive controller design and partly due to the specific implementation. With regard to the controller design, differentiators due to estimation of both input and the states are responsible for poor performance of the controller in tuning to the correct values in the presence of noise. The theory of unknown input observer is recommended in the future to eliminate this problem. With regard to the vibration coupling between actuating bimorph and reference sensor, a vibration isolator has to be installed to separated two part from each others yet still allow both parts to sense the same vibration. This will pose a difficult problem when sensor package has to be designed in real production. Because of limitations in the space for programmable gated arrays, a compromise on features is required in the implementation of the control algorithm. Namely, the mathematical operation is done using 16-bit integer with no saturation, adaptive controller loop gains are

forced to be the same for every loop, every block of transfer functions constructed are always set in a non-reentrant (reused) mode which might interfere with timing inside the controller, and because large amounts of data is transmitted between the FPGA VI and the user interface VI, the acquisition loop period has been found to be nondeterministic. This might results from insufficient system processing and memory. This equipment problem can be solved by either redesign of adaptive algorithm to be simpler or using a more spacious version of programmable gated arrays. A faster/more memory PXI controller is also needed for processing and gathering data.

Despite of all the particular requirements for equipment and the discrete controller, the programmable gate arrays would be used for experimentation only and would not be expected to be used on a production sensor. In production sensors, an analog circuit/microcontroller should be used because it naturally performs faster. This also means that the controller circuit will be a continuous version instead of discrete version as shown in this chapter. For that case, the adaptive controller design in chapter 5 can be directly transformed to analog circuit and should result in a better match to the design simulations.

Chapter 7

Conclusion and Recommendation

7.1 Brief summary of the work

The work in this dissertation can be divided into two major parts. The first part is bio-inspired design and deals with the hair cell, its function, and its mathematical model development. The second part is sensor development and deals with sensor structure design, its control algorithm, its utilization, and experimental evaluation.

A hair cell mathematical model has been developed using a bond graph approach. This required synthesis of equations governing ionic channels and an efficient way to model and integrate the electromotility mechanism of the cell's membrane. A simulation of the model is used to compare with published physiological data in both time and frequency domain and dynamic characteristics of the model are identified and discussed. The model builds a system level understanding of the hair cell and of the dependence of dynamic characteristics on the constituent elements.

Examining the arrangement of hair cells, tectorial membrane, and basilar membrane in the organ of corti using the model provides an efficient way to design a bio-inspired sensor. The sensor structure is designed based on piezoelectric bimorphs in a sensor/actuator pair configuration. The arrangement made possible a means to actively change, regulate, or control band pass characteristics of the sensor in the same way inner hair cells and outer hair cells regulate response of each section of organ of corti and the cochlea.

As a projection of how inner hair cells and outer hair cells might communicate with each other, an adaptive control algorithm was designed. Simulation studies showed that the system is controllable and would be able to tune to characteristics that have the same order of the system with relatively close resonant frequencies and damping ratios (due to power limiting issue). This research also experimented with a reduced version of the adaptive algorithm. Further, simulation showed that a smaller and simpler version of the controller could be effective and was implemented.

Experiments in the latter part of this dissertation are driven toward two objectives, verifying physical parameters for modeling and testing the adaptive control algorithm performance. It is shown that the physical parameters used to model bimorphs match well with experimental results, especially in the region close to the natural frequency of the system. The experiments on the control algorithm utilized a field programmable gated array (FPGA) with real-time operating system. It is found that a more basic PID control tracker can also be used to tune the sensor output to better match with the signal from the reference model although it is impractical to implement. Experimental results from testing the adaptive algorithm exhibited a trend that indicates the algorithm can adapt the sensor in the proper direction, although it fell short of what simulation results has predicted. The presence of derivatives in the control loops, vibration coupling between actuating bimorph and reference sensor, and limitation of programmable gated arrays were shown to be responsible for problems in implementation.

7.2 Original contribution of this study

This research aimed at developing an accelerometer with adaptive features similar to how hair cells and the organ of corti regulate the frequency selectivity

and dynamic range of the cochlea. Toward the end of this research, the objectives as discussed in chapter 1 are evaluated. The following are the contributions of this study.

1. Mathematical model of hair cells has been developed using bond graph approach. Specifically, the model provides an energetic representation of the hair cell active mechanism at a system level. Although the source of active force generation in hair cells is still under some debate, the bond graph model can also be easily expanded to capture the new feature as discovered.
2. A bio-inspired sensor system has been designed. Discussion in chapter 4 shows that the design can be made for micro-scale and macro-scale sensor. Laboratory prototyping of the macro-scale sensor has been completed.
3. Adaptive sensor algorithms have been developed based on a reduced version of gradient rule and stability rule. Switching logic has been designed and integrated to the algorithm using the output level of the sensor as an input for decision which create another tier of adaptation based on decision. The system has been shown to perform as designed in simulation. The specific experimental implementation of the prototype suggested that this adaptive sensor design may need a better state observer to eliminate derivatives in the control loop, a vibration isolator mechanism to decouple the actuating element from the reference sensor, and a spacious/more capable programmable logic gate chip for implementation.

7.3 Recommendation and future research

There are aspects of this dissertation research that can be extended and improved. For mathematical modeling of the hair cell, an impedance matrix is

used for modeling electromotility for the reason that the elements of the impedance matrix can be easily found in literature. However, it has been known that the outer hair cell electromotility mechanism can work at high frequency in range of kHz, and a non linear model for electromotility (either at the plasma membrane or cilia bundle) might be responsible for the ability to generate force at higher frequency. However, as more experimental data on this nonlinearity become available, the bond graph model can be readily modified with most of the structure remaining the same to capture this feature.

Much of the improvement can be achieved in the sensor development part. First, there are a number of passive methods that can be used for changing the frequency response characteristic of piezoelectric bimorph. For example, the length of the cantilever can be changed or the beam can be pulled such that effective stiffness of the sensor is changed. This might be an alternate solution that is more suitable where the sensor has limited power source because the actuation part would not need constant power input.

Second, the adaptive control algorithm used can be improved in at least two ways. To begin with, the bond graph model for the bimorph assumed just one approximated lumped mass. The model can be considered satisfactory in the region around and below the first resonant mode. Using a more complicated model such as Pi or T model would greatly expand the complexity of the adaptive controller, but it might result in better overall performance over a broad frequency range. In addition, the simplest adaptive algorithm developed and implemented in this dissertation is based on a reduced version of the MIT gradient rule. Approximation of the states of the system required some derivatives in the control loops. The ideal situation is to have these stand-alone derivatives lumped inside the filters. However, controller prototype as implemented in a programmable gated array (FPGA) had

limited space. Lumping the derivatives into filters in each loop creates control loops that have distinct filters which take enormous space on the FPGA chip. One solution might be to design an adaptive algorithm without any derivatives, which might be possible using the theory of unknown input observer (UIO). Another solution will be an adaptive algorithm that is less complicated and thus consumes less space. Both of these techniques are still under research in adaptive control theory.

A third area involves the prototype used in this dissertation. This prototype was designed to be relatively large compared with a typical sensor so that measurements could be performed easily. This results in relatively large signal output and good SNR due to large deflection displacement of the bimorphs in the sensing function. Due to noise and ground loop prevention, a buffer amplifier section was powered by a battery which has limited power. This is a problem in control situations where high power is required to drive bimorphs to compensate for their large motion. Further development should be run on a relatively smaller system. The expected form of such a sensor could be as a MEMS system or built using even smaller piezoelectric material such as carbon nanotubes.

Expansion of this study for future research can be done in several areas. However, the main area should be related to sensor networking. Because the sensor developed in this dissertation is based on the mechanism of the organ of corti which performs as a cascade of band-pass filters, naturally, this kind of sensor should be arranged into a network. Each sensor should target a specific natural frequency and be adaptively tuned or controlled so that it can either maintain or change its frequency characteristic as needed. Information received from an array of these sensors should be integrated together with some form of data fusion. As discussed previously, the collective information should yield frequency spectrum of an excitation by observing sensor's vibration amplitude.

The adaptive control algorithm developed should be expandable to accommodate an array of sensor. In most situations where one section of the sensor does not need a continuous tuning, adding switching in the controller loop should allow a single controller to monitor and tune each section of the array in succession. This will reduce overall power consumption of the system.

Presence of the reference sensor in the same sensor package might reduce overall accuracy in the long run due to degradation of the reference sensor from the dynamic environment. This might result in tuning of the sensor to an incorrect value. A solution might be to store the reference sensor in a separated package and establish a wireless link between the sensor system and the reference sensor only when tuning is needed. The process of tuning in this case can be done by exciting the sensor and reference sensor at the same time with a known input.

Overall, this dissertation has made a step toward understanding how to develop and use adaptive algorithms in sensor applications. Although there are many practical issues that have to be solved in order to make this concept become a reality, the benefit of having an adaptive sensor is obvious. This type of sensor should cope better with a changing environment and ultimately can reduce cost of manufacturing because less model types need to be produced to offer a solution for a range of applications.

Appendix

% Physical Parameters Used to Perform Simulations
 % function bimorph parameter updated 24/August/2004
 % Dimensional Parameters using PZT - 5H

% OHC part - Actuator

bo = 0.0127; % unit = m, beam width
 hPZTo = 0.1397*(10^-3); % unit = m, thickness of PZT layer
 hBRASSo = 1.27*(10^-4); % unit = m, thickness of bimorph layer (one layer)
 lo = 31.8*(10^-3); % unit = m, beam length
 lo0 = 6.4*(10^-3); % unit = m, part of beam that does not take stress

% IHC part - Sensor

bi = 0.0127; % unit = m, beam width
 hPZTi = 0.1397*(10^-3); % unit = m, thickness of PZT layer
 hBRASSi = 1.27*(10^-4); % unit = m, thickness of bimorph layer (one layer)
 li = 31.8*(10^-3); % unit = m, beam length
 li0 = 6.4*(10^-3); % unit = m, part of beam that does not take stress

% Material Properties (PZT - 5H) assume the same for both bimorph

D31 = -274*10^-12; % unit = C/N, Piezoelectric coupling constant D31
 K33T = 3400*8.854*10^-12; % unit = F/m, Dielectricity
 S11E = 16.5*10^-12; % unit = m^2/N, Material compliance (is = 1/E or 1/Modulus of elastic

% Material Properties (Brass Reinforcement) assume the same for both bimorph

EBRASS = 117*(10^9); % unit = Pa, Modulus of elasticity of the brass reinforcement

% Equivalent mass

m = 1.575*(10^-3); % unit = kg, (equivalent lumped mass of one bimorph) } see f
 provedmass = 0*(10^-3); % unit = kg, (proved mass at the middle of the beam) }
 mtot = 2*m + provedmass; % unit = kg, (proved mass at the middle of the beam) }

% Damping from exponential decay experiment

bco = 0.0359025; % unit = N s/m, (estimated OHC internal damping coefficient) } 0.04
 bci = 0.0359025; % unit = N s/m, (estimated IHC internal damping coefficient) }

% Electrical Components

Rs = 99; % unit = ohm, (serial resistor)

% 2-ports Capacitance (see constitutive relation sheet)

% OHC

c11o = (((D31^2)-4*K33T*S11E)*4*bo*(hPZTo^3)) / (((lo-lo0)^3)*S11E*(5*(D31^2)-2*S11E*K33T)) .
 + EBRASS*8*bo*(hBRASSo^3)/((lo-lo0)^3);

c12o = (-6*D31*(hPZTo^2))/((lo^2)*(5*(D31^2)-2*K33T*S11E));

c21o = (-6*D31*(hPZTo^2))/((lo^2)*(5*(D31^2)-2*K33T*S11E));

c22o = (-S11E*hPZTo)/(lo*bo*(5*(D31^2)-2*K33T*S11E));

% IHC

```

c11i = (((D31^2)-4*K33T*S11E)*4*bi*(hPZTi^3)) / (((li-li0)^3)*S11E*(5*(D31^2)-2*S11E*K33T)) ...
+ EBRASS*8*bi*(hBRASSi^3)/((li-li0)^3);
c12i = (-6*D31*(hPZTi^2))/((li^2)*(5*(D31^2)-2*K33T*S11E));
c21i = (-6*D31*(hPZTi^2))/((li^2)*(5*(D31^2)-2*K33T*S11E));
c22i = (-S11E*hPZTi)/(li*bi*(5*(D31^2)-2*K33T*S11E));

```

% Abbreviation in plant transfer function

```

aa = Rs*mtot;
bb = c22o*mtot + Rs*bci + Rs*bco;
cc = (bci+bco)*c22o + (c11o+c11i)*Rs;
dd = c11o*c22o+c11i*c22o-c12o^2;
ee = c22i*mtot*Rs;
ff = c21i*c22o*mtot;
gg = c12o*c21i;
hh = mtot*c12o;
ii = (bco+ bci);
jj = c11i;

```

% Referenced model characteristic (user set value !!)

```

zeta = 0.2; % reference model damping ratio
fr = 220; % reference model resonant frequency in Hz
Mp = 20*log10(1/(2*zeta*sqrt(1-zeta^2))); % reference model peak resonant magnitude in dB

```

% Abbreviation in reference model transfer function (5.26)

```

aam = 1;
bbm = (4*pi*fr*zeta)/sqrt(1-2*(zeta^2)) + 2*pi*fr;
ccm = 4*(pi^2)*(fr^2)/(1-2*(zeta^2)) + 8*(pi^2)*(fr^2)*zeta/sqrt(1-2*(zeta^2));
ddm = 8*(pi^3)*(fr^3)/(1-2*(zeta^2));
eem = 4*(pi^2)*(fr^2)/(1-2*(zeta^2));
ffm = 0;

```

% Bode diagram of the plant and reference model

```

numerator = [ee ff];
denominator = [aa bb cc dd];
numerator_m = [eem ffm];
denominator_m = [aam bbm ccm ddm];
omegarange = logspace(0,5,1000);
[mag,phase,omega] = bode(numerator, denominator,omegarange);
[magm,phasem,omegam] = bode(numerator_m, denominator_m,omegarange);
subplot(2,1,1),
semilogx(omega/(2*pi),20*log10(mag),omegam/(2*pi),20*log10(magm))
xlabel('Frequency (Hz)')
ylabel('Gain (dB)')
legend('plant', 'reference model')

```

```

grid on
title('Frequency Response of The Plant and Reference Model')
subplot(2,1,2),
semilogx(omega/(2*pi),(phase),omegam/(2*pi),(phasem))
xlabel('Frequency (Hz)')
ylabel('Phase (Deg)')
legend('plant', 'reference model')
grid on

% Matrices for Lypunov (P-Q)
% Q matrix % diagonal only
Q1 = 1;
Q2 = 1;
Q3 = 1;
% P matrix
P11 = ((bbm*(ccm^2)*Q1) - (ddm*ccm*aam*Q1) + ((bbm^2)*ddm*Q1) + (bbm*(ddm^2)*Q2) + ((ddm
    (2*ddm*(bbm*ccm - ddm*aam)));
P12 = (((bbm^2)*ccm*Q1) + (aam*(ddm^2)*Q2) + ((ddm^2)*ccm*Q3)) / ...
    (2*ddm*(bbm*ccm - ddm*aam));
P13 = (aam*Q1)/(2*ddm);
P22 = ((ddm*(aam^2)*Q1) + (ccm*ddm*aam*Q2) + ((bbm^3)*Q1) + (ddm*(bbm^2)*Q2) + (bbm*(ddm
    (2*ddm*(bbm*ccm - ddm*aam)));
P23 = (aam*((bbm^2)*Q1) + (bbm*ddm*Q2) + ((ddm^2)*Q3))) / ...
    (2*ddm*(bbm*ccm - ddm*aam));
P33 = (aam*((aam*bbm*Q1) + (aam*ddm*Q2) + (ccm*ddm*Q3))) / ...
    (2*ddm*(bbm*ccm - ddm*aam));

% Plant and Reference model in state-space format
% plant
matrixA = [0 1 0; 0 0 1; -dd/aa -cc/aa -bb/aa];
matrixB = [0 0 0; 0 0 0; ee/aa ff/aa -gg/aa];
matrixC = [1 0 0; 0 1 0; 0 0 1];
matrixD = [0 0 0; 0 0 0; 0 0 0];
iniplant = [0;0;0];
% model
matrixAm = [0 1 0; 0 0 1; -ddm/aam -ccm/aam -bbm/aam];
matrixBm = [0 0; 0 0; eem/aam ffm/aam];
matrixCm = [1 0 0; 0 1 0; 0 0 1];
matrixDm = [0 0; 0 0; 0 0];
inimodel = [0;0;0];
% Test validity of matrix P and Q
matrixP = [P11 P12 P13; P12 P22 P23; P13 P23 P33];
matrixQ = (matrixAm')*matrixP + matrixP*matrixAm;

```



```
% Adaptive loop gain (can do as dependently by adjusting gamma or independently)
gamma = 10000;
gamma111 = gamma;
gamma121 = gamma;
gamma131 = gamma;
gamma112 = gamma;
gamma122 = gamma;
gamma132 = gamma;
gamma233 = gamma;
gamma223 = gamma;
gamma213 = gamma;
gamma232 = gamma;
gamma222 = gamma;
gamma212 = gamma;
gamma231 = gamma;
gamma221 = gamma;
gamma211 = gamma;
```

Bibliography

- [1] A.S. Popel A.A. Spector, M. Ameen. Simulation of motor-driven cochlear outer hair cell electromotility. *Biophysical Journal*, 81:11–24, 2001.
- [2] A.S. Popel A.A. Spector, W.E. Brownell. Analysis of the micropipet experiment with the anisotropic outer hair cell wall. *The Journal of Acoustical Society of America*, 103(2):1001–1006, 1998.
- [3] A.S. Popel A.A. Spector, W.E. Brownell. Estimation of elastic moduli and bending stiffness of the anisotropic outer hair cell wall. *The Journal of Acoustical Society of America*, 103(2):1007–1011, 1998.
- [4] A.S. Popel A.A. Spector, W.E. Brownell. Nonlinear active force generation by cochlea outer hair cell. *The Journal of Acoustical Society of America*, 105(4):2414–2420, 1999.
- [5] A.S. Popel A.A. Spector, W.E. Brownell. Effect of outer hair cell piezoelectricity on high-frequency receptor potentials. *The Journal of Acoustical Society of America*, 113(1):453–461, 2003.
- [6] M. Adachi and K.H. Iwasa. Electrically driven motor in the outer hair cell: Effect of a mechanical constraint. *Proceeding of National Academy of Science*, 96:7244–7249, 1999.
- [7] L. Riddle A.G. Andreou, D.H. Goldberg. Heterogeneous intergration of biomimetic acoustic microsystems. *Proceeding of The 2001 IEEE International Symposium on Circuits and Systems*, 2:189–192, 2001.

- [8] A.D. Mehta P. Martin A.J. Hudspeth, Y. Choe. Putting ion channels to work: Mechanoelectrical transduction, adaptation, and amplification by hair cells. *Proceeding of the National Academy of Science*, 97(22):11765–11772, 2000.
- [9] G.N. Akoev and G.N. Andrianov. *Sensory hair cells: Synaptic transmission*. Springer–Verlag, 1993.
- [10] J.B. Allen and S.T. Neely. Micromechanical models of the cochlea. *Physics Today*, 45(7):40–48, 1992.
- [11] K.J. Astrom and B. Wittenmark. *Adaptive Control: second edition*. Adison-Wesley Longman, 1995.
- [12] L.K. Baxter. *Capacitive Sensors: Design and Applications*. IEEE Press, 1997.
- [13] J.J. Beaman and H.M. Paynter. *Modeling of Physical Systems*. The University of Texas at Austin, 1993.
- [14] F. Bezanilla. *The Nerve Impulse*. <http://pb010.anes.ucla.edu/med98a.htm>, 1998.
- [15] S. Bleack. *A New Model of Outer Hair Cell Electromotility*. <http://www.aps.org/meet/MAR00/baps/baps/abs/S4120014.html>, 1998.
- [16] J. Bor and C. Wu. Analog electronic cochlea design using multiplexing switched-capacitor circuits. *IEEE Transactions on Neural Networks*, 7(1):155–167, 1996.
- [17] J. Brignell and N. White. *Intelligent Sensor Systems : Revised Edition*. Institute of Physics Publishing, Bristol, UK., 1996.

- [18] W.E. Brownell. *Observation on a motile response in isolated hair cells in Mechanism of Hearing: edited by W.R. Webster and L.M. Aiken.* Monash University Press, 1983.
- [19] I.J. Busch-Vishniac. *Electromechanical Sensors and Actuators.* University of Texas at Austin, 1996.
- [20] I.J. Busch-Vishniac and H.M. Paynter. Bond graph models of acoustical transducers. *Journal of the Franklin Institute*, 328(5/6):663–673, 1991.
- [21] P. Cariani. To evolve an ear: epistemological implications of gordon pask’s electrochemical devices. *Systems Research*, 10(3):19–33, 1993.
- [22] P. Cariani. Epistemic autonomy through adaptive sensing. *Proceeding of the 1998 IEEE ISIC/CRA/ISAS Joint Conference, Gaithersburg, MD*, pages 718–723, 1998.
- [23] H.J. Chiel and R.D. Beer. The brain has a body: adaptive behavior emerges from interaction of nervous system, body and environment. *Trends in Neuroscience*, 20(12):553–557, 1997.
- [24] A. Cohen and M. Furst. Integration of outer hair cell activity in a one-dimensional cochlear model. *The Journal of Acoustical Society of America*, 115(5):2185–2192, 2004.
- [25] A.C. Crawford and R. Fettiplace. The mechanical properties of ciliary bundles of turtle cochlea hair cells. *Journal of Physiology*, 364:359–379, 1985.
- [26] A. Stoica M. Buehler D. Keymeulen, R. Zebulum. Initial experiment of re-configurable sensor adapted by evolution. *Proceeding of The 4th International Conference on Evolvable Systems: From Biology to Hardware, Tokyo, Japan*, 2001.

- [27] N. Klocker J. Ludwig U. Schulte S. Waldegger J.P. Ruppersberg P. Dallos B. Fakler D. Oliver, D.Z.Z. He. Intracellular anion as the voltage sensor of prestin, the outer hair cell motor protein. *Science*, 292:2340–2343, 2001.
- [28] B. Bramer T. Gessner W. Dotzel D. Scheibner, J. Mehner. Wide range tuneable resonators for vibration measurements. *Microelectronic Engineering*, 67-68:542–549, 2003.
- [29] J. Mehner B. Bramer T. Gessner W. Dotzel D. Scheibner, J.Wibbeler. A frequency selective silicon vibration sensor with direct electrostatic stiffness modulation. *Analog Integrated Circuits and Signal Processing*, 37:35–43, 2003.
- [30] J. Mehner W. Dotzel T. Gessner D. Scheibner, J.Wibbeler. Silicon vibration sensor arrays with electrically tunable band selectivity. *Microsystem Technologies*, 8:314–317, 2002.
- [31] P. Dallos and B.N. Evans. High-frequency motility of outer hair cells and the cochlear amplifier. *Science*, 267:2006–2009, 1995.
- [32] F. Davi. Dynamics of linear piezoelectric rods. *Journal of Elasticity*, 46:181–198, 1997.
- [33] R.C. Rosenberg D.C. Karnopp, D.L. Margolis. *System Dynamics: Modeling and Simulation of Mechatronic Systems*. John Wiley & Sons, 2000.
- [34] L. Deng and C.D. Geisler. A composite auditory model for processing speech sounds. *The Journal of Acoustical Society of America*, 82(6):2001–2012, 1987.
- [35] N. Deo and K. Grosh. Two-state model for outer hair cell stiffness and motility. *Biophysical Journal*, 86:2141–2146, 2004.

- [36] N. Deo and K. Grosh. Simplified nonlinear outer hair cell models. *The Journal of Acoustical Society of America*, 117(4):3519–3528, 2005.
- [37] J.R. Holt K.Y. Kwan S.Y. Lin M.A. Vollarth A. Amalfitano E.L. Cheung B.H. Derfler A. Duggan G.S.G. Geleoc P.A. Gray M.P. Hoffman H.L. Rehm D. Tamasauskas D.S. Zhang D.P. Corey, J. Garcia-Anoveros. Trpa1 is a candidate for the mechanosensitive transduction channel of vertebrate hair cells. *Nature*, 03066:1–8, 2004.
- [38] R.F. Wolffenbuttel E. Cretu, M. Bartek. Spectral analysis through electromechanical coupling. *Sensors and Actuators*, 85:23–32, 2000.
- [39] A.H. Gitter F. Rattay, I.C. Gebeshuber. The mammalian auditory hair cell: A simple electric circuit model. *The Journal of Acoustical Society of America*, 103(3):1558–1565, 1998.
- [40] R. Fettiplace and A.J. Ricci. Adaptation in auditory hair cells. *Current Opinion in Neurobiology*, 13:446–451, 2003.
- [41] J.E. Freund and R.E. Walpole. *Mathematical Statistic: third edition*. Prentice-Hall, 1992.
- [42] C. Koppl G.K. Yates G.A. Manley, D.L. Kirk. In vivo evidence for a cochlear amplifier in the hair-cell bundle of lizards. *Proceeding of the National Academy of Science*, 98(5):2826–2831, 2001.
- [43] Z. Gajic and M. Lelic. *Modern Control Systems Engineering*. Prentice Hall, 1996.
- [44] W.F. Ganong. *Review of Medical Physiology*. Appleton & Lange, 1997.

- [45] C.D. Geisler. *From Sound to Synapse: Physiology of The Mammalian Ear*. Oxford University Press, 1998.
- [46] A. Gelb and W.E. Vander Velde. *Multiple-input describing functions and nonlinear system design*. McGraw-Hill, 1968.
- [47] S.A. Gelfand. *Hearing an introduction to Psychological and Physiological Acoustics*. Marcel Dekker, 1998.
- [48] R.B. Patuzzi D. Robertson G.K. Yates, B.M. Johnstone. Mechanical pre-processing in the mammalian cochlea. *Trends in Neurosciences*, 15(2):57–62, 1992.
- [49] B.P. Gogoi and C.H. Mastrangelo. Force balanced micromachined pressure sensors. *IEEE Transactions on Electron Devices*, 48(8):1575–1584, 2001.
- [50] H. Harada. *Bird, fish homing instinct linked to iron inside ears*. Japan Times Online (May 2001), 2001.
- [51] D.Z. He and P. Dallos. Somatic stiffness of cochlear outer hair cells is voltage-dependent. *Proceeding of National Academy of Science USA.*, 96:8223–8228, 1999.
- [52] M.J. Hewitt and R. Meddis. An evaluation of eight computer models of mammalian inner hair-cell function. *The Journal of Acoustical Society of America*, 90(2):904–917, 1991.
- [53] A.L. Hodgkin and A.F. Huxley. A quantitative description of membrane current and its application to conduction and excitation to conduction and excitation in nerve. *The Journal of Physiology*, 117:500–544, 1952.

- [54] M.C. Holley and J.F. Ashmore. A cytoskeletal spring in cochlear outer hair cells. *Nature*, 335:635–637, 1998.
- [55] J.R. Holt and D.P. Corey. Two mechanism for transducer adaptation in vertebrate hair cells. *Proceeding of the National Academy of Science*, 97(22):11730–11735, 2000.
- [56] G.D. Housley and J.F. Ashmore. Ionic currents of outer hair cells isolated from the guinea-pig cochlea. *Journal of Physiology*, 448:73–98, 1992.
- [57] J. Howard and A.J. Hudspeth. Mechanical relaxation of the hair bundle mediates adaptation in mechanoelectrical transduction by the bullfrog’s saccular hair cell. *Proceeding of National Academy of Science*, 84(9):3064–3068, 1987.
- [58] A.J. Hudspeth. The cellular basis of hearing: The biophysics of hair cells. *Science*, 230(4727):745–752, 1985.
- [59] T. Ikeda. *Fundamentals of Piezoelectricity*. Oxford University Press, 1990.
- [60] K.H. Iwasa. Effect of membrane motor on the axial stiffness of the cochlear outer hair cell. *The Journal of Acoustical Society of America*, 107(5):2764–2766, 2000.
- [61] K.H. Iwasa and R.S. Chadwick. Does nonlinear capacitance of the outer hair cell really improve its high-frequency response? *The Journal of Acoustical Society of America*, 102(5):3055–3056, 1997.
- [62] K.H. Iwasa and G. Ehrenstein. Cooperative interaction as the physical basis of the negative stiffness in hair cell stereocilia. *The Journal of Acoustical Society of America*, 111(5):2208–2212, 2002.

- [63] S.A. Binder-Macleod J. Ding, A.S. Wexler. A mathematical model that predicts the force-frequency relationship of human skeletal muscle. *Muscle & Nerve*, 2002.
- [64] A.J. Hudspeth J. Howard, W.M. Roberts. Mechanoelectrical transduction by hair cells. *Annual Review of Biophysics and Biophysical Chemistry*, 17:99–124, 1988.
- [65] A.A. Platonov J. Szabatin, V.E. Melnikov. Analog-digital wide-range measurement systems with adaptively adjusted quartz glass sensors. *Proceeding of IEEE Instrumentation and Measurement Technology Conference, Brussels, Belgium*, pages 1154–1159, 1996.
- [66] D.Z.Z. He-K.B. Long L.D. Madison P. Dallos J. Zheng, W. Shen. Prestin is the motor protein of cochlear outer hair cells. *Nature*, 405:149–153, 2000.
- [67] K.L. Jackson. *The Lateralis System: Ichthyology Web Resources*. <http://www.biology.ualberta.ca/jackson.hp/IWR/content/anatomy/lateralis/index.php>, 1999.
- [68] F. Jaramillo and A.J. Hudspeth. Displacement-clamp measurement of the forces exerted by gating springs in the hair bundle. *Proceeding of the National Academy of Science*, 90:1330–1334, 1993.
- [69] D.H. Jen and C.R. Steele. Electrokinetic model of cochlear hair cell motility. *The Journal of Acoustical Society of America*, 82(5):1667–1678, 1997.
- [70] R.A. Jerry and A. Dutta. Molecular motor and electrokinetic contributions to outer hair cell electromotility. *Journal of Neurophysiology*, 79:471–473, 1998.
- [71] T.K. Cooney J.G. Smits, S.I. Dalke. The constituent equations of piezoelectric bimorphs. *Sensors and Actuators: A Physical*, 28:41–61, 1991.

- [72] J. Jin and M. Tahk. Time-delayed state estimator for linear systems with unknown inputs. *International Journal of Control, Automation, and Systems*, 3(1):117–121, 2005.
- [73] T.J. Lynch III R. Leong T.F. Weiss J.J. Rosowski, W.T. Peake. A model for signal transmission in an ear having hair cells with free-standing stereocilia. ii. macromechanical stage. *Biophysical Journal*, 20:139–155, 1985.
- [74] T. Nakagawa T.M. Jung N.J. Coker H.A. Jenkins R.A. Eatock W.E. Brownnell J.S. Oghalai, J.R. Holt. Ionic currents and electromotility in inner ear hair cells from humans. *Journal of Neurophysiology*, 79:2235–2239, 1998.
- [75] W.E. Brownell K.V. Snyder, F. Sachs. *Sensors and Sensing in Biology and Engineering*. Springer Verlag, 2003.
- [76] Y.D. Landau. *Adaptive Control: The Model Reference Approach*. Marcel Dekker, inc., 1979.
- [77] K. Liem. *Functional Anatomy of the Vertebrates: Evolutionary Perspective: Third Edition*. Harcourt College Publishers, 2001.
- [78] A.E.H. Love. *A Treatise on the Mathematical Theory of Elasticity*. Dover Publication, 1944.
- [79] A.N. Lukashkin and I.J. Russel. A descriptive model of the receptor potential nonlinearities generated by the hair cell mechanoelectrical transducer. *The Journal of Acoustical Society of America*, 103(2):973–980, 1998.
- [80] K.H. Iwasa M. Adachi, M. Sukiwara. Effect of turgor pressure on outer hair cell motility. *The Journal of Acoustical Society of America*, 108(5):2299–2306, 2000.

- [81] R. Maddis. Simulation of mechanical to neural transduction in the auditory receptor. *The Journal of Acoustical Society of America*, 79(3):702–711, 1986.
- [82] G.A. Manley. *Peripheral Hearing Mechanism in Reptiles and Birds*. Springer-Verlag, 1990.
- [83] P. Martin and A.J. Hudspeth. Active hair-bundle movements can amplify a hair cell’s response to oscillatory mechanical stimuli. *Proceeding of the National Academy of Science*, 96(25):14306–14311, 1999.
- [84] D.Z.Z. He X. Wu S. Jia J. Zuo M.C. Liberman, J. Gao. Prestin is required for electromotility of the outer hair cell and for the cochlear amplifier. *Nature*, 419:300–304, 2002.
- [85] G.F. Smoorenburg M.G. van Emst, C. Gifuere. The generation of dc potentials in a computational model of the organ of corti: effects of voltage-dependent k⁺ channels in the basolateral membrane of the inner hair cell. *Hearing Research*, 115:184–196, 1998.
- [86] D.C. Mountain and A.E. Hubbard. A piezoelectric model of outer hair cell function. *The Journal of Acoustical Society of America*, 95(1):350–354, 1994.
- [87] A. Mukherjee and A.S. Chaudhuri. Piezolaminated beams with large deformations. *International Journal of Solids and Structures*, 39:4567–4582, 2002.
- [88] A. Nygren W.E. Brownell N. Morimoto, R.M. Raphael. Excess plasma membrane and effects of ionic amphipaths on mechanics of outer hair cell lateral wall. *American Journal of Physiology - Cell Physiology*, 282:c1076–c1086, 2002.
- [89] S.T. Neely. *Electromechanical tuning in outer hair cells*. Boys Town National Research Hospital, 2001.

- [90] S.T. Neely and D.O. Kim. An active cochlear model showing sharp tuning and high sensitivity. *Hearing Research*, 9:123–130, 1983.
- [91] Notcatfish.com. *Ichthgology Web*. <http://www.notcatfish.com/ichthgology/lateralline.htm>, 2001.
- [92] R. Ohba. *Intelligent Sensor Technology*. John Wiley & Sons, England, 1992.
- [93] B.N. Evans P. Dallos, R. Hallworth. Theory of electrically driven shape changes of cochlear outer hair cells. *Journal of Neurophysiology*, 70(1):299–323, 1993.
- [94] A.J. Hudspeth P. Martin, A.D. Mehta. Negative hair-bundle stiffness betrays a mechanism for mechanical amplification by the hair cell. *Proceeding of the National Academy of Science*, 97(22):12026–12031, 2000.
- [95] H.M. Paynter. *Analysis and Design of Engineering Systems*. MIT Press, 1961.
- [96] R. Plonsey and R.C. Barr. *Bioelectricity: A Quantitative Approach*. Plenum Press, 1988.
- [97] S.S. Rao. *Mechanical Vibrations: Fourth Edition*. Pearson Education Inc., 2004.
- [98] G.P. Gibbs R.L. Clark, W.R. Saunders. *Adaptive Structures, Dynamics & Control*. John Wiley & Sons, 1998.
- [99] W.E. Brownnell R.M. Raphael, A.S. Popel. A membrane bending model of outer hair cell electromotility. *Biophysical Journal*, 76:2844–2862, 2000.
- [100] R.R. Fay R.R. Hoy, A.N. Popper. *Comparative Hearing: Insects*. Springer-Verlag, 1998.

- [101] A.V. Schalik. *A Simple Inner Hair Cell Model*. <http://diwww.epfl.ch/lami/team/vschaik/eap/ihc.html>, 1995.
- [102] C. Schwartz and R. Gran. Describing function analysis using matlab and simulink. *IEEE Control Systems Magazine*, pages 19–26, 2001.
- [103] H.E. Secker-Walker and C.L. Searle. Time-domain analysis of auditory-nerve-fiber firing rates. *The Journal of Acoustical Society of America*, 88(3):1427–1436, 1990.
- [104] L. Sellami and R.W. Newcomb. Ear-type analog and digital systems. *Recent Research and Development in Circuits and Systems*, 1:59–83, 1996.
- [105] A.A. Spector. On the mechano-electrical coupling in the cochlear outer hair cell. *The Journal of Acoustical Society of America*, 107(3):1435–1441, 2000.
- [106] S. Suranthiran and S. Jayasuriya. Utilizing sensor arrays to attain high-operating bandwidth. *Journal of Dynamic Systems, Measurement, and Control*, 126:294–302, 2004.
- [107] J.J. Rosowski T.F. Weiss, W.T. Peake. A model for signal transmission in an ear having hair cells with free-standing stereocilia. i. empirical basis for model structure. *Hearing Research*, 20:131–138, 1985.
- [108] S. Timoshenko. *Theory of Plates and Shells*. McGraw-Hill, 1940.
- [109] J.A. Tolomeo and C.R. Steele. Orthotropic piezoelectric properties of the cochlear outer hair cell wall. *The Journal of Acoustical Society of America*, 97(5):3006–3011, 1995.
- [110] J.A. Tolomeo and C.R. Steele. A dynamic model of outer hair cell motility including intracellular and extracellular fluid viscosity. *The Journal of Acoustical Society of America*, 103(1):524–534, 1998.

- [111] V. Tsuprun and P. Santi. Helical structure of hair cell stereocilia tip link in the chinchilla cochlea. *Journal of the Association for Research in Otolaryngology*, 2000.
- [112] T.D. Lamb A. Menini V. Torre, J.F. Ashmore. Transduction and adaptation in sensory receptor cells. *Journal of Neuroscience*, 15:7757–7768, 1995.
- [113] A. van Schalik and R. Maddis. Analog very large-scale integrated (vlsi) implementation of a model of amplitude-modulation sensitivity in the auditory brainstem. *The Journal of Acoustical Society of America*, 105(2):811–821, 1999.
- [114] A. Vilfan and T. Duke. Two adaptation processes in auditory hair cells together can provide an active amplifier. *Biophysical Journal*, 85:191–203, 2003.
- [115] M.H. Goldstein W. Liu, A.G. Andreou. Voiced-speech representation by an analog silicon model of the auditory periphery. *IEEE Transactions on Neural Networks*, 3(3):447–487, 1992.
- [116] C. Wangcharoenrung and R. Longoria. A bond graph model of outer hair cell active force generation. *Proceeding of 2003 International Conference on Bond Graph Modeling and Simulation*, 35(2):257–265, 2003.
- [117] E.G. Waver. *The Reptile Ear*. Princeton University Press, 1978.
- [118] E.G. Waver. *The Amphibian Ear*. Princeton University Press, 1985.
- [119] D. Bertrand Y. De Ribaupierre W.E. Brownell, C. Bader. Evoked mechanical responses of isolated cochlear outer hair cells. *Science*, 227:194–196, 1985.

- [120] R.M. Raphael A.S. Popel W.E. Brownell, A.A. Spector. Micro and nanomechanics of the cochlear outer hair cell. *Annual Reviews in Biomedical Engineering*, 3:169–194, 2001.
- [121] J.G. Webster. *Medical Instrumentation: Application and Design, third edition*. John Willey & Sons, 1998.
- [122] T.F. Weiss. Bidirectional transduction in vertebrate hair cells: A mechanism for coupling mechanical and electrical process. *Hearing Research*, 7:353–360, 1982.
- [123] T.F. Weiss and R. Leong. A model for signal transmission in an ear having hair cells with free-standing stereocilia. iii. micromechanical stage. *Hearing Research*, 20:157–174, 1985.
- [124] T.F. Weiss and R. Leong. A model for signal transmission in an ear having hair cells with free-standing stereocilia. iv. mechanoelectric transduction stage. *Hearing Research*, 20:175–195, 1985.
- [125] P. Wellstead and B. Zarrop. *Self-Tuning Systems: Control and Signal Processing*. John Willey & Sons, 1991.
- [126] R.M. White. A sensor classification scheme. *IEEE Transactions on ultrasonics, ferroelectrics, and frequency control*, 34:124–126, 1987.
- [127] J. Wilson. A practical approach to vibration detection and measurement, part 1: Physical principles and detection techniques. *Sensors Magazine*, 16(2), 1999.
- [128] A.J. Hudspeth Y. Choe, P. Martin. A model for amplification of hair-bundle motion by cyclical binding of Ca^{2+} to mechanoelectrical-transduction chan-

- nels. *Proceeding of the National Academy of Science of the United States of America*, 95(26):15321–15326, 1998.
- [129] R. Fettiplace YC. Wu, A.J. Ricci. Two components of trasducer adaptation in auditory hair cells. *Journal of Neurophysiology*, 82(5):2171–2181, 1999.
- [130] J. Zou J. Li C. Liu F. Delcomyn Z. Fan, J. Chen. Development of artificial lateral-line flow sensors. *Proceeding of Solid-state Sensor, Actuator and Microsystems Workshop*, pages 169–172, 2002.

Vita

Chayawee Wangcharoenrung was born to Chaiyaporn and Wallapa Wangcharoenrung in Bangkok, Thailand on December 26, 1974. After graduating from Kasetsart University in Bangkok, Thailand in 1994 with a B.Eng. in Mechanical Engineering, he worked as a system engineer for Konoike Construction for three years. There, he had an opportunity to supervise system installations of some of the most famous buildings in the country.

In 1997, Chayawee received one of the most prestigious scholarships in Thailand, the Government of Thailand Scholarship, to continue his studies. Later that year, he was admitted to graduate school at The University of Texas at Austin, where he received an M.S. in Mechanical Engineering (Dynamic Systems and Control) in 1999 and subsequently pursued a Ph.D. in Mechanical Engineering (Biomechanics).

Permanent address: 21/29 Intramara 3 Suttisan rd. Samsennai
Phayathai Bangkok 10400 Thailand

This dissertation was typeset with L^AT_EX[†] by the author.

[†]L^AT_EX is a document preparation system developed by Leslie Lamport as a special version of Donald Knuth's T_EX Program.